THE SEARCH FOR A CP-ODD LIGHT HIGGS BOSON IN UPSILON 1S DATA AT BELLE

A DISSERTATION SUBMITTED TO THE GRADUATE DIVISION OF THE
UNIVERSITY OF HAWAIʻI AT MĀNOA IN PARTIAL FULFILLMENT
OF THE REQUIREMENTS FOR THE DEGREE OF

DOCTOR OF PHILOSOPHY

IN

PHYSICS

AUGUST 2013

By
Jamal Tildon Rorie

Dissertation Committee:

Gary S. Varner, Chairperson
Tom Browder
Nick Kaiser
John Madey
Xerxes Tata

We certify that we have read this dissertation and that, in our opinion, it is satisfactory in scope and quality as a dissertation for the degree of Doctor of Philosophy in Physics.

DISSERTATION COMMITTEE

Chairperson

I dedicate this work to my parents, Wilson and Marilyn Rorie, who opened the path before me and were behind me for every step.

Acknowledgements

While my name alone appears on the cover of this dissertation, it would not have been possible without help from many other people. What follows is a (woefully incomplete) list of those who have contributed to my research and have helped me along the way.

First and foremost I'd like to thank Gary Varner for all of his help, his advice, and his seemingly infinite reserve of patience throughout the course of my studies. Thanks for always keeping a 5 PM time slot open for me. I also owe a great debt to Roberto Mussa: without his assistance at KEK and during our bi-weekly teleconferences, none of this would have been possible. And thank you to Bob and Doris pulley and the ARCS foundation for their support of my research.

Along the way I've received guidance from many sources. Tom Browder, Mike Jones, Igal Jeagle, Sven Vahsen, Matt Barrett, Steve Olsen and the rest of the UH Belle collaboration have given me a wealth of feedback on all aspects of my research. Karim Trabelsi, Sadaharu Uehara-san, Mikihiko Nakao-san, Kenji Inami-san, Takeo Higuchi-san, and many others made it possible for me to conduct my work with both hardware and data analysis in Japan. Finally, contributors from all over the world came together in the $\Upsilon(123S)$ meetings to share ideas, refine techniques, eliminate bugs, and prepare presentations.

My fellow Belle students were invaluable. Special thanks to Hulya Guler for getting me started by sharing her analysis code and to Kurtis Nishimura and Himansoo Sahoo for answering innumerable questions towards the end. Thanks to Kirika Uchida for showing me the ropes with Belle and making sure someone kept an eye on me during my first trips to KEK. My time in Japan would likely have been miserable without being shepherded by Jeremy Dalseno and Minori Watanabe.

I'm grateful for all of the friends I've met in Hawaii. Andrew Box, Saadia Kemal, and Nick Kent; the trio that introduced me to Honolulu and have kept me company ever since. Matt Andrew and Jess Way, two great friends that have listened to my unfunny rambling for hours. Peter Grach and his lovely family, who've so graciously opened their home to me on more occasions than I can remember. Mike, Sarah, and Adela Hadmack; who know there's always money in the banana stand. Jeremy Kowalczyk and Matt Chasse, who were always up for karaoke and down "to go beach". Elena Martin, Larry Ruckman, and the rest of the ID Lab for putting up with my forays into electronics. And last, but certainly not least, the best officemate one could ask for: Mike Cooney.

Thank you all.

ABSTRACT

We conduct a search for a CP-odd light Higgs, A^0, in a sample of $(102 \pm 2) \times 10^6$ $\Upsilon(1S)$ by looking for $\Upsilon(1S) \to \gamma A^0$ radiative decays with $A^0 \to \tau^+\tau^-$. No significant evidence of such decays is found. We set an 90% confidence level upper limit on $BR(\Upsilon(1S) \to \gamma A^0) \times BR(A^0 \to \tau^+\tau^-)$ between 4.0×10^{-6} to 4.5×10^{-5} for A^0 masses ranging from 3.6 GeV to 9.3 GeV. This represents a twofold improvement on current world limits for using $\Upsilon(1S)$ from $e^+e^- \to \Upsilon(1S)$ production and is in agreement with recent limits using $\Upsilon(1S)$ from $\Upsilon(3S) \to \pi\pi\Upsilon(1S)$ decays.

Contents

Acknowledgements **v**

Abstract **vi**

List of Tables **xi**

List of Figures **xii**

List of Acronyms **xx**

1 Physics Background & Motivation **1**
- 1.1 Overview . . . 1
- 1.2 Particles I: Leptons & Quarks . . . 1
- 1.3 Forces . . . 3
  - 1.3.1 The Electromagnetic Force . . . 3
  - 1.3.2 The Strong Force . . . 4
  - 1.3.3 The Weak Force . . . 5
  - 1.3.4 Electroweak Unification . . . 6
- 1.4 Particles II: Hadrons . . . 6
  - 1.4.1 The Υ Resonances . . . 7
- 1.5 The Higgs Boson . . . 9
  - 1.5.1 Motivation for a Higgs Boson . . . 9
  - 1.5.2 The Higgs Mechanism . . . 10
  - 1.5.3 The CP-Odd Light Higgs Boson . . . 10
  - 1.5.4 Searching for the CP-Odd Light Higgs Boson . . . 11

2 Experimental Apparatus **13**
- 2.1 Overview . . . 13
- 2.2 KEKB . . . 14
- 2.3 The Interaction Region . . . 15
- 2.4 Silicon Vertex Detector (SVD) . . . 16
- 2.5 Extreme Forward Calorimeter (EFC) . . . 18
- 2.6 Central Drift Chamber (CDC) . . . 18
- 2.7 Aerogel Cherenkov Counter (ACC) . . . 22
- 2.8 Time of Flight (TOF) . . . 24

2.9 Electromagnetic Calorimeter (ECL) 26
2.10 K_L Muon Discriminator (KLM) 30
2.11 Triggers & Data Collection 32
2.11.1 Online Triggers 32
2.11.2 Offline Triggers 33
2.12 Particle Identification 33
2.12.1 Electron Identification (eid) 33
2.12.2 Muon Identification (muid) 34
2.12.3 Photon Identification 36

3 Analysis **37**
3.1 Overview 37
3.2 Data 38
3.3 Monte Carlo 40
3.3.1 Off-Resonance $e^+e^-\to\tau^+\tau^-$ Quantity 40
3.3.2 On-Resonance $e^+e^-\to\tau^+\tau^-$ Quantity 41
3.3.3 On-Resonance $\Upsilon(1S)\to\tau^+\tau^-$ Quantity 41
3.3.4 Signal $\Upsilon(1S)\to\gamma A^0$ 41
3.3.5 $e^-e^+\to\tau^+\tau^-$ MC Generation 41
3.3.6 $\Upsilon(1S)\to\tau^+\tau^-$ MC Generation 42
3.3.7 $\Upsilon(1S)\to\gamma A^0$ MC Generation 43
3.3.8 Detector Simulation 44
3.4 Electron-Muon Off-Resonance Tau-Pair MC Study 45
3.4.1 Data Skim Criteria 45
3.4.2 Trigger Selection Cuts 45
3.4.3 Initial Tau Sample Selection Criteria 45
3.4.4 The "e+μ" and the Kinematic Boundary Selection Criteria 46
3.4.5 Fine Tau Sample Selection Criteria 49
3.4.6 Results 51
3.5 Electron-Muon Off-Resonance Photon Background MC Study 52
3.5.1 Initial Photon Cuts 52
3.5.2 Results 55
3.6 Electron-Muon On-Resonance Photon Background MC Study 55
3.7 Electron-Muon Photon Signal MC Study 57
3.7.1 Tuning 58
3.7.2 Summary of Optimized "e & μ" Cuts 72
3.7.3 Cut Signal Efficiency 73
3.8 1-Prong Off-Resonance Tau-Pair MC Study 74
3.8.1 Initial Tau Selection Criteria 74
3.8.2 Further Tau Sample Selection Criteria 75
3.8.3 Results 78
3.9 1-Prong Off-Resonance Photon Background MC Study 78
3.9.1 π^0-Decay Background Reduction 80
3.9.2 Bremsstrahlung 81
3.9.3 Initial State Radiation 81

3.9.4 Beam Background . . . 81
3.10 1-Prong On-Resonance Photon Background MC Study . . . 82
3.11 1-Prong Photon Signal MC Study . . . 86
3.11.1 Tuning . . . 86
3.11.2 Summary of Optimized 1-Prong Cuts . . . 101
3.11.3 Cut Signal Efficiency . . . 102
3.12 Fitting/Limit . . . 103
3.12.1 Algorithm Designs . . . 103
3.12.2 Testing . . . 113
3.12.3 Results . . . 113
3.13 Systematics . . . 117
3.13.1 Discrepancy Between Data and MC Photon Energy . . . 117
3.13.2 Background Fit Systematics . . . 117
3.13.3 Signal Fit Systematics . . . 119
3.13.4 Fit Window Width . . . 120
3.13.5 Efficiency Interpolation . . . 120
3.13.6 Lepton ID . . . 120
3.13.7 Tracking . . . 121
3.13.8 Photon Energy Resolution . . . 121
3.13.9 Photon Detection Efficiency . . . 122
3.13.10 Overall Systematic Error . . . 122

4 Conclusion 124

A Combined Upper Limit 129
A.1 Introduction . . . 129
A.2 Notation Change . . . 129
A.3 Selection Criteria . . . 129
A.4 Branching Ratios . . . 129
A.5 Selection Efficiency . . . 130
A.6 Photon Background Fitting . . . 131
A.7 Simultaneous Fitting . . . 131
A.8 Upper Limit Calculation . . . 131

B Tables of Results 133
B.1 Introduction . . . 133
B.2 Significance . . . 133
B.3 Upper Limit . . . 133

C The STaR Board 139
C.1 Introduction . . . 139
C.1.1 Board Overview . . . 139
C.2 Hardware . . . 140
C.2.1 Data In . . . 141
C.2.2 Data Out . . . 141
C.2.3 Clock . . . 141

C.2.4 COPPER Interface (I/O and Local Bus) 141
C.2.5 Diagnostics and FPGA Programming 141
C.3 Firmware 142
C.3.1 HPTDC Operation 142
C.3.2 LABRADOR 3 Operation 143
C.3.3 Testing 143
C.4 IEEE Abstract 144

D The Tau Skim **147**
D.1 The Tau Skim 147

List of Tables

1.1 Lepton Properties 2
1.2 Quark Properties 2
1.3 The Forces of the Standard Model 3

2.1 Summary of ECL properties 29

3.1 Summary of Effects of “e & μ” Tau Selection Cuts on Data and MC 50
3.2 Summary of Effects of “e & μ” Photon Selection Cuts on Data and MC . . 54
3.3 Summary of Effects of All Tuned “e & μ” Cuts on Off-Resonance Data and MC 73
3.4 Summary of Effects of 1-Prong Tau Selection Cuts in Data and MC 77
3.5 Summary of Effects of 1-Prong Photon Selection Cuts in Data and MC . . 82
3.6 Summary of Effects of All Tuned 1-Prong Selection Cuts on Data and MC . 102
3.7 Fit Parameters for Backgrounds with “e & μ” Selection Cuts in On-Resonance MC 105
3.8 Fit Parameters for Backgrounds with “e & μ” Selection Cuts in On-Resonance Data 106
3.9 Fit Parameters for Backgrounds with 1-Prong Selection Cuts in On-Resonance MC 106
3.10 Fit Parameters for Backgrounds with 1-Prong Selection Cuts in On-Resonance Data 106
3.11 Lepton ID Error Table 121

B.1 First table of significance results for the “1-prong ”data set. 134
B.2 Second table of significance results for the “1-prong ”data set. 135
B.3 Third table of significance results for the “1-prong ”data set. 136
B.4 First table of 90% confidence level BR upper limits in “1-prong” data. . . . 137
B.5 Second table of 90% confidence level BR upper limits in the “1-prong” data. 138

List of Figures

1.1 World data on the total cross section of $e^+e^- \rightarrow hadrons$ and the ratio $R(s) = \sigma(ee \rightarrow \text{hadrons}, s)/\sigma(ee \rightarrow \mu\mu, s)$. In this plot $\sigma(ee \rightarrow \text{hadrons}, s)$ is the experimental cross section corrected for initial state radiation and electron-positron vertex loops, $\sigma(ee \rightarrow \mu\mu, s) = 4\pi\alpha^2(s)/3s$.[2] 7
1.2 Cross section for e^+e^- annihilations to hadrons at CESR (CUSB data) [8]. 8
1.3 Diagrams [16] for the decay of an Υ to a photon and CP-odd light Higgs boson, A^0. This mechanism was first proposed by F. Wilczek as $q\bar{q} \rightarrow \gamma A^0$ [13] with the vector meson $q\bar{q}$ left unspecified. 11

2.1 Isometric cut-away view of the Belle detector showing the relative location of the e^+ and e^- beams, sub-detectors, and the main solenoid. 14
2.2 Overhead diagram of the storage rings and e^-e^+ production area at KEK. The Belle detector is located at the Tsukuba area interaction point in the upper right of this diagram. 15
2.3 The IP and surrounding beam pipe, particle masks, and location of magnets. The axes are on different scales, to highlight structural details. 16
2.4 SVD1 configuration in the Belle detector and diagram of DSSD with support structure on ladder. Left: axial view of SDV configuration showing three layers. Top: profile view of SVD layers and relation to the IP. Bottom: SVD in isometric view, detector strips highlighted. Figure modified from Ref [17]. 17
2.5 Front and back isometric views of the Bismuth Germanium Oxide (BGO) crystals that compromise the Extreme Forward Calorimeter. Figure modified from Ref [17]. 18
2.6 A cross section of the CDC in profile (left) and in axial view (right). 19
2.7 Configuration of CDC components. Left: configuration of sense and field wires with the z-axis going into the page. Wire diameters are not to scale. Right: configuration of wires near inner radius of CDC. The solid black lines are the CDC inner radius (inner black line) and a CFRP support cylinder (outer black line). 19
2.8 Gas gain (a) and drift velocity (b) plots for the helium-ethane gas mixture in the Central Drift Chamber. Plots taken from Ref. [17] 20
2.9 A scatter plot of measured mean energy loss values (labeled here as dE/dx) in the CDC versus particle momentum. Curves represent expected values for pions, kaons, protons, and electrons. 22

2.10 Layout of the Belle composite Particle Identification system. The positions of the barrel and endcap ACC modules are shown. 23
2.11 Two ACC module designs: a) An ACC module located in the barrel region. Aerogel layers are stacked into a block and encased in Goretex and a thin sheet of aluminum. One or two PMTs are attached. b) An ACC module located in the endcap region. The aerogel layers are encased in Carbon Fiber Reinforced Plastic (CFRP) and a light guide directs Cherenkov radiation to a PMT offset from the likely path of radiation created by particle interaction while traversing the detector. 23
2.12 ACC performance. Left: pulse height spectra for 3.5 GeV pions and protons in a single ACC module. Measurements taken in a 1.5 T field. Right: pulse height spectra for $K^{\pm}$ and Bhabha electrons in units of photoelectrons observed by the barrel ACC inside of the Belle detector. 24
2.13 A schematic view of a Time of Flight module. Top: A TOF scintillator bar (marked TOF), a Trigger Scintillator Counter (TSC) panel, and their respective PMTs are shown in profile. The relative positions of the TOF and TSC are shown. Lower left: light guide and panel for the TSC. Lower right: relative placement of TSC and TOF PMT's. 25
2.14 TOF timing performance. Left: TOF time resolution measured with μ-pair events. The quoted average uncertainty of 100ps taken from the maximum of the weighted average of the uncertainty from both ends of the TOF. Right: spectra of arrival times for kaons, pions, and protons below 1.2 GeV. 26
2.15 Electromagnetic Calorimeter (ECL) layout. Barrel region shown in profile; endcap region shown axially. Polar angle coverage and angle of ECL modules relative to the Interaction Point are shown. 27
2.16 The mechanical assembly of an ECL counter. A thallium doped cesium iodide (CsI(Tl)) crystal is oriented towards the interaction point. All sides of the crystal, except for the side furthest from the IP, are covered with telfon (for handling the crystal) and aluminum (for light and electrical shielding). The uncovered far face has two photodiodes mounted for signal readout. 28
2.17 ECL energy resolution as a function of incident photon energy for the (a) 3 $\times$ 3 and (b) 5 $\times$ 5 matrices with a 0.5 MeV threshold. Tests were conducted on a 6x6 array of ECL units at the VEPP-4 collider. A photon beam was incident upon the 4 central ECL units at an angle perpendicular to their surface. Plots modified from Ref [17]. 29
2.18 Cross-section of a KLM superlayer. Two resistive plate counter (RPC) layers are sandwiched between readout strips for the θ measurement on one side and ϕ measurement on the other. These superlayers are set between alternating iron layers that provide interaction materials for incident particles (not shown). 31
2.19 KLM performance. Left: muon identification efficiency as a function of transverse momentum. Right: muon fake rate as a function of transverse momentum. 31
2.20 Electron identification using multiple subsystems. Electron (solid) and pion (dashed) spectra for a) E/p b) E9/E25 c) dE/dx are shown and clearly differentiated. 35

3.1 Plot of the ratio of $\mu^+\mu^-$ to e^+e^- events during a scan of beam energies used to find the $\Upsilon(1S)$ production energy at Belle. 39
3.2 Υ(1S) accumulation using $\mu^+\mu^-$ counts in online data taken while the run was in progress. 39
3.3 Accelerator information including beam current and online luminosity measurements from KEKB during the Υ(1S) run. 40
3.4 The e+μ total momentum in the CM frame vs invariant mass, in off-resonance MC (top) and experimental data (bottom) 47
3.5 Ratio of C.M. e+μ momentum to e+μ invariant mass vs the Kinematic Boundary parameter, in MC (top) and experimental data (bottom) 48
3.6 KB parameter distribution (x-axis projection of Fig. 3.5) Data (black) and MC (red). 49
3.7 Ratio of C.M. e+μ momentum to e+μ invariant mass distribution (y-axis projection of Fig. 3.5). Data (black) and MC (red). 50
3.8 The opening angle between the two charged tracks in the cm frame. All "e & μ" tau selection cuts applied. MC and experimental data are both off-resonance. 51
3.9 The invariant mass of the e+μ combined particle. All "e & μ" tau selection cuts applied. MC and experimental data are both off-resonance. 52
3.10 Plot of α_{Brem} in off-resonance MC in both linear and (inset) log vertical scale. A clear transition between bremsstrahlung dominant and recessive regions can be seen. 53
3.11 Backgrounds in photon spectrum, all cuts in tau section applied. 54
3.12 Photon spectrum, all cuts applied, 0 to 4.5 GeV. 55
3.13 Angular distribution of beam background photons in ϕ. The red line is ten times (10x) the contribution from photons above 150 MeV. Black line is the overall contribution, unscaled. All "e & μ" tau and photon selection cuts applied. 56
3.14 Distribution of all beam background photons in ϕ and CM Cos(θ). All "e & μ" tau and photon selection cuts applied. 57
3.15 Figure of merit and efficiency for missing energy cut low side, 3.6 GeV/c^2 A^0 mass, "e & μ" cuts 59
3.16 Figure of merit and effciency for missing energy cut low side, 9.3 GeV/c^2 A^0 mass, "e & μ" cuts 59
3.17 Figure of merit and efficiency for missing energy cut high side, 3.6 GeV/c^2 A^0 mass, "e & μ" cuts 60
3.18 Figure of merit and effciency for missing energy cut high side, 9.3 GeV/c^2 A^0 mass, "e & μ" cuts 60
3.19 Figure of merit for missing angle cut low side, 3.6 GeV/c^2 A^0 mass, "e & μ" cuts 61
3.20 Figure of merit for missing angle cut low side, 9.3 GeV/c^2 A^0 mass, "e & μ" cuts 61
3.21 Figure of merit for missing angle cut high side, 3.6 GeV/c^2 A^0 mass, "e & μ" cuts 62

3.22 Figure of merit for missing angle cut high side, 9.3 GeV/c^2 A^0 mass, "e & μ" cuts 62
3.23 Figure of merit and efficiency for muon probability P(μ), 3.6 GeV/c^2 A^0 mass, "e & μ" cuts 63
3.24 Figure of merit and efficiency for muon probability P(μ), 9.3 GeV/c^2 A^0 mass, "e & μ" cuts 63
3.25 Figure of merit for electron probability P(e), 3.6 GeV/c^2 A^0 mass, "e & μ" cuts 64
3.26 Figure of merit for electron probability P(e), 9.3 GeV/c^2 A^0 mass, "e & μ" cuts 64
3.27 Figure of merit and efficiency for kinematic boundary cut, 3.6 GeV/c^2 A^0 mass, "e & μ" cuts 65
3.28 Figure of merit and efficiency for kinematic boundary cut, 9.3 GeV/c^2 A^0 mass, "e & μ" cuts 65
3.29 Figure of merit and efficiency for the cos(θ) cut in CM frame low-side cut, 3.6 GeV/c^2 A^0 mass, "e & μ" cuts 66
3.30 Figure of merit and efficiency for the cos(θ) cut in CM frame low-side cut, 9.3 GeV/c^2 A^0 mass, "e & μ" cuts 67
3.31 Figure of merit and efficiency for the cos(θ) cut in CM frame high-side cut, 3.6 GeV/c^2 A^0 mass, "e & μ" cuts 67
3.32 Figure of merit and efficiency for the cos(θ) cut in CM frame high-side cut, 9.3 GeV/c^2 A^0 mass, "e & μ" cuts 68
3.33 Figure of merit and efficiency for π^0 low-side cut, 3.6 GeV/c^2 A^0 mass, "e & μ" cuts 68
3.34 Figure of merit and efficiency for π^0 low-side cut, 9.3 GeV/c^2 A^0 mass, "e & μ" cuts 69
3.35 Figure of merit and efficiency for π^0 high-side cut, 3.6 GeV/c^2 A^0 mass, "e & μ" cuts 69
3.36 Figure of merit and efficiency for π^0 high-side cut, 9.3 GeV/c^2 A^0 mass, "e & μ" cuts 70
3.37 Figure of merit and efficiency for π^0 low-side cut, zoomed, 3.6 GeV/c^2 A^0 mass, "e & μ" cuts 70
3.38 Figure of merit and efficiency for π^0 low-side cut, zoomed, 9.3 GeV/c^2 A^0 mass, "e & μ" cuts 71
3.39 Figure of merit and efficiency for π^0 high-side cut, zoomed, 3.6 GeV/c^2 A^0 mass, "e & μ" cuts 71
3.40 Figure of merit and efficiency for π^0 high-side cut, zoomed, 9.3 GeV/c^2 A^0 mass, "e & μ" cuts 72
3.41 Efficiency of Pure Higgs MC that pass all tuned "e & μ" cuts. 74
3.42 Missing energy in the CM frame with 1-prong cuts. Red is MC, black is data. MC and experimental data are both off-resonance. 75
3.43 Angular distribution of missing energy in the CM frame, detector features noted on plot. Red is MC, black is experimental data. MC and experimental data are both off-resonance. 76

3.44 The θ and ϕ distribution of missing momentum in the CM frame with 1-prong cuts. 76
3.45 Opening angle between positive and negative tracks with all 1-prong cuts applied. 77
3.46 Photon spectrum in off-resonance data, all 1-prong cuts applied. Red is MC, black is experimental data. 78
3.47 Plot of the contributions of γ sources to the photon background in off-resonance MC a) before and b) after photon background reduction cuts are applied. π^0 (red) dominates over the spectrum above 100 MeV 79
3.48 Plot of the 2 photon invariant mass in on-resonance 1-prong MC. For each event, $\gamma_{fake\_candidate}$ was paired with all $\gamma_{fake\_partner}$ and every $M_{\gamma\gamma}$ is entered on the histogram. 80
3.49 Plot of the angular distribution of ISR in the CM frame for on-resonance data. ISR photons identified by having a mother with GenHepEvent ID of either 1 or 2. 82
3.50 Angular distributions of photons in tuned on-resonance 1-prong MC, $\cos(\theta)_{CM}$ and ϕ. E_γ is restricted to: a) 0.150 GeV $< E_\gamma <$ 0.500 GeV, b) 0.5 GeV $< E_\gamma <$ 0.8 GeV, c) 0.8 GeV $< E_\gamma <$ 1.5 GeV, d) 1.5 GeV $< E_\gamma <$ 4.0 GeV. 84
3.51 Distribution of peaking beam background in tuned on-resonance 1-prong MC. E_γ is restricted to be between 0.150 GeV and 0.300 GeV in the CM frame. The beam background contribution is localized in angular distribution. . . . 85
3.52 Angular distribution of beam background in 1-prong MC for Eγ energies from 150 MeV to 300 MeV (left) and from 180 MeV to 300 MeV (right). . 85
3.53 Figure of merit and efficiency for missing energy cut low side, 3.6 GeV/c^2 A^0 mass, 1-prong cuts 87
3.54 Figure of merit and efficiency for missing energy cut low side, 9.3 GeV/c^2 A^0 mass, 1-prong cuts 87
3.55 Figure of merit and efficiency for missing energy cut high side, 3.6 GeV/c^2 A^0 mass, 1-prong cuts 88
3.56 Figure of merit and effciency for missing energy cut high side, 9.3 GeV/c^2 A^0 mass, 1-prong cuts 88
3.57 Figure of merit for missing angle cut low side, 3.6 GeV/c^2 A^0 mass, 1-prong cuts 89
3.58 Figure of merit for missing angle cut low side, 9.3 GeV/c^2 A^0 mass, 1-prong cuts 89
3.59 Figure of merit for missing angle cut high side, 3.6 GeV/c^2 A^0 mass, 1-prong cuts 90
3.60 Figure of merit for missing angle cut high side, 9.3 GeV/c^2 A^0 mass, 1-prong cuts 90
3.61 Figure of merit and efficiency for muon probability P(μ), 3.6 GeV/c^2 A^0 mass, 1-prong cuts 91
3.62 Figure of merit and efficiency for muon probability P(μ), 9.3 GeV/c^2 A^0 mass, 1-prong cuts 91
3.63 Figure of merit for electron probability P(e), 3.6 GeV/c^2 A^0 mass, 1-prong cuts 92

3.64 Figure of merit for electron probability P(e), 9.3 GeV/c^2 A^0 mass, 1-prong cuts . . . 92
3.65 Figure of merit for electron bremsstrahlung cut. Left: 9.3 GeV/c^2 A^0 mass. Right: 3.6 GeV/c^2 A^0 mass. 1-prong cuts. . . . 93
3.66 Figure of merit and efficiency for E9/E25 cut, 9.3 GeV/c^2 A^0 mass, 1-prong cuts . . . 94
3.67 Figure of merit and efficiency for the cos(θ) cut in CM frame low-side cut, 3.6 GeV/c^2 A^0 mass, 1-prong cuts . . . 95
3.68 Figure of merit and efficiency for the cos(θ) cut in CM frame low-side cut, 9.3 GeV/c^2 A^0 mass, 1-prong cuts . . . 95
3.69 Figure of merit and efficiency for the cos(θ) cut in CM frame high-side cut, 3.6 GeV/c^2 A^0 mass, 1-prong cuts . . . 96
3.70 Figure of merit and efficiency for the cos(θ) cut in CM frame high-side cut, 9.3 GeV/c^2 A^0 mass, 1-prong cuts . . . 96
3.71 Figure of merit and efficiency for π^0 low-side cut, 3.6 GeV/c^2 A^0 mass, 1-prong cuts . . . 97
3.72 Figure of merit and efficiency for π^0 low-side cut, 9.3 GeV/c^2 A^0 mass, 1-prong cuts . . . 98
3.73 Figure of merit and efficiency for π^0 high-side cut, 3.6 GeV/c^2 A^0 mass, 1-prong cuts . . . 98
3.74 Figure of merit and efficiency for π^0 high-side cut, 9.3 GeV/c^2 A^0 mass, 1-prong cuts . . . 99
3.75 Figure of merit and efficiency for π^0 low-side cut, zoomed, 3.6 GeV/c^2 A^0 mass, 1-prong cuts . . . 99
3.76 Figure of merit and efficiency for π^0 low-side cut, zoomed, 9.3 GeV/c^2 A^0 mass, 1-prong cuts . . . 100
3.77 Figure of merit and efficiency for π^0 high-side cut, zoomed, 3.6 GeV/c^2 A^0 mass, 1-prong cuts . . . 100
3.78 Figure of merit and efficiency for π^0 high-side cut, zoomed, 9.3 GeV/c^2 A^0 mass, 1-prong cuts . . . 101
3.79 Efficiency of 1-Prong Higgs MC that pass all tuned cuts. . . . 103
3.80 Plot of fitted Gaussian σ values vs the peak photon energy. Decays are $\Upsilon(1S) \to \gamma A^0 \to \tau\tau$ with the τ-pair decaying generically, all "e & μ" mode cuts applied. . . . 105
3.81 An example of a fit using the combined model in the on-resonance "e & μ" MC sample. The upper left is the fitted data, upper right is the residuals, lower left is the normalized residuals, and lower right shows the fit parameters. . 108
3.82 Examples of fits using the combined model in the on-resonance "1-prong" MC sample in all four E_γ regions. . . . 109
3.83 An example of the CLs method implemented in RooStats with the Hybrid-CalculatorOriginal function. A point in the on-resonance "e & μ" MC sample is used. . . . 111
3.84 An example of the 90% confidence level upper limit obtained from integration of a Bayesian likelihood function in RooStats. A point in the on-resonance "e & μ" MC sample is used. . . . 112

3.85 An example of the 90% confidence level upper limit obtained from the ProfileLikelihoodCalculator. A point in the on-resonance "e & μ" MC sample is used. 112
3.86 Significance plot in "e & μ" on-resonance MC with 1% binning obtained from the ProfileLikelihoodCalculator. 113
3.87 Combined distribution of nsig in On-Resonance MC with "e & μ" Cuts. . . 114
3.88 Distribution as a function of A^0 mass of nsig in On-Resonance MC with "e & μ" Cuts. 114
3.89 Combined distribution of nsig in On-Resonance MC with 1-prong cuts. . . . 115
3.90 Distribution as a function of A^0 mass of nsig in On-Resonance MC with 1-prong cuts. 115
3.91 90% Confidence Level Upper Limit for A^0 in On-Resonance MC with "e & μ" Cuts. 116
3.92 90% Confidence Level Upper Limit for A^0 in On-Resonance MC with 1-Prong Cuts. 117
3.93 Fitted π^0 peak and pulls of fit in on-resonance MC (top) and data (bottom). 118
3.94 Upper limit of combined branching ratio with a fixed polynomial background (blue) and with a floating polynomial background (green). 119
3.95 Upper limit of branching ratio with normal signal width (blue) and signal width increased by 5% (green). 120
3.96 Percent difference between measured and expected energies of photons from π^0 decays in "e & μ" off-resonance data. 122
3.97 Percent difference between measured and expected energies of photons from π^0 decays in "e & μ" off-resonance MC. 123

4.1 The 90% confidence level upper limit in data vs A^0 mass for $BR(\Upsilon(1S) \to A^0) \times BR(A^0 \to \tau\tau)$ with e & μ selection criteria. Systematic error is included. 125
4.2 Comparison of the 90% confidence level upper limit vs A^0 mass for $BR(\Upsilon(1S) \to A^0) \times BR(A^0 \to \tau\tau)$ with e & μ selection criteria in data and MC. Systematic error is included. 126
4.3 Comparison of the 90% confidence level upper limit vs A^0 mass for $BR(\Upsilon(1S) \to A^0) \times BR(A^0 \to \tau\tau)$ with e & μ selection criteria in data and averaged MC. Each point in MC above 4.3 GeV/c^2 is averaged with the 7 nearest points on either side; the point at 4.3 GeV/c^2 is averaged with the 3 nearest points on either side. 2% binning, systematic error is included. 126
4.4 Significance in data vs A^0 mass for $BR(\Upsilon(1S) \to A^0) \times BR(A^0 \to \tau\tau)$ with 1-prong selection criteria. 1% binning. 127
4.5 The 90% confidence level upper limit in data vs A^0 mass for $BR(\Upsilon(1S) \to A^0) \times BR(A^0 \to \tau\tau)$ with 1-prong selection criteria. 2% binning, systematic error is included. 127
4.6 Comparison of the 90% confidence level upper limit vs A^0 mass for $BR(\Upsilon(1S) \to A^0) \times BR(A^0 \to \tau\tau)$ with 1-prong selection criteria in data and MC. 2% binning, systematic error is included. 128

4.7 Comparison of the 90% confidence level upper limit vs A^0 mass for $BR(\Upsilon(1S) \rightarrow A^0) \times BR(A^0 \rightarrow \tau\tau)$ with 1-prong selection criteria in data and averaged MC. Each point in MC above 4.3 GeV/c^2 is averaged with the 7 nearest points on either side; the point at 4.3 GeV/c^2 is averaged with the 3 nearest points on either side. 2% binning, systematic error is included. 128

A.1 Efficiency plot for the $!e\mu$ mode fit with a 4th order polynomial. Efficiencies are in percent. 130
A.2 Upper limit comparison between the 1-Prong mode (red) and the combined $!e\mu$ and $e\mu$ channels (blue). 132

C.1 Block diagram and photograph of the STaR board. Left: diagram showing the placement of the signal inputs, the LABRADOR 3 ADCs, the HPTDC TDCs, the FPGA used for control logic, and the output signal to the COPPER. Right: photograph of the STaR. 140
C.2 HPTDC Testing. Measurement of the time delay between timing signal and a trigger signal routed through a 160 ns delay line. No INL correction has been applied. 144

List of Acronyms

ATLAS A Toroidal LHC Apparatus

BR Branching Ratio

BF Branching Fraction

CB Crystal Ball

CFRP Carbon Fiber Reinforced Plastic

CMS Compact Muon Solenoid

F.o.M. Figure of Merit

FSR Final State Radiation

HER High Energy Ring

ISR Initial State Radiation

IP Impact Parameter

KEK Kō Enerugī Kasōki Kenkyū Kikō

LER Low Energy Ring

MCMC Markov Chain Monte Carlo

NMSSM Next-to-Minimal Supersymmetric Standard Model

PMT Photomultiplier Tube

QCD Quantum Chromodynamics

QED Quantum Electrodynamics

RPC Resistive Plate Counter

SSB Spontaneous Symmetry Breaking

TSC Trigger Scintillation Counter

VEV Vacuum Expectation Value

Chapter 1

Physics Background & Motivation

1.1 Overview

The Standard Model is the most successful theory of subatomic interactions to date. According to this theory, three generations of leptons and three generations of quarks make up the fundamental building blocks of all matter. These particles interact via four forces: electromagnetic, weak, strong, and gravitational. Such interactions allow the formation of stable and semi-stable states made from the aforementioned fermions. Additionally, the theory predicts that some fundamental particles acquire mass via interactions with a Higgs field. Some more exotic extensions to the Standard Model include the possibility of more than one Higgs field; it is this possibility that this analysis explores.

This chapter is a brief summary of the physics concepts important to this analysis. The information on the non-Higgs sectors of the Standard Model contained in this chapter is taken from Refs. [1, 2, 3, 4, 5, 6, 7] unless otherwise noted.

1.2 Particles I: Leptons & Quarks

The most basic components of stable matter are leptons and quarks. These particles are fermions; each having a spin $\frac{1}{2}$. There are six leptons and six quarks, each set of six is divided into three generations. For the leptons, these generations contain a particle and an associated neutrino: the electron, $\begin{pmatrix} e \\ \nu_e \end{pmatrix}$, the muon, $\begin{pmatrix} \mu \\ \nu_\mu \end{pmatrix}$, and the tau, $\begin{pmatrix} \tau \\ \nu_\tau \end{pmatrix}$. Associated with each family is quantity known as lepton number. Both the e and the ν_e have an electron number of 1 and a muon and tau number of zero. There are similiar numbers for particles within the muon and tau generations. The quarks come in six flavors paired into

Table 1.1: Lepton Properties

Particle	Name	Q (Charge)	Mass [MeV/c^2]
e	electron	-1	0.511
ν_e	electron neutrino	0	$< 2 \times 10^{-6}$
μ	muon	-1	105.658
ν_μ	muon neutrino	0	$< 2 \times 10^{-6}$
τ	tau	-1	1,776.82
ν_τ	tau neutrino	0	$< 2 \times 10^{-6}$

Summary of the properties of the three lepton generations [2][3][5]. By convention, charge is given in terms of the magnitude of the charge of the electron, charge = $Q_{lepton}/|Q_e|$. While neutrino masses are not directly measured, the observation of mixing between neutrinos is evidence that they are not massless.

Table 1.2: Quark Properties

Particle	Name	Q (Charge)	Mass [MeV/c^2]
u	up	$+\frac{2}{3}$	2.3
d	down	$-\frac{1}{3}$	4.8
c	charm	$+\frac{2}{3}$	1275
s	strange	$-\frac{1}{3}$	95
t	top	$+\frac{2}{3}$	172,900
b	bottom	$-\frac{1}{3}$	4180

Summary of the properties of the three lepton generations [2][3][5]. Bare quarks are never seen, so the given masses are not exact. By convention, charge is given in terms of the magnitude of the charge of the electron, charge = $Q_{lepton}/|Q_e|$.

up and down, $\begin{pmatrix} u \\ d \end{pmatrix}$, charm and strange, $\begin{pmatrix} c \\ s \end{pmatrix}$, and top and bottom, $\begin{pmatrix} t \\ b \end{pmatrix}$. In addition, each quark also carries a quantum number called "color". An introductory table of lepton and quark properties is presented in Tables 1.1 and 1.2. For each particle listed in Tables 1.1 and 1.2, there exists an antiparticle with the same mass and lifetime but opposite charge and lepton number/flavor.

The six leptons can be found as free particles; the quarks are always bound in multi-quark particles as will be described in Section 1.3.2.

Table 1.3: The Forces of the Standard Model

Force	Strength	Mediator	Mass [GeV/c^2]	Spin
strong	1	gluon, G	0	1
electromagnetic	10^{-2}	photon, γ	0	1
weak	10^{-7}	$W^{\pm}, Z^0$	80, 91	1
gravity	10^{-39}	graviton, g	0	2

The relative magnitudes of forces between two protons when separated by approximately twice the proton charge radius [5]

.

1.3 Forces

The quarks and leptons interact with each other via four forces: the strong, electromagnetic, weak, and gravitational forces. Each force has an associated force carrier, or mediator, with integer spin (bosons). These bosons are massless, with the notable exception of the weak force's $W^{\pm}$ and Z^0. This exception and its implications will be explored in greater detail later. Table 1.3 summaries properties of the four forces, including their propagators and relative strengths at a characteristic subatomic scale. As seen in Table 1.3, the gravitational force is many orders of magnitudes smaller than even the weak force. Because of this, it is safely neglected in interactions on the subatomic scale and will not be considered further.

1.3.1 The Electromagnetic Force

The interactions of charged particles are described by the theory of quantum electrodynamics (QED), a $U(1)$ gauge theory. This is the oldest of the dynamical theories, with its roots in the first hypothesis of the quantization of light as a photon. The photon is observed to be a massless gauge boson that itself carries no charge. In QED, the interactions between charged particles are mediated via the exchange of virtual photons. These virtual photons, like all virtual particles, exist only as force mediators and are never directly observed. As such, virtual photons are not constrained to the physical kinematic properties of observable photons.

It should be noted that the electromagnetic force is just a special case of the more general "electroweak" force. However, at typical energies seen at accelerators during the development of the Standard Model (below 100 GeV), the electromagnetic force dominates the weak force unless QED interactions are suppressed or forbidden. As such, electromagnetic and weak forces are considered separately.

The electrostatic potential takes on the familiar form of Eq. 1.3.1, where α_{EM} is the electromagnetic coupling constant (a.k.a. the "fine structure constant") and r is the radial distance between two charges.

$$V_{EM} = -\frac{\alpha_{EM}}{r} \tag{1.3.1}$$

1.3.2 The Strong Force

The interactions between the quarks are described by the strong force. Of interest in high energy particle physics is its role in describing interactions inside of particles composed of multiple quarks. On this scale the strength of the strong force is over a hundred times greater than any of the other forces and thus dominates all other interactions. It also plays a role in the interaction between these particles composed of quarks, notably in the binding of atomic nuclei.

At the most fundamental level, the strong force is mediated by a massless gauge boson known as the gluon; this is similar to the way the electromagnetic force is mediated by the photon. Unlike the the photon, gluons have a "charge" that interacts with the strong field; thus they are also participants in strong interactions.

QCD is an $SU(3)$ gauge theory, so one expects three separate charges for the fundamental constituents. These charges as known as "colors", and commonly denoted as red, blue, and green. Free quarks and gluons are not seen in nature; quarks carry a single color charge (or anti-charge) and gluons carry a color charge and an anti-color charge. All observed particles are color singlets and carry no net charge.

The strong potential is typically written in the form of Eq. 1.3.2, where where α_S is the strong coupling constant and k is a scale factor on the order of 1 GeV/fm.

$$V_S = -\frac{4\alpha_s}{3r} + kr \tag{1.3.2}$$

In contrast to the electrostatic potential presented in Eq. 1.3.1, the strong potential given in Eq. 1.3.2 has a term that grows with r. It is thus more energetically favorable to create a quark pair from the vacuum than to have an individual quarks separated by large distances, giving rise to the aforementioned quark confinement.

1.3.3 The Weak Force

Unlike the electromagnetic and strong interactions, all of the fundamental fermions participate in weak interactions. These weak interactions are dominated by electromagnetic and/or strong processes, but their effects are easily seen in processes forbidden by strong and electromagnetic interactions. The neutrino, for example, lacks both color and charge and thus only interacts via the weak force[1].

This force is mediated by three gauge bosons: the W^+, W^-, and the Z^0. Unlike the previous two forces, these gauge bosons are found experimentally to be massive. Their massiveness is what gives rise to the apparent "weakness" of this force: at typical energies (e.g., where the interaction energy is less than $M_W c^2$) the magnitude of the weak propagator is inversely proportional to the mediator's mass. On this scale, an *intrinsic* "weak coupling constant", α_W, is actually larger than α_{EM} by almost a factor of five.

Unlike strong and electromagnetic interactions, weak interactions are not symmetric under conjugation of charge (C), parity (P), or CP together. Weak interactions involving quarks do not even conserve quark flavor. Quark flavor eigenstates of weak interactions (denoted as "q'") are not eigenstates of mass (denoted as "q"); they are related by Eq. 1.3.3.

$$\begin{pmatrix} d' \\ s' \\ b' \end{pmatrix}_L = V \begin{pmatrix} d \\ s \\ b \end{pmatrix}_L \tag{1.3.3}$$

The "L" is included to make explicit that only left-handed quarks are involved in charged weak interactions. The "V" in Eq. 1.3.3 is the CKM matrix, presented in Eq. 1.3.4.

$$V_{\mathrm{CKM}} = \begin{pmatrix} V_{ud} & V_{us} & V_{ub} \\ V_{cd} & V_{cs} & V_{cb} \\ V_{td} & V_{ts} & V_{tb} \end{pmatrix} \tag{1.3.4}$$

where V_{ij} is the element that describes the coupling between the mass eigenstates of quarks i and j. The magnitudes and phases of these coupling constants are measured by Belle.

[1] As mentioned previously, the gravitational force is so weak at the scales we study that it is neglected.

1.3.4 Electroweak Unification

The electromagnetic and weak forces are manifestations of a single "electroweak" force that arises from a simple $SU(2) \times U(1)$ gauge theory. In this framework, the $SU(2)$ sector has three gauge bosons that we will refer to as W^1, W^2, and W^3 and the $U(1)$ sector has a single gauge boson B. The chiral nature of weak interactions is folded into the representation of the particles, allowing for similar descriptions of both weak and QED interaction vertices[2]. This simple $SU(2) \times U(1)$ electroweak model looks promising: the W^1, W^2, and W^3 could be the W^+, W^-, and Z^0 of weak interactions and the B could be the photon of QED. This formulation does not, however, address why the $W^\pm$ and Z^0 have mass. The reason this is important and how it is resolved will be covered in Section 1.5; for now it is interesting to note a result. The photon we observe is not actually B, as implied earlier, but a linear combination of the neutral W^3 and B. The Z^0 is the orthogonal compliment to that linear combination of W^3 and B, and acquires mass along with the two charged W bosons.

1.4 Particles II: Hadrons

As mentioned previously, while we can see single leptons, quarks are bound via the strong force into states of two or more. These states are called hadrons, and fall into two classes: mesons and baryons. Mesons are composed of a $q\bar{q}$ pair and have a spin with integer magnitude. One common example is the π^+; it is a spin zero meson composed a u-quark and a $\bar{d}$-quark. Baryons are composed of a qqq triplet and have spins with half-integer magnitude. The proton, for example, is composed of uud and has spin $\frac{1}{2}$.

These states are often unstable[3] and only exist on average for a period of time τ. We can relate the lifetime to decay rate, Γ, via Eq. 1.4.1.

$$\tau = \frac{1}{\Gamma_{Total}} \tag{1.4.1}$$

As implied by the subscript, Γ_{Total} includes all possible decay processes. We are are often only concerned with a single decay or a small subset; it is therefore useful to define a

[2]QED vertices are purely vectorial, whereas weak vertices are a mixture of vector and axial before this reclassification

[3]The only hadron that has not been observed to decay is the proton.

compact notation for the branching ratio:

$$BR_X = \frac{\Gamma \text{ for decay process "X" alone}}{\Gamma_{Total}} \tag{1.4.2}$$

For example, the branching ratio for the decay $\pi^0 \to \gamma\gamma$ is described as "$BR_{\pi^0\to\gamma\gamma}$".

We traditionally make a distinction between hadrons that are long-lived enough to be directly observed and those that are only evidenced through enhancements of the scattering cross-section seen in particle collisions. The first are the familiar particles, the second are the more exotic resonances. These enhancements in the the cross section near resonance energies can be seen as one varies the center of mass energy, $\sqrt{s}$, of a scattering experiment. A plot of world data on the $\sigma(ee \to \text{hadrons})$ cross-section scaled to the $\sigma(ee \to \mu\mu)$ cross-section is taken from Ref. [2] and shown in Fig. 1.2.

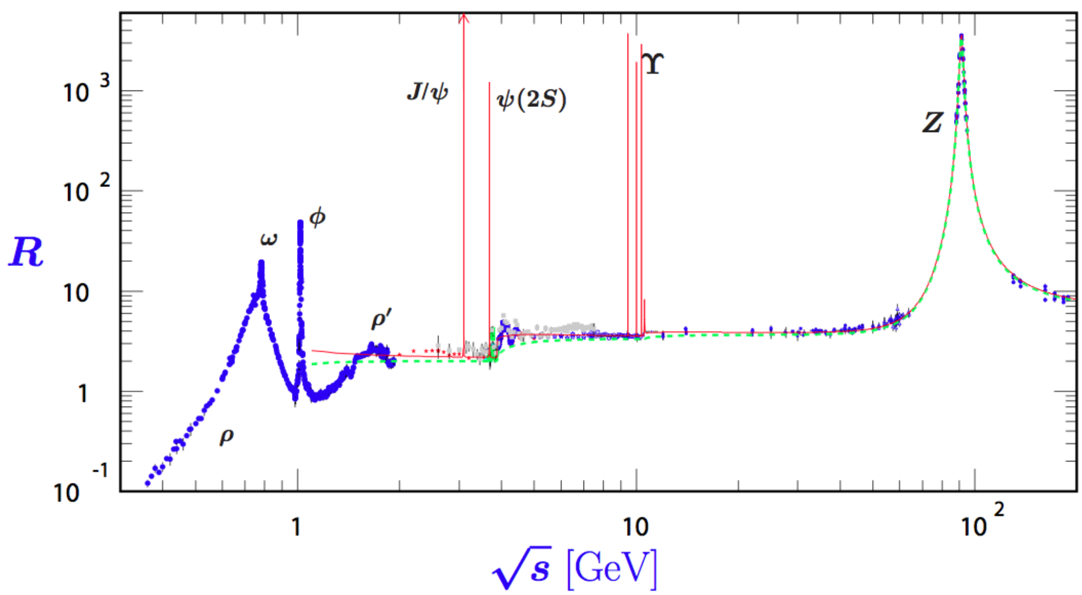

Figure 1.1: World data on the total cross section of $e^+e^- \to hadrons$ and the ratio $R(s) = \sigma(ee \to \text{hadrons}, s)/\sigma(ee \to \mu\mu, s)$. In this plot $\sigma(ee \to \text{hadrons}, s)$ is the experimental cross section corrected for initial state radiation and electron-positron vertex loops, $\sigma(ee \to \mu\mu, s) = 4\pi\alpha^2(s)/3s$.[2]

1.4.1 The Υ Resonances

The first evidence of the Υs mesons came from Fermilab in 1977 as an unresolved enhancement of the $\sigma(ee \to \mu\mu)$ cross section in stationary target experiments. Later

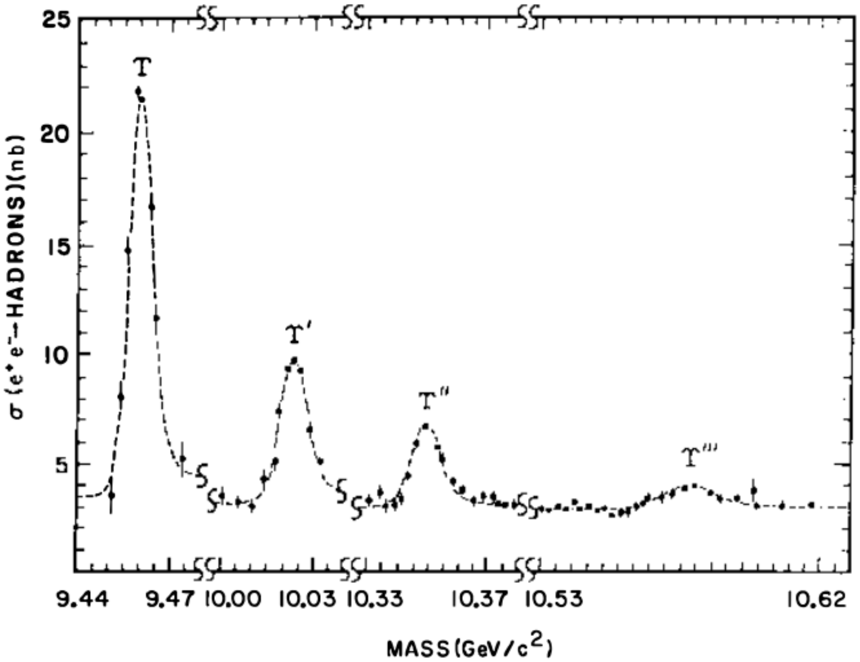

Figure 1.2: Cross section for e^+e^- annihilations to hadrons at CESR (CUSB data) [8].

experiments resolved this enhancement into 3 narrow resonances: e^+e^- experiments at DESY resolved the $\Upsilon(1S)$ and $\Upsilon(2S)$, then experiments at CESR resolved the $\Upsilon(4S)$. In 1980, experiments at CESR discovered the $\Upsilon(4S)$, the first Υ heavy enough to decay to $B\bar{B}$ pairs. It was later seen in later experiments that the neutral B particles, B^0 and B_s^0, oscillate between their particle and anti-particle states via flavor changing weak neutral currents [9]. This lead to the creation of B-factories like Belle and BaBar.

The Υs are $b\bar{b}$ vector mesons with masses near 10 GeV/c^2. The motion of the b-quarks in this bound state is small enough that the quarks can be considered non-relativistic. Decays of the lightest Υ occur primarily from $b\bar{b}$ annihilation that result in hadrons, but it is important for this analysis to note the not inconsiderable branching ratio for leptonic decays (approximately 2.5% each for decays to $\Upsilon(1S)$ going to e^+e^-, $\mu^+\mu^-$, and $\tau^+\tau^-$).

1.5 The Higgs Boson

1.5.1 Motivation for a Higgs Boson

The Standard Model, as summarized here, still has unresolved issues; one of the most important is the massiveness of the $W^{\pm}$ and Z^0 bosons. To see why this is problematic, specific aspects of particle interaction must be examined. The interactions between particles are described in terms of a Lagrangian

$$L = \int \mathfrak{L}(\phi, \partial_\mu \phi; \phi^\dagger, \partial_\mu \phi^\dagger) d^4x \tag{1.5.1}$$

where ϕ is a particle field, $\phi^\dagger$ is its hermitian conjugate, and $\mathfrak{L}(\phi, \partial_\mu \phi; \phi^\dagger, \partial_\mu \phi^\dagger)$ is a Lagrange density. For concision, let $\mathfrak{L}$ denote $\mathfrak{L}(\phi, \partial_\mu \phi; \phi^\dagger, \partial_\mu \phi^\dagger)$. To illustrate the problem that arises from massive gauge bosons it is helpful to follow the prescription of Ref. [3] and study a simple Lagrange density. Starting with the Dirac Lagrange density $\mathfrak{L}_{Dirac}$ and a Dirac spinor ψ,

$$\mathfrak{L}_{Dirac} = i\bar{\psi}\gamma^\mu \partial_\mu \psi - m\bar{\psi}\psi \tag{1.5.2}$$

we can apply a change of phase $\psi \to e^{i\theta}\psi$. This is equivalent to a global gauge transformation and we can see that the Lagrange density is invariant under this transformation. However, if θ becomes a function of location in space-time, x, such that $\psi \to e^{i\theta(x)}\psi$, then $\mathfrak{L}_{Dirac}$ changes to

$$\mathfrak{L}_{Dirac} \to \mathfrak{L}_{Dirac} - \left(\partial_\mu \theta\left(x\right)\right) \bar{\psi}\gamma^\mu \psi \tag{1.5.3}$$

which means that unless $\partial_\mu \theta(x) = 0$, $\mathfrak{L}_{Dirac}$ not locally invariant. This is remedied by the addition of a gauge field, A_μ, to the derivative. This new derivative, D_μ is defined as

$$D_\mu \equiv \partial_\mu - iqA_\mu \tag{1.5.4}$$

where q is the charge of the particle under consideration and the vector field A_μ undergoes gauge transforms as

$$A_\mu \to A_\mu + \frac{1}{q}\partial_\mu \theta(x) \tag{1.5.5}$$

The addition of this gauge field will eliminate the unwanted $\left(\partial_\mu \theta(x)\right) \bar{\phi}\gamma^\mu \phi$ term, but adding a new field requires the addition of a new particle and a term corresponding to the new particle's kinetic energy. Such a term is described by the Proca Lagrangian, which is cited[4] from Ref. [3] as:

$$\mathfrak{L}_{Proca} = -\frac{1}{16\pi} F^{\mu\nu} F_{\mu\nu} + \frac{1}{8\pi} m^2 A^\mu A_\mu \tag{1.5.6}$$

[4] with $\hbar = c = 1$

where

$$F^{\mu\nu} \equiv \partial^\mu A^\nu - \partial^\nu A^\mu \tag{1.5.7}$$

and m is the mass of the particle (i.e., the gauge boson) associated with the A_μ field. The $F^{\mu\nu}F_{\mu\nu}$ term of the Proca Langrangian is invariant under transformations of the form seen in Eq. 1.5.5, but $A^\mu A_\mu$ is not. In the case where $m = 0$ this term drops away, preserving local invariance. The strong and electromagnetic sectors, with massless gauge bosons, are thus automatically locally invariant. The weak force, with massive $W^\pm$ and Z^0, appear to violate local gauge invariance.

1.5.2 The Higgs Mechanism

The general solution to this problem comes from the application of spontaneous symmetry breaking (SSB) and algebraic manipulations of the fields in the Lagrangian. Symmetry can be broken by re-expressing the fields of the Lagrangian in terms one of the ground states of the system, otherwise referred to as a vacuum expectation value (VEV). This broken symmetry will produce an apparently *massive* field and at least one *massless* boson, known as a Goldstone boson, but with an appropriate choice of gauge this boson can be shown to be unphysical. Demonstrations of this, with simplified Lagrangians, are given in Ref. [3] and Ref. [10]. The application in the Standard Model is more complicated than the examples in these references, requiring the addition of a Higgs sector that is used to produce the symmetry breaking. For a Standard Model Higgs, this is achieved through the addition of a single scalar doublet. This Higgs field ends up coupling to the $W^\pm$, Z^0, and all fermions to give them their masses. A more detailed application of the Higgs Mechanism to the Standard Model can be found in Ref. [4].

1.5.3 The CP-Odd Light Higgs Boson

Recents results from CMS [11] and ATLAS [12] strongly suggest the discovery of a Higgs boson generated via the Higgs Mechanism described in Ref. [4]. The Higgs Mechanism also can be applied with Higgs sectors that consist of more than one Higgs doublet. In a minimal extension of the Higgs sector there are two complex doublet scalar fields, ϕ_1 and ϕ_2, and a requirement that CP be conserved in the Higgs sector. This results in a charged Higgs sector and a neutral Higgs sector that are linked by the VEVs of the two scalar fields, v_1 and v_2. The charged Higgs sector produces two physical Higgs, H^+ and H^-. The physical products of the neutral Higgs sector are a heavy and a light neutral CP-even scalar Higgs, H^0 and h^0, and a CP-odd scalar Higgs, A^0 [10].

1.5.4 Searching for the CP-Odd Light Higgs Boson

One method of probing the Higgs sector, proposed by F. Wilczek, is with a search for a Standard Model Higgs in decays of vector mesons [13]. This proposal was later adapted by R. Dermíšek, J. Gunion, and B. McElrath for searches for an A^0 in Υ decays [14]. In this proposal, one looks for the process $q\bar{q} \to \gamma A^0$ by examining the photon spectrum for a monochromatic peak that results from this two-body decay. The Higgs couples preferentially to heavier fermions, so the $b\bar{b}$ compostion of the Υ states make B-factories prime candidates for this search. This is presented in [15]. The two Feynman diagrams that contribute to $\Upsilon \to \gamma A^0$ are presented in Fig 1.3.

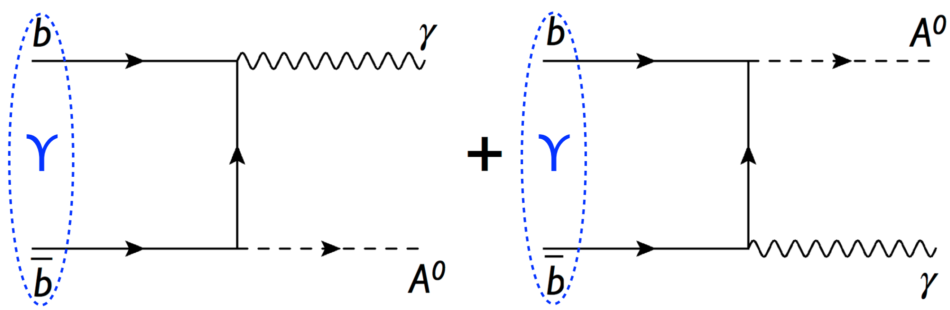

Figure 1.3: Diagrams [16] for the decay of an Υ to a photon and CP-odd light Higgs boson, A^0. This mechanism was first proposed by F. Wilczek as $q\bar{q} \to \gamma A^0$ [13] with the vector meson $q\bar{q}$ left unspecified.

An A^0 is expected to be short-lived, so we should see any products of its decay inside the detector. As previously stated, the A^0 will couple preferentially to heavy fermions, so if $M_{A^0} > 2M_\tau$ then we should expect decays of $A^0 \to \tau^+\tau^-$ to dominate. The τ is relatively short-lived, but decays of the τ are easily identifiable (if not easily reconstructable) by the missing energy carried off by one or more neutrinos. One-prong leptonic τ decays are of particular interest, as the decays $\tau \to e\bar{\nu_e}\nu_\tau$ and $\tau \to \mu\bar{\nu_\mu}\nu_\tau$ have comparatively high branching ratios ($\sim 18\%$) and each contain a particle that interacts directly with detectors. Finally, decays of τ-pairs can lead to final states that contain both an e and a μ with only two charged tracks in the event. This is a very clear signal that can be used to reduce background events.

Though we cannot observe $\Upsilon \rightarrow \gamma A^0$ directly, we can use the decay channel $\Upsilon \rightarrow \gamma A^0$; $A^0 \rightarrow \tau^+\tau^-$ to find evidence of an A^0 or set an upper limit the product of branching ratios $BR_{\Upsilon\rightarrow\gamma A^0} \times BR_{A^0\rightarrow\tau^+\tau^-}$. This search is conducted at KEK, with the KEKB accelerator generating Υ states and the Belle detector recording their decays.

Chapter 2

Experimental Apparatus

2.1 Overview

The Belle detector was created to study rare B-meson decay modes with a primary focus on CP-violation effects. Belle is operated by the Belle Collaboration, an organization comprised of more than 400 physicists from around the world. The detector is located in Tsukuba, Japan, at the KEKB asymmetric e^+e^- collider. The detector is comprised of several sub-detectors, each used to identify particles generated from the e^+e^- collisions.

Each sub-detector is described, starting from the innermost component of the Belle detector and working outward; see Figure 2.1 for a visual guide. Each subsection section addresses what the sub-system does, why it is needed, and general description of how it works. This is followed by a discussion of how the information collected from each of these subsystems is combined to reconstruct an event. Unless otherwise noted, the information, figures, and plots for this chapter are taken from [17]. Some plots and figures are modified; this is noted in their captions.

The coordinate system used at Belle aligns the z-axis anti-parallel to the positron beam and the x-axis pointing towards the center of the storage rings illustrated in Fig. 2.2. For convenience, this document uses cylindrical coordinates (z, r, ϕ) or the polar angle (θ). In both the cylindrical and spherical coordinates, the z-axis is defined as before. In cylindrical coordinates the radial, r, vector extends from the detector's center outward and in spherical coordinates θ is defined with respect to the z-axis.

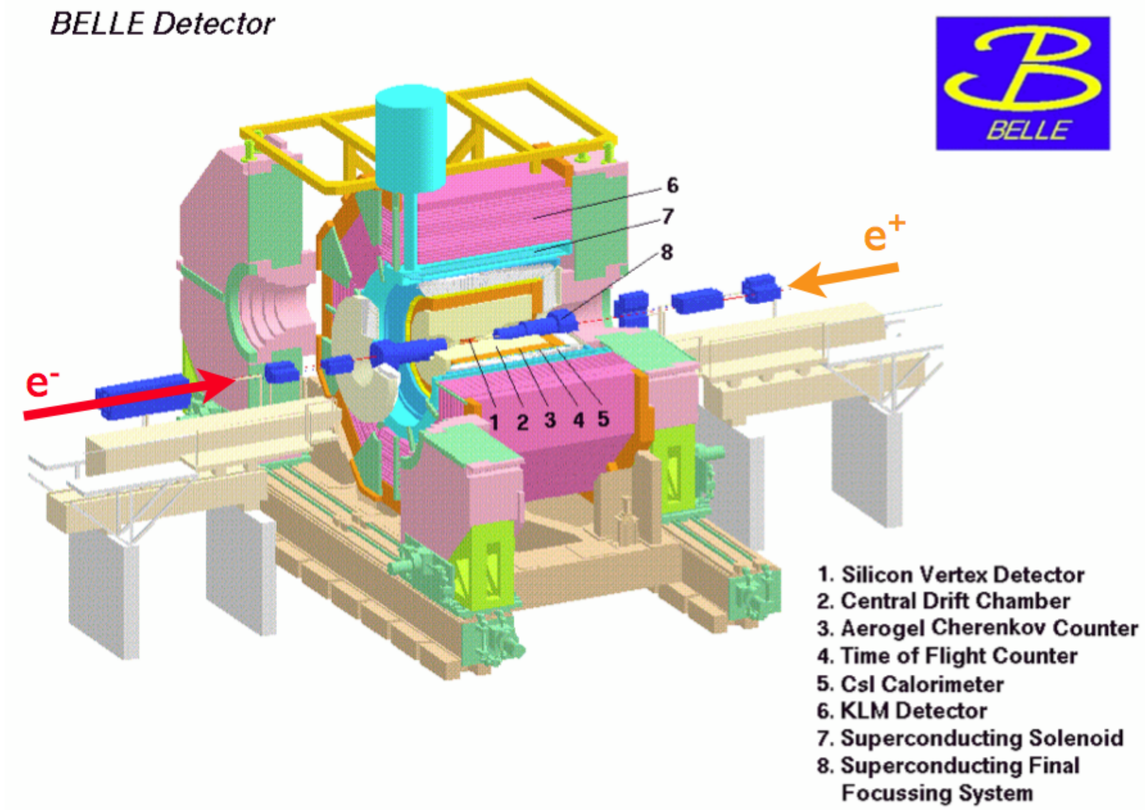

Figure 2.1: Isometric cut-away view of the Belle detector showing the relative location of the e^+ and e^- beams, sub-detectors, and the main solenoid.

2.2 KEKB

The KEKB accelerator provides bunched electron and positron beams in the High Energy Ring (HER) and Low Energy Ring[1] (LER), respectively. These rings are shown in Figure 2.2. For the majority of the approximately 3km circumference of the beam line, the storage rings run parallel to one another. The Belle detector sits at a point along the beam line where the LER and HER intersect, allowing for the electron-positron collisions that generate Υ events. KEKB was designed to operate with a peak luminosity of approximately 1×10^{34} cm^{2}s^{-1}, but subsequent improvements more than doubled that to a world-record luminosity of 2.11×10^{34} cm^{2}s^{-1}.

[1] The vast majority of the data taken at Belle uses a beam in the HER at 8 GeV and LER of 3.5 GeV, generating collisions with an center of mass energy equal to that of the resonant energy of the $\Upsilon(4S)$ (10.580 GeV). While the HER and LER may be referred to as the 8 GeV or 3.5 GeV rings in this document's references and figures, it is important to note that the energies used in this analysis were 7 GeV and 3 GeV, respectively.

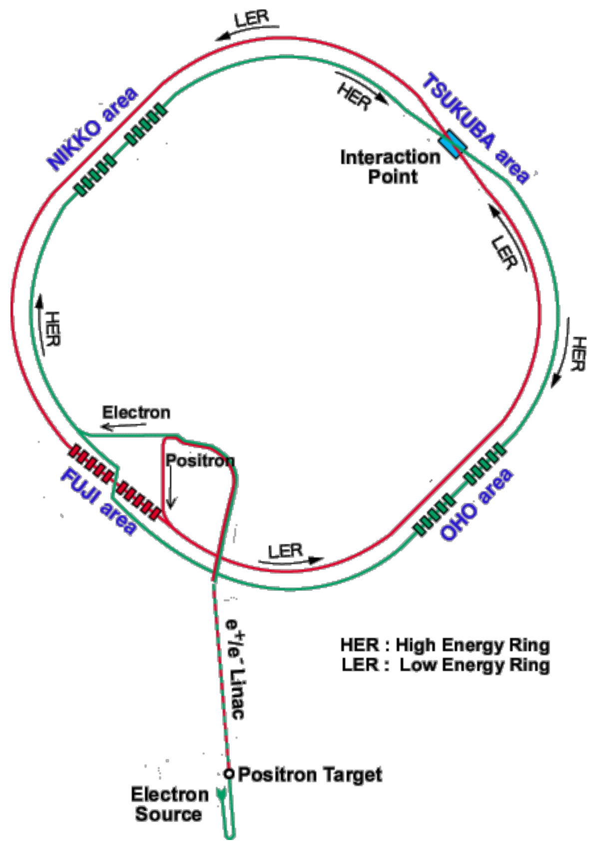

Figure 2.2: Overhead diagram of the storage rings and e^-e^+ production area at KEK. The Belle detector is located at the Tsukuba area interaction point in the upper right of this diagram.

2.3 The Interaction Region

Both the electron and positron beams are organized into "bunches", collections of electrons and positrons that circle the storage rings together in distinct groups separated by an integer number of 508.9 MHz RF spacings. The beams continually cross at a 22 mrad angle at a point inside the Belle detector called the Interaction Point (IP). The beam pipe has a section 4.6 cm before the IP and 10 cm after that is thin, double-walled, and made of beryllium. This construction reduces the rate of multiple coulomb scattering. PF-200 coolant to be pumped between the beam pipe walls to remove heat deposited in the IP chamber.

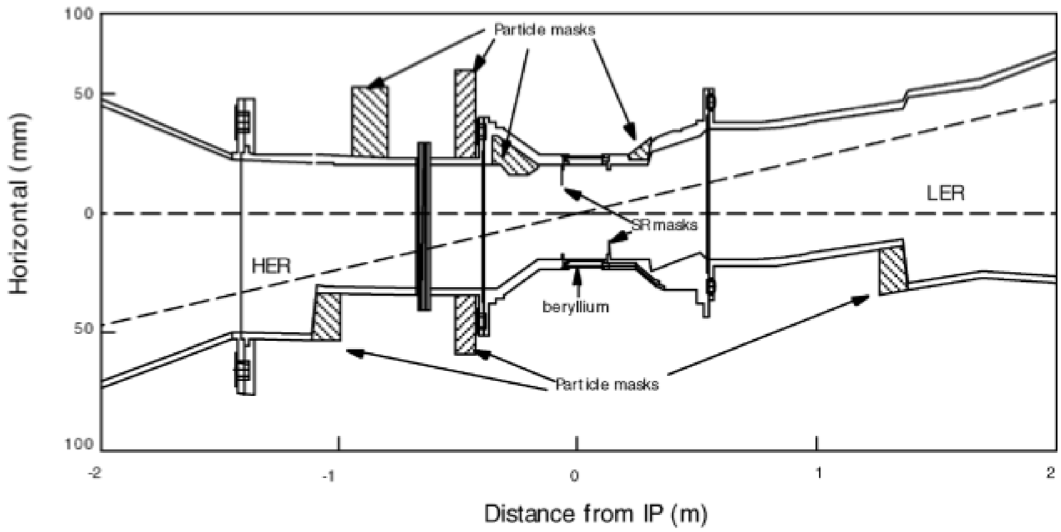

Figure 2.3: The IP and surrounding beam pipe, particle masks, and location of magnets. The axes are on different scales, to highlight structural details.

2.4 Silicon Vertex Detector (SVD)

Belle was designed for the study of time-dependent CP asymmetries of B-meson decays. Studies of this asymmetry require the ability to differentiate between vertices separated by lengths on the order of 100μm. This level of precision also makes it useful for detection of τ vertices, which is of particular use to this analysis.

The SVD consists of multiple 57.5 x 33.5mm double-sided silicon strip detectors (DSSD) placed end-to-end to form "ladders". In SVD1, the SVD configuration used until 2003, these ladders are arranged such that they form 3 layers as shown on the left side of Fig 2.4. Starting from the inner-most layer and counting outward, the ladders have 2, 3, and 4 DSSDs per ladder; covering a polar angle (θ) from 23° to 139°. Each DSSD is a low-doped silicon wafer that has been depleted of any free charge carriers and has had 1280 8 μm wide sense strips placed on each side. The sense strips on either side of the silicon wafer are oppositely biased so that when an ionizing particle passes through the silicon wafer the electrons drift towards the n-side and the "holes" drift towards the p-side. Sense strips on the n-side are laid perpendicular to the beam axis with a separation of 42 μm; those on p-side are laid parallel with a pitch of 25 μm. The n-side thus measures the z positions of impacts, while the p-side measures the $r-\phi$ positions.

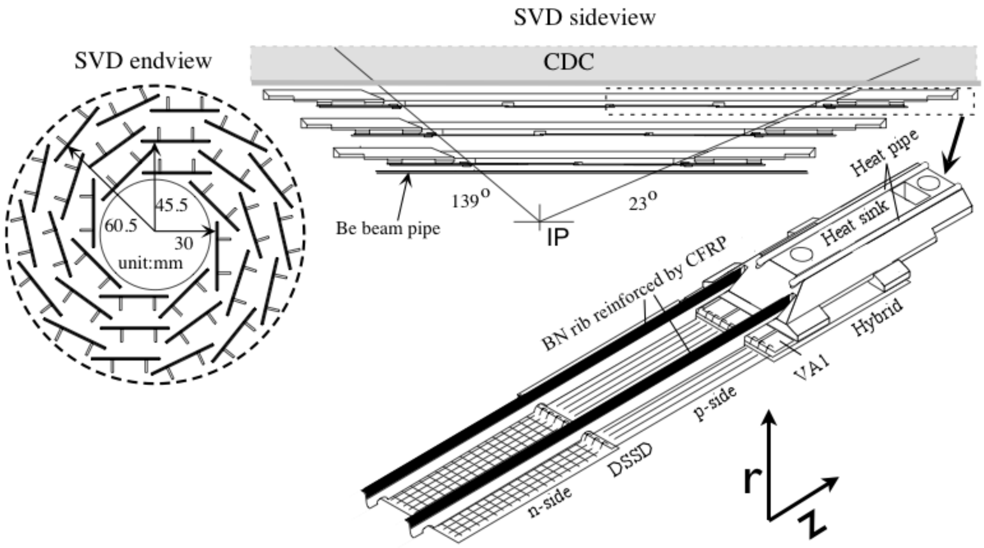

Figure 2.4: SVD1 configuration in the Belle detector and diagram of DSSD with support structure on ladder. Left: axial view of SDV configuration showing three layers. Top: profile view of SVD layers and relation to the IP. Bottom: SVD in isometric view, detector strips highlighted. Figure modified from Ref [17].

In the summer of 2003, the SVD was upgraded to a new configuration called SVD2. SVD2 extends the angular acceptance such that it spans a polar angle from 17° to 150°. It also adds a fourth layer to the SVD, and moves the nearest layer 5mm closer to the IP. All data used in this analysis were performed after the SVD2 upgrade.

SVD performance is characterized in terms of the resolution of the point of closest approach to the IP. The z and $\phi - r$ measurements are independent, thus their performance is measured independently as well. The uncertainty of the resolution as a function of a track's polar angle (θ), relativistic velocity (β), and momentum are given by [18]:

$$\sigma_{r\phi}(\mu\text{m}) = 21.9 \oplus \frac{35.5}{p\beta sin^{3/2}\theta} \text{ , where } p\beta \text{ is in } \frac{GeV}{c} \tag{2.4.1}$$

$$\sigma_{z}(\mu\text{m}) = 27.8 \oplus \frac{31.9}{p\beta sin^{5/2}\theta} \text{ , where } p\beta \text{ is in } \frac{GeV}{c} \tag{2.4.2}$$

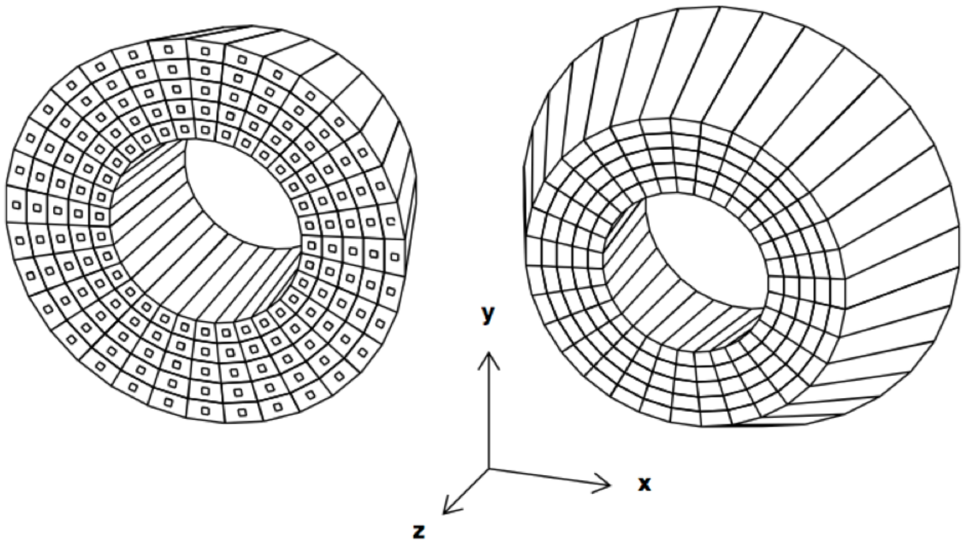

Figure 2.5: Front and back isometric views of the Bismuth Germanium Oxide (BGO) crystals that compromise the Extreme Forward Calorimeter. Figure modified from Ref [17].

2.5 Extreme Forward Calorimeter (EFC)

The EFC was originally designed to extend the polar angle over which calorimetry measurements can be done, serve as a beam monitor for KEKB operators, and serve as a luminosity monitor for Belle. The ECL covers a polar angle of $17°$ to $150°$; the EFC compliments this by covering $6.4°$ to $11.5°$ in the forward direction and $162.3°$ to $171.2°$ in the backward direction. Due to its proximity to the interaction point, the EFC sees higher backgrounds and more degradation than the main calorimeter. Bismuth Germanium Oxide crystals (BGO) were used to try to compensate for this due to their radiation hardness. The EFC is not directly used in analysis.

2.6 Central Drift Chamber (CDC)

The CDC is critical for recording the trajectory of charged particles in an event. Information from the CDC is also used to evaluate ionizing energy loss (dE/dx), the decrease in the particle's energy as it passes through the gas in the drift chamber. This is used

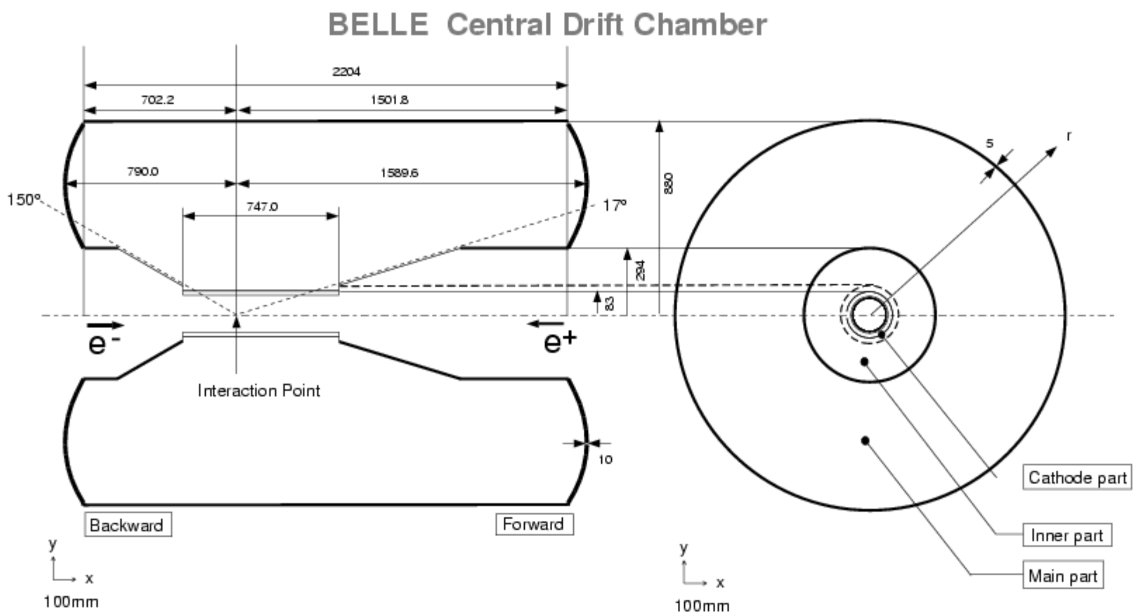

Figure 2.6: A cross section of the CDC in profile (left) and in axial view (right).

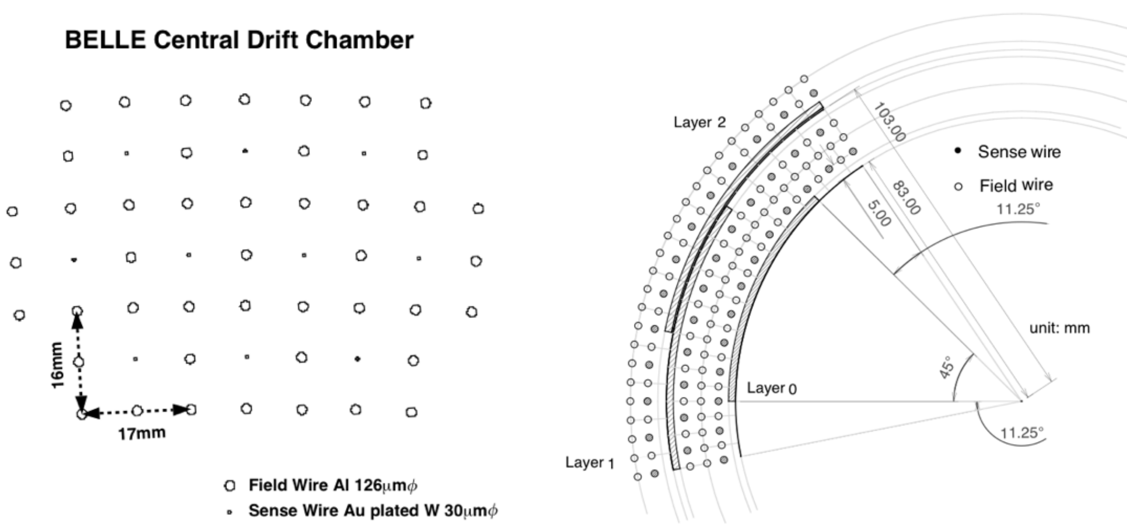

Figure 2.7: Configuration of CDC components. Left: configuration of sense and field wires with the z-axis going into the page. Wire diameters are not to scale. Right: configuration of wires near inner radius of CDC. The solid black lines are the CDC inner radius (inner black line) and a CFRP support cylinder (outer black line).

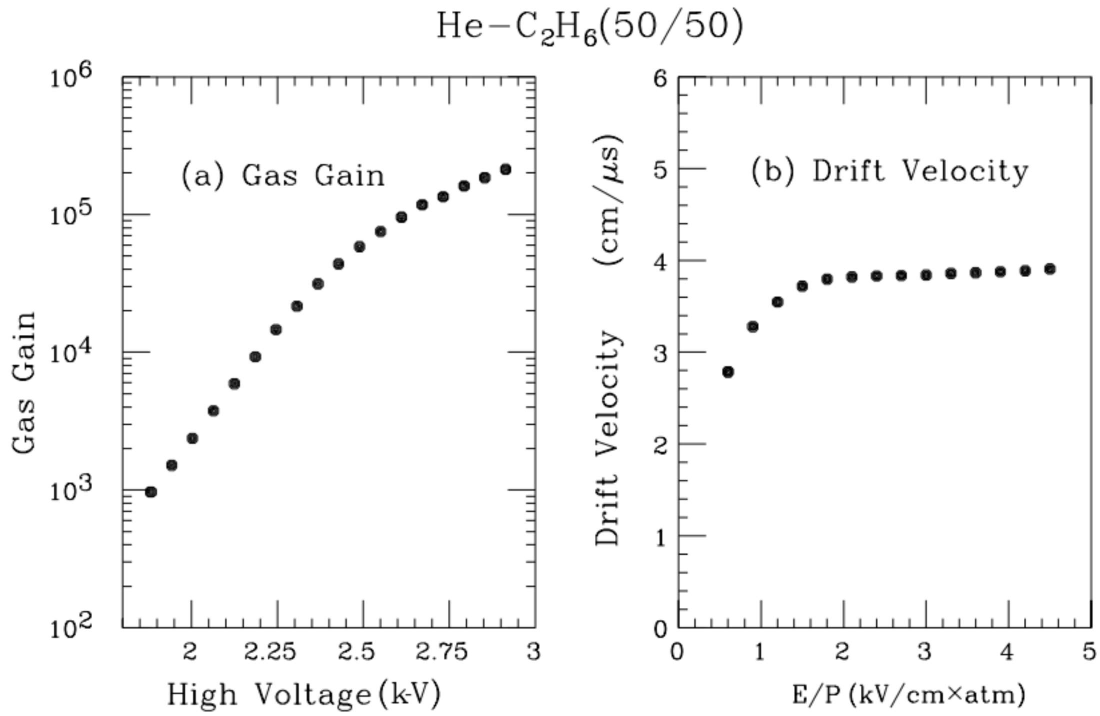

Figure 2.8: Gas gain (a) and drift velocity (b) plots for the helium-ethane gas mixture in the Central Drift Chamber. Plots taken from Ref. [17]

in particle identification for long-lived charged particles, as particle species have different energy loss spectra in the CDC.

The primary sensor in the CDC is the "sense wire". These are arranged in layers that form concentric cylinders around the z-axis of the detector. Surrounding each sense wire is an arrangement of "field wires"; these wires have a static potential on them which creates a potential well with a sense wire at its center. The result is a lattice of "cells" illustrated in Fig. 2.7. The CDC chamber is filled with equal parts ethane and helium gas, a low-Z mixture that has a drift velocity that saturates at 4 cm/μs in low electric fields. This trail of ionized particles starts an avalanche of electrons that is funneled by the potential well of the field wires to the nearest sense wire. By combining the time of hits in the CDC relative to the event start time and the drift velocity of electrons in the gas, a distance of closest approach for each wire hit can be calculated. The trajectory of the particle can be determined from the best-fit of a helix to this data; the helical path is due to a 1.5T magnetic field provided by a superconducting solenoid.

Measurement of the z-component of the charged particle's trajectory is accomplished by having layers that are at a slight angle to the sense wires parallel to the z-axis. The position of these rotated wires with respect to the z-parallel wires changes as a function of position along the z-axis. This change, when combined with the aforementioned information in the x-y plane, provides an estimate of the track's z-axis.

The CDC is required to have a momentum resolution of charge particles traverse to the z-axis, p_t, of

$$\frac{\sigma_{p_t}}{p_t} \sim 0.5\% \sqrt{1 + {p_t}^2} \tag{2.6.1}$$

where p_t is given in $\frac{GeV}{c}$. The measured momentum resolution with the CDC alone was

$$\frac{\sigma_{p_t}}{p_t}[\%] = 0.28 p_t \oplus \frac{0.35}{\beta} \tag{2.6.2}$$

When combined with vertex information from the SVD, this uncertainty decreases to

$$\frac{\sigma_{p_t}}{p_t}[\%] = 0.19 p_t \oplus \frac{0.30}{\beta} \tag{2.6.3}$$

The CDC p_t performance was characterized by analyzing $e^+e^- \rightarrow \mu^+\mu^-$ events in the center of mass frame. No appreciable ϕ dependence was seen. The dE/dx performance was characterized by examining the average energy loss, $\langle dE/dx \rangle$, for each track in various decays. Clear particle species differentiation can be seen in Fig 2.9.

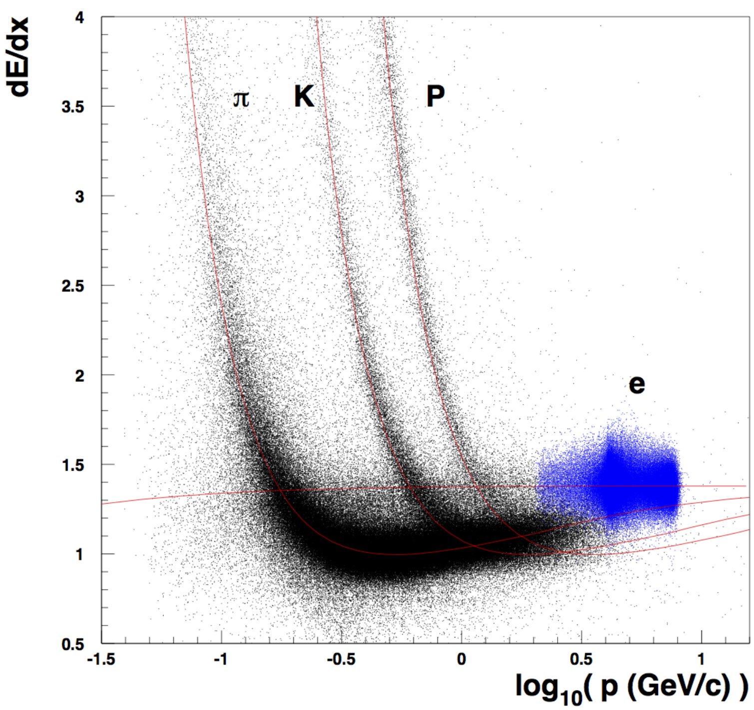

Figure 2.9: A scatter plot of measured mean energy loss values (labeled here as dE/dx) in the CDC versus particle momentum. Curves represent expected values for pions, kaons, protons, and electrons.

2.7 Aerogel Cherenkov Counter (ACC)

The ACC is used to distinguish $\pi^{\pm}$ from $K^{\pm}$ using Cherenkov radiation. This radiation is produced by a particle passing through a material with index of refraction n at a velocity greater than c/n. If n is suitably chosen, $\pi^{\pm}$ and $K^{\pm}$ with similar momenta can be differentiated: the $\pi^{\pm}$ will have higher velocity and emit more Cherenkov photons than the more massive $K^{\pm}$.

There are 1188 modules that comprise the ACC; 960 of these modules are segmented into 60 cells in the ϕ direction for the barrel part and 228 are arranged into 5 concentric layers in the forward endcap. There is no ACC system in the backward endcap. The modules themselves are small aluminum boxes, each containing a stack of aerogel tiles

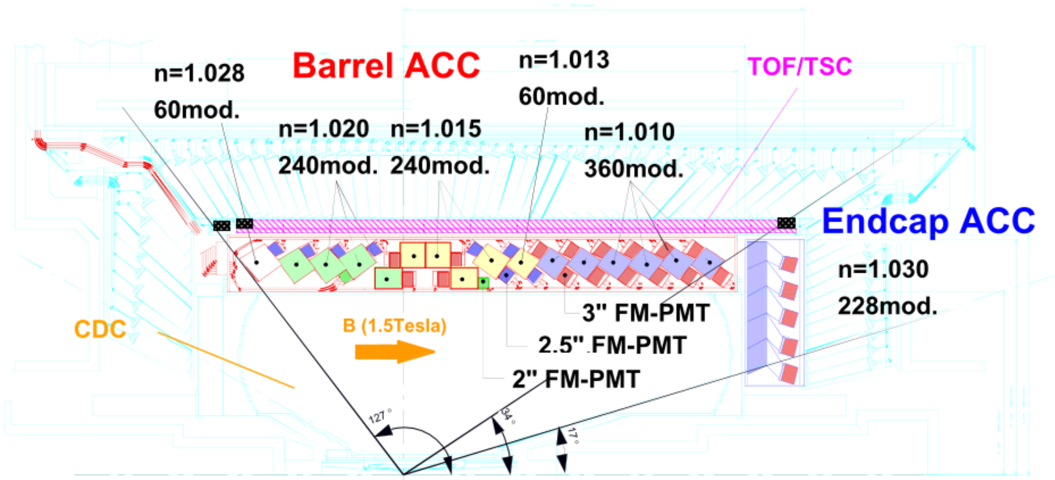

Figure 2.10: Layout of the Belle composite Particle Identification system. The positions of the barrel and endcap ACC modules are shown.

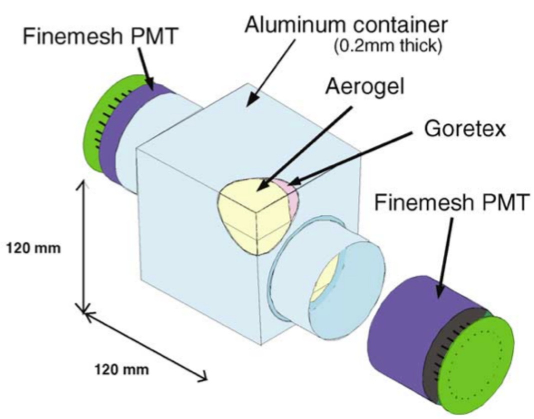

(a) ACC barrel module

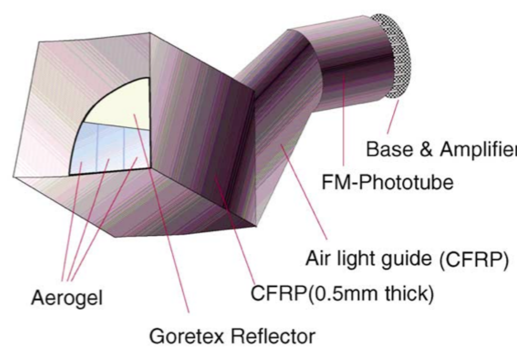

(b) ACC endcap module

Figure 2.11: Two ACC module designs: a) An ACC module located in the barrel region. Aerogel layers are stacked into a block and encased in Goretex and a thin sheet of aluminum. One or two PMTs are attached. b) An ACC module located in the endcap region. The aerogel layers are encased in Carbon Fiber Reinforced Plastic (CFRP) and a light guide directs Cherenkov radiation to a PMT offset from the likely path of radiation created by particle interaction while traversing the detector.

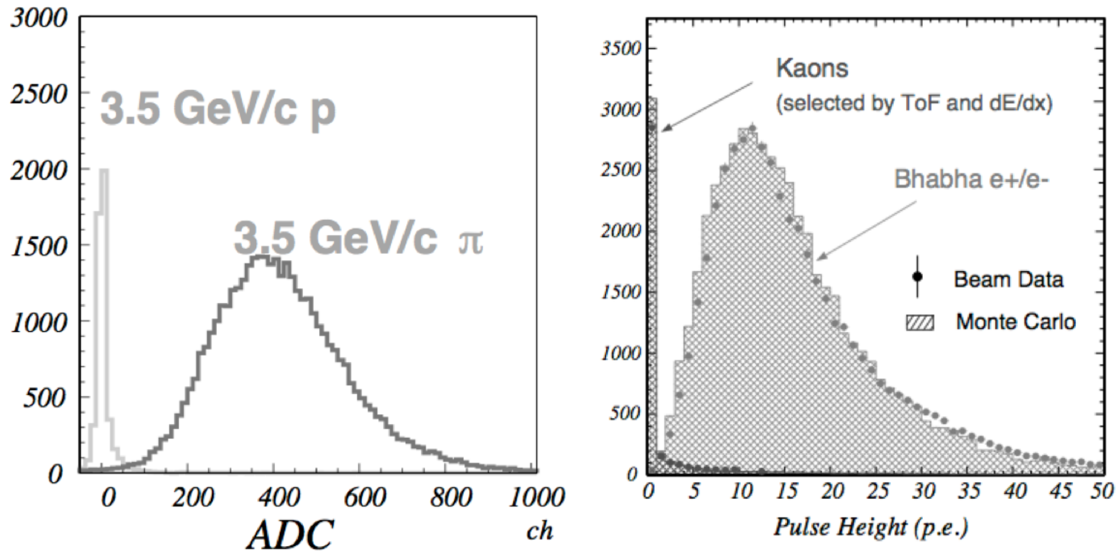

Figure 2.12: ACC performance. Left: pulse height spectra for 3.5 GeV pions and protons in a single ACC module. Measurements taken in a 1.5 T field. Right: pulse height spectra for $K^{\pm}$ and Bhabha electrons in units of photoelectrons observed by the barrel ACC inside of the Belle detector.

with an index of refraction, n, between 1.01 and 1.03, depending on the box's θ position (see Fig 2.10). Attached to the aerogel in each box are one or two fine-mesh PMTs to detect Cherenkov radiation emitted as a particle passes through the aerogel. Examples of such modules are shown in Fig 2.11.

The performance of the ACC was initially studied at KEK, and a clear differentiation of pulse height spectra was seen between protons and pions. After installation in the Belle detector, the ACC performance was tested with Bhabha electrons and $K^{\pm}$ candidates identified via TOF and dE/dx measurements. Again, a clear differentiation of pulse height spectra was observed. The results of both tests can be seen in Fig. 2.12.

2.8 Time of Flight (TOF)

The TOF system measures the time between a charged particle's production at the IP and its passage through the TOF scintillator bar. Knowing a particle's path, as well as the time it took to travel, allows us to determine the particle's velocity. Fast triggering

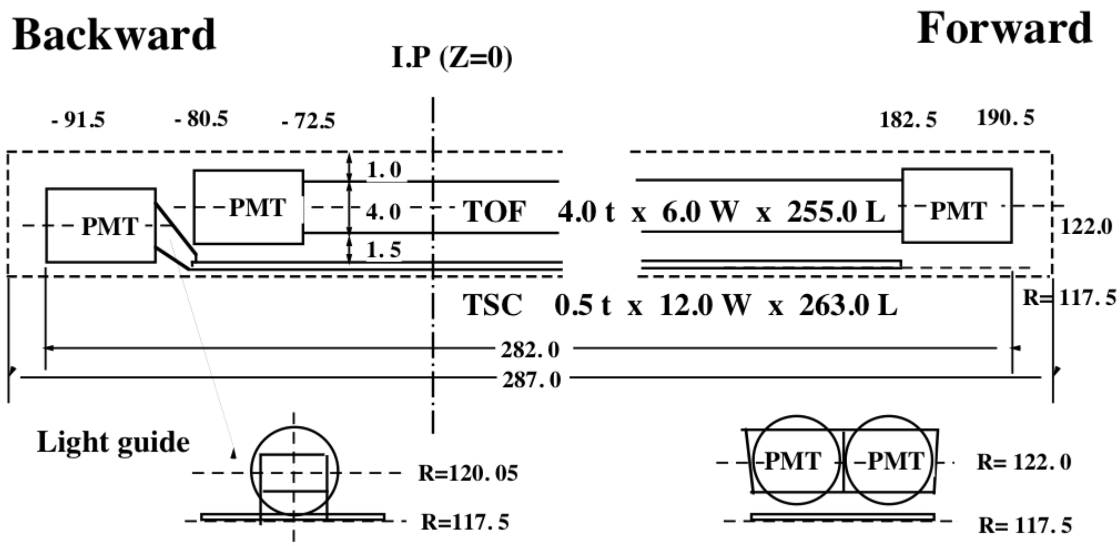

Figure 2.13: A schematic view of a Time of Flight module. Top: A TOF scintillator bar (marked TOF), a Trigger Scintillator Counter (TSC) panel, and their respective PMTs are shown in profile. The relative positions of the TOF and TSC are shown. Lower left: light guide and panel for the TSC. Lower right: relative placement of TSC and TOF PMT's.

information is also provided by the TOF, as well as discrimination between K and π below 1.5 GeV.

The basic component of the TOF is a 255 cm long and 4 cm thick trapezoidal plastic scintillator bar, parallel to the z-axis, with a photomultiplier tube (PMT) at either end. The scintillator material is Bicron BC408; TOF scintillator bars made of this material initially have a mean attenuation length of 390 cm and a light propagation velocity of 14.4 cm/ns. The TOF is made of 128 of these basic components arranged such that they form a barrel around the IP that is parallel to the z-axis. The trapezoidal scintillator bars are grouped into pairs, and beneath each pair is a thin rectangular scintillator bar called the Trigger Scintillation Counter (TSC). When used in coincidence with the main TOF models, the TSC reduces the trigger rate.

When a charged particle hits the bar, light is produced in the scintillator bar, propagated down the length of the bar via internal reflection, and arrives at the PMT. The light hitting the photocathode creates electrons via the photoelectric effect; these electrons are then multiplied. This electron cascade produces a voltage that is passed to readout electronics downstream. The mean time given by averaging the time recorded from PMTs on both ends is used for the timing information. The measurement of the flight time has an uncertainty of approximately 100 ps when measurements at either end of the TOF are averaged, with a slight dependence on the location of the hit along the z-axis. The TOF can provide 2σ particle differentiation for particles with momentum below 1.25 GeV. Both aspects of performance can be seen in Fig. 2.14.

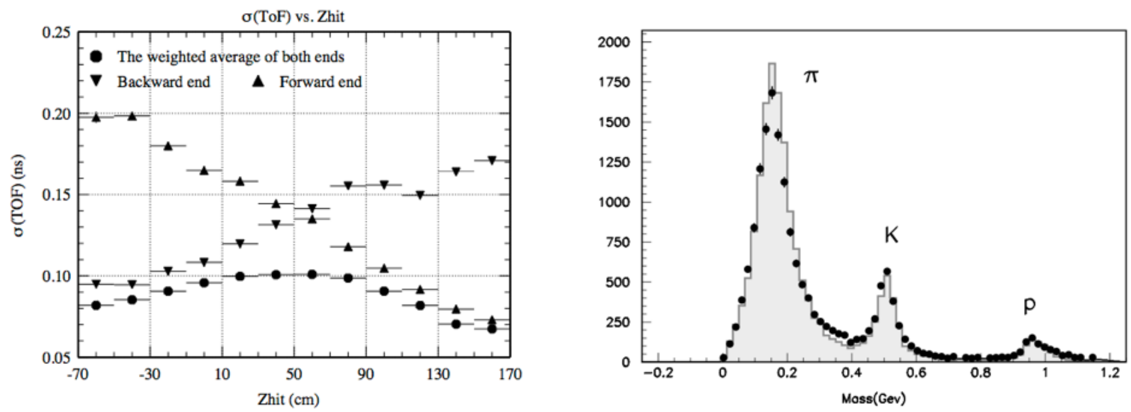

Figure 2.14: TOF timing performance. Left: TOF time resolution measured with μ-pair events. The quoted average uncertainty of 100ps taken from the maximum of the weighted average of the uncertainty from both ends of the TOF. Right: spectra of arrival times for kaons, pions, and protons below 1.2 GeV.

2.9 Electromagnetic Calorimeter (ECL)

As mentioned earlier, the requirement of this analysis to detect narrow photon peaks makes the electromagnetic calorimeter an essential component. The calorimeter is also used in the identification of other particles: an electron candidate can be identified by combining its momentum with the amount of energy it deposits in the calorimeter. The calorimeter has spatial resolution for photons of approximately 3-5 cm, making it useful in identifying photon pairs from π^0 decays.

The ECL is divided into three segments: a barrel segment and two endcaps. These segments are arrays of thallium-doped cesium iodide crystals (CsI(Tl)) with each individual crystal connected to a pair of photodiodes as seen in Fig. 2.16. The coverage and distribution of crystals in the ECL are summarized in Table 2.1. The crystals in the barrel region are 30 cm long, roughly 55 mm $\times$ 55mm on the face nearest the IP, and roughly 65 mm $\times$

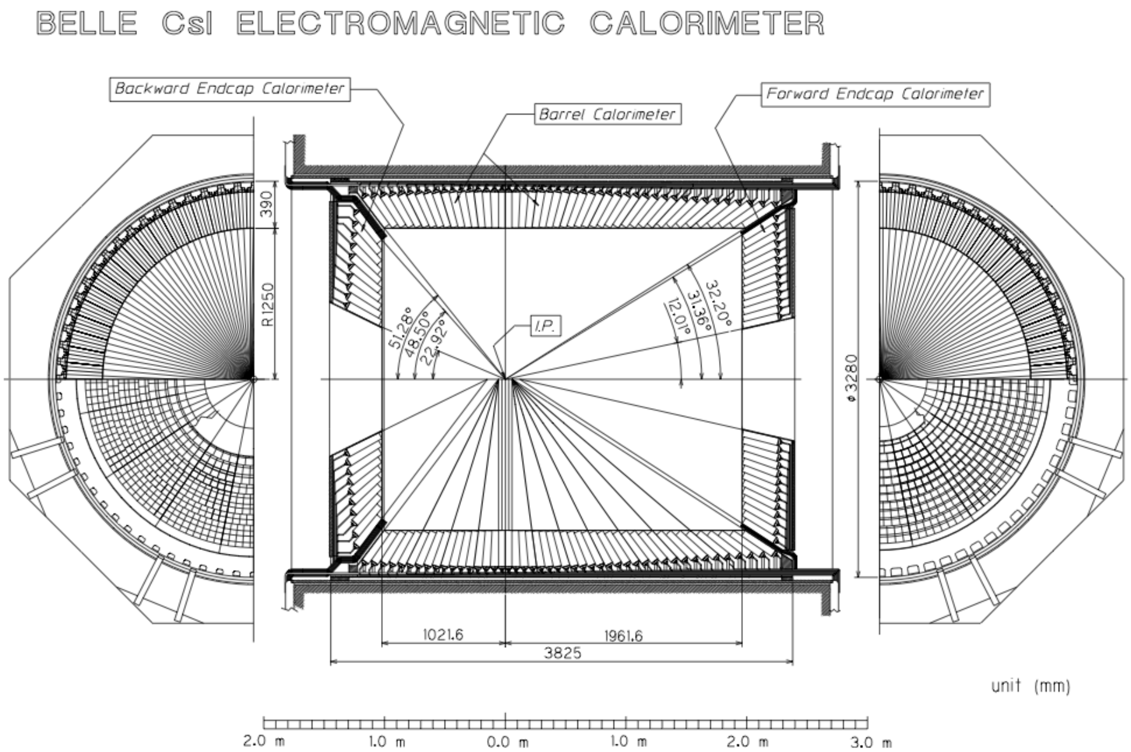

Figure 2.15: Electromagnetic Calorimeter (ECL) layout. Barrel region shown in profile; endcap region shown axially. Polar angle coverage and angle of ECL modules relative to the Interaction Point are shown.

65 mm on the opposite face. The 30 cm length corresponds to 16.2 radiation lengths[2], so showers from high energy particles remain mostly within the crystals and energy resolution is determined.

The characterization of energy resolution for 3×3 and 5×5 matrices of crystals was performed two ways: one with a "threshold" energy applied to each crystal and one without. This threshold is applied to reduce degradation of resolution for low energy photons due to electronic noise. In the threshold case, energy deposited in a crystal is only counted if it is above 0.5 MeV. No such restriction is applied in the non-threshold case. The energy resolution with respect to incident particle energy (in GeV) for the threshold case is

[2]A radiation length is the mean distance over which an incident electron's energy is reduced by a factor of e^{-1} via bremsstrahlung It is also $\frac{7}{9}$ of the mean free path for pair production by an incident high energy photon

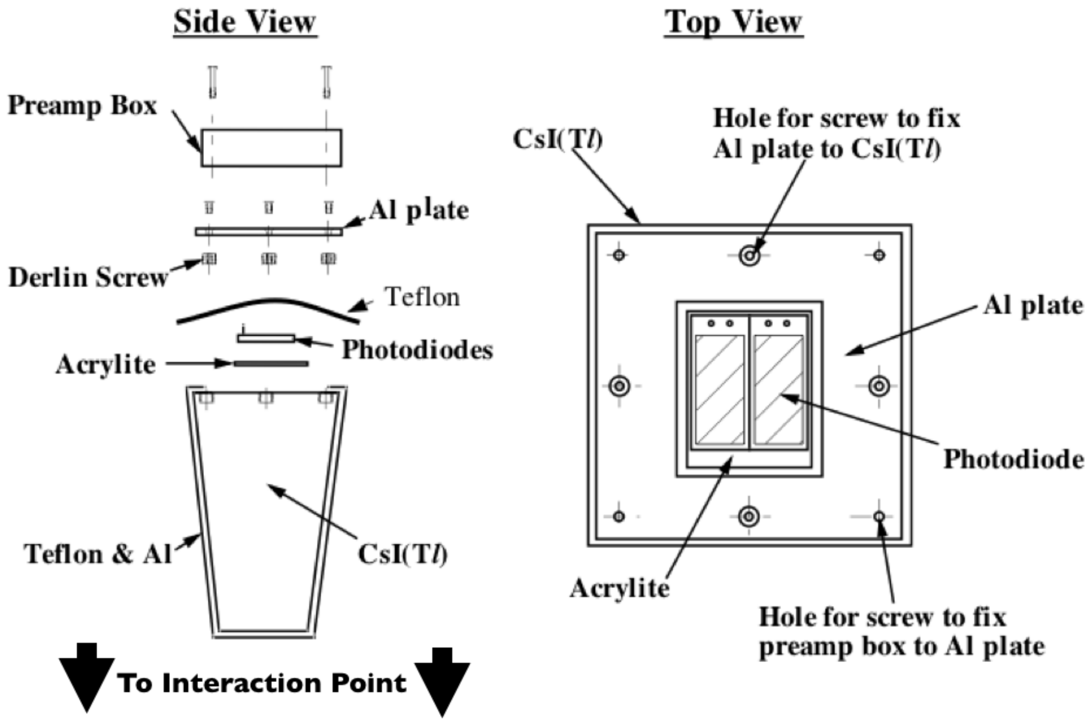

Figure 2.16: The mechanical assembly of an ECL counter. A thallium doped cesium iodide (CsI(Tl)) crystal is oriented towards the interaction point. All sides of the crystal, except for the side furthest from the IP, are covered with telfon (for handling the crystal) and aluminum (for light and electrical shielding). The uncovered far face has two photodiodes mounted for signal readout.

described by equations 2.9.1 and 2.9.2. For 3×3 matrices:

$$\frac{\sigma_E}{E} = \frac{0.0066(\%)}{E} \oplus \frac{1.53(\%)}{E^{1/4}} \oplus 1.18\% \tag{2.9.1}$$

For 5×5 matrices:

$$\frac{\sigma_E}{E} = \frac{0.0066(\%)}{E} \oplus \frac{0.81(\%)}{E^{1/4}} \oplus 1.18\%(5 \times 5) \tag{2.9.2}$$

The first terms of Eqs. 2.9.1 and 2.9.2 are due to the stochastic nature of the interactions of incoming particles with the crystal of the ECL. Particles interact with the ECL crystal and result primarily in excitations and ionizations. These processes have a characteristic energy loss, so for an infinitely long detector the total energy of the incident particle, E is proportional to the number of interactions inside the crystal, N. Since $E \propto N$ and $\sigma_N \propto \sqrt{N}$, we can see that $\sigma_E \propto \sqrt{E}$. The second terms arise from noise in the readout

Table 2.1: Summary of ECL properties

Section	θ Coverage	θ Segmentation	ϕ Segmentation	No. of Crystals
Forward Endcap	12.3°-31.4°	13	48-144	1152
Barrel	32.2°-128.7°	46	144	6624
Backward Endcap	130.7°-155.1°	10	64-144	960

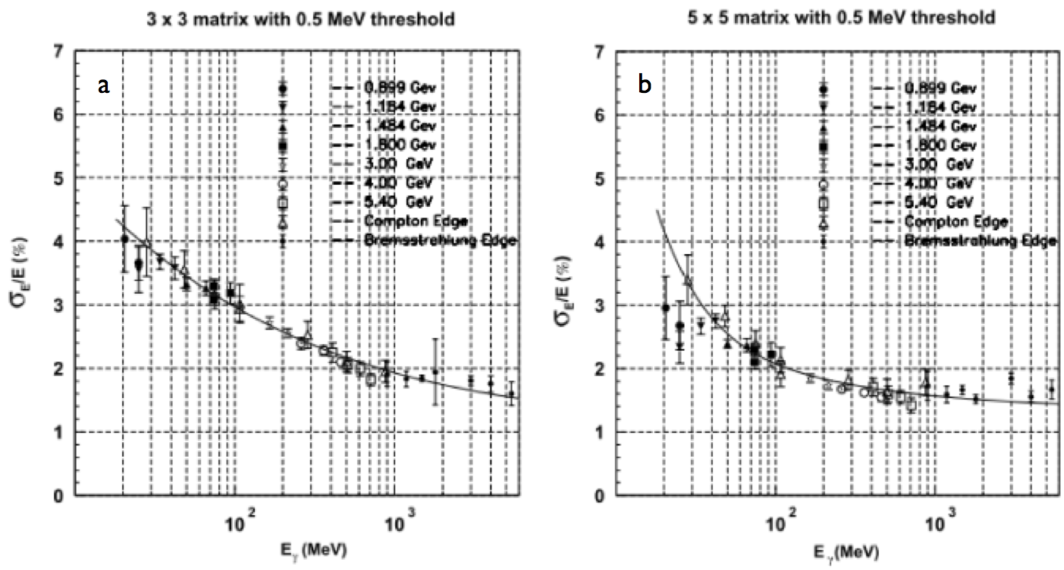

Figure 2.17: ECL energy resolution as a function of incident photon energy for the (a) 3 × 3 and (b) 5 × 5 matrices with a 0.5 MeV threshold. Tests were conducted on a 6x6 array of ECL units at the VEPP-4 collider. A photon beam was incident upon the 4 central ECL units at an angle perpendicular to their surface. Plots modified from Ref [17].

electronics (any PMTs, amplifiers, etc) of each individual channel. This electronic noise can also have a constant component that contributes to the third terms. The remainder of the third term is from static systematic uncertainties like anomalies in the detector geometry [19]. These functions and their fit to the ECL test data is shown in Fig. 2.17

ECL energy resolution is also a function of the position in the detector: at the start of Belle, the forward and backwards endcaps had significantly poorer resolution than the barrel region (see Fig. 94 of [17]). This has not improved with subsequent operation due to higher backgrounds. This has motivated a "standard" Belle prescription of restricting photons used in analysis to energies above 100 MeV in the endcaps and above 50 MeV in the barrel.

The photon position and energy information provided by the ECL are critical to this analysis. Techniques that reduce two of the biggest contributors to our backgrounds, the decay of $\pi^0 \to \gamma\gamma$ and final state radiation (FSR) from bremsstrahlung, require it. Using the energy and position information from the ECL, the momentum 4-vector of all the photons in the event is reconstructed. The invariant mass of pairs of these 4-vectors are used to find π^0 candidates and eliminate them. The position information from the ECL is directly related to the photon momentum vector; the opening angle between the photon momentum vector and the momentum of any changed track is used to reduce FSR. Both of these techniques will be discussed more thoroughly in Chapter 3.

2.10 K$_L$ Muon Discriminator (KLM)

The outermost subdetector is the KLM, used to detect long lived neutral kaons (K_L) and discriminate muons from hadrons ($\pi^{\pm}$, $K^{\pm}$, K_L). Isolated energy deposited in the KLM (i.e., no associated charge track) differentiates the neutral K_L from the $\mu^{\pm}$ and charged hadrons. A muon will penetrate the KLM much further and with less deflection than strongly interacting hadrons, differentiating it from the charged hadrons.

The KLM is composed of 14 alternating layers of 4.7 cm thick iron plates from Belle's magnetic flux return and 15 particle detecting "super-layers". The layout of a KLM super-layer is shown in Fig. 2.18. Each super-layer contains two glass-electrode resistive plate counters (RPC) that have pickup strips on either end that are oriented for signal readout in θ and ϕ. These RPCs are two highly resistive parallel plates that are separated by a gap filled with a gas made of argon, butane, and freon. Each RPC is surrounded by a layer of mylar for electrical insulation. The 14 iron layers provide approximately 3.9 interaction lengths for the K_L in addition to the four-fifths of an interaction length provided by the ECL. When a K_L interacts with matter in the KLM, it initiates a hadronic shower. Particles pass through the aforementioned gas-filled gap, causing ionization and a subsequent discharge that is read by the pickup strips.

Most pertinent to this analysis is the KLM's performance identifying muons; a plot of identification efficiency versus muon momentum is presented in Fig 2.19. Cosmic muons were used for determining efficiency: particle momenta was determined from the CDC and muon likelihood was determined from its depth of penetration into the KLM. The fake rate was determined by using a sample of $K_s \to \pi^+\pi^-$. For muons with a momentum above

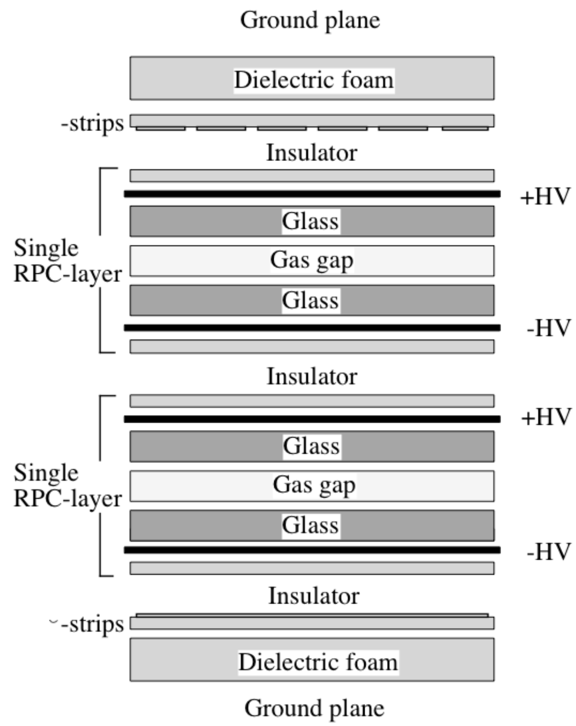

Figure 2.18: Cross-section of a KLM superlayer. Two resistive plate counter (RPC) layers are sandwiched between readout strips for the θ measurement on one side and ϕ measurement on the other. These superlayers are set between alternating iron layers that provide interaction materials for incident particles (not shown).

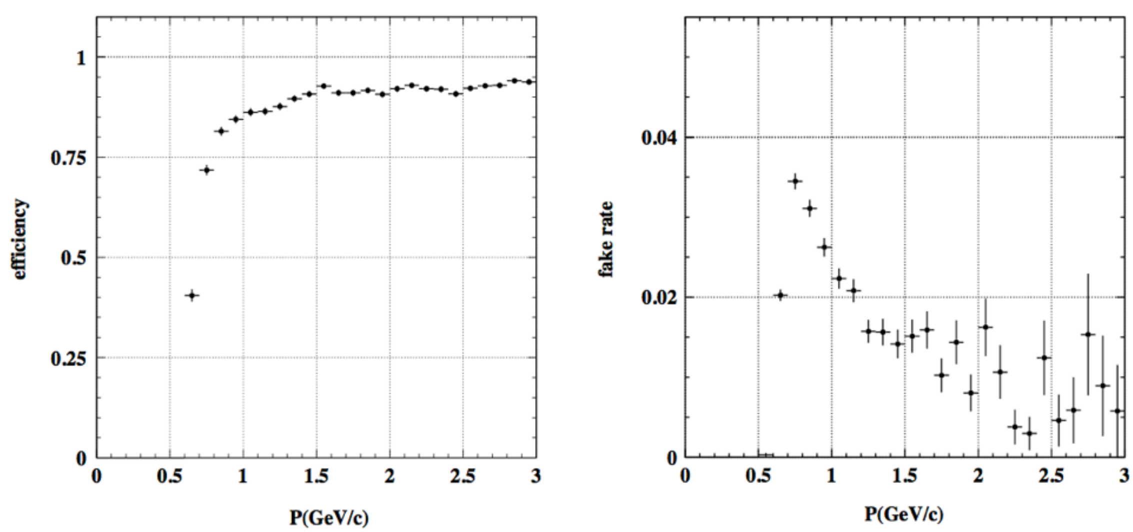

Figure 2.19: KLM performance. Left: muon identification efficiency as a function of transverse momentum. Right: muon fake rate as a function of transverse momentum.

1.5 GeV, the KLM has an identification efficiency in excess of 90%. For muons with a momentum above 0.6 GeV, the KLM has a fake rate below 5%.

2.11 Triggers & Data Collection

The high luminosity at Belle requires a triggering system that can discriminate between events of interest and those that are background. The trigger is used to reject background events and avoid exceeding the maximum data logging rate, approximately 500 Hz, of the data acquisition system. A first pass is made with two online triggers (implemented while the data is being read from detector subsystems) and later evaluation is made with an offline trigger (implemented after data is written to storage).

2.11.1 Online Triggers

The trigger system at Belle is designed to reject background events while preserving physics events with high efficiency. Physics events are $e^+e^- \to B\bar{B}$, $e^+e^- \to \gamma\gamma$, $e^+e^- \to q\bar{q}$ ($q =$ quark), and $e^+e^- \to l\bar{l}$ ($l =$ lepton). In the quark case, we are primarily interested in $b\bar{b}$, the Υs. In the lepton case, τ-pairs are interesting for physics analysis and e-pairs and μ-pairs are used for luminosity and detector calibration. Background events come primarily from spent electrons and positrons from the beam. In the initial design for Belle, a background trigger rate of $\sim$100Hz was expected, but it was known that such rates fluctuate depending upon accelerator conditions and are difficult to estimate.

The Level 1 (L1) trigger is the first online trigger. Information from all of the subdetectors are passed to the Global Decision Logic (GDL), a central trigger system. For charged particles, trigger information is based on information from the TOF and CDC. For neutral particles, energy deposits in the ECL and cluster counting form the basis for trigger conditions.The overall latency between event start and a trigger from the GDL is fixed to be 2.2 μs, so information from all subdetectors must be available to the GDL within 1.85 μs. After this, the GDL is left with 350 ns to issue a final L1 trigger signal. The L1 trigger is 96% efficient for Bhabha and μ-pair events [20] and over 99% efficient for hadronic events [17].

The Level 3 (L3) trigger is the second online trigger. The L3 trigger was implemented in 2001 to address the high L1 trigger rate: the L1 trigger rate was 200 $\approx$ 300 Hz instead of the expected $\sim$100 Hz. As luminosity increased, the L1 trigger rate would overwhelm the data acquisition system. The L3 trigger examines tracks in events that pass the L1 trigger. To be saved, events must have at least one track within 5.0 cm of the IP along the z-axis ($|dz| < 5.0cm$), an energy deposit in the ECL>3 GeV, or pass a specific event profile (e.g. "2 charged tracks, a hit in the KLM, and more than 1 GeV deposited in the ECL") passed on from the L1. The reconstruction of charged tracks is done online using a fast reconstruction algorithm. The L3 trigger efficiency is 98.8 for the TauPair skim, 98.2 for LowMulti skim, >99% for hadronic skims; and rejects 50 $\sim$ 60% of events coming from the L1 trigger.

2.11.2 Offline Triggers

The L4 trigger is implemented after the data is written to disk in raw form. Like the L3 trigger, it will accept an event if the track passes near the IP or if it matches a specific event profile passed on by the L1 trigger. For the L4 trigger, "near the IP" is defined as $|dz| < 4.0$cm and $|dr| < 1.0$cm. A further criterion is placed on the track's transverse momentum, p_t: $p_t > 300$ MeV. The L4 trigger rejected ~80% of events coming from the L1 trigger and kept the LowMulti trigger above 92% [21].

2.12 Particle Identification

2.12.1 Electron Identification (eid)

The electron identification at Belle uses the following information[3]:

- The matching between the extrapolated track position and cluster position in the ECL
- The ratio of energy deposited in ECL and charged track momentum measured by the CDC, which gives E/p
- The transverse shower shape in the ECL, parameterized by E9/E25
- The value of dE/dx measured by the CDC

First, an attempt is made to match a charged track to a cluster in the ECL. We define $\Delta\theta$ and $\Delta\phi$ as the difference in θ and ϕ between the extrapolated position of the

[3] Information in this subsection comes primarily from Ref. [22]

charged track at the surface of the ECL and the center of a the cluster being matched. We then find the "matching χ^2", defined as:

$$\chi^2_{matching} = \left(\frac{\Delta\theta}{\sigma_\theta}\right)^2 + \left(\frac{\Delta\phi}{\sigma_\phi}\right)^2 \tag{2.12.1}$$

For each charged track, the cluster with the smallest $\chi^2_{matching}$ is taken as the ECL impact location for that track and is used in the calculation of E/p. The cluster's E9/E25 is also associated with that track. If there is no cluster for which $\chi^2_{matching} < 50$, then the charged track is assumed to have not created a cluster in the ECL.

Differentiation between hadrons and electrons is based on their different spectra in E/p, E9/E25, and dE/dx. As seen in Fig. 2.20, there is a clear separation in the peaks of π and e for E/p and dE/dx. In E9/E25, we can see that the distributions are markedly different, with electrons having a peak further towards E9/E25 of one and a greater distribution in the tail. Because of these differences, each of these parameters is used as a discriminant in electron identification. For a single discriminant, say E/p, we find a confidence level (CL) by using the following equation:

$$CL(E/p) = \frac{CL(E/p)_e}{CL(E/p)_e + CL(E/p)_{not}} \tag{2.12.2}$$

where $CL(E/p)_e$ is the confidence level for the candidate being an electron and $CL(E/p)_{not}$ is the confidence level for other hypotheses. We typically use multiple discriminants (E/p, E9/E25, dE/dx and the light yield from the ACC), in which case we look for a likelihood, L_{eid}, determined by

$$L_{eid} = \frac{\Pi_{i=1}^{n} CL(i)_e}{\Pi_{i=1}^{n} CL(i)_e + \Pi_{i=1}^{n} CL(i)_{not}} \tag{2.12.3}$$

where i is the ith discriminant and n is the total number of discriminants (in our case, four).

2.12.2 Muon Identification (muid)

The muon identification at Belle uses the following information[4]:

- The tracking information from the CDC and SVD
- The location of interactions in the KLM

[4]Information in this subsection comes primarily from Ref. [23]

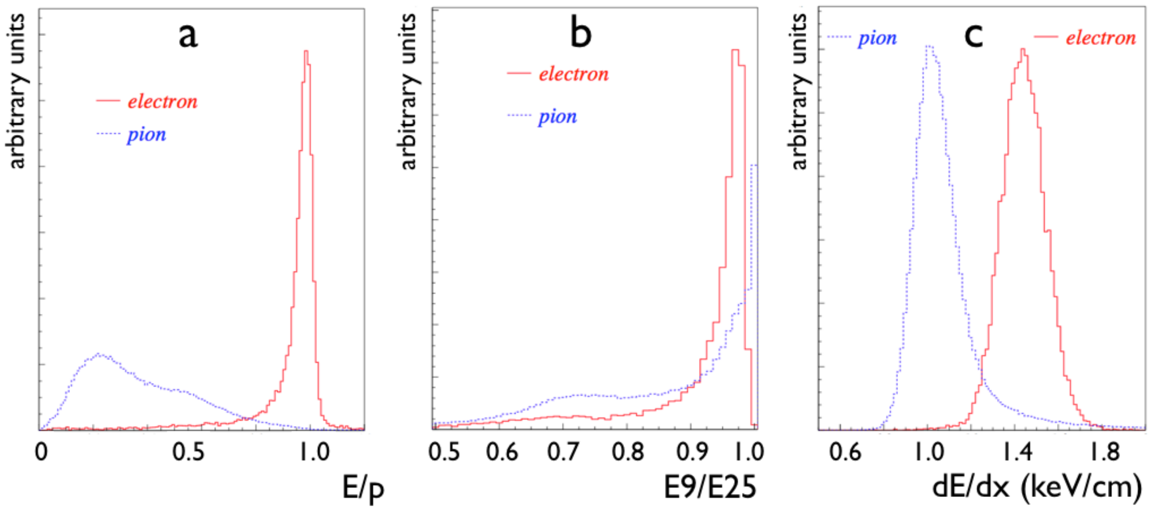

Figure 2.20: Electron identification using multiple subsystems. Electron (solid) and pion (dashed) spectra for a) E/p b) E9/E25 c) dE/dx are shown and clearly differentiated.

A charged track found in the the CDC (and SVD, if available) will be extrapolated from the outermost CDC hit point to the innermost layer of the KLM. An iterative fitting algorithm is then applied; it minimizes the distance between the projected track an the nearest interaction on the subsequent layer of the KLM. Once all interactions have been found, the offset between the projected track and all of the associated KLM interactions, χ^2_{KLM}, is minimized.

The muon likelihood is found using the depth of penetration into the KLM and χ^2_{KLM}. The difference between the expected penetration depth of penetration based on track momentum and the measured penetration is denoted as ΔR. Probability density distributions for ΔR and χ^2_{KLM}, $P(\Delta R)$ and $P(\Delta\chi^2_{KLM})$, were constructed using 100,00 single-track kaon, pion, and muon events. The ΔR and χ^2_{KLM} variables are uncorrelated, so the joint probability density is

$$P_\mu = P(\Delta R) \times P(\Delta\chi^2_{KLM}) \tag{2.12.4}$$

The normalized likelihood is then described as

$$L_{muid} = \frac{P_\mu}{(P_\mu + P_K + P_\pi)} \tag{2.12.5}$$

and stored in the muid table.

2.12.3 Photon Identification

Photons are identified by events in the ECL that are not associated with a charged track[5].

An ECL event, or “shower”, is reconstructed from a 5×5 matrix of ECL crystals. The crystal with the highest energy deposit above 10 MeV is selected as the center of the 5×5 matrix. The average position, weighted by energy deposition, is used to determine the center of the shower. In some cases, there will be multiple 5×5 matrices that overlap at the edges; these areas are called Connected Regions (CR). If an extrapolated charge track reaches the central crystal of a 5×5 matrix, the shower is rejected as a photon candidate. If a track reaches a crystal in a CR associated with that shower, it is kept but flagged as a possible fake photon. If there is no track associated with either the center of the 5×5 or the CR, it is flagged as a good photon candidate.

[5] Information in this subsection comes primarily from Ref. [24]

Chapter 3

Analysis

3.1 Overview

This chapter explains the analysis of $\Upsilon(1S)$ data from a search for a CP-odd light Higgs, denoted as "A^0", at the Belle detector. This sample includes 5.712 fb^{-1} [$(102 \pm 2)\times 10^6$ events] at the $\Upsilon(1S)$ production energy, compared with 1.1 fb^{-1} [$(21.5 \pm 0.4)\times 10^6$ events] for CLEO. This data set included runs with center-of-mass beam energies at the $\Upsilon(1S)$ production threshold (henceforth referred to as "on-resonance") and center-of-mass beam energies slightly below the $\Upsilon(1S)$ production threshold (henceforth referred to as "off-resonance"). We first established a $\tau^+\tau^-$ sample based on the loose criteria used at CLEO and BaBar. We then further purify the sample using tau selection cuts specific to Belle. Next we examine at the photons produced in the remaining events. Finally we measure a spectrum of the highest energy photon from each event and look for evidence of a $\Upsilon(1S) \to \gamma A^0$ transition.

The tau samples are selected first, beginning with the off-resonance case. This allows us to develop τ-pair and photon selection cuts with both real data and a Monte Carlo (MC) sample while learning more about the $\Upsilon(1S)$ continuum in the process. After the off-resonance data is seen to be correctly modeled, MC of on-resonance data is created simulating both the peak and continuum production at the $\Upsilon(1S)$ production energy in the experiment. The selection criteria for the off-resonance case are applied to the on-resonance sample and a similar result is seen. From a $\tau^+\tau^-$ sample in on-resonance MC, we examine the photon spectrum to reduce gamma contributions from known background sources. Using the expected Higgs signal MC as a reference, we adjust the cuts to maximize the Figure of Merit (F.o.M.). The remaining MC photon spectrum is then used to test fitting algorithms designed to detect a photon peak associated with the A^0.

3.2 Data

The data for this analysis was taken during the summer of 2008 at the end of a set of experimental runs known collectively as Experiment 65. Runs #1-999 of Experiment 65 were performed at the $\Upsilon(4S)$ production energy and will not be detailed here.

Runs #1000-1039 were used to move the e^+e^- beam energy to the $\Upsilon(1S)$ production energy. For these tests, the relative production rate of $\mu^+\mu^-$ compared e^+e^- was compared for various beam energies within ± 30 MeV of the expected $\Upsilon(1S)$ production energy. Once a peak in $\mu^+\mu^-$ events was found with this coarse scan, a finer scan of ± 4 MeV in steps of 2 MeV was performed, starting at 4 MeV below the measured peak production energy and increasing monotonically. The result of this scan is included as Fig. 3.1. The peak production energy was found to be 2 MeV below the peak found with the coarse scan and the beam energy was adjusted.

Runs#1040-1103 were "on-resonance", performed at the $\Upsilon(1S)$ production energy found from Fig. 3.1. Runs #1104-1142 were "off-resonance", where the beam energy was set 30 MeV below the $\Upsilon(1S)$ resonance. Finally, for runs #1143-1232, the beam was set back to on-resonance running. The beam conditions for both on- and off-resonance running is included in Fig. 3.3.

The accumulated number of $\Upsilon(1S)$ events was estimated from the number of $\mu^+\mu^-$ events recorded by Belle's online μ-pair monitoring system during the runs. The result of this estimate is shown in Fig 3.2. A more accurate measure of the number of $\Upsilon(1S)$ that uses hadronic cross-section information in offline data, is used in this analysis [25].

The Tau Skim B data set is selected for this analysis. To re-create the effect of the Tau Skim B skim in MC, evt_cls.flag(4) is recorded and only events with flag(4)>0 are included in the analysis. The tau skim criteria are described in Belle Note #0629 [26], and updated information is located online [27]. For convenience, the criteria are listed in Appendix D.

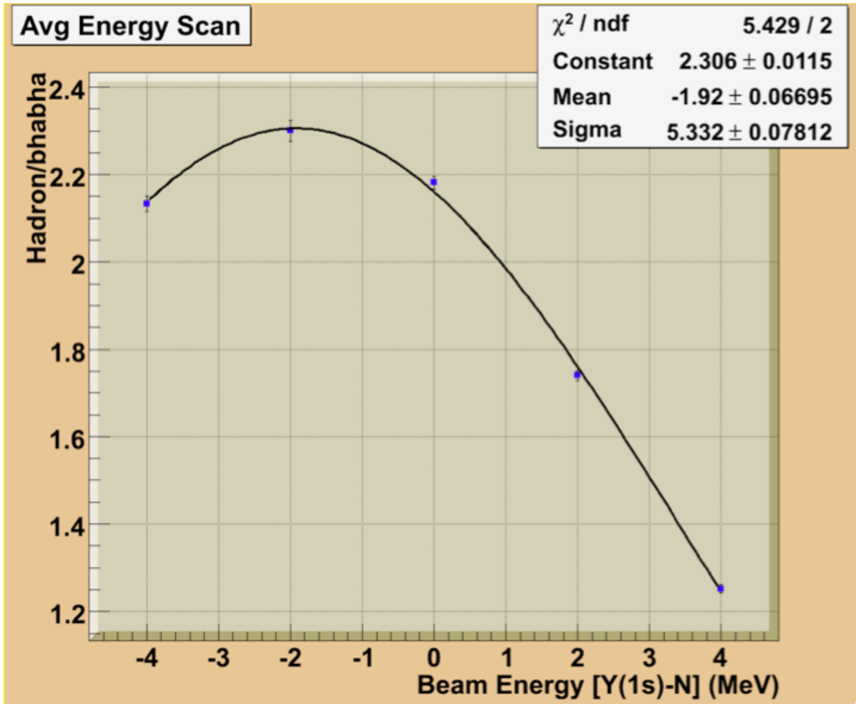

Figure 3.1: Plot of the ratio of $\mu^+\mu^-$ to e^+e^- events during a scan of beam energies used to find the $\Upsilon(1S)$ production energy at Belle.

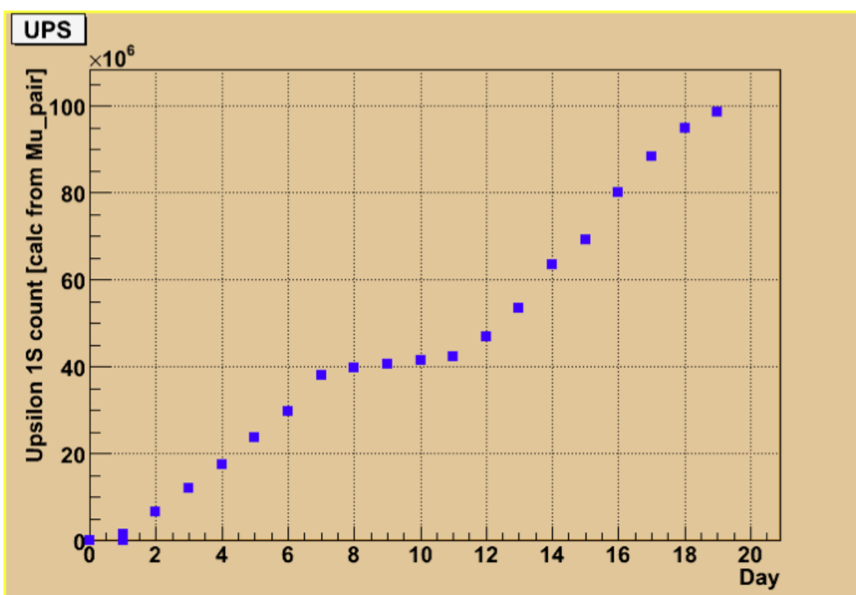

Figure 3.2: Υ(1S) accumulation using $\mu^+\mu^-$ counts in online data taken while the run was in progress.

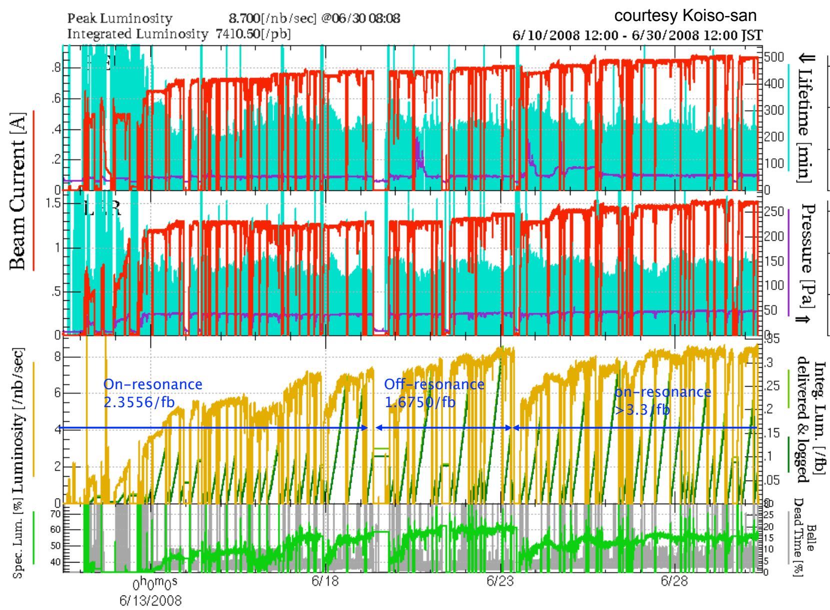

Figure 3.3: Accelerator information including beam current and online luminosity measurements from KEKB during the Υ(1S) run.

3.3 Monte Carlo

3.3.1 Off-Resonance $e^+e^-\to\tau^+\tau^-$ Quantity

In this experiment, 1.8022 fb^{-1} of data was collected 30 MeV below the $\Upsilon(1S)$ resonance. To determine how many τ-pair events that should be expected in off-resonance data, we use the following formula:

$$N^{off}_{\tau pair} = \sigma_{\tau^-\tau^+} k_{scale} L_{off} \tag{3.3.1}$$

- $N^{off}_{\tau pair}$ is the number of predicted tau pair events
- $\sigma_{\tau^-\tau^+}$= 0.919 nb is the cross section of $e^-e^+\to\tau^-\tau^+$ at the $\Upsilon(4S)$ resonance [28][29]
- $k_{scale} = (\frac{10.58GeV}{9.43GeV})^2$, the energy scaling between the $\Upsilon(4S)$ resonance and $\Upsilon(1S)$ off-resonance running energy
- σ_{off}= 1.802 fb^{-1}, the total integrated luminosity for off-resonance $\Upsilon(1S)$ running[30]

The result is an $N_{\tau pair}$ of 2.085×10^6 τ-pairs.

3.3.2 On-Resonance $e^+e^- \to \tau^+\tau^-$ Quantity

This experiment collected 5.712 fb^{-1} of data at the Υ(1S) peak. To determine how many τ-pair events we should expect in on-resonance data, we need to consider the contributions of both the $e^-e^+ \to \tau^-\tau^+$ continuum and $e^-e^+ \to \Upsilon(1S) \to \tau^-\tau^+$ production τ-pairs.

$N^{on}_{\tau pair} = \mathrm{N}_{e^-e^+\to\tau^-\tau^+} + \mathrm{N}_{e^-e^+\to\Upsilon(1S)\to\tau^-\tau^+}$

The calculation of the continuum contribution is similar to what was shown in section 3.3.1. The result is a continuum contribution to the number of τ-pairs in our sample, $\mathrm{N}_{e^-e^+\to\tau^-\tau^+}$, of 6.566×10^6 τ-pairs.

3.3.3 On-Resonance $\Upsilon(1S) \to \tau^+\tau^-$ Quantity

To calculate $\mathrm{N}_{e^-e^+\to\Upsilon(1S)\to\tau^-\tau^+}$, we take the estimated number of Υ(1S) determined by X.L.Wang et al. [25] and use the PDG branching ratios.

$N_{estimated} = (100 \pm 2) \times 10^6$

$N_{e^-e^+\to\Upsilon(1S)\to\tau^-\tau^+} = N_{estimated} \times BR_{\Upsilon(1S)\to\tau^-\tau^+}$

$N_{e^-e^+\to\Upsilon(1S)\to\tau^-\tau^+} = 2.574 \times 10^6$

It is also useful to calculate the number of τ-pairs in this sample that will have a specific leptonic decay, one where one τ decay includes an electron flavor particle and the other τ decay includes a muon flavor particle.

$N_{\tau^\pm\tau^\mp\to e^\pm\mu^\mp} = 159.4 \times 10^3$

3.3.4 Signal $\Upsilon(1S) \to \gamma A^0$

Batches of 10^3 and 10^4 events were generated to simulate $BR(\Upsilon(1S) \to \gamma A^0) \times BR(A^0 \to \tau^+\tau^-)$ ranging from 10^{-5} to 10^{-4}, respectively. The A^0 mass was varied from 3.6 GeV/c^2 (consistent with an associated γ with E_γ = 4.2 GeV) to 9.3 GeV/c^2 (consistent with an associated γ of E_γ=160 MeV) to probe a mass region starting at twice the mass of the τ and extending up to the point at which we could have mixing with the η_b.

3.3.5 $e^-e^+ \to \tau^+\tau^-$ MC Generation

KKMC [31] was used to simulate the continuum production of $e^+e^- \to \tau^+\tau^-$ for both on- and off-resonance MC. Some modifications were made to the default files used by Belle's Tau 2-Photon group [32]. With KKMC, users can set beam energies and momenta for the e^+ and e^- beams separately. The vectors take the form [$\mathbf{p}_x$, $\mathbf{p}_y$, $\mathbf{p}_z$, E] where all values are in GeV and $\hbar$=c=1. In off-resonance MC, the LER (e^+) and HER (e^-) 4-vectors were set to

[0, 0, -3.128603, 3.128603] (GeV)

and

[0.157311, 0, 7.149363, 7.151093] (GeV)

respectively, consistent with a crossing angle of 0.022 radians. The CM energy was set to 9.430D0 (read: 9.43 GeV). In on-resonance MC, the LER and HER 4-vectors were set to

[0, 0, -3.118687, 3.118687] (GeV)

and

[0.156813, 0, 7.126704, 7.128429] (GeV)

respectively, also consistent with a crossing angle of 22 milliradians. The CM energy was set to 9.46 GeV. For both on and off-resonance cases, the "long lived" switch remained set to 1 (no decay), the $c \times \tau_\tau$ was kept at 0.08711 mm, and no modifications were made to the spin polarization. The τ-pairs created were allowed to decay generically according to the default KKMC decay table.

Using these settings, 20 batches of 104,250 events were generated to match the total number of off-resonance generic τ-pairs calculated in subsection 3.3.1. Off-resonance MC plots in this note are obtained from a sample of 2.086×10^6 τ-pairs unless otherwise noted.

GSIM was used to simulate the detector response and fill the default PANTHER tables as well as PANTHER tables specific to TSIM and tsim_skin.

3.3.6 $\Upsilon(1S) \to \tau^+\tau^-$ MC Generation

EvtGen [33] was used to model the contribution to the tau sample from the production of $\Upsilon(1S)$. The top level decay, 2.6 million $\Upsilon(1S) \to \tau^+\tau^-$ events, was generated with the packages VLL and PHOTOS. These packages are, respectively, used to properly handle the helicity angles of vector decays to lepton pairs and to include final state radiative (FSR) photons from the decay products. The resulting τ-pairs were then decayed generically using the standard decay table, DECAY.DEC, with 2006 PDG values for τ-decays.

3.3.7 $\Upsilon(1S) \to \gamma A^0$ MC Generation

Monochromatic photons were generated using EvtGen. The top level particle is an $\Upsilon(1S)$ as defined in the standard DECAY.DEC. A set of A^0s with varied masses were added to the standard DECAY.DEC to allow for the $\Upsilon(1S) \to \gamma A^0$ decays. This step in the decay mode was modeled with the HELAMP package; specifically invoking "HELAMP 1 0 1 0" to simulate $vector \to \gamma + pseudoscalar$. The next step, $A^0 \to \tau^+\tau^-$; was modeled using the packages "PHSP" and "PHOTOS" to simulate $pseudoscalar \to l^+l^-$ and to again model radiative photons from the decay products.

After this point, three different types of signal MC were created. To model signal events expected to pass all the cuts in the tau sample (including misidentified modes), the τ-pair generated from $A^0 \to \tau^+\tau^-$ was allowed to decay generically using the previously mentioned DECAY.DEC. This is called the "Generic Higgs MC"; it is used when adding a Higgs signal onto a background. To model desired decay modes in the "e & μ" case, *i.e.*, those that have both $\tau \to e\bar{\nu}_e\nu_\tau$ and $\tau \to \mu\bar{\nu}_\mu\nu_\tau$ in the last step of the decay chain, the decay of each of the τ was set explicitly. This is called called the "Pure e & μ Higgs MC". Finally, MC was generated where one track was either an e or a μ and the other was one of the 1-prong decay modes. The primary contributors to the"1-prong" decay modes are as follows:

- $\tau \to e\nu_\tau\bar{\nu}_e$
- $\tau \to \mu\nu_\tau\bar{\nu}_\mu$
- $\tau \to \pi^-\nu_\tau$
- $\tau \to \rho\nu_\tau$
- $\tau \to a_1\nu_\tau$

This is called the "Pure 1-prong Higgs MC".

No ISR effects were considered: the $\Upsilon(1S)$ is narrow enough that any photons produced via initial state radiation (ISR) in $\Upsilon(1S) \to \gamma A^0$ would be below our photon energy thresholds.

3.3.8 Detector Simulation

To simulate the detector response, we use two programs based on GEANT [34, 35]: GSIM and TSIM. The MC generated by KKMC and EvtGen is passed to GSIM; GSIM is then used simulates the response of the Belles various subdetectors. GSIM is also used to include the results from subsystems taken at times outside of a trigger windows; this is a sampling of the beam background. This analysis uses beam background files 0-19 and samples randomly from each of them. TSIM is used to simulate Belle's the trigger response for the MC events. The copy of TSIM used for this analysis has been updated to revision 11329 released on 2011-06-30

3.4 Electron-Muon Off-Resonance Tau-Pair MC Study

By requiring an electron and a muon to be the only charged particles in the final state, we produce a sample of τ-pairs that we know to be very pure. This final state will be dominated by modes whose final decays are $\tau^{\pm}\tau^{\mp} \rightarrow e^{\pm}\mu^{\mp}\bar{\nu}_{\mu,e}\nu_{e,\mu}\bar{\nu}_{\tau}\nu_{\tau}$. The tradeoff is that only 6.2% of τ-pairs will decay to this type of final state, limiting our sample statistics.

For shorthand, we refer to this set of cuts as "e & μ cuts" or just "e & μ".

3.4.1 Data Skim Criteria

Passes Tau Skim B as defined in the event classification system. The criteria of the Tau Skims are presented in Appendix . In the Belle event classification code, events that pass Tau Skim criteria are assigned a value greater than zero to their fourth event classification flag (evt_cls). The value assigned to this flag is dependent upon which set of criteria were passed; for this experiment the only requirement for the flag is that it is greater than zero.

- evt_cls.flag(4)>0

3.4.2 Trigger Selection Cuts

MC generates some events that pass the selection criteria but would not meet trigger conditions, leading to an over-production of events in MC. To account for this , we use TSIM via the tsim_skin module to determine whether trigger conditions would be satisfied for each event. The standard Belle trigger criteria is used: the first and second ("0" and "1") trigger flags of "RecTRG_summary3.final" must satisfy "RecTRG_summary3.final(0) + RecTRG_summary3.final(1) != 0". The trigger configurations are set by 20070531_col19d.psnm and ftdlv8_08.alg.dat. With no other cuts applied, a trigger efficiency of 91.5% for off-resonance τ-pair MC is observed.

- RecTRG_summary3.final(0) + RecTRG_summary3.final(1) != 0

3.4.3 Initial Tau Sample Selection Criteria

The user analysis module adds several cuts in addition to the Tau Skim B. We look for a clean τ-pair sample by looking for events where where both τ go through single-prong decays. For a decay of τ^+ and τ^- we look for opposite charge in the two resulting tracks. To further refine the sample, we select events where there is both an $e^\pm$ and a $\mu^\mp$ candidate in the final state.

- Exactly two charged tracks with charge balance
- Either $e^+\mu^-$ or $e^-\mu^+$ in the final state
- Electron probability (eID) must be greater than 0.9 and muon probability (μID) must be greater than 0.6.

3.4.4 The "e+μ" and the Kinematic Boundary Selection Criteria

We can reconstruct a fake particle, the "e+μ", and study its kinematic properties in order to further characterize the quality of our sample. This particle is constructed by taking the final state e and μ, boosting them into the CM frame, summing their Lorentz vectors and assigning it the status of "particle". Quantities such as the angular distribution and invariant mass can be used to further assess the quality of our sample and make cuts to remove suspected non-τ-pair events. The Kinematic Boundary (KB) selection cut is an example of that. First, the motivation for the KB cut: while misidentification of e^+e^- and $\mu^+\mu^-$ as (e, μ) events may be rare, there remains a class of continuum di-lepton final state events that we can easily isolate and remove. The process $e^+e^- \to l^+l^-$, with $l = e, \mu$ will produce particles whose combined energy in the CM frame will be extremely close to the initial CM energy and will have oppositely aligned CM-frame momenta. When plotting the $e + \mu$ total momentum vs. invariant mass in Fig. 3.4, di-lepton pairs that are generated through this process will fall along the boundary of the kinematically accessible region.

Note the band along the kinematic boundary of the system that appears in data but not in MC. These events are, as mentioned previously, most likely misidentified $e^+e^- \to \mu^+\mu^-$ or $e^+e^- \to e^+e^-$ events. Re-parameterization in terms of KB defined in Eq. 3.4.1:

$$KB = s - M_{e+\mu}^2 - 2E_{e+\mu}P_{e+\mu}, \text{ all parameters in CM frame} \qquad (3.4.1)$$

allows us to more easily exclude the band. Plotting KB against $\frac{P_{e+\mu}}{M_{e+\mu}}$ yields Fig. 3.5 for Monte Carlo and data.

If we project onto the X-axis as in Fig. 3.6, it becomes clear that there is a distribution of events with KB very near zero that appears in data to a much greater extent

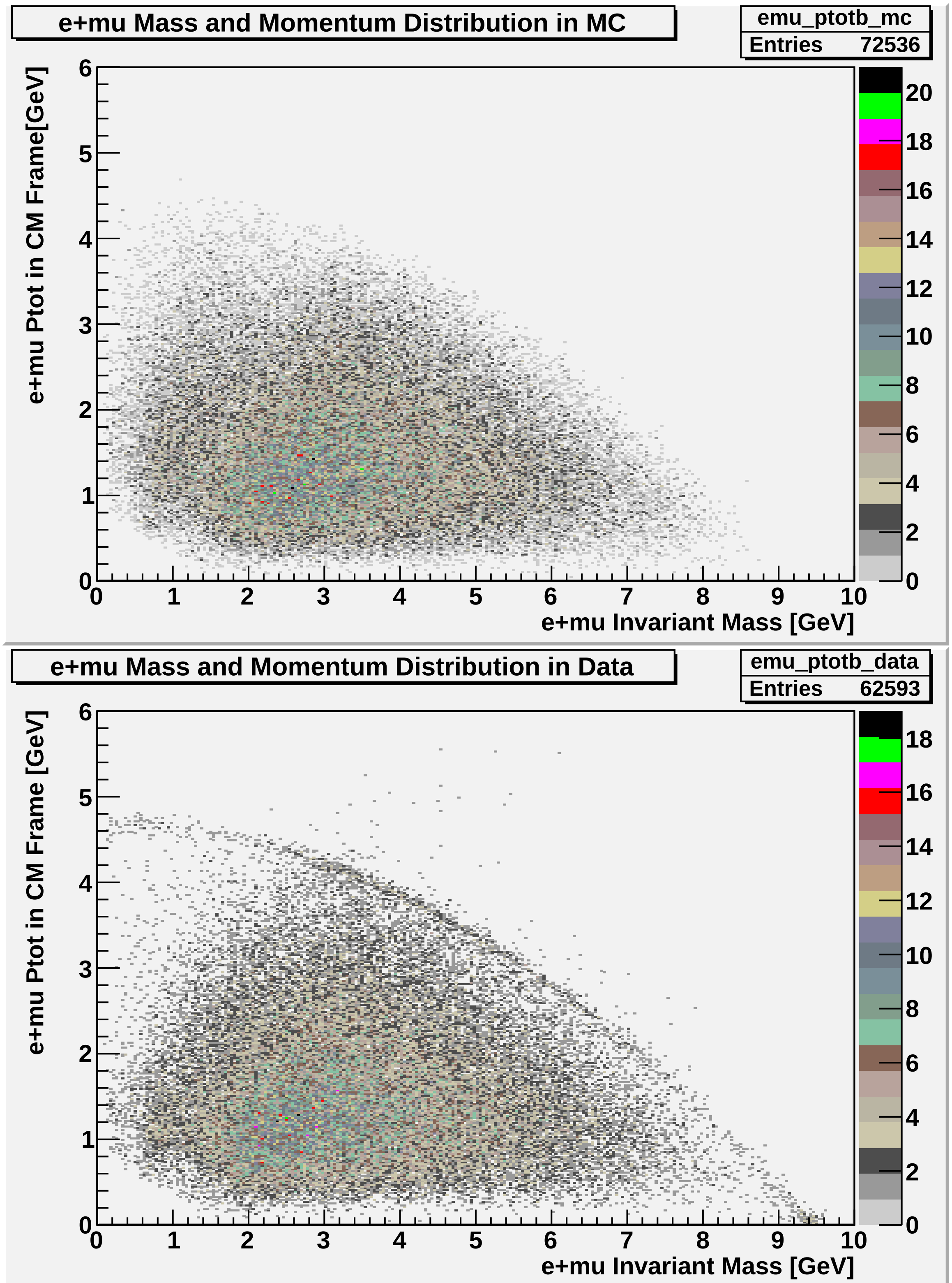

Figure 3.4: The e+μ total momentum in the CM frame vs invariant mass, in off-resonance MC (top) and experimental data (bottom)

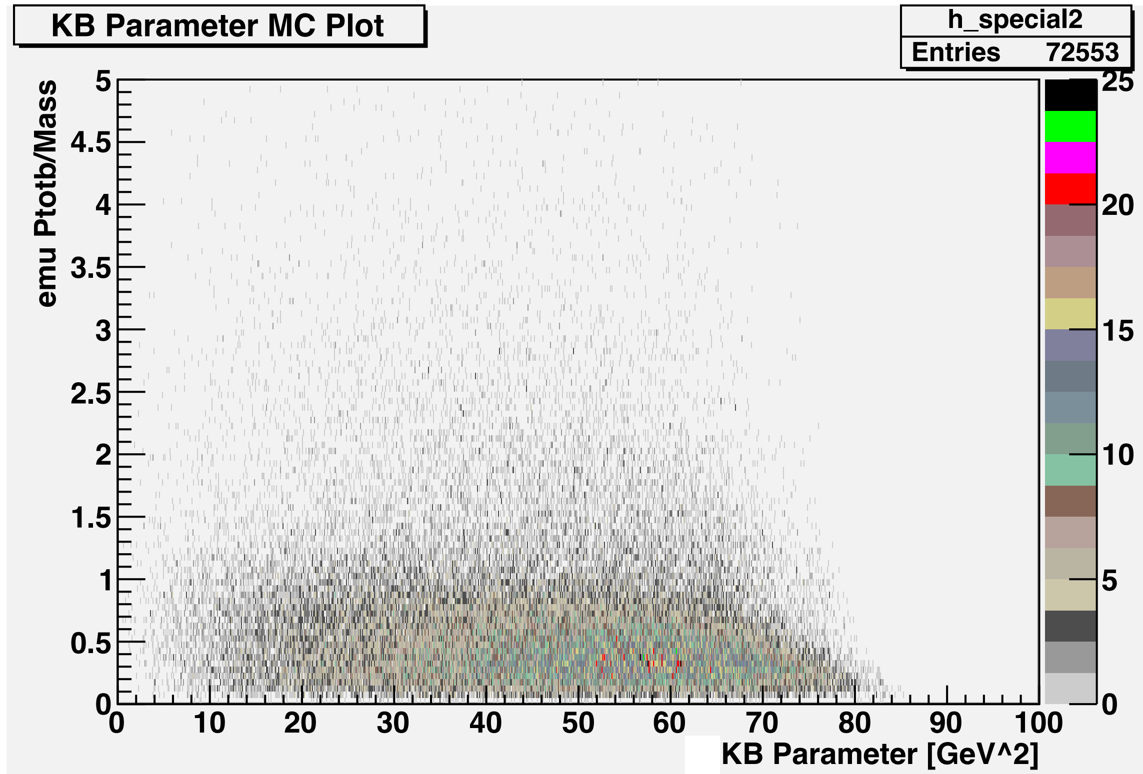

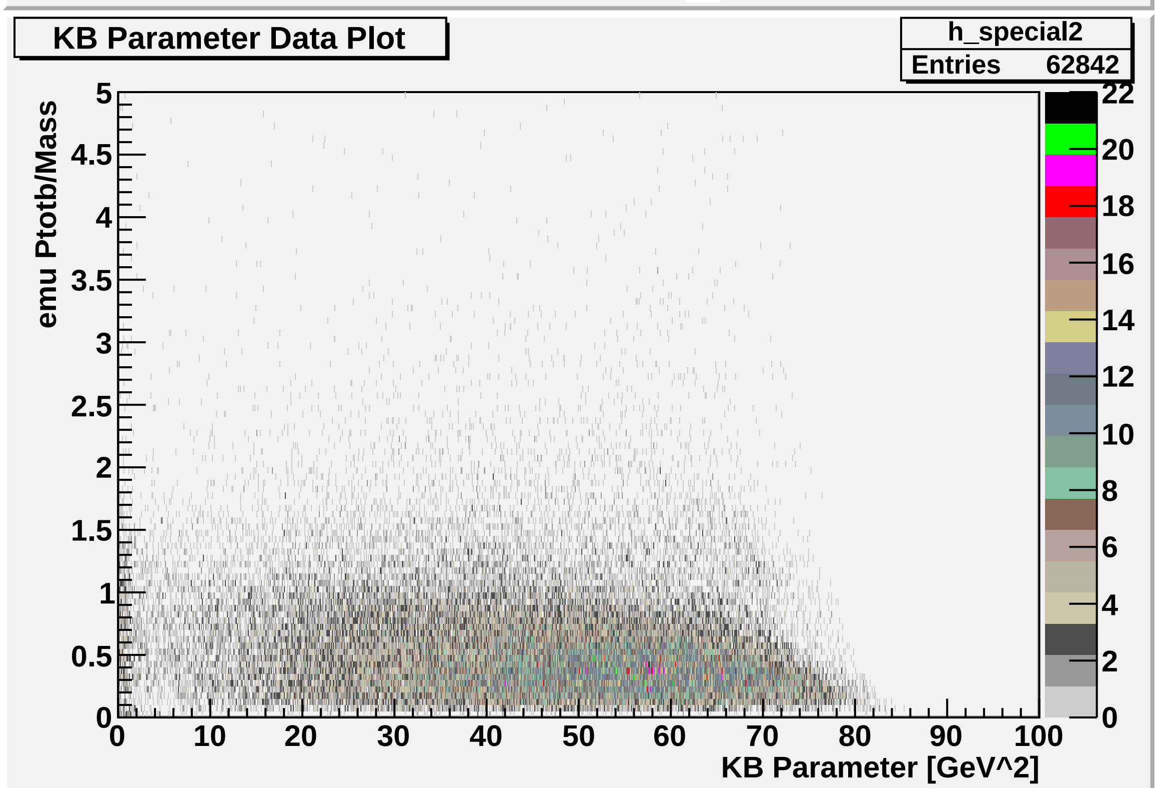

Figure 3.5: Ratio of C.M. e+μ momentum to e+μ invariant mass vs the Kinematic Boundary parameter, in MC (top) and experimental data (bottom)

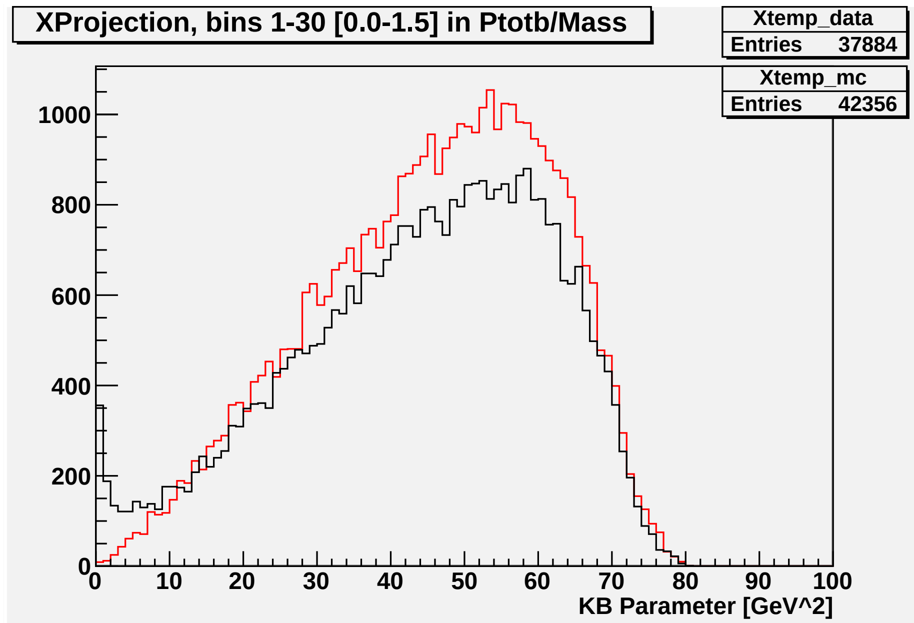

Figure 3.6: KB parameter distribution (x-axis projection of Fig. 3.5) Data (black) and MC (red).

than in Monte Carlo. If we project onto the $\frac{P_{e+\mu}}{M_{e+\mu}}$ axis and remove the band at KB near zero GeV^2, we expect to see similar results for both MC and data. This is verified in Fig. 3.7. This leads us to the following selection criteria.

- KB >10 GeV^2

3.4.5 Fine Tau Sample Selection Criteria

Further refinements are made to the τ-pair sample selection based on MyeongJae Lee's work in calculating the number of τ-pair in $\Upsilon(4S)$ data [36] and in his analysis of $\tau \rightarrow hh^+h^-\nu$ [37]. Applied to this analysis are his cut on the missing mass $M_{missing}$, the angle of the missing momentum vector $\theta_{missing}$, the probability of identification of an e or a μ, and the opening angle between the e and the μ momentum vectors, $\alpha_{e\mu}$. The quantities $M_{missing}$, $\theta_{missing}$, and $\alpha_{e\mu}$ are all measured in the center of mass frame.

- Missing Mass Cut: 1.0 GeV^2 $< M_{missing} <$ 7.0 GeV^2

- Missing Angle Cut: $30^\circ < \theta_{missing} < 150^\circ$

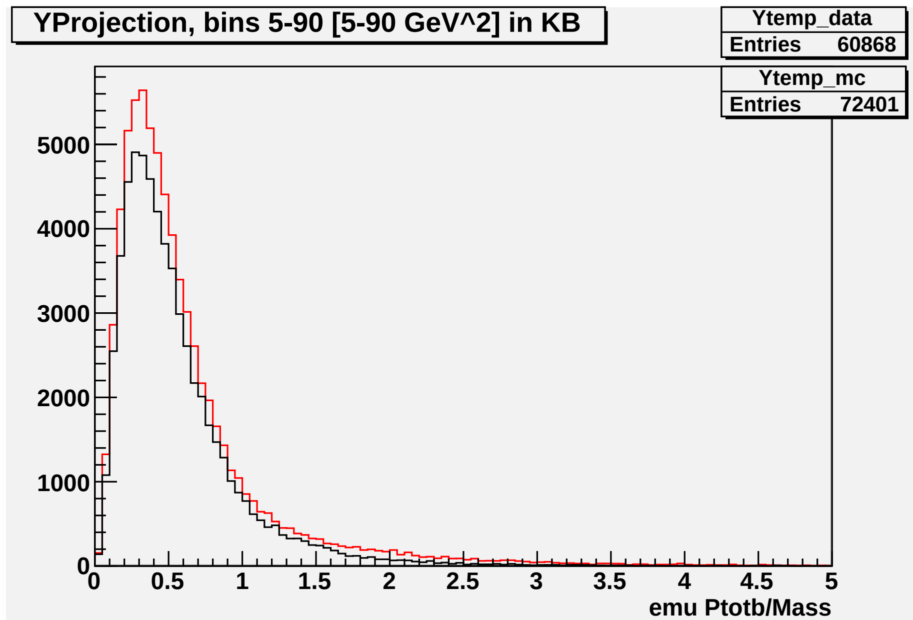

Figure 3.7: Ratio of C.M. e+μ momentum to e+μ invariant mass distribution (y-axis projection of Fig. 3.5). Data (black) and MC (red).

Table 3.1: Summary of Effects of "e & μ" Tau Selection Cuts on Data and MC

Cut	# Retained (MC)	Efficiency (MC)	# Retained (Data)	Efficiency (Data)
No Cuts/Skim	2,085,000	N/A	6,467,416	N/A
Tau Skim B	1,459,195	0.700	-	-
Trigger	1,313,885	0.630	-	-
Two Charged Tracks w/ Balance	733,779	0.352	4,435,159	0.686
$N_\mu = N_e = 1$	58,806	0.028	62,633	0.010
Lepton Probability Cut	45,796	0.022	51,169	0.008
KB Cut	45,338	0.022	49,057	0.008
Missing Mass Cut	41,967	0.020	44,944	0.007
Missing Angle Cut	34,973	0.017	35,025	0.005

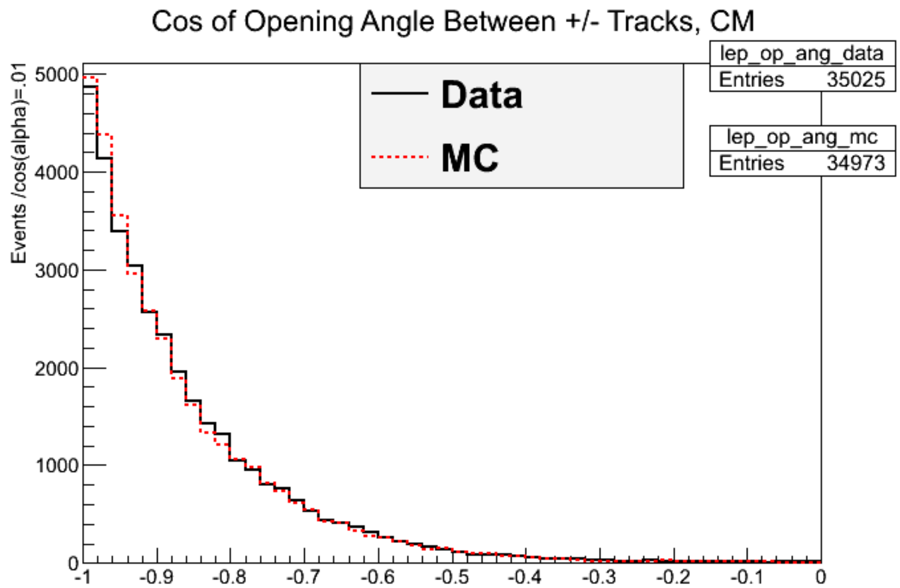

Figure 3.8: The opening angle between the two charged tracks in the cm frame. All "e & μ" tau selection cuts applied. MC and experimental data are both off-resonance.

3.4.6 Results

The effects of each cut on data and MC are shown in Table 3.1. Characteristic quantities of τ-pair events are plotted in both MC and Tau Skim data. In addition to the opening angle between the charged tracks of the two 1-prong decays seen in Fig 3.8 , information about a particle reconstructed from the final state e+μ are examined as well. The reconstructed particle's invariant mass and momentum in the center-of-mass frame are plotted against one another in Fig. 3.9.

Based upon the agreement between data and MC, we believe that the τ-pair sample is accurately modeled.

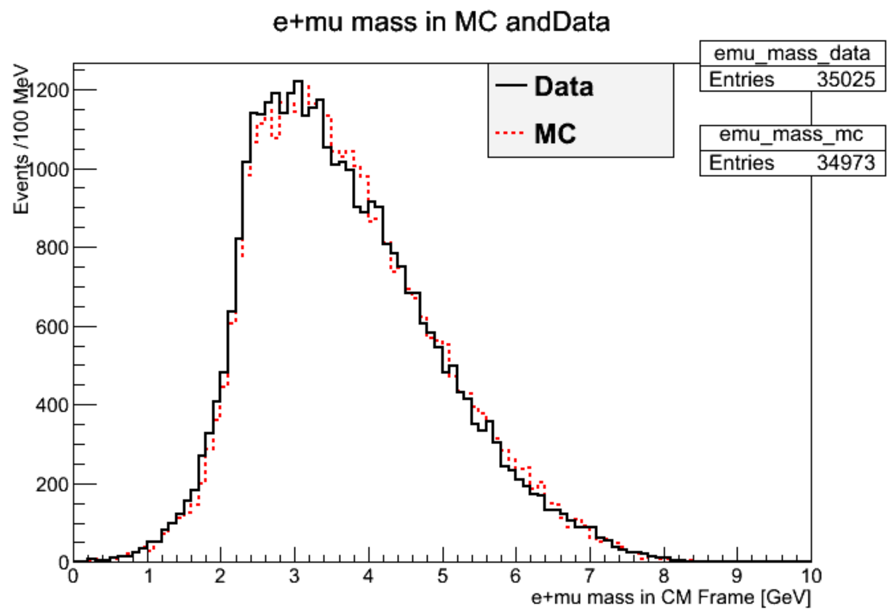

Figure 3.9: The invariant mass of the e+μ combined particle. All "e & μ" tau selection cuts applied. MC and experimental data are both off-resonance.

3.5 Electron-Muon Off-Resonance Photon Background MC Study

3.5.1 Initial Photon Cuts

A first set of loose cuts are applied to the off-resonance photon spectrum that are produced after the final tau cuts described previously. Barrel photons (defined as having an angular distribution of -0.6 $<\cos(\theta)<$0.8 in the lab frame) and endcap photons (photons detected outside of the previously defined region) have different criteria for being included in the set of photons under analysis. Endcap photons are required to deposit least 100 MeV in the calorimeter whereas barrel photons need only deposit more than 50 MeV.

Photons that are candidates for being the γ in $\Upsilon(1S) \to \gamma A^0$ have further requirements. They must pass the barrel photon cuts, a bremsstrahlung cut based on the opening angle α_{Brem} between the photon momentum vector and the electron or positron track, and a π^0 cut based on the invariant mass of the candidate photon and any other photon (barrel or endcap) in the event.

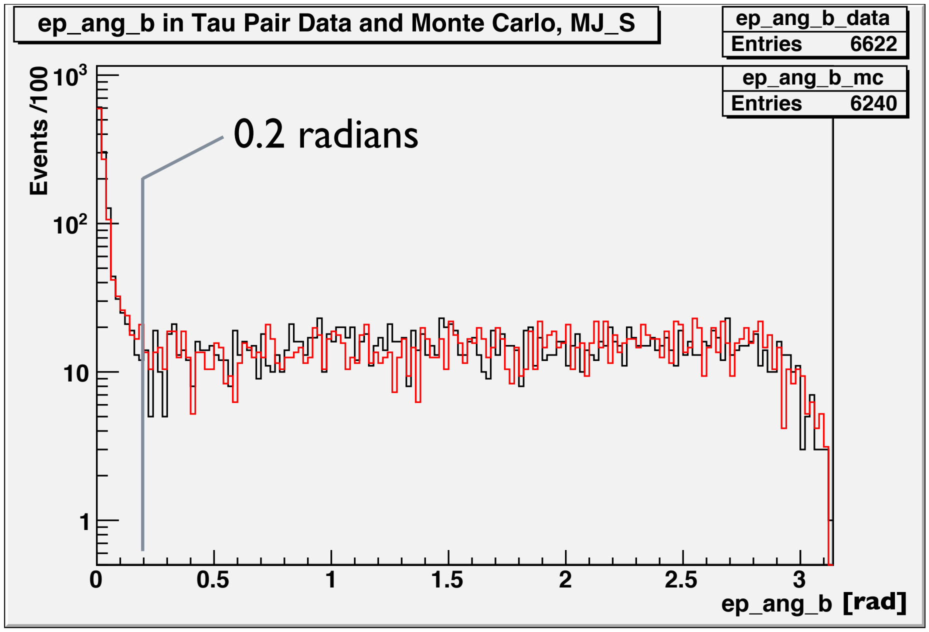

Figure 3.10: Plot of α_{Brem} in off-resonance MC in both linear and (inset) log vertical scale. A clear transition between bremsstrahlung dominant and recessive regions can be seen.

- Gamma Quantity Cut: at least one photon must be present in the event. The most energetic photon is selected.
- Barrel Cut: Photons outside of the barrel region are excluded from being signal photon candidates.
- Bremsstrahlung Cut : α_{Brem} must be greater than 0.2 radians in the CM frame. As this differs slightly from the standard Belle prescription for eliminating bremsstrahlung gammas, a plot in support of this decision has been included as Fig. 3.10.
- π^0 Cut : The A^0 photon candidate cannot be combined with any other photon in the event to form a particle with mass $< 3\sigma$ away from M_{π^0}

The relative contributions of these background sources across the photon spectrum are shown in Fig. 3.11.

Table 3.2: Summary of Effects of "e & μ" Photon Selection Cuts on Data and MC

Cut	# Retained (MC)	Efficiency (MC)	# Retained (Data)	Efficiency (Data)
Tau Selection Cuts	34,973	0.017	35,025	0.005
Gamma Quantity	12,576	0.006	12,995	0.002
π^0 Cut	10,554	0.005	10,765	0.002
bremsstrahlung	6,807	0.003	7,088	0.0011
Barrel Cut	5,138	0.002	5,385	0.0008

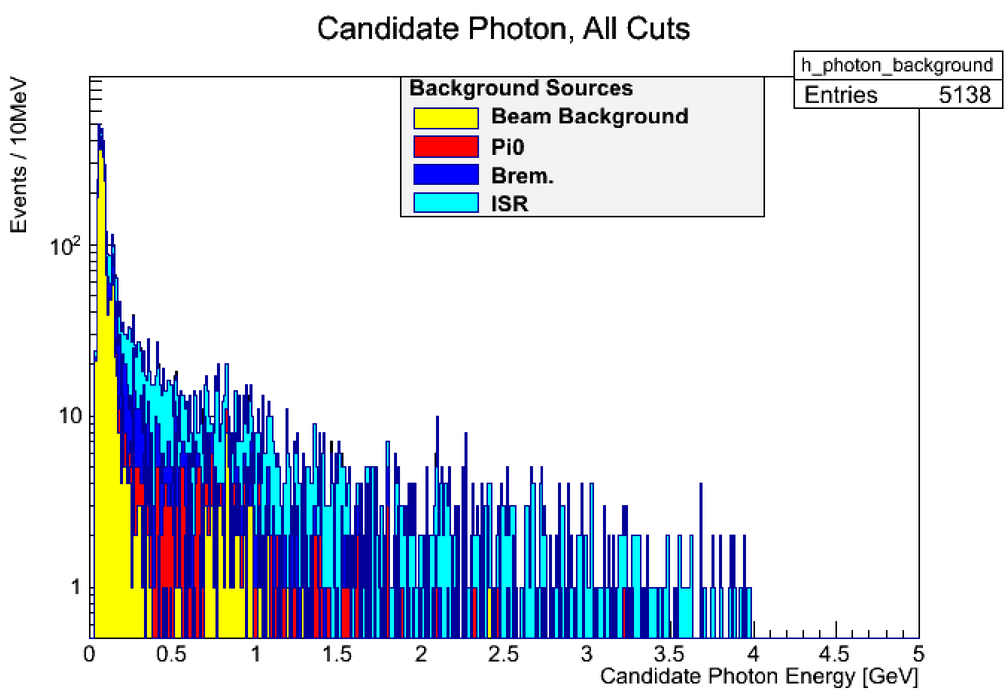

Figure 3.11: Backgrounds in photon spectrum, all cuts in tau section applied.

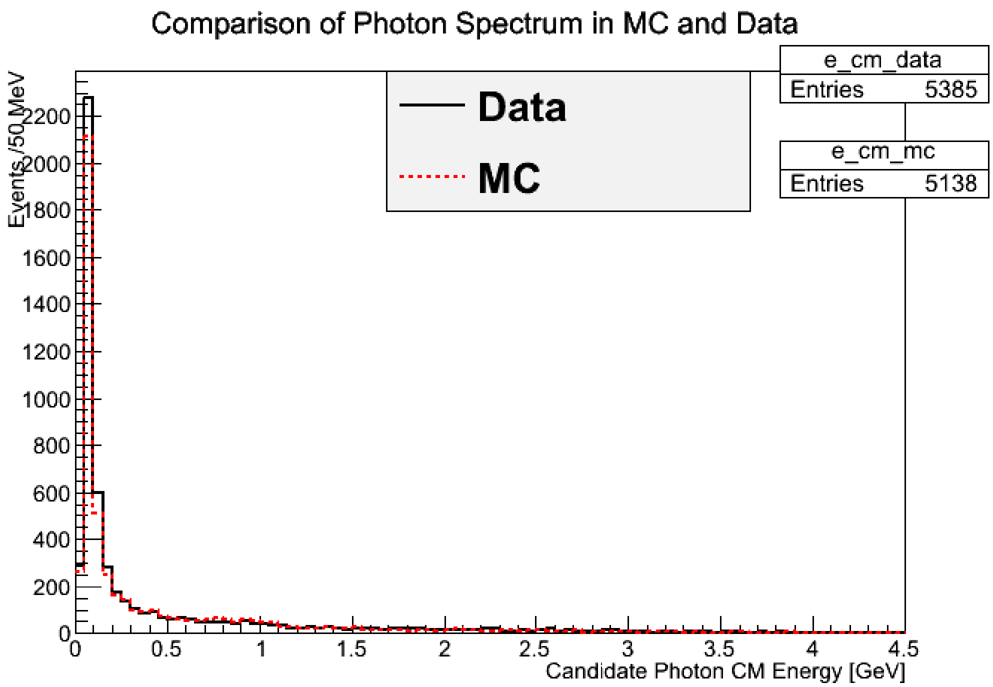

Figure 3.12: Photon spectrum, all cuts applied, 0 to 4.5 GeV.

3.5.2 Results

The effects of each cut on data and MC are listed in Table 3.2. Based upon the agreement between data and MC seen in Figure 3.12, we believe the photon spectrum from the decay of tau pairs is accurately modeled above 150 MeV and that backgrounds have been reduced. Further study in Sec. 3.6 indicates that beam background events are the largest contributor to the photon background below 150 MeV.

3.6 Electron-Muon On-Resonance Photon Background MC Study

With a larger sample of beam background photons to examine, we study the angular distribution of the beam background contribution to the photon spectrum. Above a photon energy of 150 MeV the distribution is uniform; below 150 MeV there is a clear ϕ dependence to the contribution (see Figs 3.13 and 3.14). This ϕ dependence may be due to noisy channels in the readout electronics.

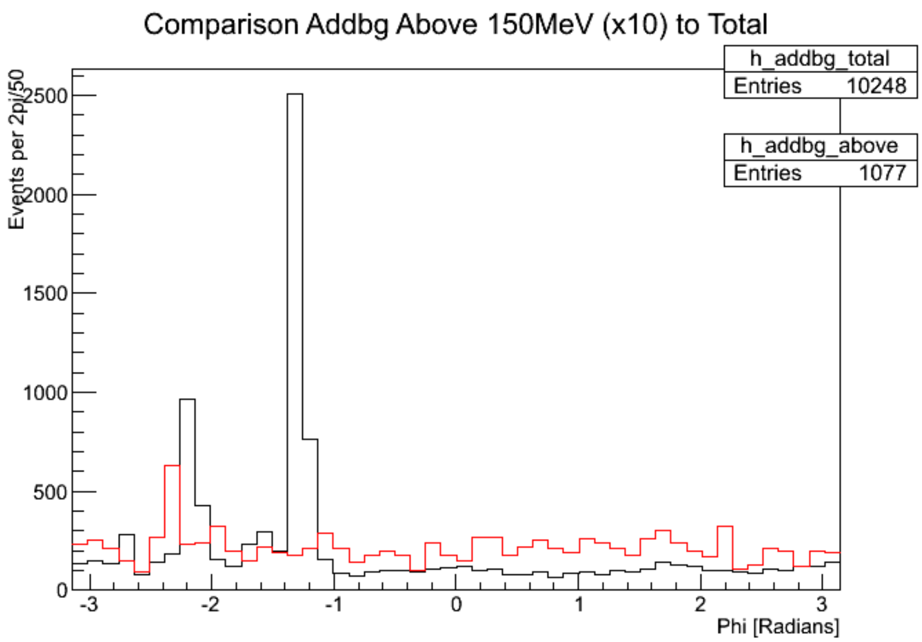

Figure 3.13: Angular distribution of beam background photons in ϕ. The red line is ten times (10x) the contribution from photons above 150 MeV. Black line is the overall contribution, unscaled. All "e & μ" tau and photon selection cuts applied.

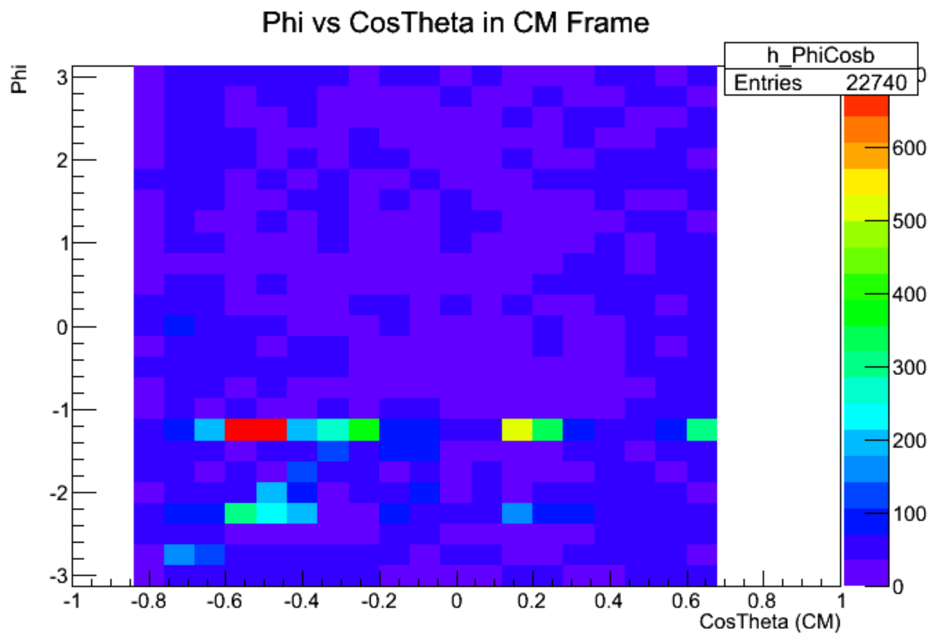

Figure 3.14: Distribution of all beam background photons in ϕ and CM Cos(θ). All "e & μ" tau and photon selection cuts applied.

3.7 Electron-Muon Photon Signal MC Study

For tuning, we attempt to balance the maximization of the Figure of Merit (Eq 3.7.1) with the maximization of the efficiency for that cut.

$$FoM = \frac{signal}{\sqrt{signal + background}} \tag{3.7.1}$$

We also examine Relative Efficiency, defined here as

$$RE = \frac{signal}{background} \tag{3.7.2}$$

as opposed to the Cut Efficiency,

$$CE = \frac{FinalSignal}{InitialSignal} \tag{3.7.3}$$

Some selection criteria are bounded on two sides. For these, we use the convention "low side" $\leq$ Parameter of Cut $\leq$ "high side" to differentiate between the two boundaries of the cut.

Lastly, some selection criteria overlap with previous selection criteria applied via the Tau Skim. For example, the total energy deposited into the ECL by charged tracks must be less than 5.3 GeV, the visible energy must be greater than 3 GeV, and total energy inferred from visible energy and missing momentum must be less than 9 GeV (see Appendix D). These requirements impose a selection criteria on missing energy and momentum before this analysis' selection criteria are even considered, one that eliminates events with low likelihood of being $ee \rightarrow \tau\tau$ or $ee \rightarrow \Upsilon(1S) \rightarrow \tau\tau$. This results in FoM plots that do not "turn over", or reach a maximum that is not at the edge of their range. this can be seen when comparing Fig 3.22 and Fig. 3.15: the first is said to turn over, the second does not.

3.7.1 Tuning

This analysis searches for A^0 decays across a range of A^0 masses from the minimum τ-pair production mass up to a mass approaching the mass of the $\Upsilon(1S)$. The kinematics of these decays, such as missing energy or angular distribution, can be very different. In tuning the cuts, we must be careful to not maximize signal for one region at the expense of greatly reducing the signal from another. To avoid this, we use Figures of Merit to tune for both a 3.6 GeV/c^2 and 9.3 GeV/c^2 A^0 and select the looser of the two cuts motivated by the Figure of Merit.

Missing Energy Cut Tuning

The distribution of missing energy is dependent upon the energy of the photon associated with the A^0. Missing energy cutoffs are tuned against on-resonance MC using two sets of 10,000 $\Upsilon(1S) \rightarrow \gamma A^0 \rightarrow \gamma\tau\tau$ with the τ-pair decaying to e and μ. The low side of the missing energy cut is tuned with $M_{A^0} = 3.6$ GeV/c^2, the high end is tuned with M_{A^0} $= 9.3$ GeV/c^2. In both cases, cuts on event classification, trigger, charge balance, number of tracks, and lepton flavor are applied. Results for the FoM and efficiency are shown in Figures 3.15, 3.16, 3.17, 3.18.

The tuning motivated a slight modification of the missing energy cut;
1.5 GeV $\leq E_{missing} \leq$ 7.5 GeV

Missing Angle Cut Tuning

The angular distribution of the missing momentum vector is tuned after the missing energy cut is applied. Missing angle cutoffs are tuned against on-resonance MC using two sets of 10,000 $\Upsilon(1S) \rightarrow \gamma A^0 \rightarrow \gamma\tau\tau$ with the taus decaying to e, μ states ("pure MC").

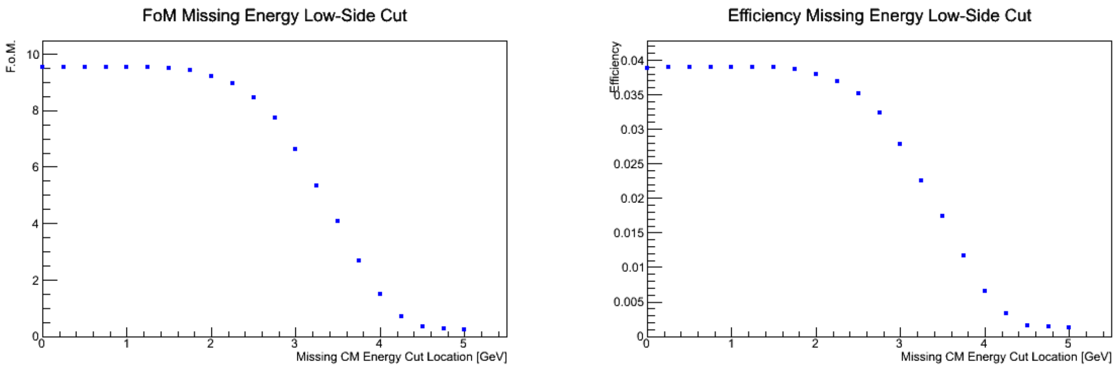

Figure 3.15: Figure of merit and efficiency for missing energy cut low side, 3.6 GeV/c^2 A^0 mass, “e & μ” cuts

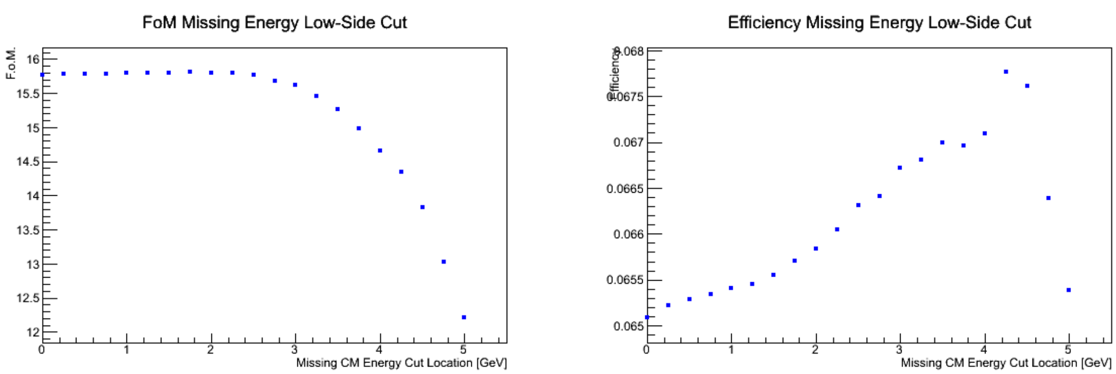

Figure 3.16: Figure of merit and effciency for missing energy cut low side, 9.3 GeV/c^2 A^0 mass, “e & μ” cuts

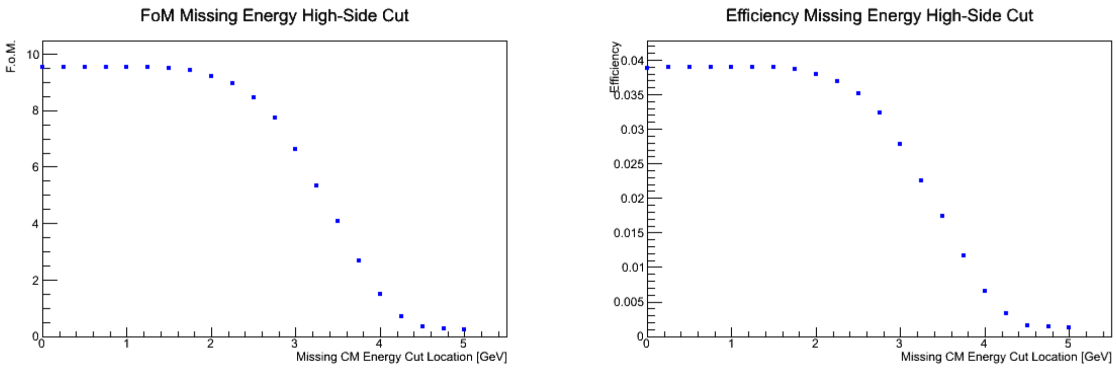

Figure 3.17: Figure of merit and efficiency for missing energy cut high side, 3.6 GeV/c^2 A^0 mass, "e & μ" cuts

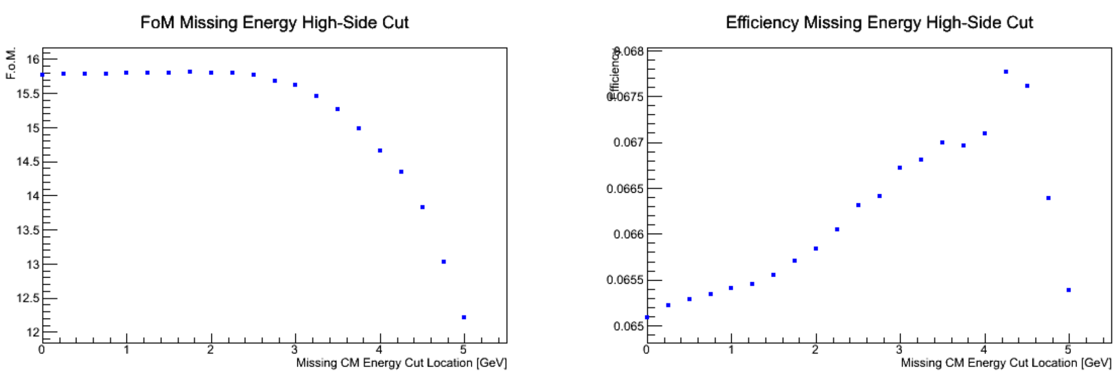

Figure 3.18: Figure of merit and effciency for missing energy cut high side, 9.3 GeV/c^2 A^0 mass, "e & μ" cuts

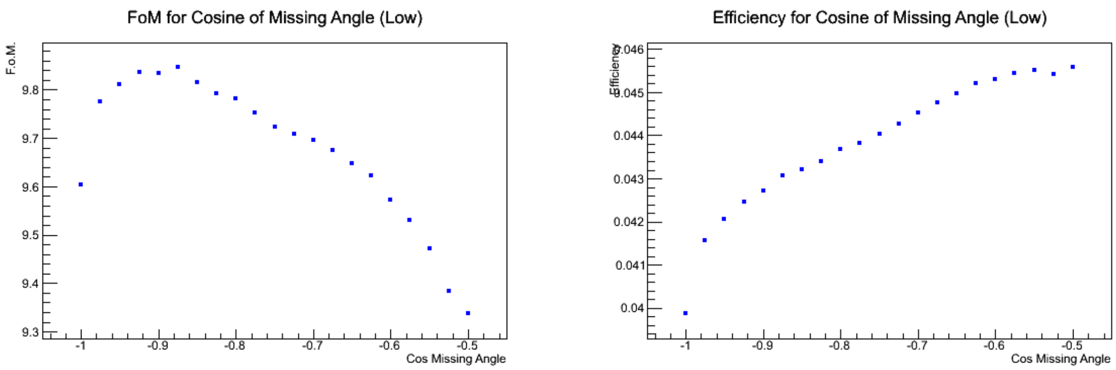

Figure 3.19: Figure of merit for missing angle cut low side, 3.6 GeV/c^2 A^0 mass, "e & μ" cuts

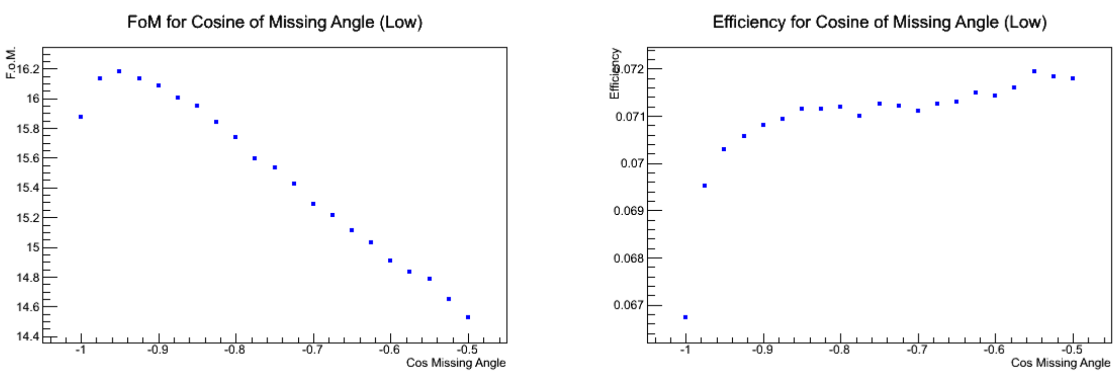

Figure 3.20: Figure of merit for missing angle cut low side, 9.3 GeV/c^2 A^0 mass, "e & μ" cuts

A balance is found between the maximization of the M_{A^0} = 3.6 GeV/c^2 and M_{A^0} = 9.3 GeV/c^2 cases. In both cases, cuts on event classification, trigger, charge balance, number of tracks, and lepton flavor are applied. Results for the FoM are shown in Figures 3.19, 3.20, 3.21, and 3.22.

$-0.9 < \mathrm{Cos}(\theta_{Missing}) < 0.96$

Lepton ID Cut Tuning

Cuts are placed on both the electron and muon ID when selecting a tau sample. The cuts are optimized using $\Upsilon(1S) \to \gamma A^0 \to \gamma\tau\tau$ decays where M_{A^0} = 3.6 GeV/c^2 and the

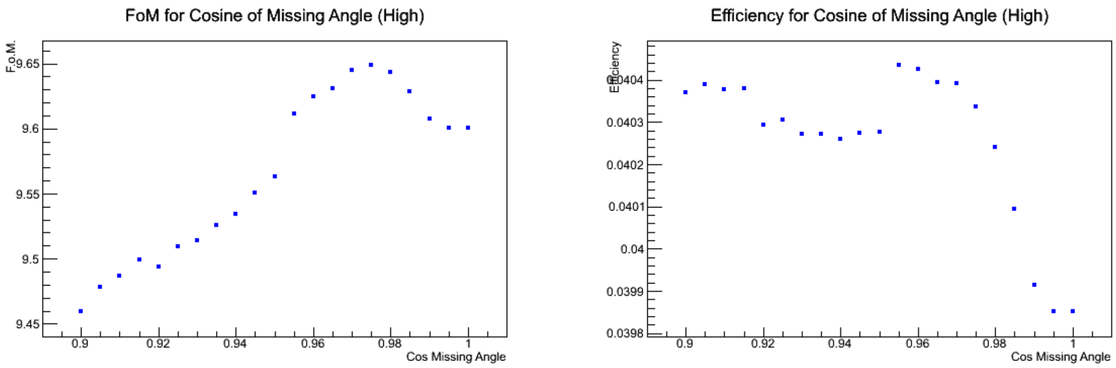

Figure 3.21: Figure of merit for missing angle cut high side, 3.6 GeV/c^2 A^0 mass, "e & μ" cuts

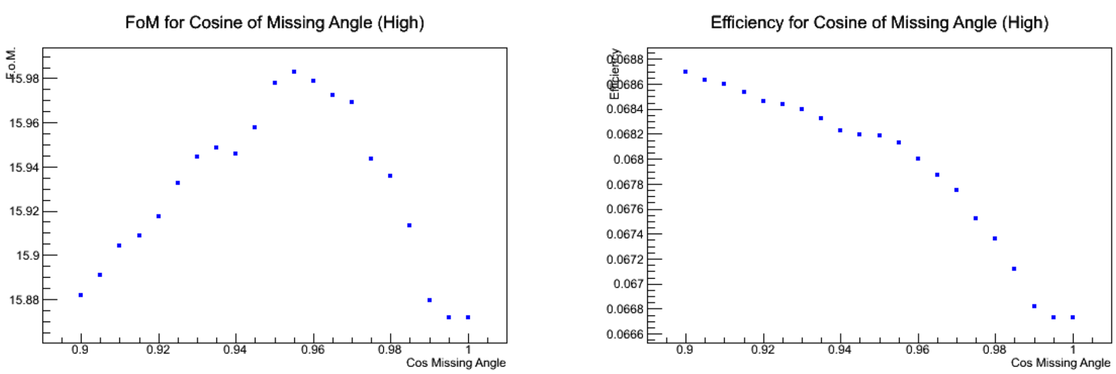

Figure 3.22: Figure of merit for missing angle cut high side, 9.3 GeV/c^2 A^0 mass, "e & μ" cuts

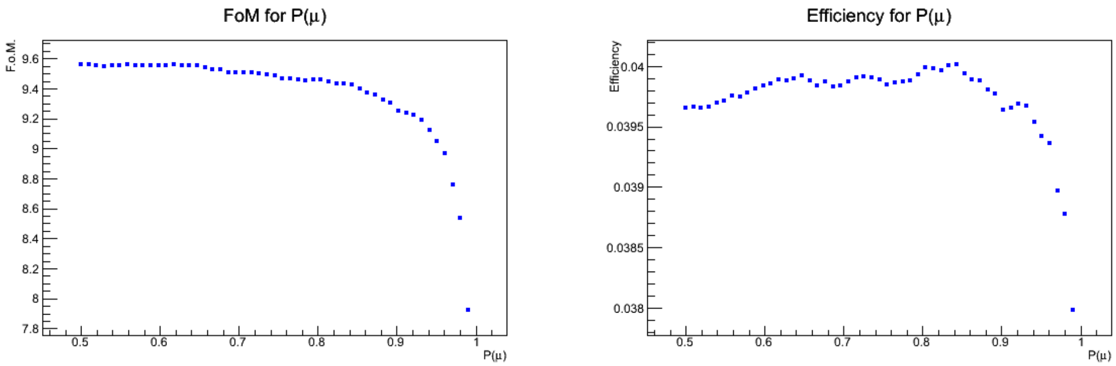

Figure 3.23: Figure of merit and efficiency for muon probability P(μ), 3.6 GeV/c^2 A^0 mass, "e & μ" cuts

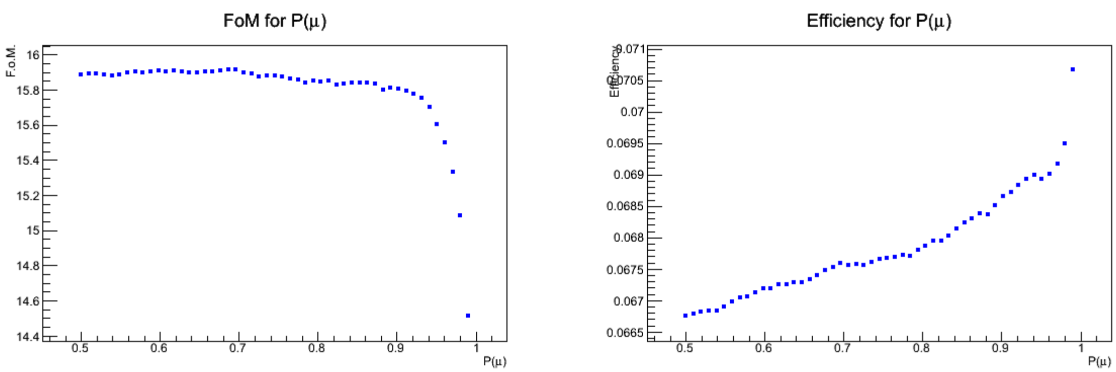

Figure 3.24: Figure of merit and efficiency for muon probability P(μ), 9.3 GeV/c^2 A^0 mass, "e & μ" cuts

taus decay to an electron and a muon. The case where M_{A^0} =9.3 GeV/c^2 is checked as well. In both cases, cuts on event classification, trigger, charge balance, number of tracks, and lepton flavor are applied. The results of these cuts are seen in plots of FoM and efficiency in Figs 3.23, 3.24, 3.25, and 3.26. The tuned probability cut for the electron and muon, P(e) and P(μ) respectively, are:

$P(\mu) > 0.8$

$P(e) > 0.05$

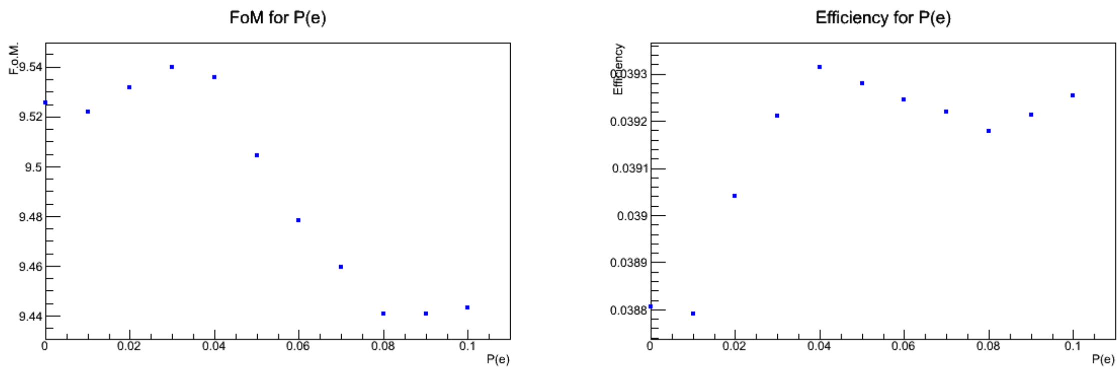

Figure 3.25: Figure of merit for electron probability P(e), 3.6 GeV/c^2 A^0 mass, “e & μ” cuts

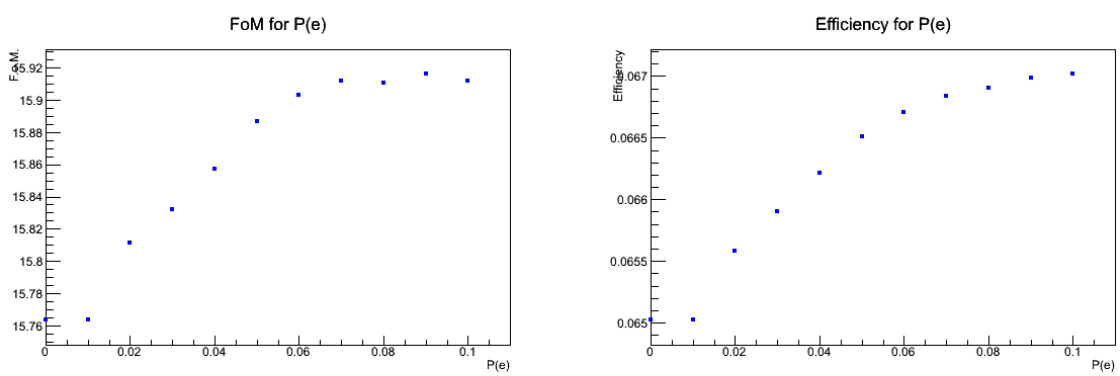

Figure 3.26: Figure of merit for electron probability P(e), 9.3 GeV/c^2 A^0 mass, “e & μ” cuts

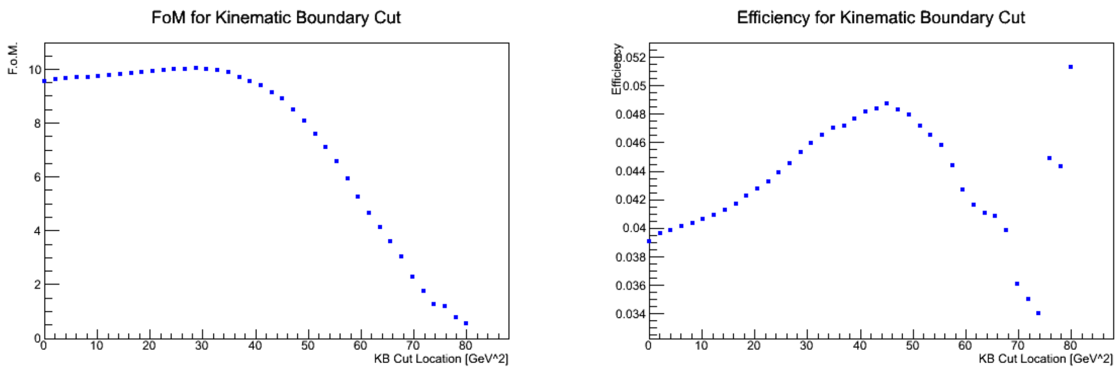

Figure 3.27: Figure of merit and efficiency for kinematic boundary cut, 3.6 GeV/c^2 A^0 mass, "e & μ" cuts

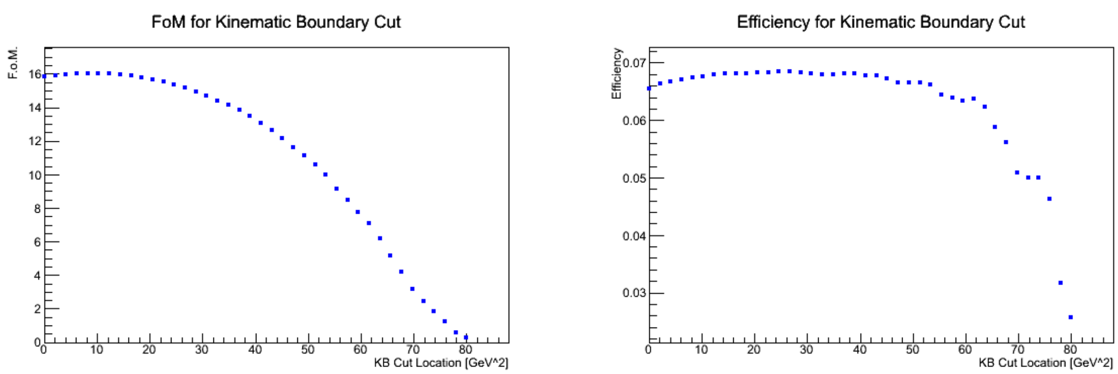

Figure 3.28: Figure of merit and efficiency for kinematic boundary cut, 9.3 GeV/c^2 A^0 mass, "e & μ" cuts

Kinematic Boundary Cut Tuning

A loose cut is placed on the kinematic boundary condition when selecting a tau sample. This cut is optimized with $\Upsilon(1S) \to \gamma A^0 \gamma \to \tau\tau$ where $M_{A^0} = 3.6$ GeV/c^2. The case where $M_{A^0} = 9.3$ GeV/c^2 is also checked. In both cases, cuts on event classification, trigger, charge balance, number of tracks, and lepton flavor are applied. The results for FoM and efficiency are shown in Figures 3.27, 3.28.

The cut has been modified to KB Parameter > 20 GeV^2.

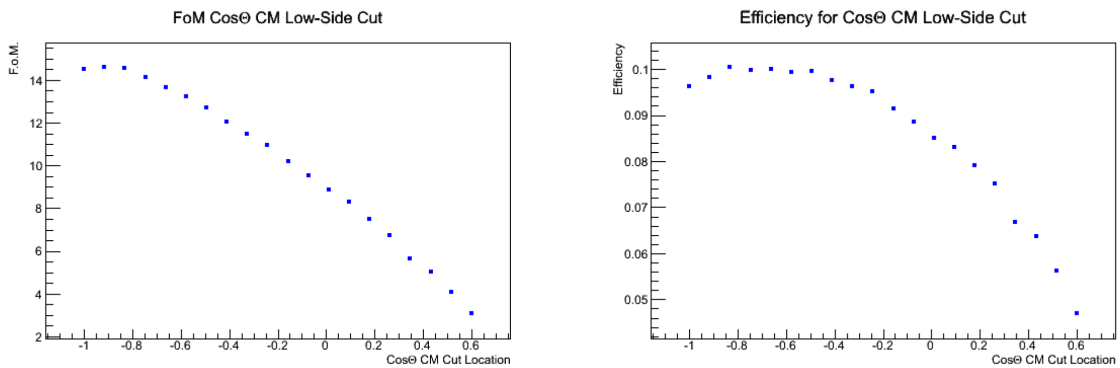

Figure 3.29: Figure of merit and efficiency for the cos(θ) cut in CM frame low-side cut, 3.6 GeV/c^2 A^0 mass, "e & μ" cuts

Bremsstrahlung Cut Tuning

The justification for the bremsstrahlung cut is presented in Fig. 3.10.

Barrel Cut Tuning

While ISR has a 1+cos$^2(\theta)$ distribution that leads to most of it being deposited in the endcaps, the complete elimination of data from the endcaps is found to reduce signal as well. A narrower cut is made on the θ distribution in the CM frame. This cut is optimized with $\Upsilon(1S) \to \gamma A^0 \to \gamma\tau\tau$ where $M_{A^0} = 3.6$ GeV/c^2. The case where $M_{A^0} = 9.3$ GeV/c^2 is checked as well. In both cases, cuts on event classification, trigger, charge balance, number of tracks, and lepton flavor are applied. The low side FoM and efficiency results are displayed in Figs 3.29 and 3.30. The results for FoM and efficiency for the high side of the cut are shown in Figs 3.31 and 3.32.

-0.9<Cos(θ_{CM})<0.9

π^0 Cut Tuning

The upper and lower boundaries of the π^0 cut are optimized using 10,000 $\Upsilon(1S) \to \gamma A^0 \to \gamma\tau\tau \to \gamma e\mu + invisible$ events. A^0 masses of 3.6 GeV/c^2 and 9.3 GeV/c^2 were used. To optimize the lower boundary, the upper boundary is fixed at $M_{\gamma\gamma} < 160$ MeV/c^2 while the lower boundary is varied between 50 MeV/c^2 and 130 MeV/c^2. To optimize the upper boundary, the lower boundary is fixed at $M_{\gamma\gamma} > 80$MeV/c^2 while the upper boundary is

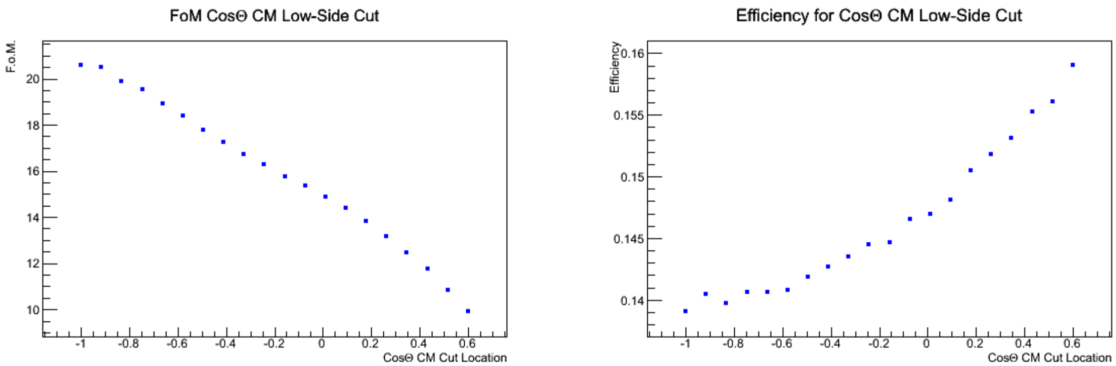

Figure 3.30: Figure of merit and efficiency for the cos(θ) cut in CM frame low-side cut, 9.3 GeV/c^2 A^0 mass, "e & μ" cuts

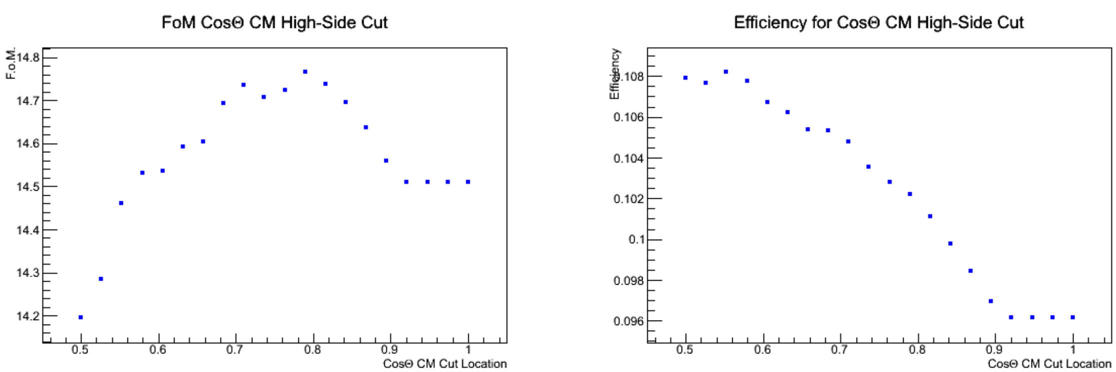

Figure 3.31: Figure of merit and efficiency for the cos(θ) cut in CM frame high-side cut, 3.6 GeV/c^2 A^0 mass, "e & μ" cuts

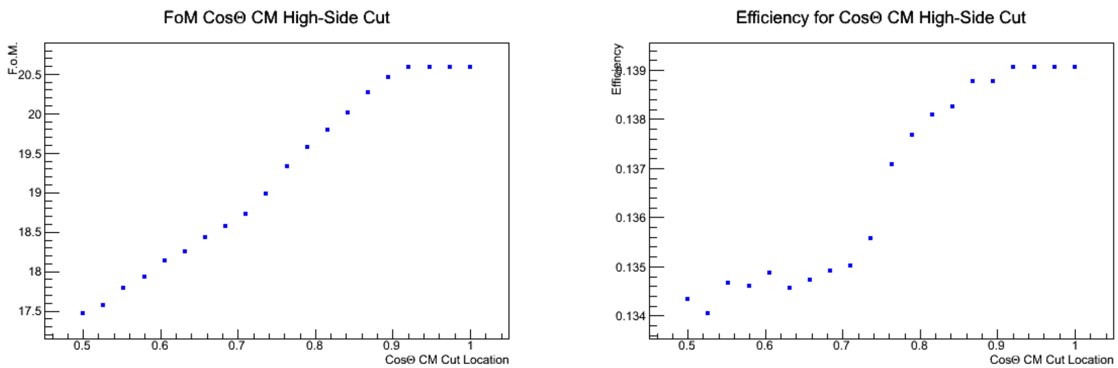

Figure 3.32: Figure of merit and efficiency for the $\cos(\theta)$ cut in CM frame high-side cut, 9.3 GeV/c^2 A^0 mass, "e & μ" cuts

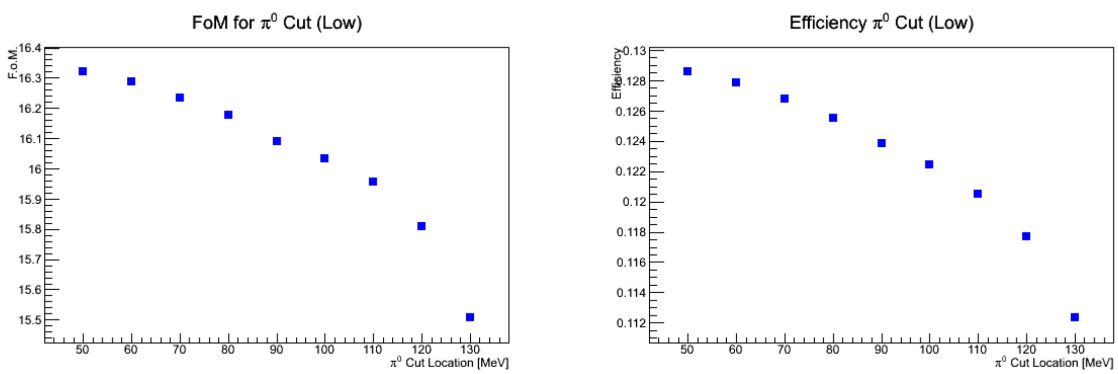

Figure 3.33: Figure of merit and efficiency for π^0 low-side cut, 3.6 GeV/c^2 A^0 mass, "e & μ" cuts

varied between 140 MeV/c^2 and 220 MeV/c^2. Results for the FoM and efficiency are shown in Figs. 3.33, 3.34, 3.35, and 3.36. These figures are then replotted with boundaries closer to the point at which we make our cuts in Figs. 3.37, 3.38, 3.39, and 3.40.

The high boundary is kept at 160 MeV/c^2, the lower boundary is reduced to 110 MeV/c^2. 110 MeV/c^2 $< M_{\gamma\gamma} <$ 160 MeV/c^2

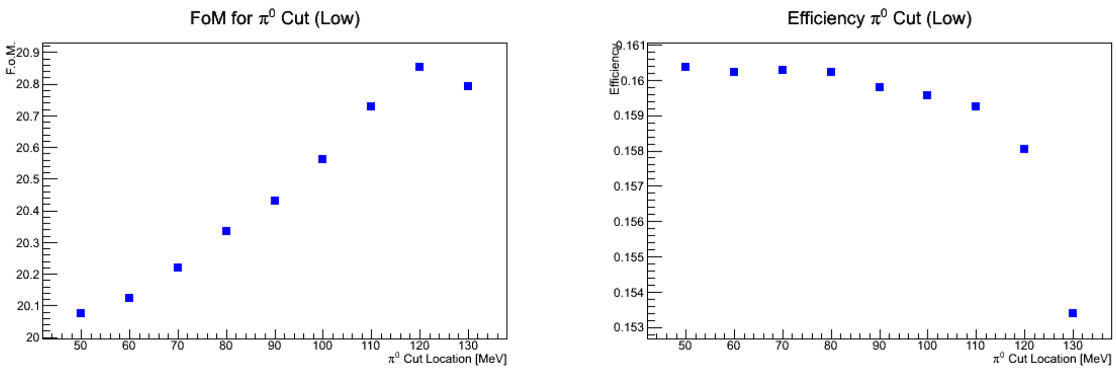

Figure 3.34: Figure of merit and efficiency for π^0 low-side cut, 9.3 GeV/c^2 A^0 mass, "e & μ" cuts

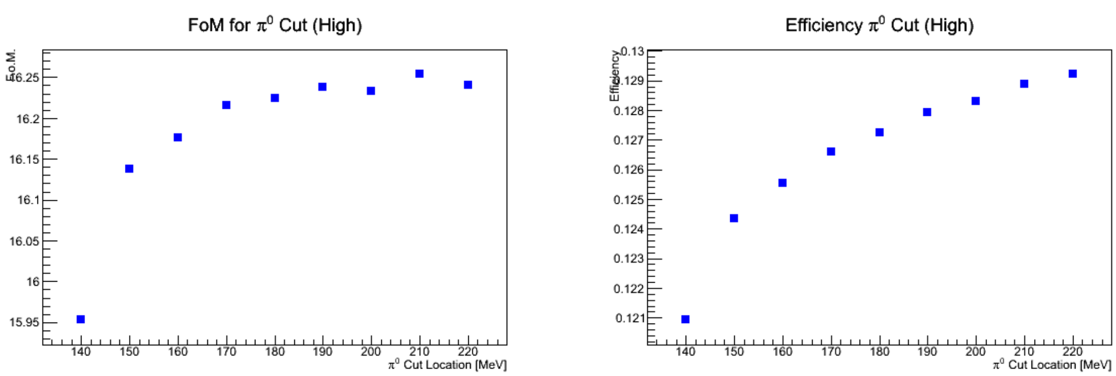

Figure 3.35: Figure of merit and efficiency for π^0 high-side cut, 3.6 GeV/c^2 A^0 mass, "e & μ" cuts

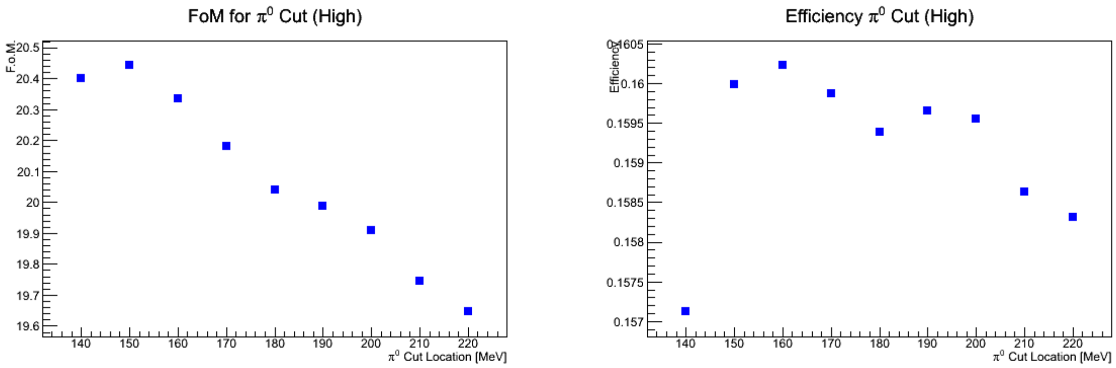

Figure 3.36: Figure of merit and efficiency for π^0 high-side cut, 9.3 GeV/c^2 A^0 mass, “e & μ” cuts

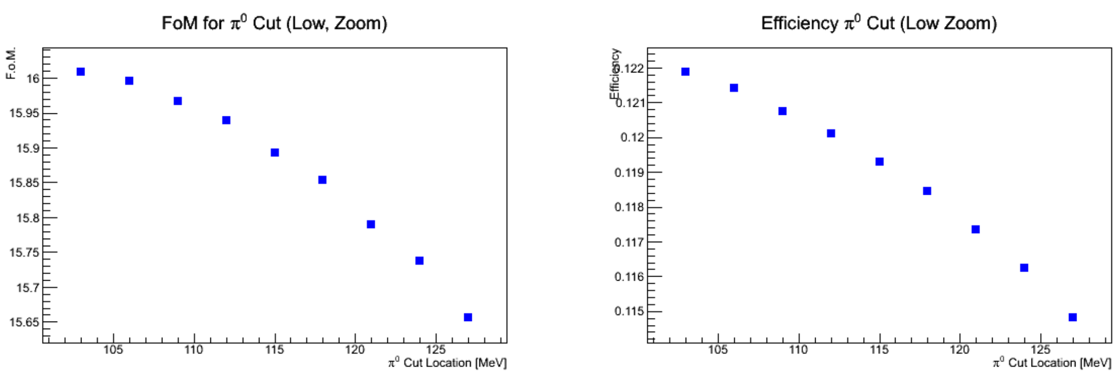

Figure 3.37: Figure of merit and efficiency for π^0 low-side cut, zoomed, 3.6 GeV/c^2 A^0 mass, “e & μ” cuts

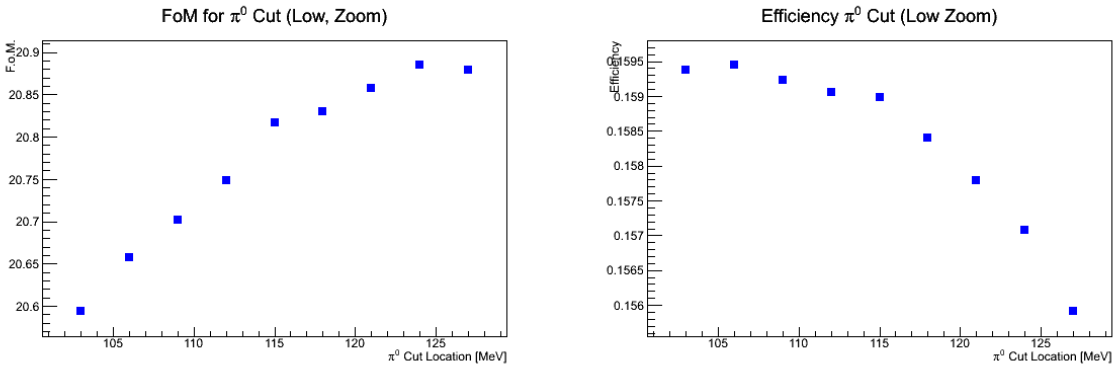

Figure 3.38: Figure of merit and efficiency for π^0 low-side cut, zoomed, 9.3 GeV/c^2 A^0 mass, "e & μ" cuts

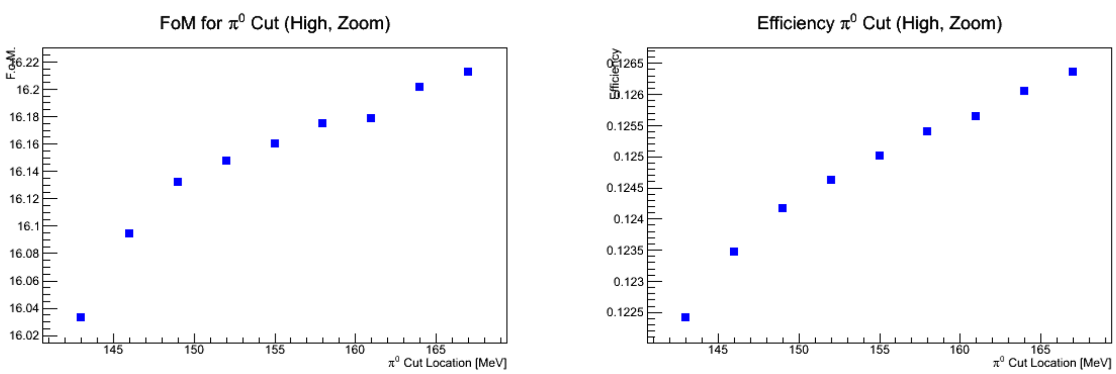

Figure 3.39: Figure of merit and efficiency for π^0 high-side cut, zoomed, 3.6 GeV/c^2 A^0 mass, "e & μ" cuts

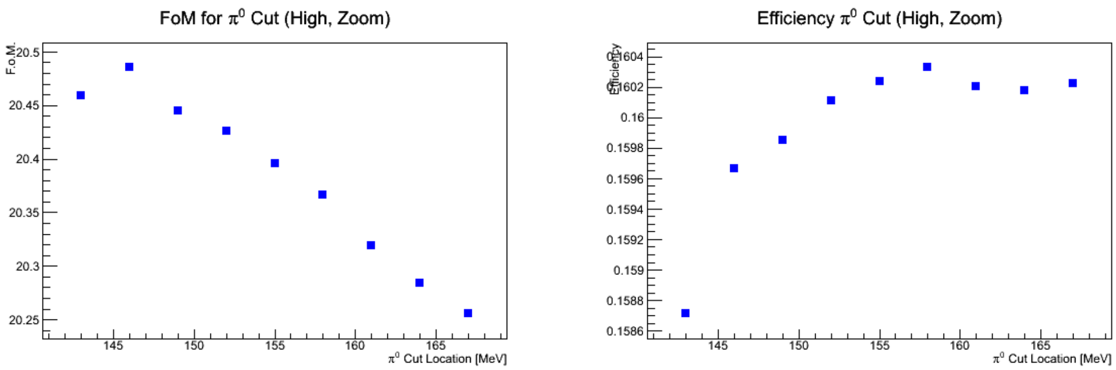

Figure 3.40: Figure of merit and efficiency for π^0 high-side cut, zoomed, 9.3 GeV/c^2 A^0 mass, "e & μ" cuts

3.7.2 Summary of Optimized "e & μ" Cuts

The full set of optimized selection cuts is presented here for the convenience of anyone who wishes to make use of them without having to search through the text.

1. Tau Skim B: evt_cls.flag(4)>0
2. Trigger: RecTRG_summary3.final(0) + RecTRG_summary3.final(1) != 0
3. Two Charged Tracks w/ Balance
4. N_μ=N_e=1
5. Lepton Probability cut: $P(e) > 0.05$ and $P(\mu) > 0.8$
6. KB Cut: KB Parameter > 20 GeV^2
7. Missing Energy Cut: 1.5 GeV $\leq E_{missing} \leq$ 7.5 GeV in CM frame
8. Missing Angle Cut: -0.9<Cos($\theta_{Missing}$)<0.96 in CM frame
9. Gamma Quantity: $N_\gamma > 0$
10. π^0 Cut: 110 MeV/c^2 $< M_{\gamma\gamma} <$ 160 MeV/c^2
11. Bremsstrahlung: α_{Brem} >0.2 radians in CM frame
12. CM θ Distribution Cut: -0.9<Cos(θ_{CM})<0.9

Table 3.3: Summary of Effects of All Tuned "e & μ" Cuts on Off-Resonance Data and MC

Cut	Retained (MC)	Efficiency (MC)	Retained (Data)	Efficiency (Data)
No Cuts/Skim	2,085,000	N/A	6,467,416	N/A
Tau Skim B	1,459,195	0.700	-	-
Trigger	1,314,885	0.630	-	-
Two Charged Tracks	733,779	0.352	4,435,159	0.686
$N_\mu = N_e = 1$	58,806	0.028	62,633	0.010
Lepton Probability Cut	51,158	0.025	56,664	0.009
KB Cut	48,109	0.023	51,220	0.008
Missing Energy Cut	47,253	0.023	49,796	0.008
Missing Angle Cut	45,281	0.022	45,833	0.007
Gamma Quantity	17,296	0.008	17,604	0.003
π^0 Cut	14,819	0.007	15,398	0.002
Bremsstrahlung	9,762	0.005	10,290	0.002
CM θ Distribution Cut	9,152	0.004	9,589	0.001

3.7.3 Cut Signal Efficiency

Sets of 10^4 Pure Higgs MC events are used to determine the signal detection efficiency after the selection cuts listed in Table 3.3 are applied. The percentage of events that pass the cuts at each trial mass is displayed in Fig. 3.41. The fit equation is

$$\epsilon_{cut} = -0.3658 + 0.39x - 0.1012x^2 + 0.01254x^3 - 0.0005807x^4 \text{ where x} = \mathrm{M}_{A^0}[\mathrm{GeV}/c^2] \tag{3.7.4}$$

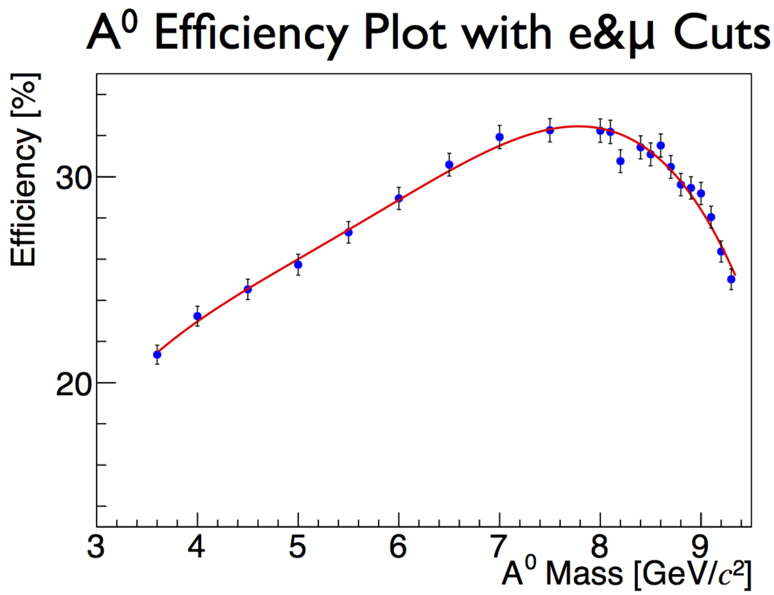

Figure 3.41: Efficiency of Pure Higgs MC that pass all tuned "e & μ" cuts.

3.8 1-Prong Off-Resonance Tau-Pair MC Study

The 1-prong mode has a relaxed particle identification criteria on the two charged tracks. One track must be positively identified as either an electron or a muon, whereas the other track need only have the opposite charge opposite to the lepton track's. To remove events that have no signal, at least one photon must be detected. Events must satisfy the data skim criteria and trigger condition. Further criteria are then placed on the missing energy and angular distribution of the missing momentum.

3.8.1 Initial Tau Selection Criteria

- Passes Tau Skim B (see Sec. 3.4.1)
- Passes Trigger Condition (see Sec. 3.4.2)
- Exactly two charged tracks with charge balance and at least one photon
- Either $\mu \geq 1$ or $e = 1$ in the final state, with eID ≥ 0.9 or μID ≥ 0.9.

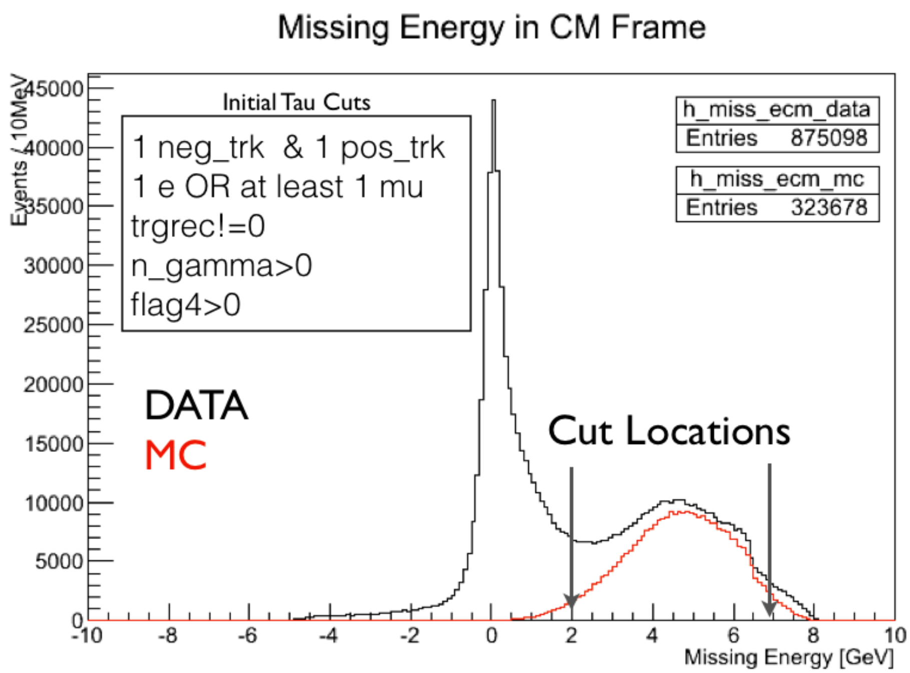

Figure 3.42: Missing energy in the CM frame with 1-prong cuts. Red is MC, black is data. MC and experimental data are both off-resonance.

3.8.2 Further Tau Sample Selection Criteria

Further refinements were made to the τ-pair sample selection based the missing energy ($E_{missing}$) and the angular distribution of the missing momentum in the detector ($\theta_{missing}$, $\phi_{missing}$). The $E_{missing}$ cut was examined first, then the angular distribution of $\theta_{missing}$ was plotted after the $E_{missing}$ cut was applied. For a track without a definite particle ID, the mass is assumed to be a pion mass. The CM missing energy distribution is shown in Fig. 3.42, the CM cos(θ) projection of the distribution of the missing momentum is shown in Fig. 3.43, and the ϕ vs cos(θ) distribution of the missing momentum is shown in Fig. 3.44.

- Missing Energy Cut: 2.0 GeV $< E_{missing} <$ 7.0 GeV
- Missing Angle Cut: -0.8$< Cos(\theta_{missing})$ <0.8

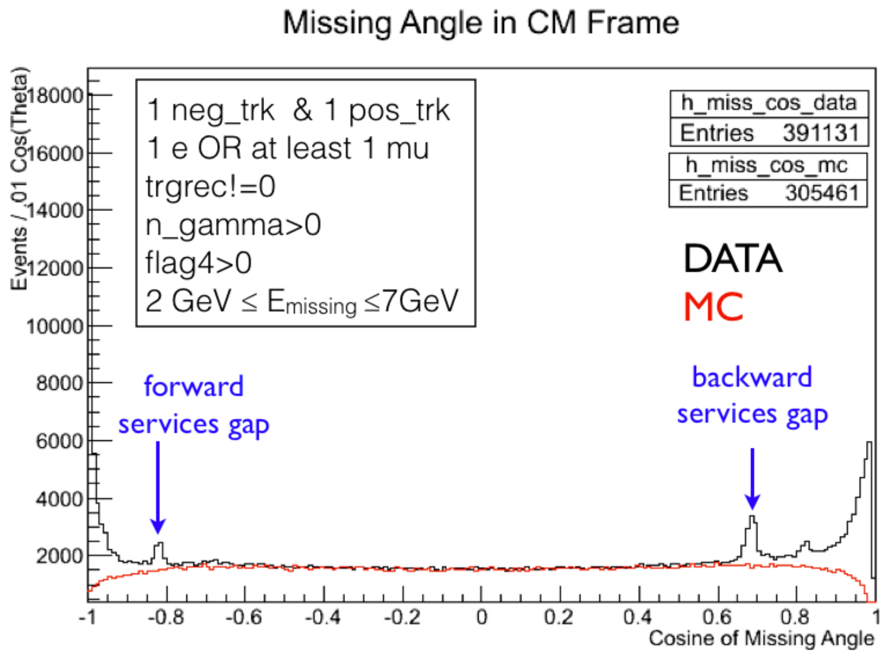

Figure 3.43: Angular distribution of missing energy in the CM frame, detector features noted on plot. Red is MC, black is experimental data. MC and experimental data are both off-resonance.

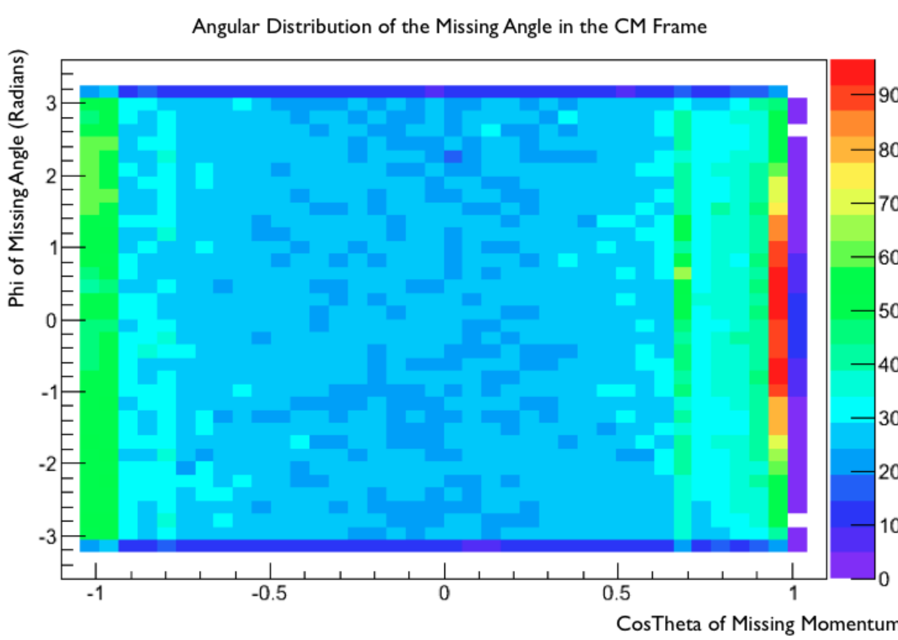

Figure 3.44: The θ and ϕ distribution of missing momentum in the CM frame with 1-prong cuts.

Table 3.4: Summary of Effects of 1-Prong Tau Selection Cuts in Data and MC

Cut	# Retained (MC)	Efficiency (MC)	# Retained (Data) (Data)	Efficiency (Data)
No Cuts/ Skim	2,085,000	N/A	6,467,416	N/A
Tau Skim B	1,459,195	0.70	-	
Trigger	1,313,885	0.63	-	
Two Charged Tracks and $> 0\ \gamma$	592,245	0.28	2,472,017	0.38
Either $\mu \geq 1$ or $e = 1$	323,678	0.16	875,439	0.14
P(e) > 0.9 & P(μ) > 0.9	283,824	0.14	820,505	0.13
Missing Energy Cut	279,448	0.13	403,155	0.06
Missing Angle Cut	255,572	0.12	292,507	0.05

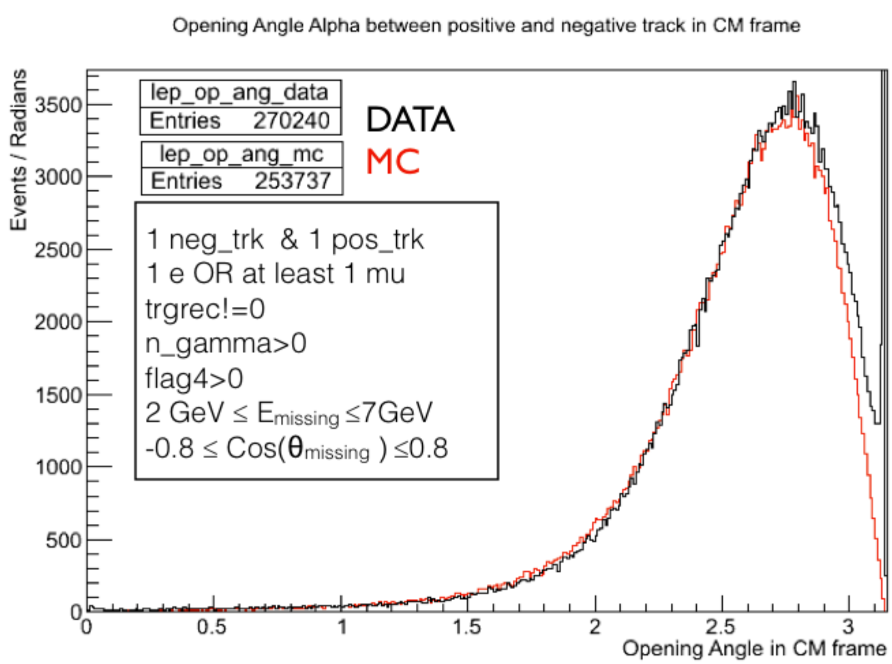

Figure 3.45: Opening angle between positive and negative tracks with all 1-prong cuts applied.

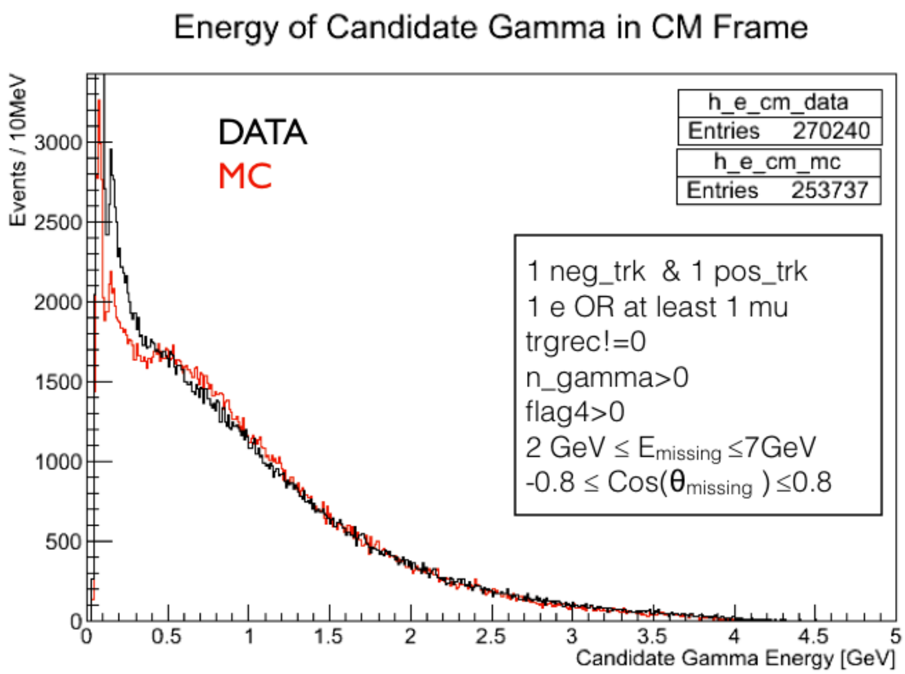

Figure 3.46: Photon spectrum in off-resonance data, all 1-prong cuts applied. Red is MC, black is experimental data.

3.8.3 Results

Characteristic quantities for τ-pair events were plotted in both MC and Tau Skim B data . In addition to the opening angle between the charged tracks of the two 1-prong decays; we also plot the distribution of photon energy in the center of mass frame. Based upon the agreement between data and MC seen in Figs. 3.45 and 3.46, we believe that the τ-pair sample is accurately modeled.

3.9 1-Prong Off-Resonance Photon Background MC Study

After isolating a continuum tau sample, we examine the photons in the sample. These photons will be the background to our $\Upsilon(1S) \to \gamma A^0$ signal. We again find that the these photons come from four sources: ISR, bremsstrahlung, beam background, and π^0 decays. This is displayed in Fig. 3.47.

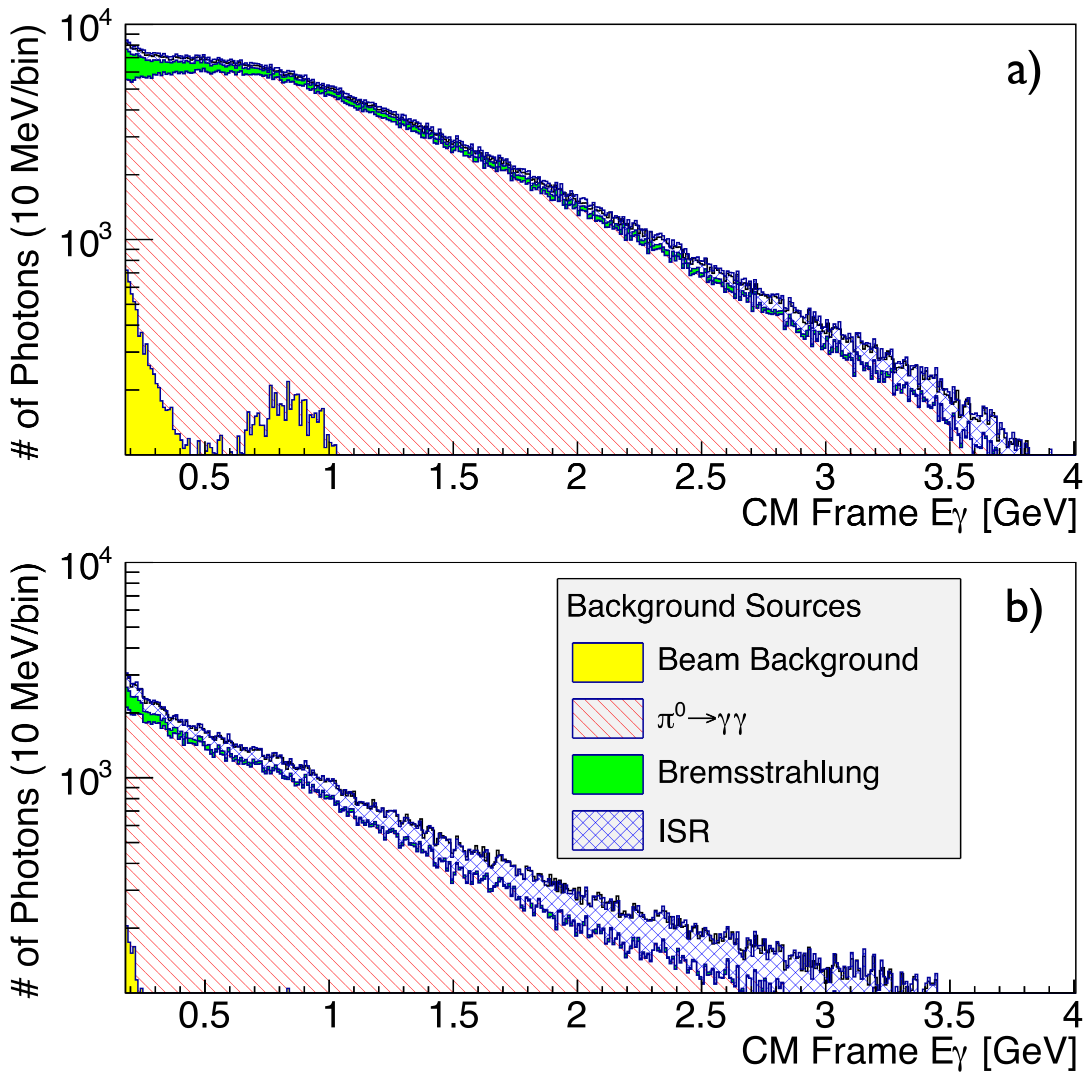

Figure 3.47: Plot of the contributions of γ sources to the photon background in off-resonance MC a) before and b) after photon background reduction cuts are applied. π^0 (red) dominates over the spectrum above 100 MeV

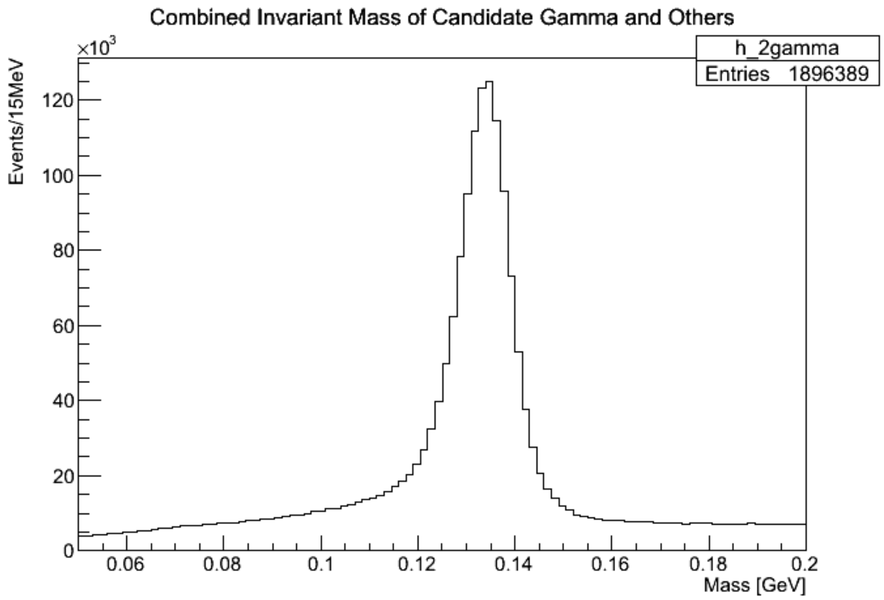

Figure 3.48: Plot of the 2 photon invariant mass in on-resonance 1-prong MC. For each event, $\gamma_{fake\_candidate}$ was paired with all $\gamma_{fake\_partner}$ and every $M_{\gamma\gamma}$ is entered on the histogram.

3.9.1 π^0-Decay Background Reduction

Photons from $\pi^0 \to \gamma\gamma$ decays are the dominant source of photon background for CM energy above 100 MeV. In this background, a π^0 decays into two photons: $\gamma_{fake\_candidate}$ and $\gamma_{fake\_partner}$. The $\gamma_{fake\_candidate}$ is the highest energy photon found in MDST_Gamma and is taken as a candidate photon. Originally, this analysis followed CLEO's prescription [38] of pairing the candidate photon with each other photon in the event and removing the event if

$$|M_{\pi^0} - M_{\gamma\gamma}| < 3\sigma_{\pi^0} \tag{3.9.1}$$

for any $M_{\gamma\gamma}$. Here, σ_{π^0} is the width of the π^0 peak as fit with a gaussian. Our MC showed that a significant fraction of events in the low energy tail lay outside of this cutoff (see Fig. 3.48) due to the asymmetric nature of the peak, so the cut was extended to account for this. Further, $\gamma_{fake\_partner}$ is not subjected to the same energy cuts in the endcap as the candidate photon: it can have an energy as low as 50 MeV in that region.

Even with this change, a significant faction of π^0 are not recovered. After checking against MDST_GenHepEvt, we see that $\gamma_{fake\_partner}$ is not reconstructed as a photon and has no entry in MDST_Gamma in these cases.

3.9.2 Bremsstrahlung

The opening angle between the candidate photon momentum vector and the momentum vector of the positive track was measured in the CM frame. The same measurement was repeated for the candidate photon momentum vector and the momentum vector of the negative track. In both cases there was a spike in the photon background where the opening angle lay within 0.2 radians of the charged track. This is similar to what has already been shown in Fig. 3.10 of Section 3.5.

3.9.3 Initial State Radiation

The initial state radiation (ISR) of $ee \rightarrow \gamma ee$ has an angular distribution of the photon that goes as $1 + cos^2(\theta)$ in the CM frame as seen in Fig. 3.49, leading to a greater proportion of the ISR being found in the endcaps as opposed to the barrel region.

3.9.4 Beam Background

The beam background contribution can be identified by checking the particle identification (idhep) entry of the MC truth table, GenHepEvent. Beam background events injected by using addbg in MC generation have an idhep value of "911". Beam background has a broad (read: much larger than expected the signal width) peaking contribution between 500 MeV and 1 GeV and narrower peaking contribution below 200 MeV. The broad contribution does not affect a fit for signal, but must be considered when characterizing the background. Narrow peaking contributions must be eliminated or avoided entirely.

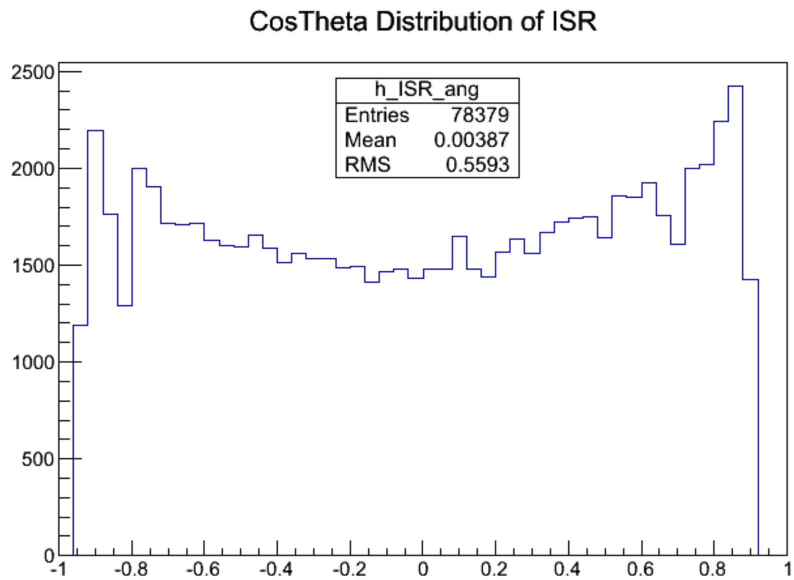

Figure 3.49: Plot of the angular distribution of ISR in the CM frame for on-resonance data. ISR photons identified by having a mother with GenHepEvent ID of either 1 or 2.

Table 3.5: Summary of Effects of 1-Prong Photon Selection Cuts in Data and MC

Cut	# Retained (MC)	Efficiency (MC)	# Retained (Data)	Efficiency (Data)
Previous Selection Cuts	255,572	0.12	292,507	0.05
π^0 Cut	107,227	0.05	136,394	0.02
Bremsstrahlung	90,682	0.04	106,102	0.02
Barrel Cut	71,163	0.03	81,141	0.01

3.10 1-Prong On-Resonance Photon Background MC Study

Studies of on-resonance 1-Prong MC and "e & μ" on-resonance MC and data revealed a point at $E_\gamma = 2.36$ GeV that peaks in all three samples. In these three samples, this peak had a significance below 3σ. In 1-prong on-resonance data, this point had a significance in excess of 4σ. This prompted a more thorough examination of the 1-Prong MC sample, which led to the discovery of a peaking distribution in beam background. This background has been determined to be isolated to a small area of the detector and localized to $0.3181 < Cos(\theta)_{CM} < 0.3184$ and $-2.33250 < \phi < -2.33245$. This is most likely due to an irregularity in the Belle detector itself. Possible sources of this irregularity include anomaly in a single CsI(Tl) crystal (aka, a “hot crystal”) or degradation of the readout electronics for that crystal. The $\Upsilon(1S)$ data has not been used in many analyses at Belle, so it is not unlikely that such issues would not have been detected until now.

This discovery prompted an examination of the rest of the photon energy spectrum. The background fitting technique, to be discussed in Subsection 3.12.1, divides the photon spectrum into four regions. We examine the angular distribution of photons in those four regions to see if there are other small, localized regions of the detector that could contribute a previously unseen peaking background. These plots are shown in Fig. 3.50.

Two peaking backgrounds are seen in Fig. 3.50: the previously discovered peak in the region “d” and a peaking background found in region “a”. This peaking background in region “a” is shown in Fig. 3.51; it was thought to be so wide that it would not register as a false-positive in the signal fitter. Upon further examination, the wide peak in Fig. 3.50 is found to be a combination of at least three narrow, spatially separated peaks. Study in MC showed that these peaks can result in a fit with positive signal yield and a significance greater than 3σ. Such peaks in region “a” do not appear above 180 MeV, as can be seen in Fig. 3.52.

We remove photons located in the area $0.3181 < \cos(\theta)_{CM} < 0.3184$ and $-2.3325 < \phi < -2.33245$ from our sample and raise the lower bound of the photon energy spectrum from 150 MeV to 180 MeV.

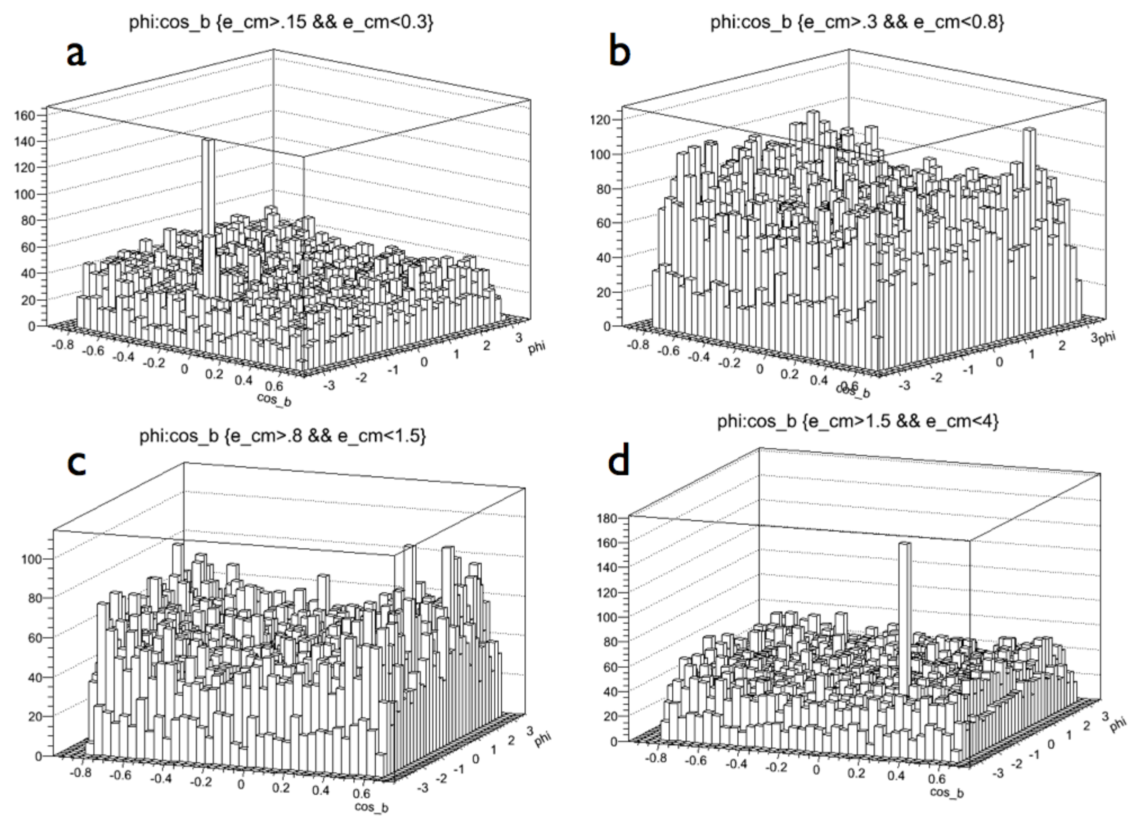

Figure 3.50: Angular distributions of photons in tuned on-resonance 1-prong MC, $\cos(\theta)_{CM}$ and ϕ. E_γ is restricted to: a) 0.150 GeV $< E_\gamma <$ 0.500 GeV, b) 0.5 GeV $< E_\gamma <$ 0.8 GeV, c) 0.8 GeV $< E_\gamma <$ 1.5 GeV, d) 1.5 GeV $< E_\gamma <$ 4.0 GeV.

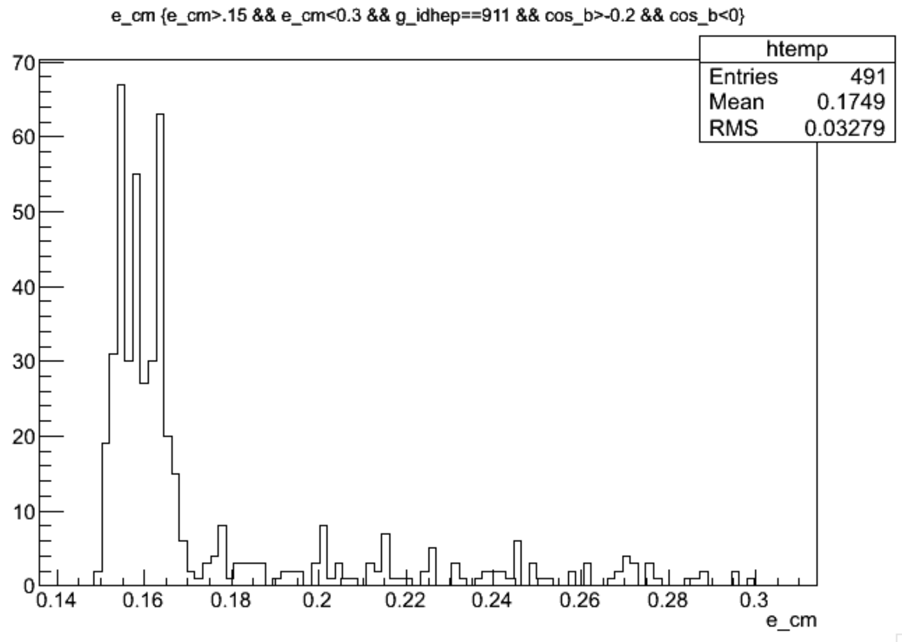

Figure 3.51: Distribution of peaking beam background in tuned on-resonance 1-prong MC. E_γ is restricted to be between 0.150 GeV and 0.300 GeV in the CM frame. The beam background contribution is localized in angular distribution.

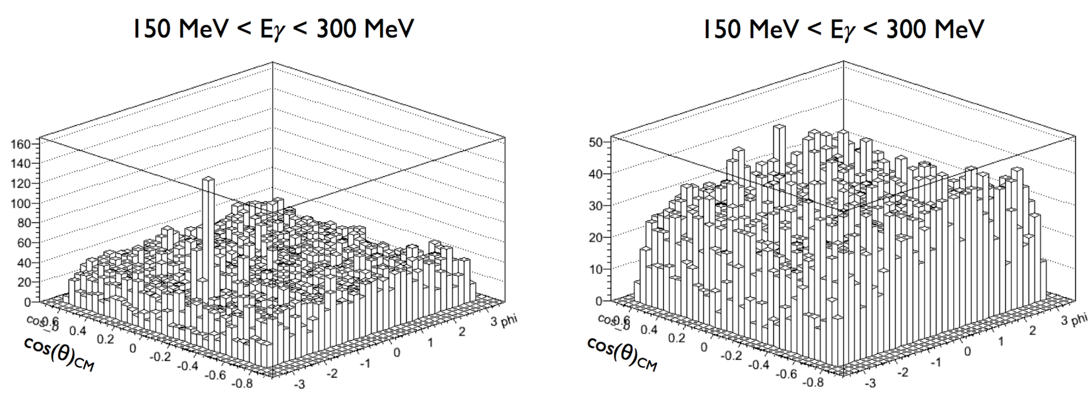

Figure 3.52: Angular distribution of beam background in 1-prong MC for Eγ energies from 150 MeV to 300 MeV (left) and from 180 MeV to 300 MeV (right).

3.11 1-Prong Photon Signal MC Study

3.11.1 Tuning

For a description of the approach toward tuning, please see Subsection 3.7.1.

Missing Energy Cut Tuning

The distribution of missing energy is heavily dependent upon the energy of the photon associated with the A^0. Missing energy cutoffs were tuned against on-resonance MC using two sets of 10,000 $\Upsilon(1S) \to \gamma A^0 \to \gamma\tau\tau$ decays with the τ-pair decaying to a lepton and one of the 1-prong decays listed in Subsection 3.3.7. The low side of the missing energy cut was tuned with $M_{A^0} = 3.6$ GeV/c^2, the high end was tuned with $M_{A^0} = 9.3$ GeV/c^2. In both cases, cuts on event classification, trigger, charge balance, number of tracks, and lepton flavor were applied. Results for the FoM and efficiency are shown in Figures 3.53, 3.54, 3.55, 3.56.

The tuning motivated a slight modification of the missing energy cut. We set the missing energy cut to 1.5 GeV $\leq E_{missing} \leq$ 7.5 GeV.

Missing Angle Cut Tuning

The angular distribution of the missing momentum vector is tuned after the missing energy cut is applied. Missing angle cutoffs are tuned against on-resonance MC using two sets of 10,000 $\Upsilon(1S) \to \gamma A^0 \to \gamma\tau\tau$ decays with the τ-pair decaying to a lepton and one of the 1-prong decays. A balance is found between the maximization of the $M_{A^0} = 3.6$ GeV/c^2 and $M_{A^0} = 9.3$ GeV/c^2 cases. In both cases, cuts on event classification, trigger, charge balance, number of tracks, and lepton flavor are applied. Results for the FoM are shown in Figures 3.57, 3.58, 3.59, and 3.60.

We set the missing angle cut at -0.95<Cos($\theta_{Missing}$)<0.90.

Lepton ID Cut Tuning

Cuts are placed on the lepton track ID when selecting a tau sample. These cuts are optimized with decays of $\Upsilon(1S) \to \gamma A^0 \to \gamma\tau\tau$ where $M_{A^0} = 3.6$ GeV/c^2 and the τ-pair decay to a lepton and a 1-prong decay. The case where $M_{A^0} = 9.3$ GeV/c^2 is checked as well. In both cases, cuts on event classification, trigger, charge balance, number of tracks, and

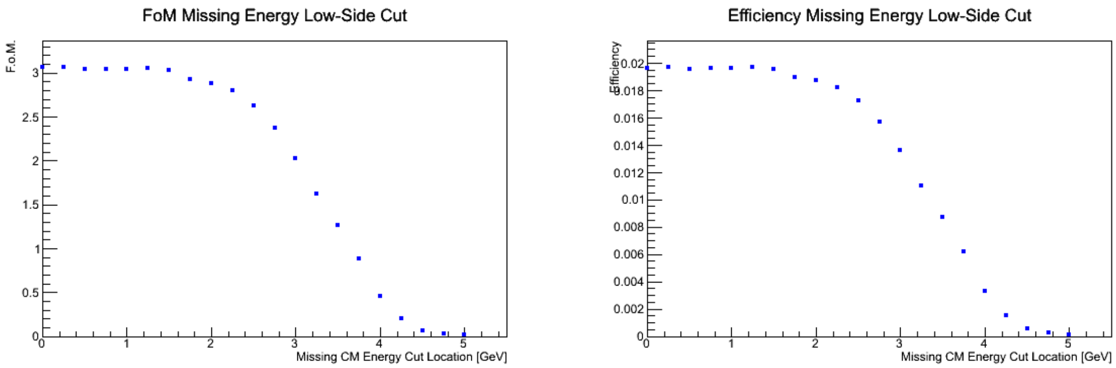

Figure 3.53: Figure of merit and efficiency for missing energy cut low side, 3.6 GeV/c^2 A^0 mass, 1-prong cuts

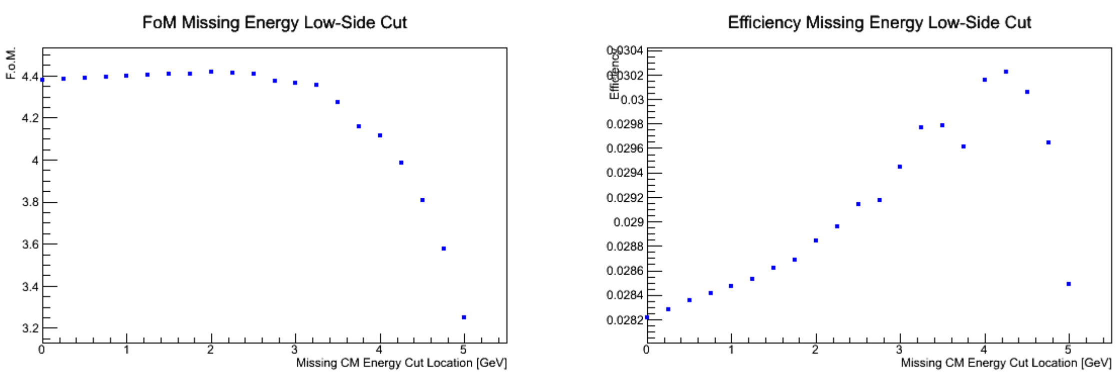

Figure 3.54: Figure of merit and efficiency for missing energy cut low side, 9.3 GeV/c^2 A^0 mass, 1-prong cuts

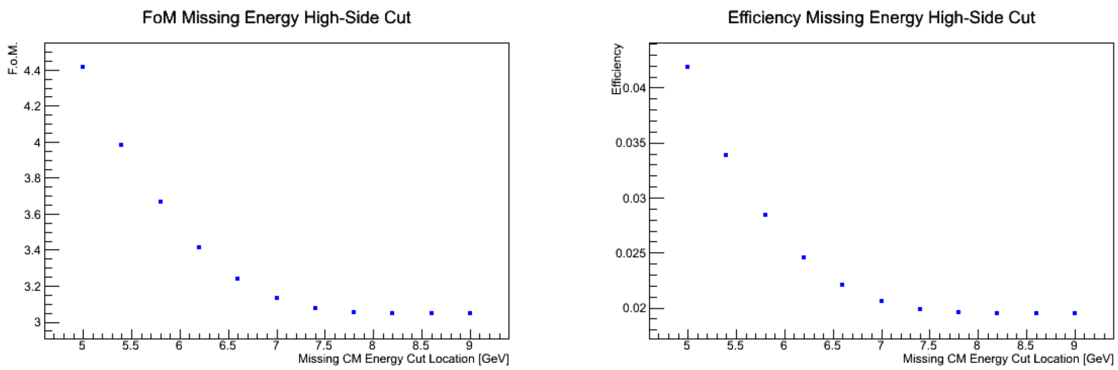

Figure 3.55: Figure of merit and efficiency for missing energy cut high side, 3.6 GeV/c^2 A^0 mass, 1-prong cuts

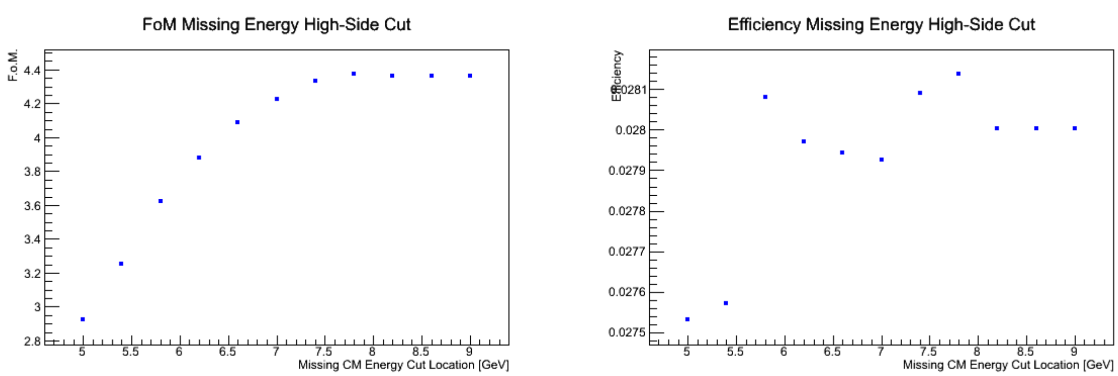

Figure 3.56: Figure of merit and effciency for missing energy cut high side, 9.3 GeV/c^2 A^0 mass, 1-prong cuts

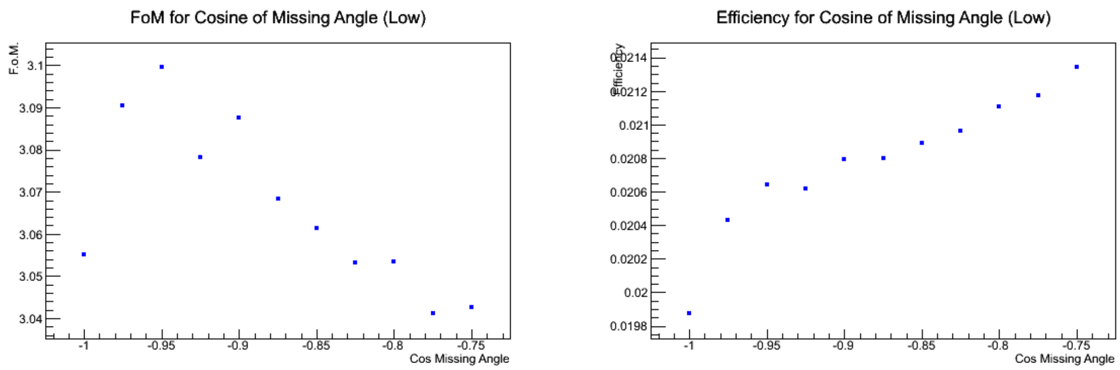

Figure 3.57: Figure of merit for missing angle cut low side, 3.6 GeV/c^2 A^0 mass, 1-prong cuts

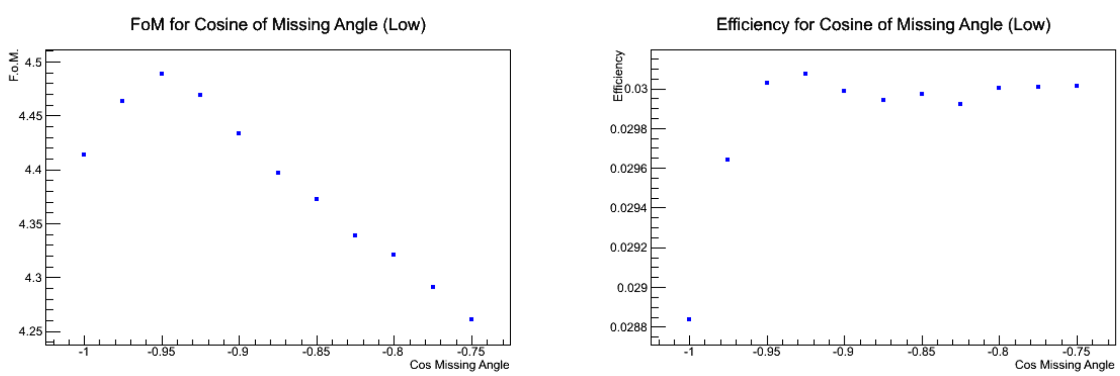

Figure 3.58: Figure of merit for missing angle cut low side, 9.3 GeV/c^2 A^0 mass, 1-prong cuts

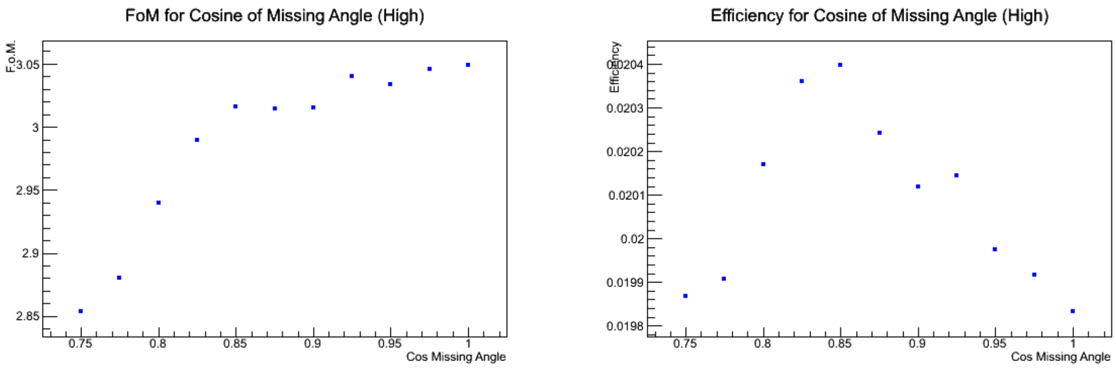

Figure 3.59: Figure of merit for missing angle cut high side, 3.6 GeV/c^2 A^0 mass, 1-prong cuts

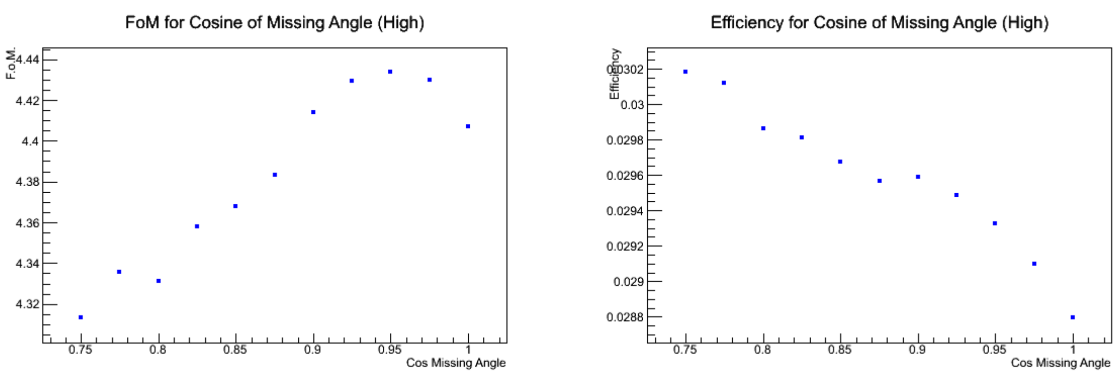

Figure 3.60: Figure of merit for missing angle cut high side, 9.3 GeV/c^2 A^0 mass, 1-prong cuts

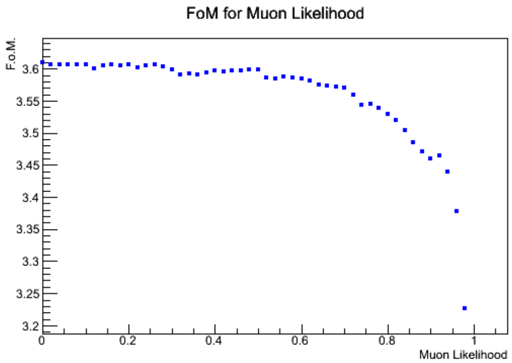

Figure 3.61: Figure of merit and efficiency for muon probability P(μ), 3.6 GeV/c^2 A^0 mass, 1-prong cuts

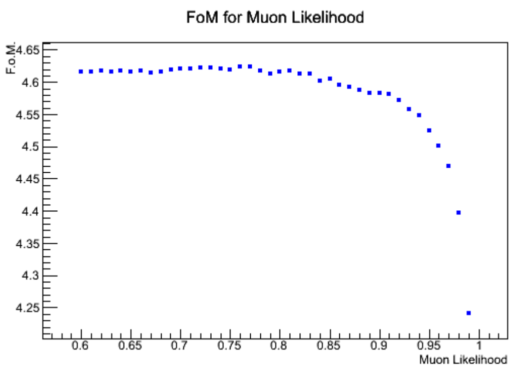

Figure 3.62: Figure of merit and efficiency for muon probability P(μ), 9.3 GeV/c^2 A^0 mass, 1-prong cuts

lepton flavor are applied. The results of these cuts are seen in plots of FoM and efficiency in Figs 3.61, 3.62, 3.63, and 3.64.

The tuned probability cut for the electron and muon, P(e) and P(μ) respectively, are:

$P(\mu) > 0.7$

$P(e) > 0.8$

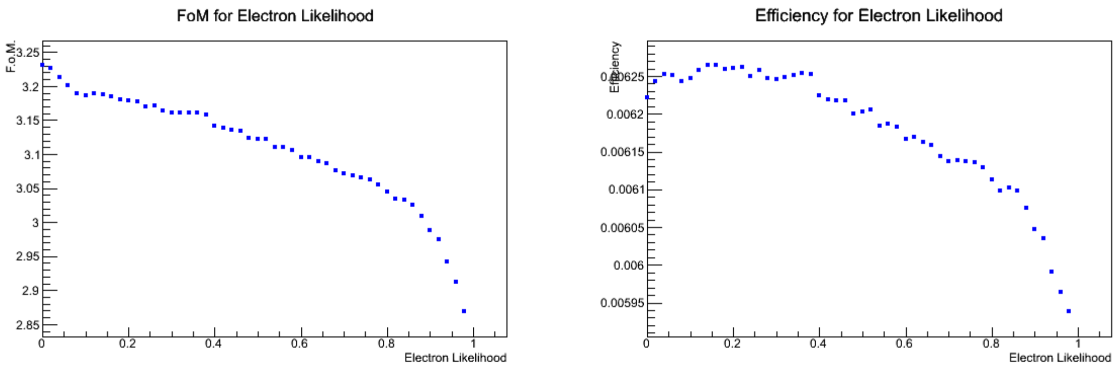

Figure 3.63: Figure of merit for electron probability P(e), 3.6 GeV/c^2 A^0 mass, 1-prong cuts

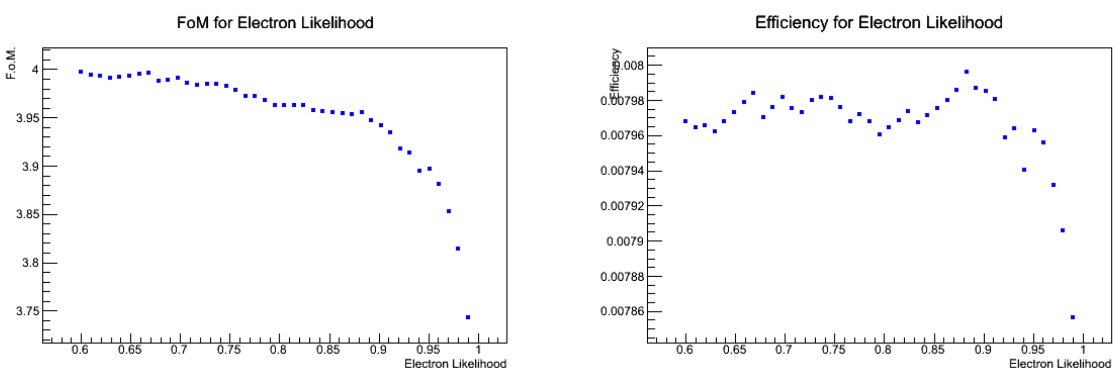

Figure 3.64: Figure of merit for electron probability P(e), 9.3 GeV/c^2 A^0 mass, 1-prong cuts

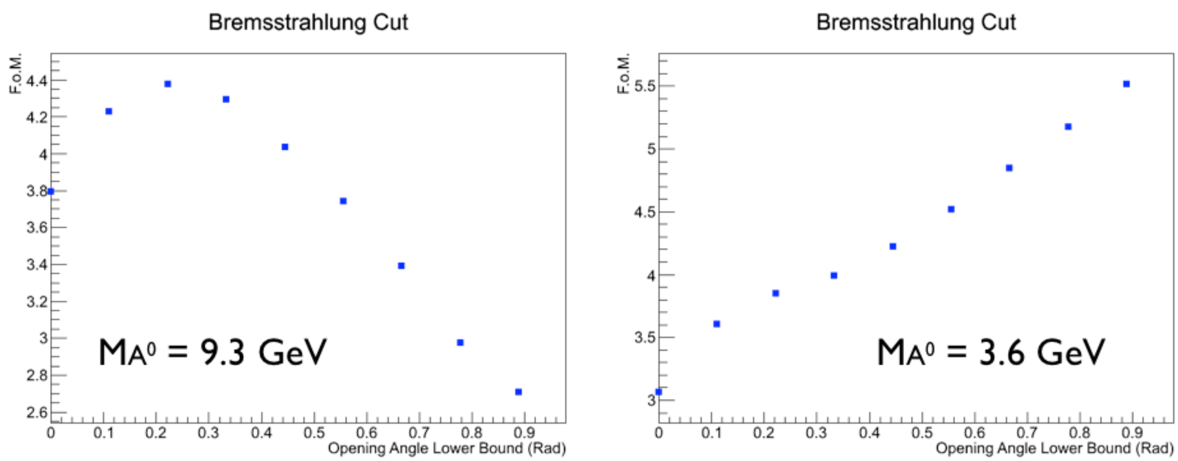

Figure 3.65: Figure of merit for electron bremsstrahlung cut. Left: 9.3 GeV/c^2 A^0 mass. Right: 3.6 GeV/c^2 A^0 mass. 1-prong cuts.

Bremsstrahlung Cut Tuning

A cut is placed on the opening angle between the candidate photon and each of the charged tracks. These cuts are optimized with decays of $\Upsilon(1S) \to \gamma A^0 \to \gamma\tau\tau$ where $M_{A^0} = 9.3$ GeV/c^2 and the τ-pair decay via a lepton decay and a 1-prong decay. The case where $M_{A^0} = 3.6$ GeV/c^2 is checked as well. In both cases, cuts on event classification, trigger, charge balance, number of tracks, and lepton flavor are applied. The results of these cuts are seen in plots of FoM and efficiency in Fig. 3.65.

We set the bremsstrahlung cut at 20 mrad.

E9/E25 Cut Tuning

For 1-prong cuts, an improvement was seen in the figure of merit for the E9/E25 cut that was not seen with "e & μ" cuts. We examine the case where the mass of the A^0 is 9.3 GeV/c^2. The photons associated with such an A^0 have an E9/E25 spectrum similar to the background we attempt to discriminate against and thus provide a lower limit for an E9/E25 cut. We can be sure that such a cut will not attenuate signals from lower mass A^0s. The FoM and efficiency are presented in Fig. 3.66.

The cut was set at E9/E25 > 0.9.

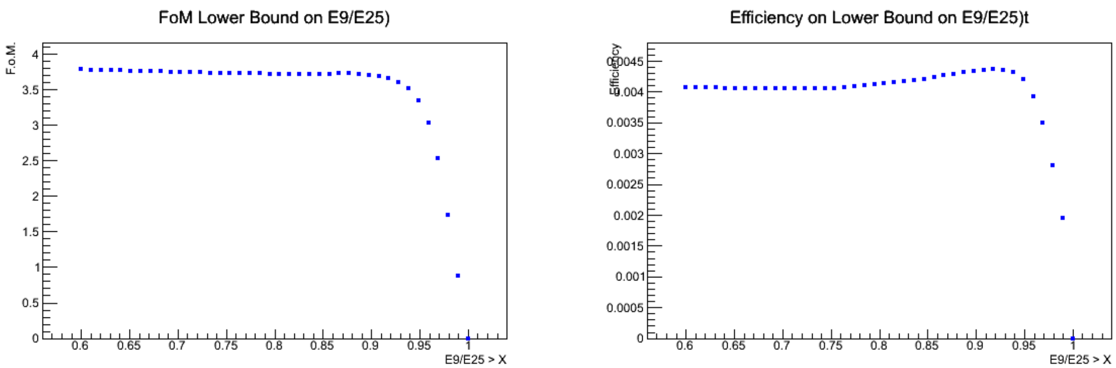

Figure 3.66: Figure of merit and efficiency for E9/E25 cut, 9.3 GeV/c^2 A^0 mass, 1-prong cuts

Barrel Cut Tuning

While ISR has a 1+cos$^2(\theta)$ distribution that leads to most of it being deposited in the endcaps, the complete elimination of data from the endcaps is found to reduce the FoM as well. A narrower cut is made on the θ distribution in the CM frame. This cut is optimized with decays of $\Upsilon(1S) \rightarrow \gamma A^0 \rightarrow \gamma\tau\tau$ where $M_{A^0} = 3.6$ GeV/c^2 and the τ-pair decays to a lepton and a 1-prong decay. The case where $M_{A^0} = 9.3$ GeV/c^2 is checked as well. In both cases, cuts on event classification, trigger, charge balance, number of tracks, and lepton flavor are applied. The low side FoM and efficiency results are displayed in Figs 3.67 and 3.68. The results for FoM and efficiency for the high side of the cut are shown in Figs 3.69 and 3.70.

We apply the barrel cut, or -0.82<Cos(θ_{CM})<0.65.

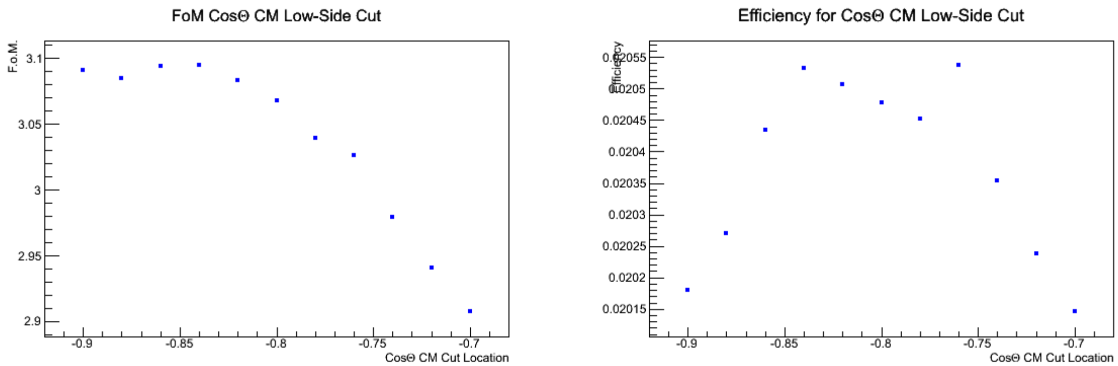

Figure 3.67: Figure of merit and efficiency for the $\cos(\theta)$ cut in CM frame low-side cut, 3.6 GeV/c^2 A^0 mass, 1-prong cuts

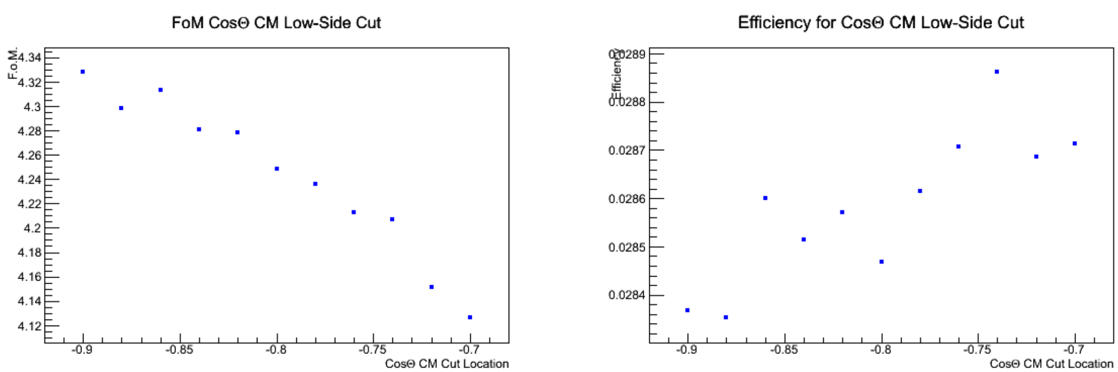

Figure 3.68: Figure of merit and efficiency for the $\cos(\theta)$ cut in CM frame low-side cut, 9.3 GeV/c^2 A^0 mass, 1-prong cuts

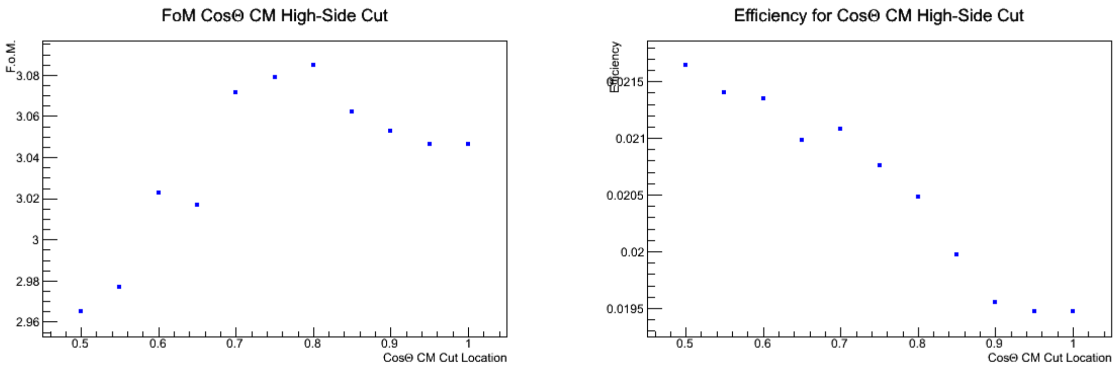

Figure 3.69: Figure of merit and efficiency for the cos(θ) cut in CM frame high-side cut, 3.6 GeV/c^2 A^0 mass, 1-prong cuts

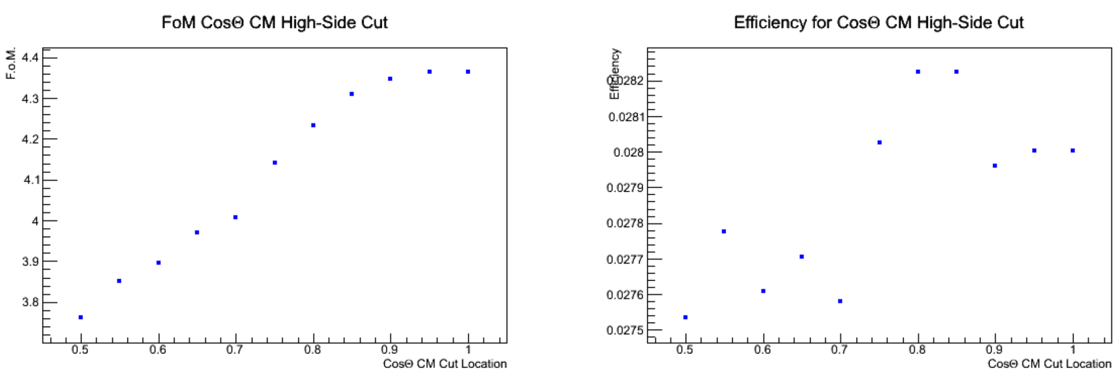

Figure 3.70: Figure of merit and efficiency for the cos(θ) cut in CM frame high-side cut, 9.3 GeV/c^2 A^0 mass, 1-prong cuts

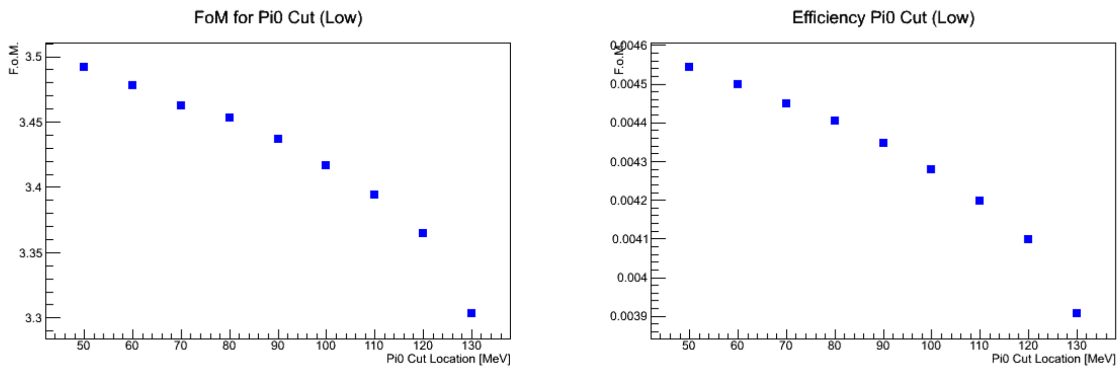

Figure 3.71: Figure of merit and efficiency for π^0 low-side cut, 3.6 GeV/c^2 A^0 mass, 1-prong cuts

π^0 Cut Tuning

The upper and lower boundaries of the π^0 cut are optimized using 10,000 decays of $\Upsilon(1S) \to \gamma A^0 \to \gamma\tau\tau$ with the τ-pair decaying to a lepton and one of the 1-prong decays. A^0 masses of 3.6 GeV/c^2 and 9.3 GeV/c^2 were used. To optimize the lower boundary, the upper boundary is fixed at $M_{\gamma\gamma} < 160$ MeV/c^2 while the lower boundary is varied between 50 MeV/c^2 and 130 MeV/c^2. To optimize the upper boundary, the lower boundary is fixed at $M_{\gamma\gamma} > 80$ MeV/c^2 while the upper boundary is varied between 140 MeV/c^2 and 220 MeV/c^2. Results for the FoM and efficiency are shown in Figures 3.71, 3.72, 3.73, and 3.74. These figures are then replotted with boundaries closer to the point at which we make our cuts in Figs. 3.75, 3.76, 3.77, and 3.78.

The high boundary is kept at 160 MeV/c^2, the lower boundary is lowered to 110 MeV/c^2, so the selection criteria is 110 MeV/c^2 $< M_{\gamma\gamma} <$ 160 MeV/c^2

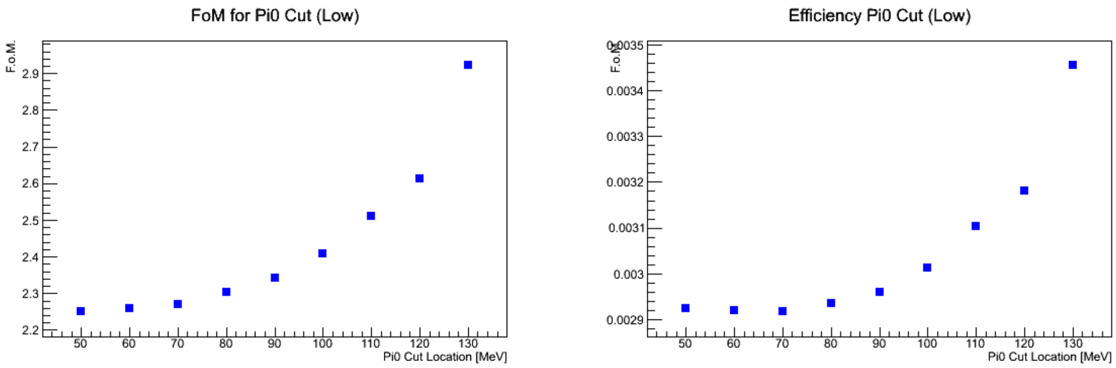

Figure 3.72: Figure of merit and efficiency for π^0 low-side cut, 9.3 GeV/c^2 A^0 mass, 1-prong cuts

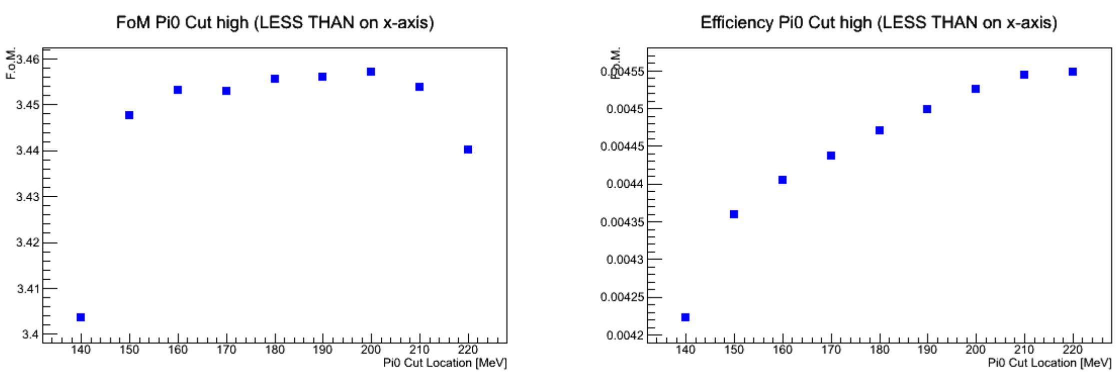

Figure 3.73: Figure of merit and efficiency for π^0 high-side cut, 3.6 GeV/c^2 A^0 mass, 1-prong cuts

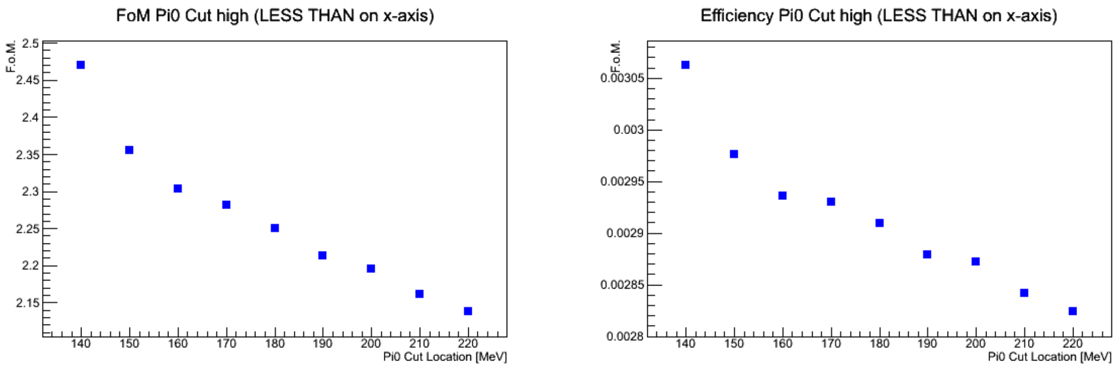

Figure 3.74: Figure of merit and efficiency for π^0 high-side cut, 9.3 GeV/c^2 A^0 mass, 1-prong cuts

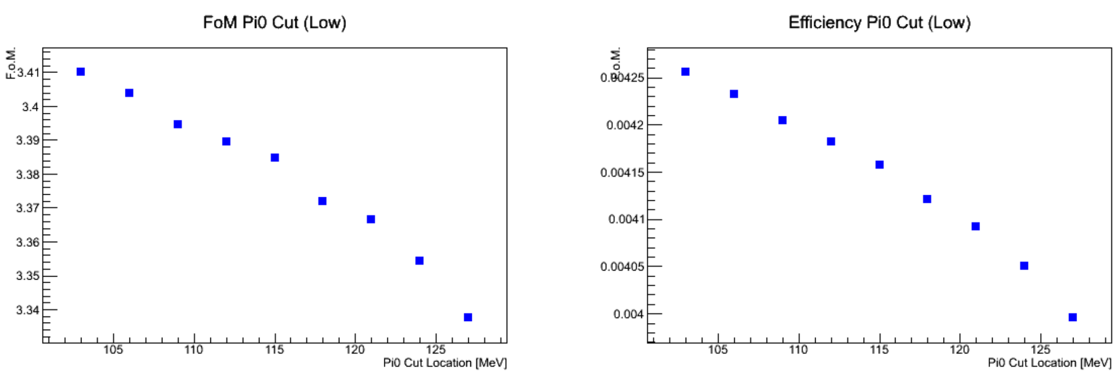

Figure 3.75: Figure of merit and efficiency for π^0 low-side cut, zoomed, 3.6 GeV/c^2 A^0 mass, 1-prong cuts

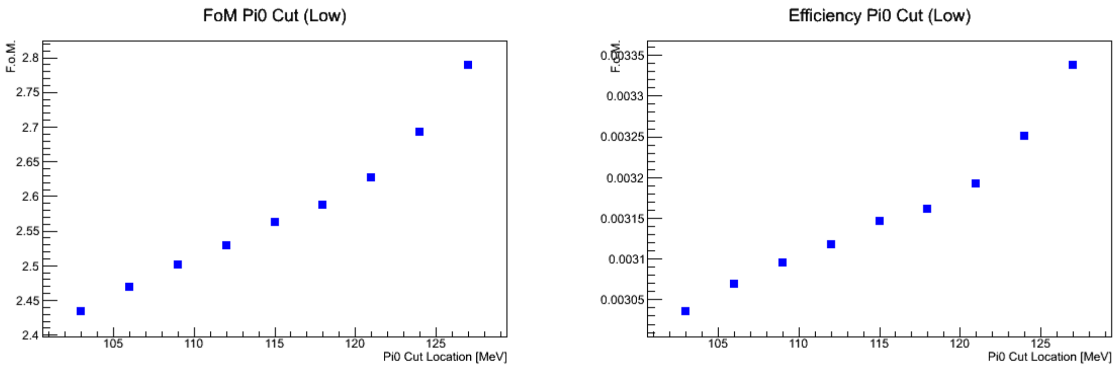

Figure 3.76: Figure of merit and efficiency for π^0 low-side cut, zoomed, 9.3 GeV/c^2 A^0 mass, 1-prong cuts

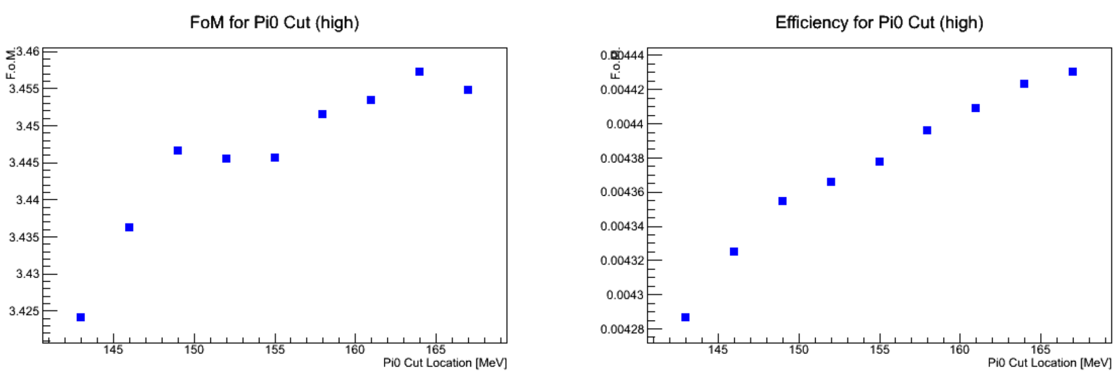

Figure 3.77: Figure of merit and efficiency for π^0 high-side cut, zoomed, 3.6 GeV/c^2 A^0 mass, 1-prong cuts

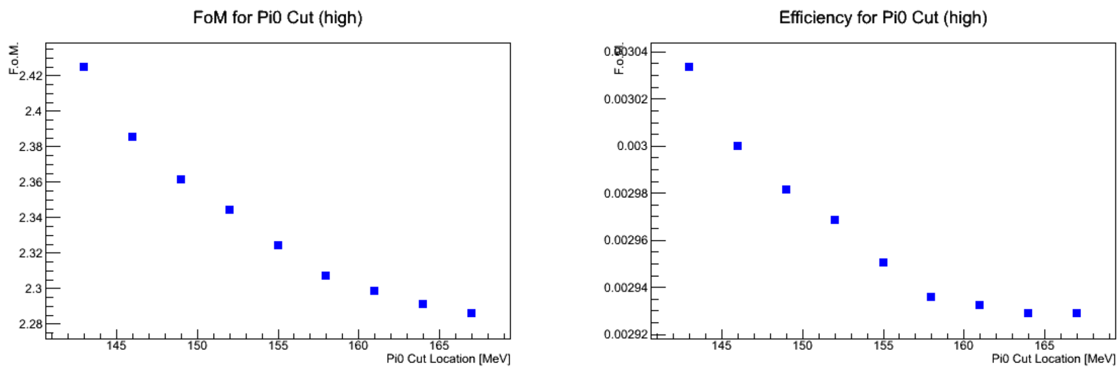

Figure 3.78: Figure of merit and efficiency for π^0 high-side cut, zoomed, 9.3 GeV/c^2 A^0 mass, 1-prong cuts

3.11.2 Summary of Optimized 1-Prong Cuts

The full set of optimized selection cuts is presented here for the convenience of anyone who wishes to make use of them without having to search through the text.

1. Tau Skim B: evt_cls.flag(4)>0
2. Trigger: RecTRG_summary3.final(0) + final(1) != 0
3. Two Charged Tracks w/ Balance
4. $N_\mu \geq 1$ or N_e=1
5. Lepton Probability cut: $P(e) > 0.8$ and $P(\mu) > 0.7$
6. Missing Energy Cut: 1.5 GeV $\leq E_{missing} \leq$ 7.5 GeV in CM frame
7. Missing Angle Cut: -0.95<Cos($\theta_{Missing}$)<0.90 in CM frame
8. Gamma Quantity: $N_\gamma > 0$
9. π^0 Cut: 110 MeV/c^2 $< M_{\gamma\gamma} <$ 160 MeV/c^2
10. Bremsstrahlung: α_{Brem} >20 milliradians in CM frame
11. CM θ Distribution Cut: -0.82<Cos(θ_{CM})<0.65
12. E9/E25 Cut: E9/E25> 0.90

Table 3.6: Summary of Effects of All Tuned 1-Prong Selection Cuts on Data and MC

Cut	# Retained (MC)	Efficiency (MC)	# Retained (Data)	Efficiency (Data)
No Cuts/Skim	2,085,000	N/A	6,467,416	N/A
Tau Skim B	1,459,195	0.70	-	-
Trigger	1,314,885	0.63	-	-
Two Charged Tracks and > 0 N_γ	592,245	0.28	2,472,017	0.382
$N_\mu \geq 1 or N_e = 1$	323,678	0.16	875,439	0.135
Lepton Probability Cut	293,146	0.14	835,619	0.129
Missing Energy Cut	288,538	0.14	413,367	0.064
Missing Angle Cut	274,192	0.13	333,647	0.052
π^0 Cut	134,169	0.06	200,964	0.031
Bremsstrahlung	113,430	0.06	148,677	0.023
CM θ Distribution Cut	86,916	0.04	110,016	0.017

There is a clear discrepancy in the 1-prong case between the number of events in MC and data. This discrepancy comes from the lack of a kinematic boundary cut as discussed in Subsection 3.4.4. The KB cut eliminated $e^+e^- \rightarrow e^+e^-$ and $e^+e^- \rightarrow \mu^+\mu^-$ events in the "e & μ" case. However, this cannot be replicated in the 1-prong case because we only require affirmative lepton identification on one of the tracks.

3.11.3 Cut Signal Efficiency

The batches of 10^4 1-Prong MC is used to determine the signal detection efficiency after the selection cuts listed in Table 3.6 are applied. The percentage of events that pass the cuts at each trial mass is displayed in Figure 3.79. The fit equation is

$$\epsilon_{cut} = -0.1443 + 0.2542x - 0.06835x^2 + 0.008741x^3 - 0.0004296x^4 \text{ where x} = \mathrm{M}_{A^0}[\mathrm{GeV}]. \tag{3.11.1}$$

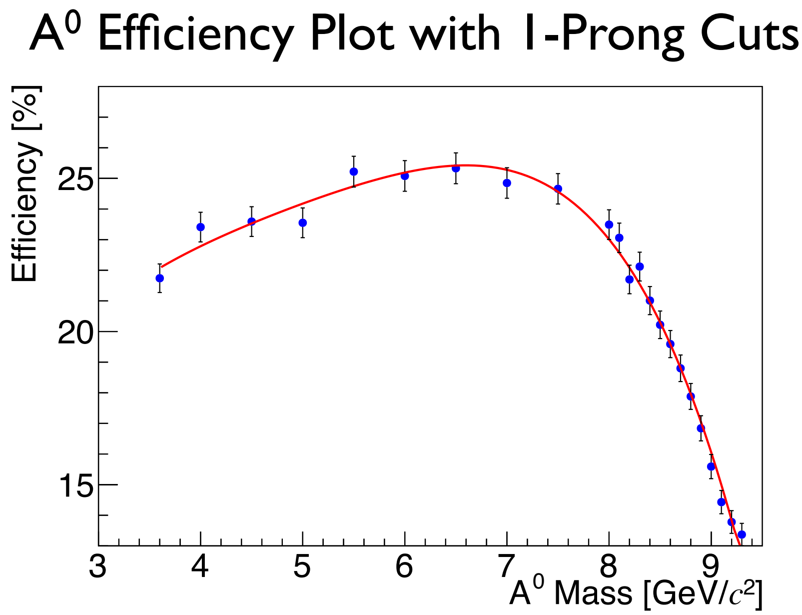

Figure 3.79: Efficiency of 1-Prong Higgs MC that pass all tuned cuts.

3.12 Fitting/Limit

To search for a peak in both the "e & μ" and "1-prong" data sets, we use ROOT [39], RooFit [40] and RooStats [41]. ROOT provides the framework in which RooFit and RooStats works. RooFit allows us to fit probability distribution functions (PDFs) in our data sets, and RooStats provides an easy way to run various statistical tests that can be compared between different experiments.

3.12.1 Algorithm Designs

The peak finder and limit setter both have the same basic structure: first, the fit characteristics of the signal peak for the photon associated with the A^0 is parameterized in terms of energy. Second, a smooth, analytic background shape is fitted to the on-resonance background MC. These two fits are then combined into a combined model and this combined model is fit to the data with varying median energies for the signal peak in a process called a "scan". Values such as the number of signal events (nsig), number of background events (nbkg), upper limit on the number of signal events, χ^2, and significance are reported.

Signal Fitting

While a Crystal Ball (CB) shape was originally chosen for the signal PDF of the candidate gamma peak, we discovered that for the number of signal events passing our cuts precise modeling of the tail region was not necessary. In fact, CB modeling proved detrimental to convergence of the combined model. The CB PDF has been replaced with a Gaussian PDF of Eq. 3.12.1 centered on the peak energy, $E_{\gamma peak}$; similar results for signal events are found and convergence of the combined model is much improved.

$$P(x) = \frac{1}{\sigma_{gauss}\sqrt{2\pi}} e^{-\left(E_\gamma - E_{\gamma peak}\right)^2/2\sigma^2_{gauss}} \tag{3.12.1}$$

To determine the gaussian width, σ_{gauss}, as a function of peak E_γ energy , we use 10,000 $\Upsilon(1S) \to \gamma A^0 \to \tau\tau$ events with the τ-pair decaying generically. This is consistent with a branching ratio on the order of 10^{-4}, approximately 5-10 times the limit set at CLEO [38]. The fit window is selected to have edges at ±10% of the peak E_γ energy unless that the edge is below 150 MeV or above 4.2 GeV. In that case, the window is truncated. The signal is fit with a gaussian whose sigma value is seeded at $0.01\times E_\gamma$ and allowed to float between $0.001\times E_\gamma$ and $0.1\times E_\gamma$. The mean is allowed to float between ±5% of the peak energy being fitted.

The σ_{gauss} is found to be $\approx 0.02 E_\gamma$ as seen in Fig. 3.80.

Background Fitting

The photon CM energy spectrum is broken up into 4 regions: 4.2 GeV to 1.5 GeV (4.0 GeV to 1.5 GeV in the 1-prong case), 1.5 GeV to 0.8 GeV, 0.8 GeV to 0.3 GeV, and 0.3 GeV to 0.15 GeV. These regions are fit independently with cubic polynomials. A summary of their fit parameters is in Table 3.7. While the fits are unbinned, χ^2/ndf is used as an estimator of “goodness of fit” following a recommendation from the RootTalk forums.

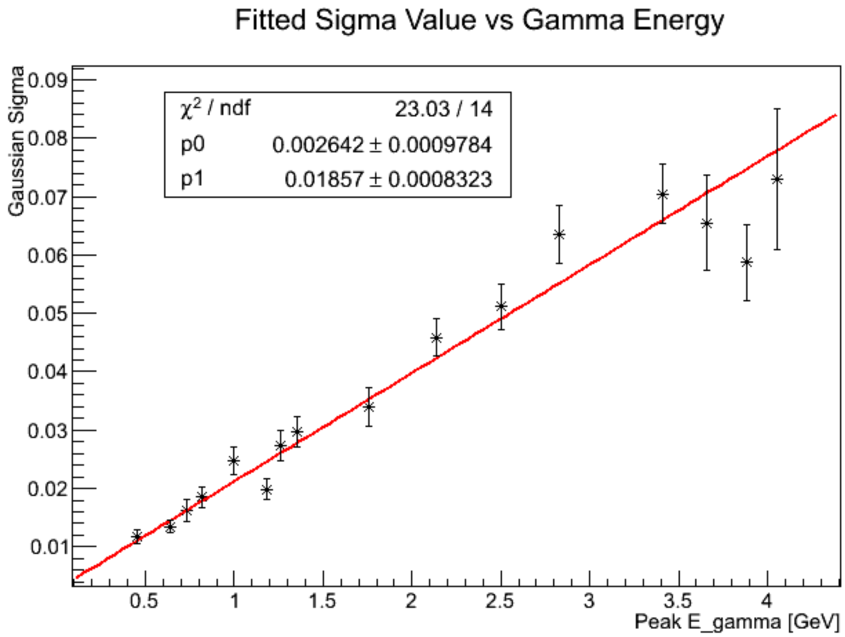

Figure 3.80: Plot of fitted Gaussian σ values vs the peak photon energy. Decays are $\Upsilon(1S) \to \gamma A^0 \to \tau\tau$ with the τ-pair decaying generically, all "e & μ" mode cuts applied.

Table 3.7: Fit Parameters for Backgrounds with "e & μ" Selection Cuts in On-Resonance MC

Range (GeV)	c1	c2	c3	χ^2/ndf
4.2 - 1.5	-0.59482 $\pm$ 0.0066	0.1510 $\pm$ 0.0019	-0.0157 $\pm$ .0004	0.68
1.5 - 0.8	-0.847 $\pm$ 0.19	-0.016 $\pm$ 0.24	0.130 $\pm$ 0.082	1.1
0.8 - 0.3	-3.216 $\pm$ 0.13	4.25 $\pm$ 0.31	-1.940 $\pm$ 0.22	0.77
0.3 - .15	-6.178 $\pm$ 0.17	10.0 $\pm$ 1.2	2.4 $\pm$ 1.3	.79

Table 3.8: Fit Parameters for Backgrounds with "e & μ" Selection Cuts in On-Resonance Data

Range (GeV)	c1	c2	c3	χ^2/ndf
4.2 - 1.5	-0.77805 $\pm$ 0.0057	0.2290 $\pm$ 0.0022	-0.0023886 $\pm$ .00032	0.93
1.5 - 0.8	-0.736 $\pm$ 0.15	-0.009 $\pm$ 0.16	0.099 $\pm$ 0.066	0.83
0.8 - 0.3	-3.5308 $\pm$ 0.092	5.05 $\pm$ 0.22	-2.532 $\pm$ 0.16	1.17
0.3 - .15	-5.981 $\pm$ 0.16	10.0 $\pm$ 1.7	0.3 $\pm$ 1.4	1.06

Table 3.9: Fit Parameters for Backgrounds with 1-Prong Selection Cuts in On-Resonance MC

Range (GeV)	c1	c2	c3	χ^2/ndf
4.0 - 1.5	-0.79344 $\pm$ 0.00035	0.2336 $\pm$ 0.0018	-0.024161 $\pm$ 0.00025	1.14
1.5 - 0.8	-1.2423 $\pm$ 0.052	0.614 $\pm$ 0.061	-0.1132 $\pm$ 0.021	1.22
0.8 - 0.3	-1.999 $\pm$ 0.14	2.13 $\pm$ 0.32	-0.865 $\pm$ 0.21	1.13
0.3 - .15	-3.260 $\pm$ 0.19	0.70 $\pm$ 0.58	9.9 $\pm$ 1.1	1.23

Table 3.10: Fit Parameters for Backgrounds with 1-Prong Selection Cuts in On-Resonance Data

Range (GeV)	c1	c2	c3	χ^2/ndf
4.0 - 1.5	-0.77680 $\pm$ 0.0053	0.2251 $\pm$ 0.0027	-0.022906 $\pm$ 0.00037	1.52
1.5 - 0.8	-0.6780 $\pm$ 0.083	-0.0074 $\pm$ 0.094	0.076 $\pm$ 0.031	0.88
0.8 - 0.3	-1.571 $\pm$ 0.17	1.31 $\pm$ 0.37	-0.516 $\pm$ 0.23	0.89
0.3 - .15	-5.198 $\pm$ 0.16	10.00 $\pm$ 0.35	-3.781 $\pm$ 9.4	1.47

Combined Model

The combined model is a combination of the signal fit and the background fit in RooFit's extended likelihood procedure. For each photon peak energy, E_γ, a fit window of $\pm 6\sigma$ is selected around that central value. If the window extends beyond the fit region's boundary (e.g., if the lower edge of the fit window is less than $E_\gamma = 0.150$ GeV), the fit function for the region of the central value is used and the background fit function is extended beyond the boundary. Both the signal fit function and background fit function are continuous at all points within the combined fit window. The number of events in that window, N, is passed to the fitter. The initial number of signal events is set to 1 and allowed to fluctuate between -N and N. The initial number of background events set to N-1 and allowed to fluctuate between 0 and N. All other parameters are fixed.

The fit results are stored in a RooFit object and the 90% confidence upper limit and significance are returned by RooStats. For significance, we use a method based the standard significance formula $\sigma_{significance} = \sqrt{2ln(L_{max}/L_0)}$. For the 90% confidence limit, we integrats the likelihood function from the fit.

Scanning

We scan the photon spectrum by fitting the combined model with different E_γ values from 0.150 GeV to 4.0 GeV in steps consistent with 1% energy binning when searching for a peak, and 2% energy binning when setting an upper limit across the A^0 mass range. The 1% scan is oversampling to be certain that no possible peak is missed. If a peak is present, there will be several consecutive points with significance greater than 3σ. Testing in MC shows that this will be approximately 3 points with high significance. When setting an upper limit, we scan in steps consistent with the detector resolution.

Because of the issue with peaking backgrounds noted in Sec 3.10, test points below 0.180 GeV are discarded. The fit window is centered around E_γ with boundaries at $\pm 6\sigma_{gauss}$. At the end of each fit, the fit quality status returned in the fit result is checked to ensure that the fit has converged. After the fit is completed, a significance and 90% C.L. is calculated for that value of E_γ. And example of such a point is shown in Fig. 3.81.

Significance

Significance testing is done with two RooStats packages: the ProfileLikelihoodCalculator (PLC) and the HybridCalculatorOriginal (HCO). The PLC uses Wilks' Theorem [42] to relate the relative likelihood of signal+background fit and background fit to a confidence level. The HCO is an implementation of the CLs method used in other searches for rare decays. The technique generates 2000 sets of toy MC based on data and compares the confidence level of the background-only model (CL$_b$) to the confidence level of the signal+background model (CL$_{s+b}$)[43]. An example of the output from the HCO can be seen

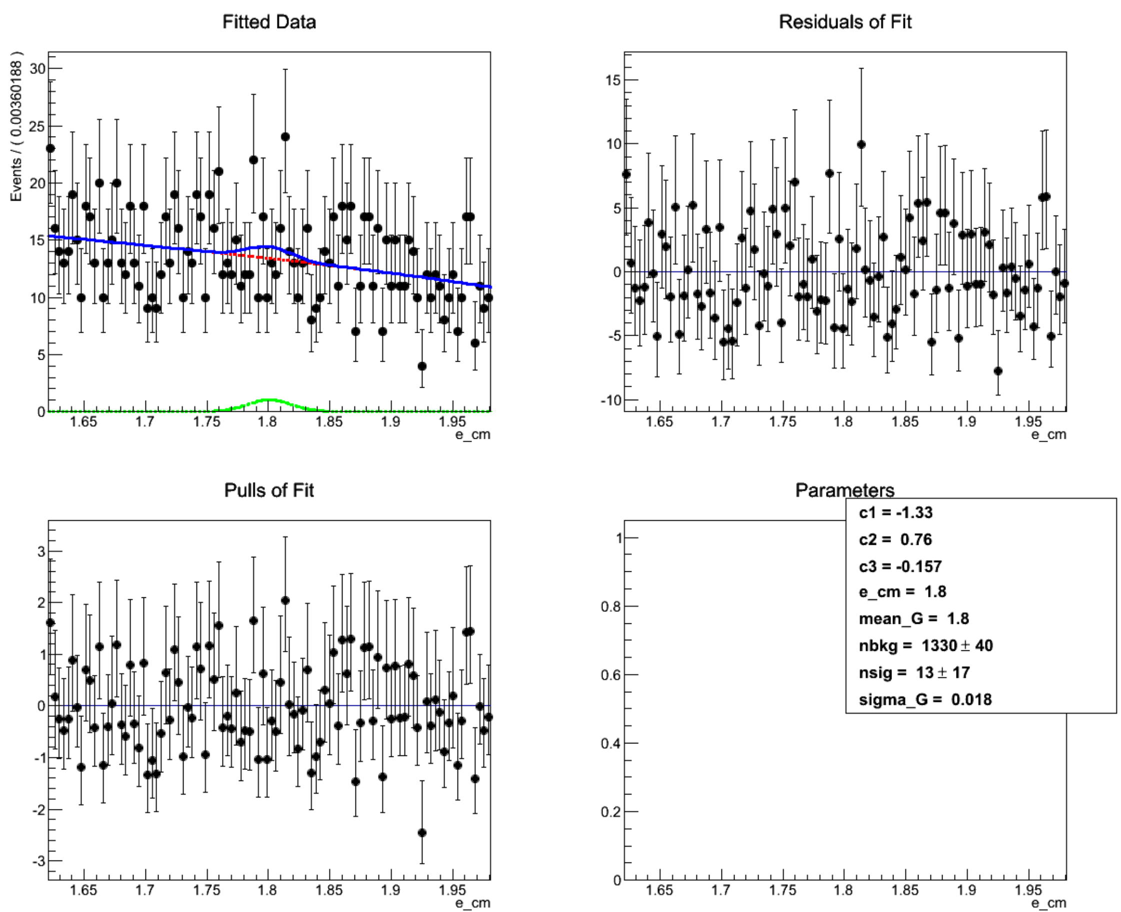

Figure 3.81: An example of a fit using the combined model in the on-resonance "e & μ" MC sample. The upper left is the fitted data, upper right is the residuals, lower left is the normalized residuals, and lower right shows the fit parameters.

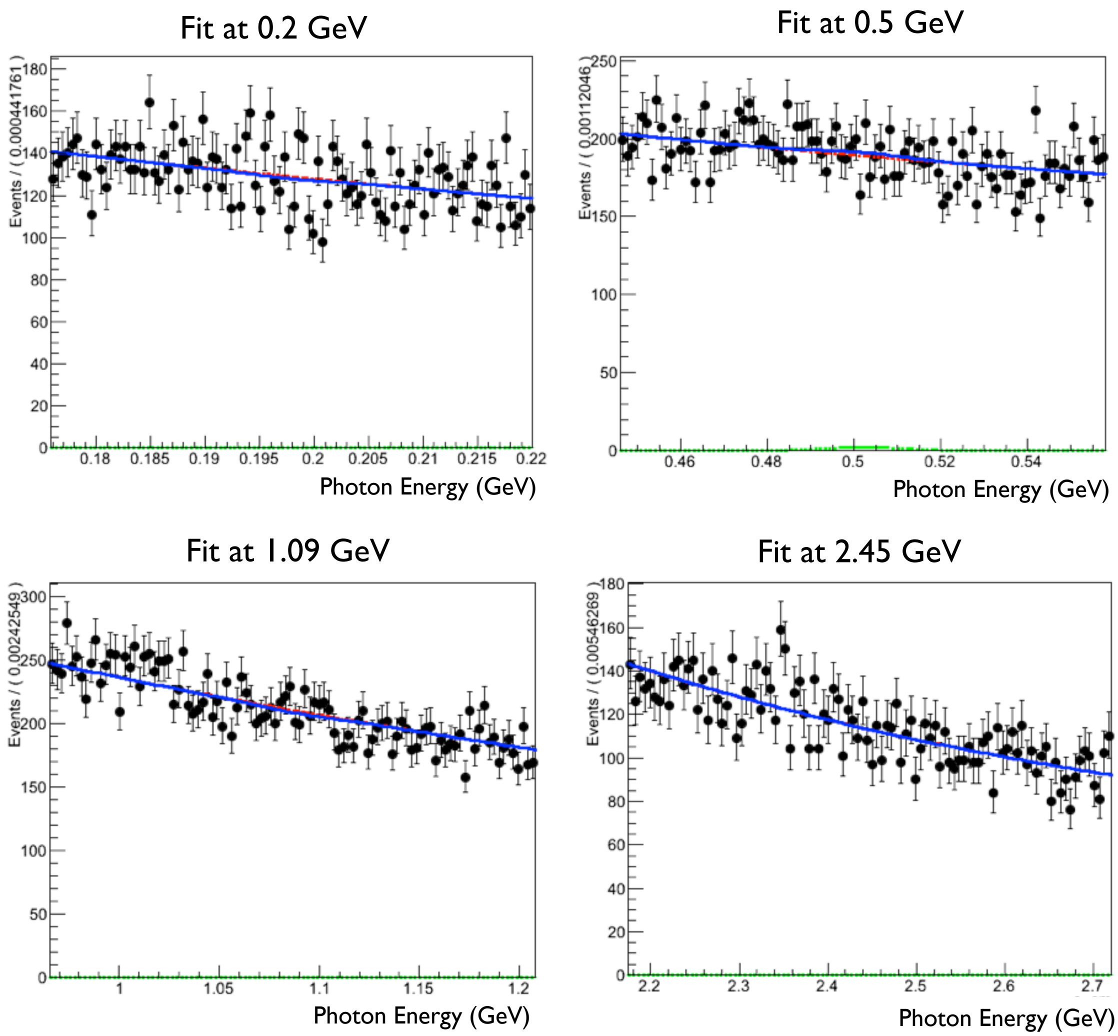

Figure 3.82: Examples of fits using the combined model in the on-resonance “1-prong” MC sample in all four E_γ regions.

in Fig. 3.83. More information on the implementation of these techniques can be found in Reference [44].

For this analysis, the PLC method was used as the primary and the HCO method was used for corroboration of the results. This allows us to make an approximation of $\sigma_{significance} = \sqrt{2ln(L_{max}/L_0)}$ which we can use for a direct comparison with CLEO.

Branching Ratio

In the event that a signal is found in the significance scan, nsig will be used to determine a branching ratio. Let us begin with the case where the τ-pair decays to 1e and 1μ. It starts with the number of signal events expected from branching ratios with no empirical corrections:

$$N_{PDG\_expected} = N_{\Upsilon(1S)} BR_{\Upsilon(1S)\to\gamma A^0} BR_{A^0\to\tau\tau} BR_{\tau\to e\nu_e\nu_\tau} BR_{\tau\to\mu\nu_\mu\nu_\tau} \tag{3.12.2}$$

where

$$BR_{\tau\to e\nu_e\nu_\tau} BR_{\tau\to\mu\nu_\mu\nu_\tau} = BR_{\tau^+\to e^+\nu_e\bar{\nu_\tau}} BR_{\tau^-\to\mu^-\bar{\nu_\mu}\nu_\tau} + BR_{\tau^-\to e^-\bar{\nu_e}\nu_\tau} BR_{\tau^+\to\mu^+\nu_\mu\bar{\nu_\tau}} = 6.2\% \tag{3.12.3}$$

This needs to be modified by including the loss of efficiency due to cuts, ϵ_{cuts}.

$$nsig = N_{PDG\_expected}\epsilon_{cuts} \tag{3.12.4}$$

Substitution leads us to

$$BR_{\Upsilon(1S)\to\gamma A^0} BR_{A^0\to\tau\tau} = \frac{nsig}{\epsilon_{cuts} N_{\Upsilon(1S)} BR_{\tau\to e\nu_e\nu_\tau} BR_{\tau\to\mu\nu_\mu\nu_\tau}} \tag{3.12.5}$$

The 1-prong case takes a similar form:

$$BR_{\Upsilon(1S)\to\gamma A^0} BR_{A^0\to\tau\tau} = \frac{nsig}{\epsilon_{cuts} N_{\Upsilon(1S)} BR_{\tau\to l\nu_l\nu_\tau} BR_{\tau\to 1prong}} \tag{3.12.6}$$

where

$$BR_{\tau\to l\nu_l\nu_\tau} BR_{\tau\to 1prong} = BR_{\tau^+\to l^+\nu\bar{\nu_\tau}} BR_{\tau^-\to 1prong} + BR_{\tau^-\to l^-\bar{\nu_l}\nu_\tau} BR_{\tau^+\to\overline{1prong}} = 60.15\% \tag{3.12.7}$$

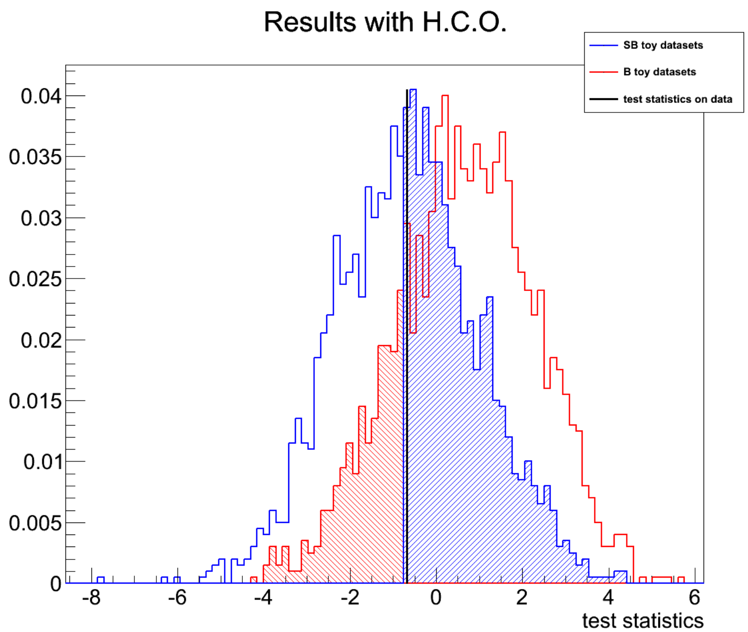

Figure 3.83: An example of the CLs method implemented in RooStats with the HybridCalculatorOriginal function. A point in the on-resonance "e & μ" MC sample is used.

Upper Limit

Upper limit calculations are performed with BayesianCalculator and the ProfileLikelihoodCalculator (PLC). The integration using the BayesianCalculator is performed by redefining the range of nsig to have a lower bound at zero. This truncation is performed after the fit so that it does not affect the likelihood function. The likelihood function is then integrated from zero upward to find the point at which 90% of the curve is covered, nsig$_{UL}$. The PLC is also used to find an upper limit; this serves as a check on the BayesianCalculator. The BayesianCalculator is chosen as the primary method because it allows for the most direct comparison with the CLEO upper limit and the PLC does not always return a valid numerical result. The BayesianCalculator is set to perform integration using the adaptive mode; this the default integration scheme and provides reliable results for simple likelihood functions. Examples of the upper limit outputs of the BayesianCalculator and PLC are shown in Figs. 3.84 and 3.85, respectively. More information about the algorithms uses here can be found in Ref. [41] and the RootTalk forums.

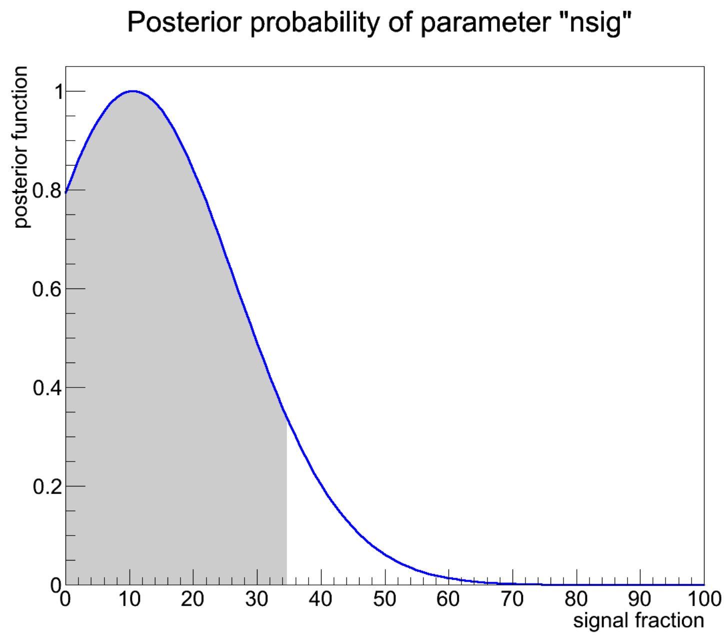

Figure 3.84: An example of the 90% confidence level upper limit obtained from integration of a Bayesian likelihood function in RooStats. A point in the on-resonance "e & μ" MC sample is used.

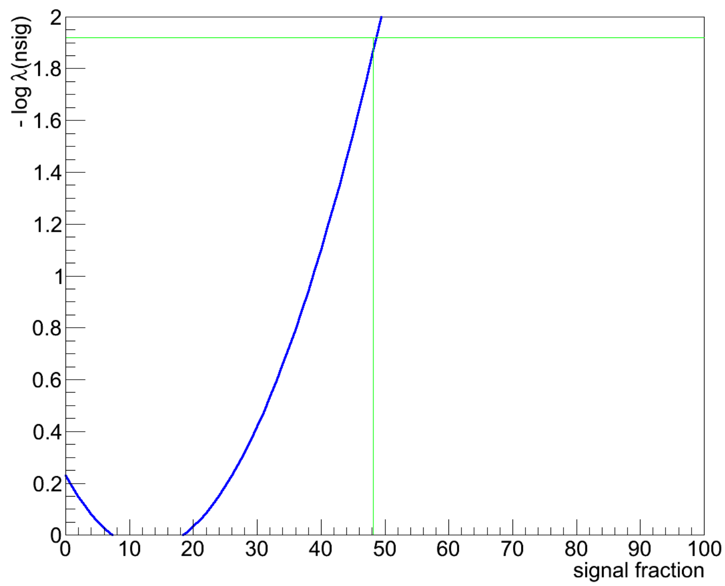

Figure 3.85: An example of the 90% confidence level upper limit obtained from the Profile-LikelihoodCalculator. A point in the on-resonance "e & μ" MC sample is used.

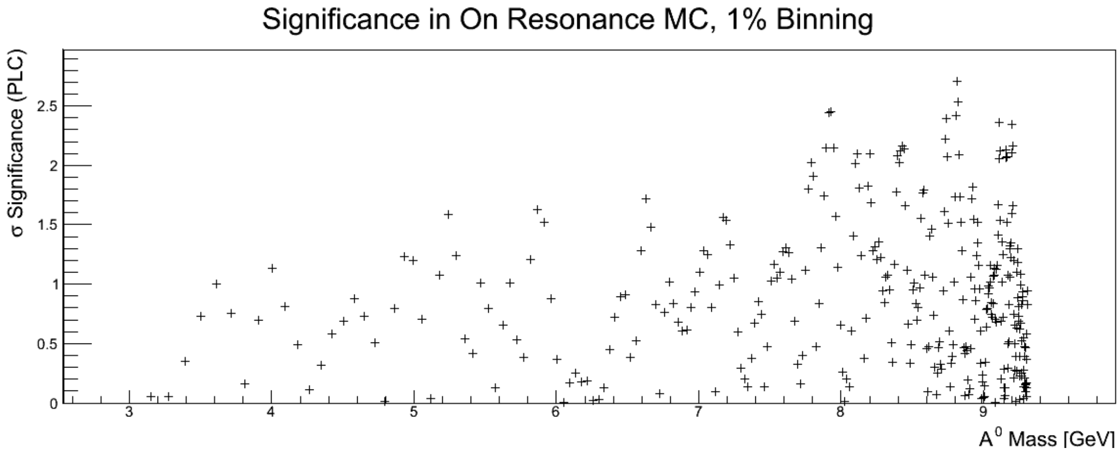

Figure 3.86: Significance plot in "e & μ" on-resonance MC with 1% binning obtained from the ProfileLikelihoodCalculator.

3.12.2 Testing

False Positive

The fitter is run on an on-resonance MC data set with no A^0 signal added and a significance plot is generated. No points are found with both a positive number of nsig and a significance greater than 3σ. A significance plot using on-resonance MC is included in Fig. 3.86.

Bias

To check for positive or negative bias in the signal yield, we plot a 1-D histogram of the signal yields in each region on a background sample with no A^0 events. If there is no bias, this histogram should show a guassian distribution with a mean statistically consistent with $\overline{nsig} = 0$. This is found to be the case in all fit regions. A histogram of the distribution in MC for the "e & μ" case is shown in Fig. 3.87, and for the 1-prong case in Fig. 3.89. The signal yield as a function of A^0 mass in MC for the "e & μ" case is presented in Fig. 3.88 and for the 1-prong case in Fig. 3.90.

3.12.3 Results

Using the on-resonance MC data, an upper limit on the branching ratio of $\Upsilon(1S) \to \gamma A^0 \to \gamma\tau\tau$ has been established to be between 1×10^{-5} and 9×10^{-5} with a 90% confidence

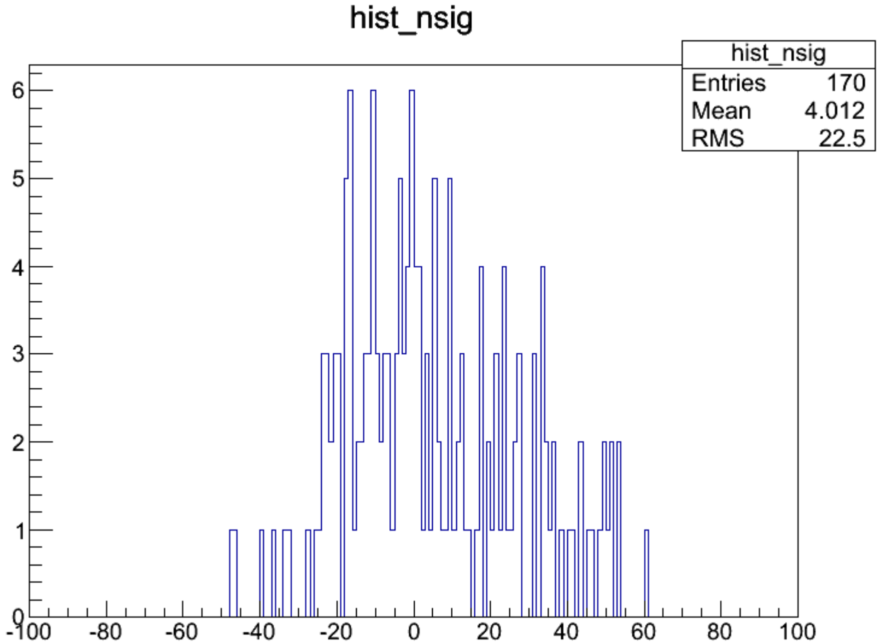

Figure 3.87: Combined distribution of nsig in On-Resonance MC with "e & μ" Cuts.

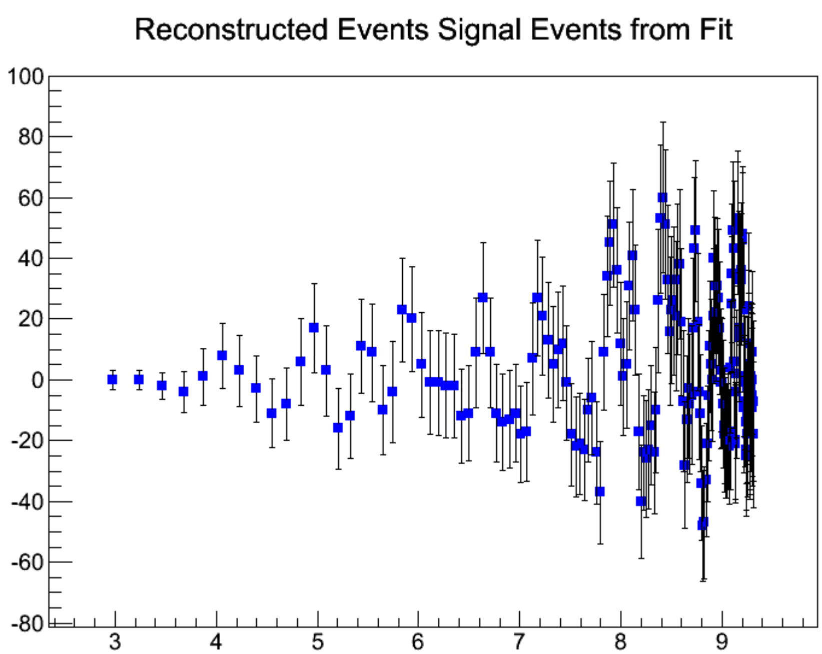

Figure 3.88: Distribution as a function of A^0 mass of nsig in On-Resonance MC with "e & μ" Cuts.

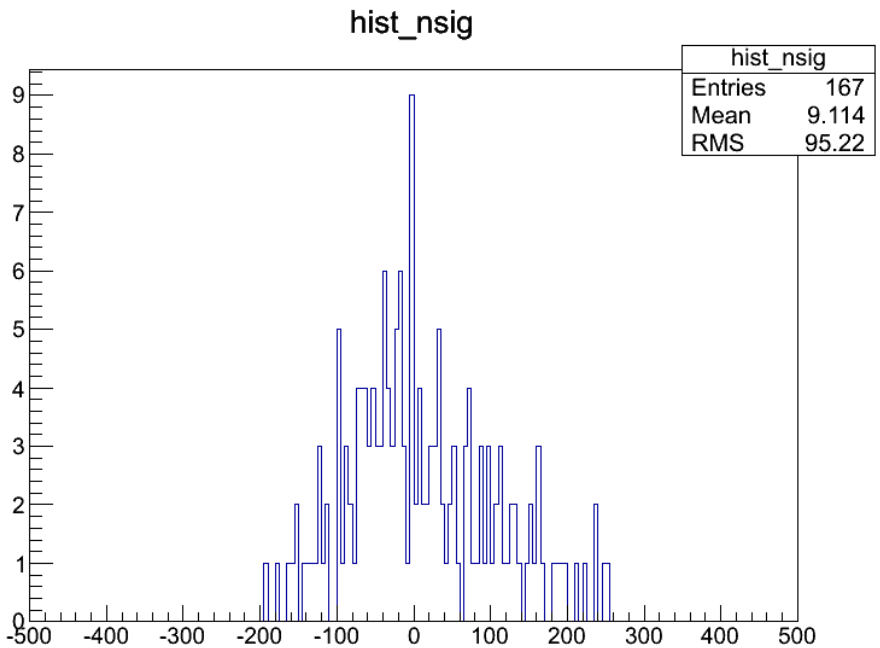

Figure 3.89: Combined distribution of nsig in On-Resonance MC with 1-prong cuts.

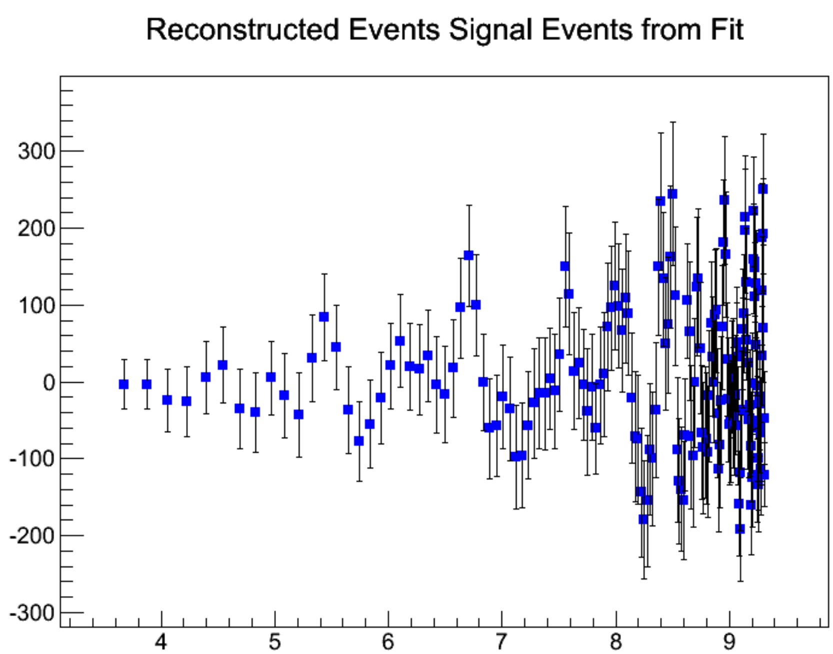

Figure 3.90: Distribution as a function of A^0 mass of nsig in On-Resonance MC with 1-prong cuts.

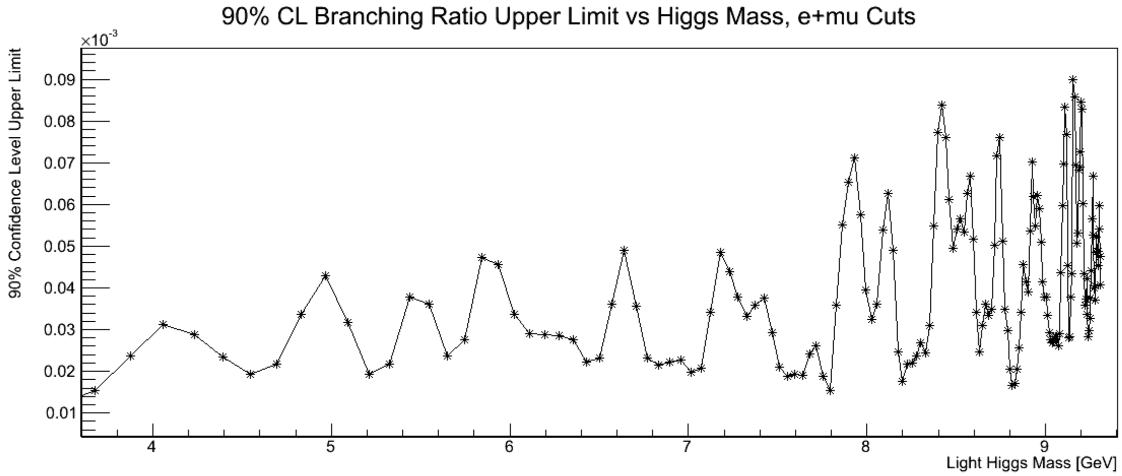

Figure 3.91: 90% Confidence Level Upper Limit for A^0 in On-Resonance MC with "e & μ" Cuts.

level. Greater sensitivity is seen towards low mass A^0. The result in MC for e & μ cuts is presented in Fig. 3.91 and the result for 1-prong cuts is presented in Fig. 3.92.

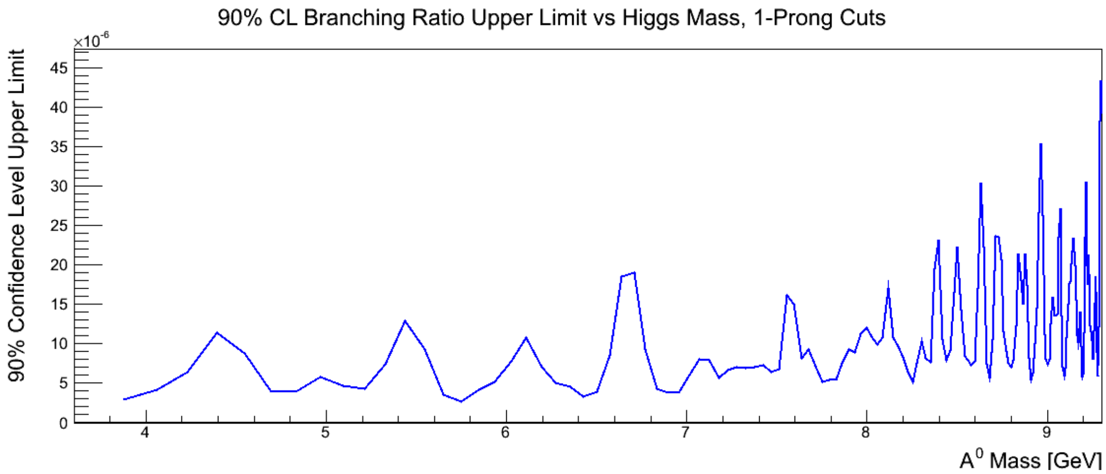

Figure 3.92: 90% Confidence Level Upper Limit for A^0 in On-Resonance MC with 1-Prong Cuts.

3.13 Systematics

3.13.1 Discrepancy Between Data and MC Photon Energy

To determine the difference between E_γ in MC and E_γ in data, a π^0 peak was fitted and mean value found in both MC and data. The sample selection cuts require events to have 1 e, 1 μ, two charged tracks, the TauSkimB flag, and to pass the trigger condition. The highest energy photon in each event is combined with all other photons in the event. The invariant mass of each of the gamma pairs, $M_{\gamma\gamma}$ is plotted in a histogram. The π^0 peak is fit with a CB function and the background is fit with a 4th order polynomial. The fits are shown in Fig. 3.93. The peak position in data is $M_{\gamma\gamma}$=134.768 $\pm$ 0.074 MeV/c^2 and in MC is $M_{\gamma\gamma}$=134.011 $\pm$ 0.044 MeV/c^2. With this method, we estimate a 0.6% uncertainty. This applies for both modes.

3.13.2 Background Fit Systematics

The decision to fit the background over a small number of wide (compared to the signal width) regions instead of letting the background float in each fit window is motivated primarily by a desire to avoid local inflections in the background fit that would artificially boost the signal yield. To see if this choice of technique greatly affects the upper limit set by the scanner, we run the scanner as described in Section 3.12, but allow the background

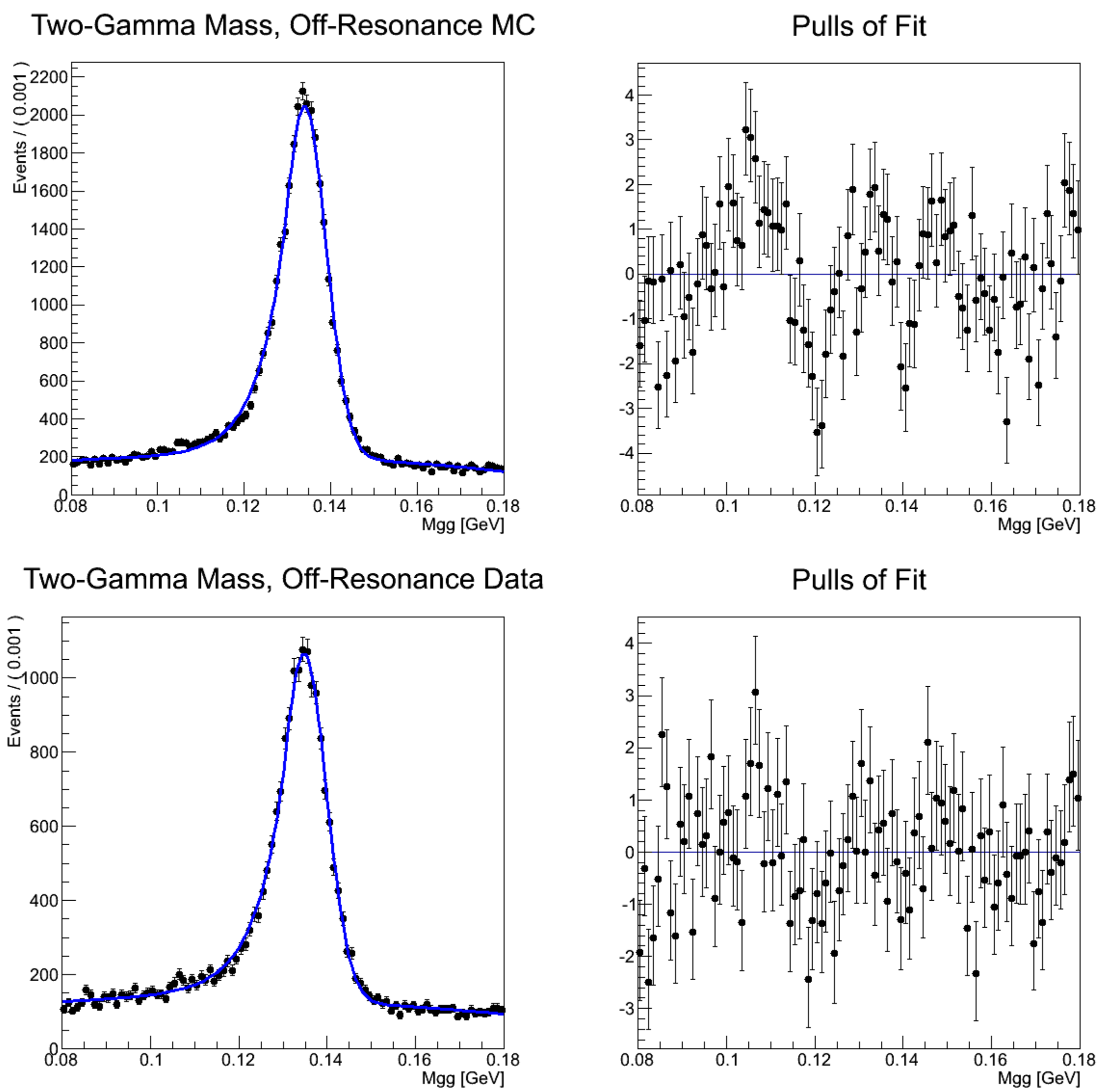

Figure 3.93: Fitted π^0 peak and pulls of fit in on-resonance MC (top) and data (bottom).

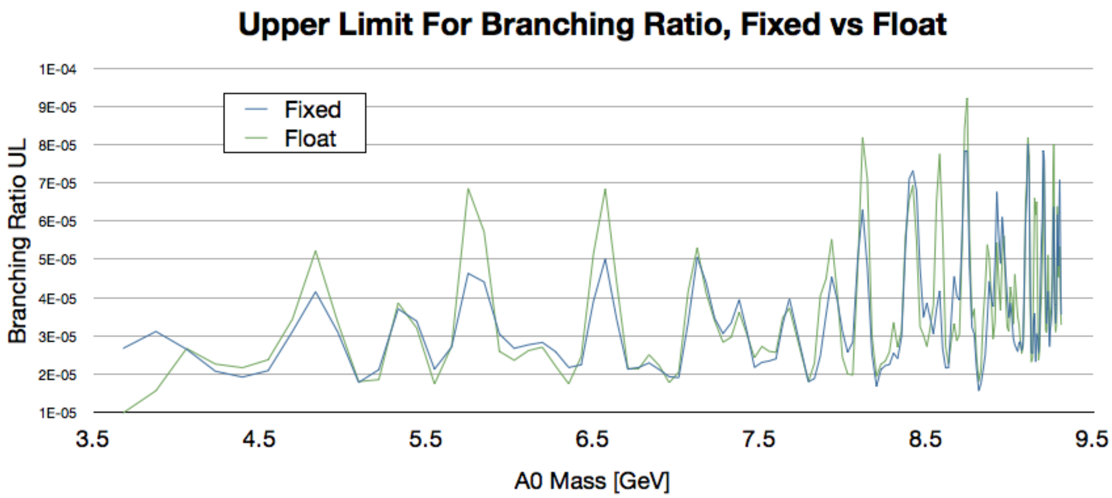

Figure 3.94: Upper limit of combined branching ratio with a fixed polynomial background (blue) and with a floating polynomial background (green).

parameters to float within the fit window. A comparison of the upper limits set using these two techniques is shown in Fig. 3.94.

To determine the average percent difference across the spectrum, we use Eq. 3.13.1:

$$\frac{1}{N}\sum\left|\frac{UL_{float} - UL_{fixed}}{UL_{fixed}}\right|, \text{ where N is the total number of points} \tag{3.13.1}$$

Using this method, we estimate a 20% uncertainty in the "e & μ" mode and 25% uncertainty in the "1-prong" mode.

3.13.3 Signal Fit Systematics

The signal is fit with a gaussian, so the uncertainty in σ_{gauss} will be a major contributor to systematic error. Previous work at Belle suggested the photon spectrum had a "fudge factor" of about 5%. The width of the gaussian, σ_{gauss}, is increased by 5% and the scan is performed again. The average of the absolute values of the percent difference between the two scans is calculated and is taken to be the systematic uncertainty of the signal fit. A comparison of the upper limits set using these two techniques is shown in Fig. 3.95. Using this method, we estimate a 4.5% uncertainty in the "e & μ" mode and an 11% uncertainty in the "1-prong" mode.

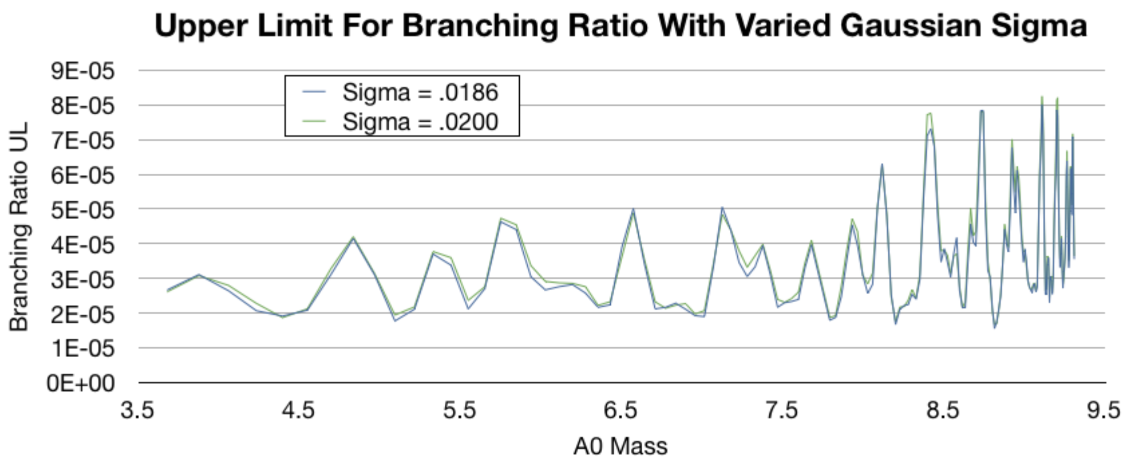

Figure 3.95: Upper limit of branching ratio with normal signal width (blue) and signal width increased by 5% (green).

3.13.4 Fit Window Width

The width of the fit window is varied to determine if the width impacts the value of the upper limit. Window widths between $7.5\sigma_{gauss}$ and $5\sigma_{gauss}$ are evaluated; widths outside of this range produce fits that were obviously unacceptable by visual inspection. Varying between these two extremes yields an 8% difference in the "1-prong" mode.

3.13.5 Efficiency Interpolation

Uncertainty is introduced via the efficiency fit function shown in Fig. 3.41. The fit is purely empirical, so a conservative estimate of systematic uncertainty is made by comparing the interpolated efficiency and residual at each point and selecting the largest error. Using this method, we estimate a 5% uncertainty in both modes.

3.13.6 Lepton ID

Uncertainty for lepton identification is taken from standard the Belle lepton identification (LID) error tables [45]. The uncertainty is estimated with off-resonance data and MC from this experiment; the efficiency tables are the 2010 Case B "new tracking set". The results are summarized in Table 3.11. Using this method, we estimate a 2% uncertainty for electrons and a 3% uncertainty for muons. This applies for both modes.

Table 3.11: Lepton ID Error Table

	Correction	Uncertainty
electron, MC	0.9771	$\pm$ 0.0176
muon, MC	0.9869	$\pm$ 0.0265
electron, data	0.9765	$\pm$ 0.0176
muon, data	0.9879	$\pm$ 0.0256

3.13.7 Tracking

The tracking resolution was reported in BN1165 [46] to be 0.34%. This applies for both modes.

3.13.8 Photon Energy Resolution

The uncertainty in photon energy resolution is addressed directly in Ref. [17]. In the 100 MeV range, the uncertainty approaches 2% with a 5×5 ECL matrix and 3% with a 3×3 ECL matrix. We did not use an E9/E25 cut due to its low efficiency for high A^0 mass signals, so we select the more conservative 3%. This applies for both modes.

As a separate check, we examine the difference between the expected and measured photon energy from decays of the π^0. We take the candidate photon 4-vector, $\mathbf{p_{candidate\_meas}}$, and combine it with the photon from another 4-vector in the event, $\mathbf{p_{other}}$. We then boost into the rest frame of $\mathbf{p_{candidate\_meas}} + \mathbf{p_{other}}$ (the "prime" frame) and create a $\mathbf{p}'_\pi$ vector. We set the energy component of the $\mathbf{p}'_\pi$ 4-vector to the π^0 rest mass, all other components are zero. We then calculate $\mathbf{p'_{candidate\_calc}} = \mathbf{p}'_\pi - \mathbf{p'_{other}}$. We then boost $\mathbf{p'_{candidate\_calc}}$ back into the lab frame and find the energy component of $\mathbf{p_{candidate\_calc}}$-$\mathbf{p_{candidate\_meas}}$. The ratio of this difference is then compared to the energy component of $\mathbf{p_{candidate\_meas}}$. Plots of this comparison are shown in Figs. 3.97 and 3.96.

The event selection criteria are as follows: one electron, one muon, two charged tracks, charge balance, must pass trigger condition, and must be a part of TauSkim B. The invariant mass of $\mathbf{p_{candidate\_meas}} + \mathbf{p_{other}}$ must be between 120 MeV/c^2 and 150 MeV/c^2.

The uncertainty was initially characterized by the RMS of the distributions in Figs. 3.96 and 3.97. Using this technique assumes all of the uncertainty lies with the measurement of the candidate photon. To account for this, the uncertainty from the RMS

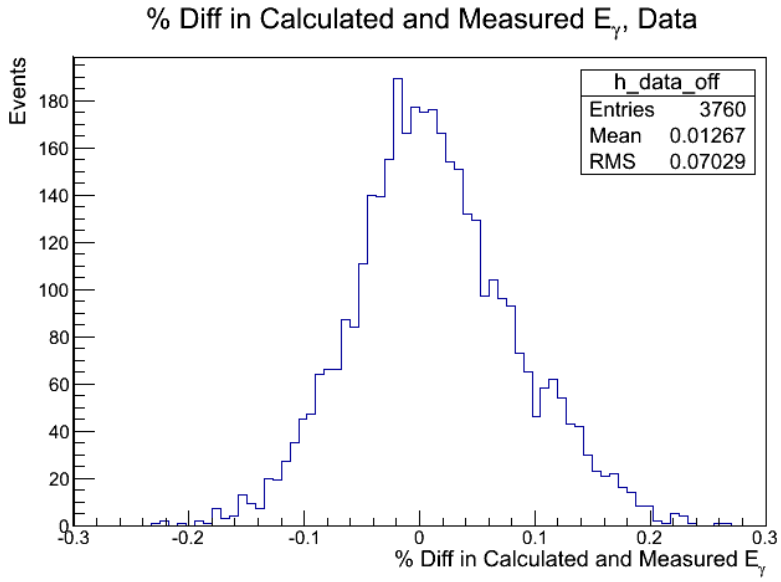

Figure 3.96: Percent difference between measured and expected energies of photons from π^0 decays in "e & μ" off-resonance data.

is scaled by a factor of $\sqrt{2}$. Using this technique, we find a systematic uncertainty of 4.5%. This applies for both modes.

3.13.9 Photon Detection Efficiency

This was measured to be 2% in Belle Note 499 [47]. This applies for both modes.

3.13.10 Overall Systematic Error

The individual contributions to the systematic uncertainty are summed in quadrature and applied to the upper limit of the combined branching ratio. For the "e & μ" mode, it is found to be 22%. For the "1-prong" mode, it is found to be 30%.

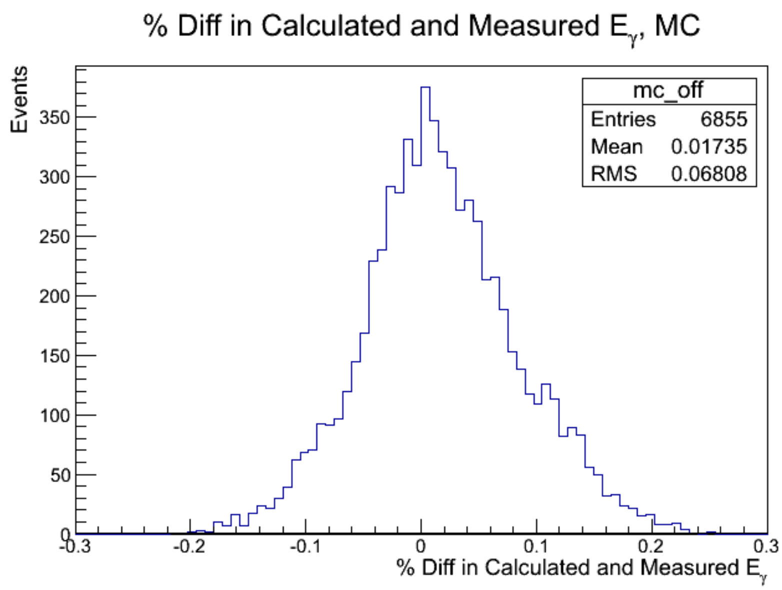

Figure 3.97: Percent difference between measured and expected energies of photons from π^0 decays in "e & μ" off-resonance MC.

Chapter 4

Conclusion

We conduct a search for a CP-odd light Higgs, A^0, in a sample of $(102 \pm 2) \times 10^6$ $\Upsilon(1S)$ by looking for $\Upsilon(1S) \to \gamma A^0$ radiative decays with $A^0 \to \tau^+\tau^-$. The motivation for this search is presented in Sections 1.5.3 and 1.5.4. Because $\Upsilon(1S) \to \gamma A^0$ is a two-body decay, the emitted photon will be mono-energetic and have a narrow peak in the photon CM energy spectrum dependent upon the mass of the A^0. We search for such a peak as evidence of the $\Upsilon(1S) \to \gamma A^0$; $A^0 \to \tau^+\tau^-$ decay.

To identify a sample of events where an $\Upsilon(1S)$ decays to τ-pairs, we use two sets of selection criteria: "e & μ" and "1-prong". Both sets require there to be exactly two oppositely-charged tracks in the event, at least one photon, and have selection requirements on parameters such as missing energy in the event, location of the candidate photon in the detector, whether the candidate photon could be used to reconstruct a π^0 with other photons in the event, etc. The "e & μ" criteria requires both an electron and a muon in the final state, whereas the "1-prong" criteria requires there to be an electron or at least muon in the final state while the other charged track may remain unidentified. The full lists of selection cuts for the "e & μ" and "1-prong" modes are located in Sections 3.7.2 and 3.11.2, respectively.

Using the "e & μ" selection criteria, we set an upper limit for the branching ratio $BR(\Upsilon(1S) \to A^0) \times BR(A^0 \to \tau\tau)$ between 1.6×10^{-5} to 1.01×10^{-4} for A^0 masses ranging from 3.6 GeV/c^2 to 9.3 GeV/c^2. This result matches the sensitivity seen in CLEO's $\Upsilon(1S)$ sample using a different selection criteria. The upper limit is plotted against A^0 mass in Fig. 4.1. A comparison between what is seen in data and what was predicted by MC is presented in Fig. 4.2. We find that the limit found in data is consistent with what was predicted by MC.

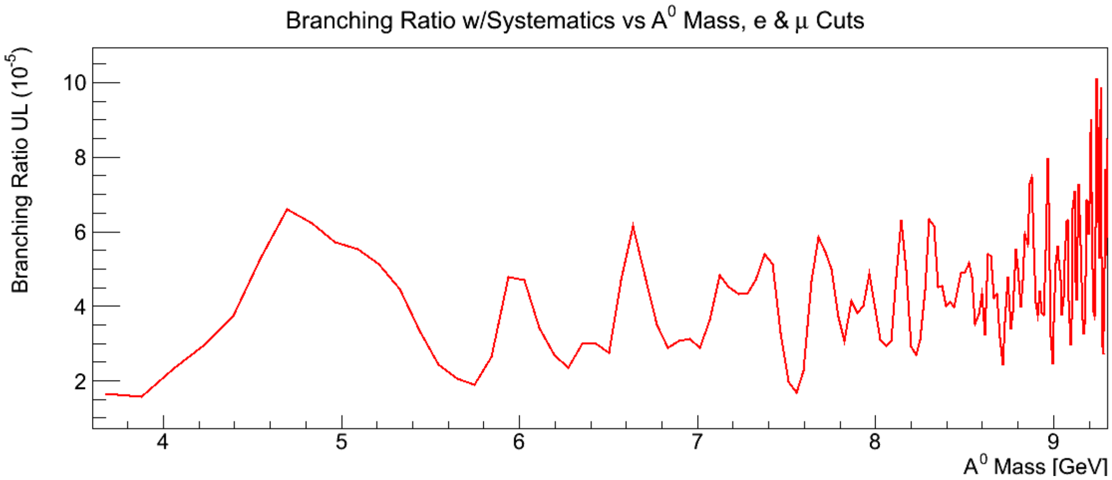

Figure 4.1: The 90% confidence level upper limit in data vs A^0 mass for $BR(\Upsilon(1S) \to A^0) \times BR(A^0 \to \tau\tau)$ with e & μ selection criteria. Systematic error is included.

Using the 1-prong selection criteria, we search for evidence of an A^0 with a mass between 3.6 GeV/c^2 and 9.3 GeV/c^2. We find no evidence for a peak in data that has a significance greater than 3σ. The significance is plotted against A^0 mass in Fig. 4.4. We then set an upper limit for the branching ratio $BR(\Upsilon(1S) \to A^0) \times BR(A^0 \to \tau\tau)$ between 4.0×10^{-6} to 4.5×10^{-5} for A^0 masses ranging from 3.6 GeV/c^2 to 9.3 GeV/c^2. Our upper limit is plotted against A^0 mass in Fig. 4.5. A comparison between what is seen in data and what was predicted by a MC sample representative of the data set is presented in Fig. 4.6; a comparison between the result in data and a running average of the results MC is presented in Fig. 4.7. The result in data is similar to what was predicted by MC.

The "1-prong" result is consistent with the approximately $\sqrt{5}$ improvement in sensitivity compared to CLEO one would expect with a data sample that is five times larger and limited by background. This also compares favorably with recent results [48] from BaBar using a sample of $\Upsilon(1S)$ taken from decays of $\Upsilon(2S) \to \pi^+\pi^-\Upsilon(1S)$ in a total sample of 9.8×10^7 $\Upsilon(2S)$.

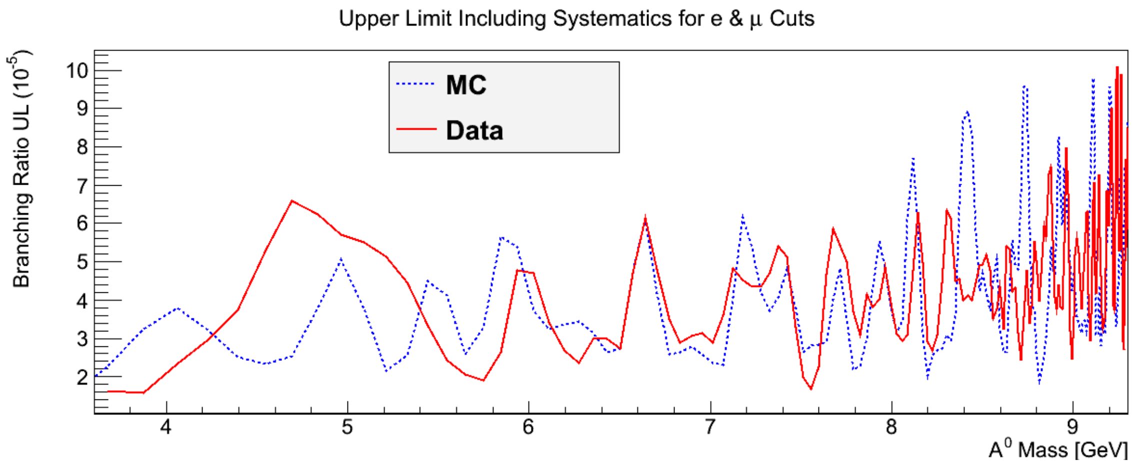

Figure 4.2: Comparison of the 90% confidence level upper limit vs A^0 mass for $BR(\Upsilon(1S) \rightarrow A^0) \times BR(A^0 \rightarrow \tau\tau)$ with e & μ selection criteria in data and MC. Systematic error is included.

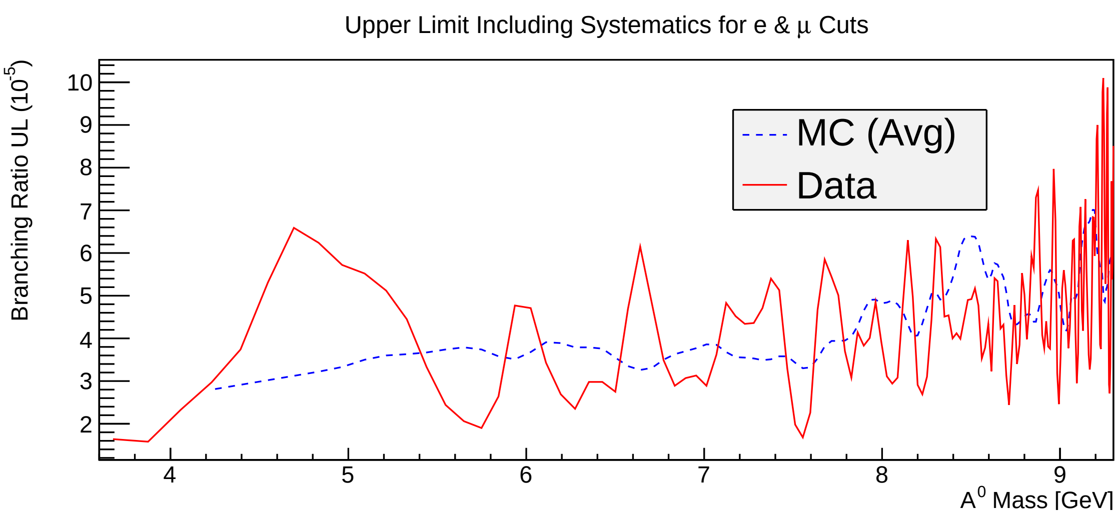

Figure 4.3: Comparison of the 90% confidence level upper limit vs A^0 mass for $BR(\Upsilon(1S) \rightarrow A^0) \times BR(A^0 \rightarrow \tau\tau)$ with e & μ selection criteria in data and averaged MC. Each point in MC above 4.3 GeV/c^2 is averaged with the 7 nearest points on either side; the point at 4.3 GeV/c^2 is averaged with the 3 nearest points on either side. 2% binning, systematic error is included.

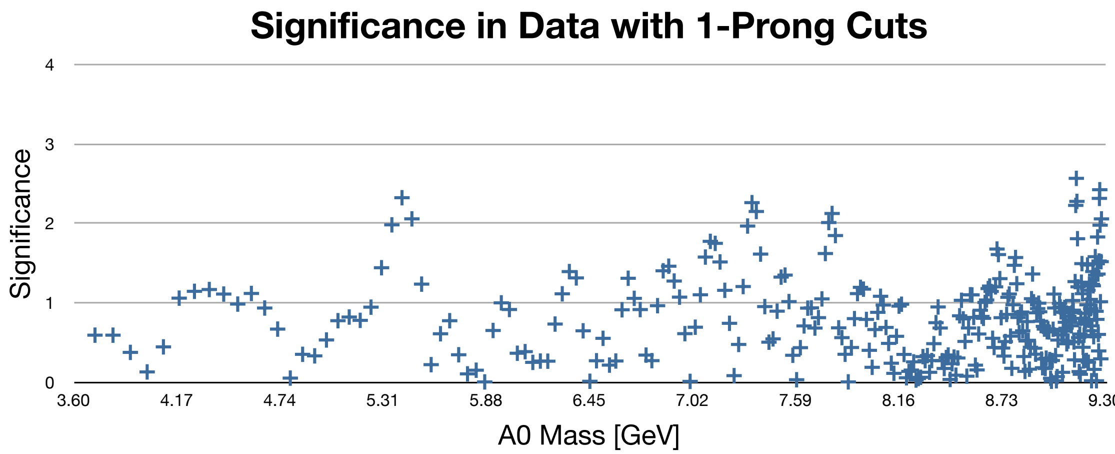

Figure 4.4: Significance in data vs A^0 mass for $BR(\Upsilon(1S) \to A^0) \times BR(A^0 \to \tau\tau)$ with 1-prong selection criteria. 1% binning.

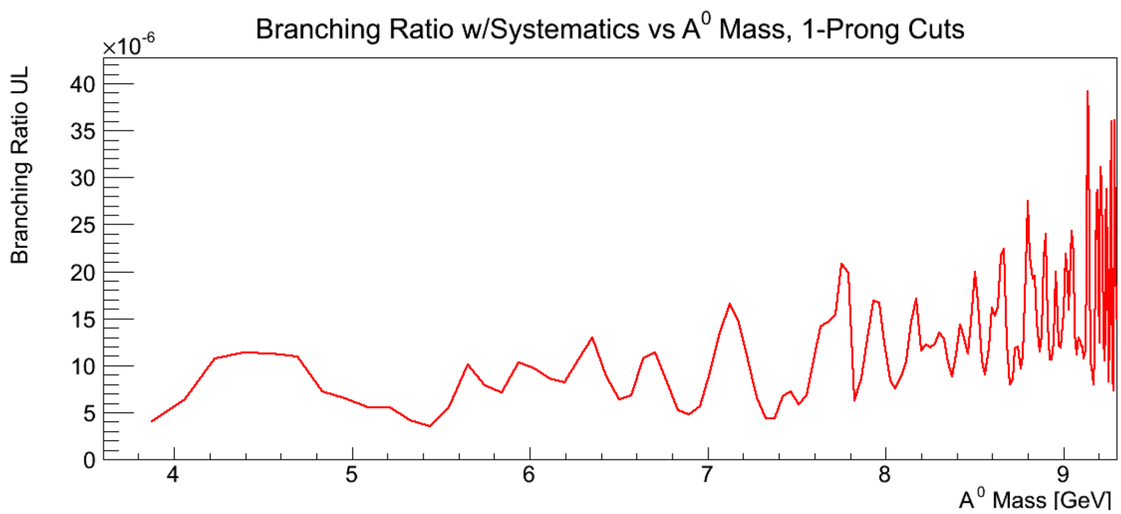

Figure 4.5: The 90% confidence level upper limit in data vs A^0 mass for $BR(\Upsilon(1S) \to A^0)\times BR(A^0 \to \tau\tau)$ with 1-prong selection criteria. 2% binning, systematic error is included.

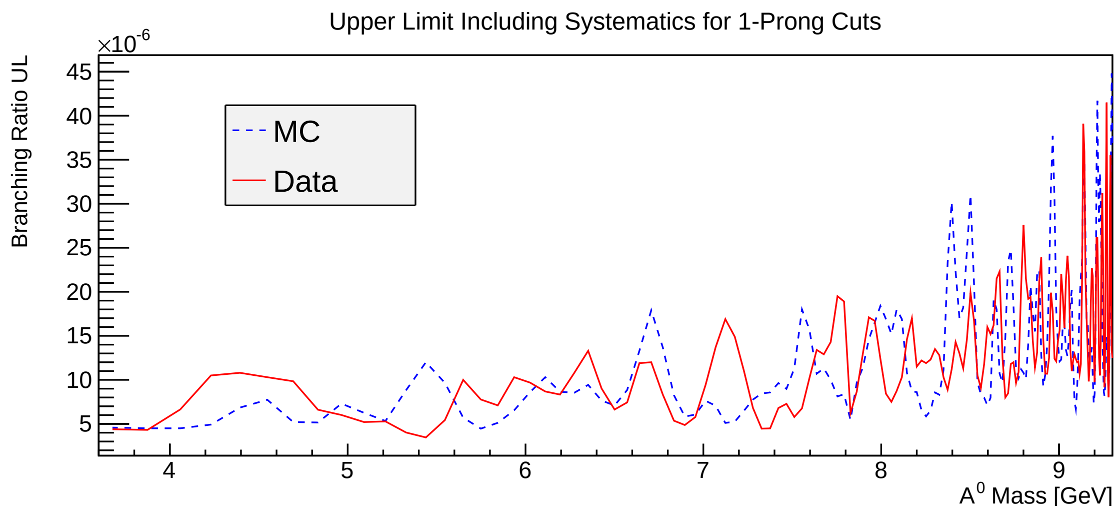

Figure 4.6: Comparison of the 90% confidence level upper limit vs A^0 mass for $BR(\Upsilon(1S) \to A^0) \times BR(A^0 \to \tau\tau)$ with 1-prong selection criteria in data and MC. 2% binning, systematic error is included.

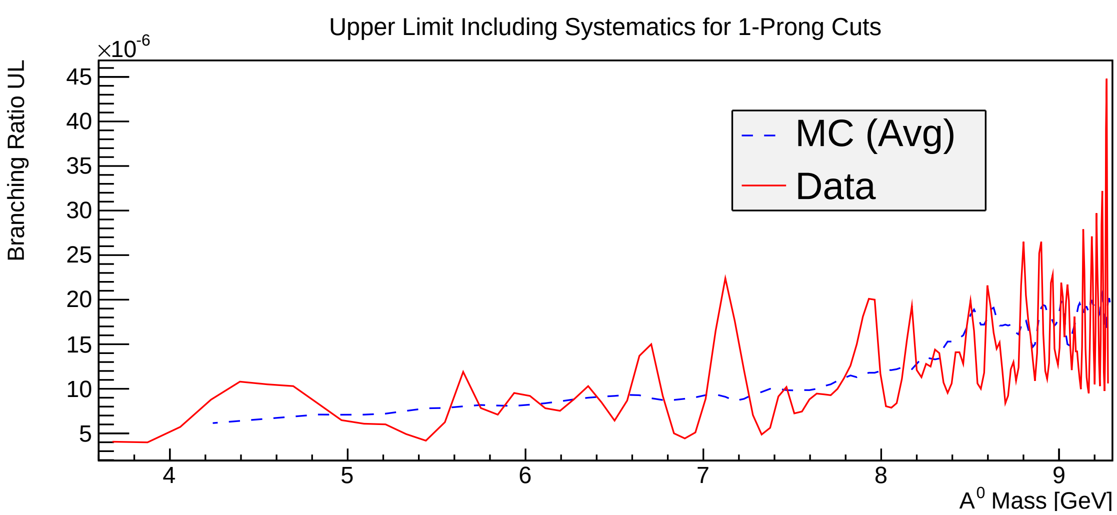

Figure 4.7: Comparison of the 90% confidence level upper limit vs A^0 mass for $BR(\Upsilon(1S) \to A^0) \times BR(A^0 \to \tau\tau)$ with 1-prong selection criteria in data and averaged MC. Each point in MC above 4.3 GeV/c^2 is averaged with the 7 nearest points on either side; the point at 4.3 GeV/c^2 is averaged with the 3 nearest points on either side. 2% binning, systematic error is included.

Appendix A

Combined Upper Limit

A.1 Introduction

After the study of the 1-prong mode was completed, it was suggested that we set a limit using the 1-prong mode with "e&μ" events removed. We would then combine this upper limit with the upper limit found for the "e&μ" mode and hopefully set an even lower 90% confidence level upper limit than what was seen with the 1-prong mode. A procedure for doing so was developed and implemented, but no such improvement was seen.

A.2 Notation Change

To simplify notation, the "e&μ" mode will be called the $e\mu$ mode, and the 1-prong mode with no events with both e and μ in the final state will be called the $!e\mu$ mode.

A.3 Selection Criteria

- The selection criteria for the $e\mu$ mode are the same as those in Section 3.7.
- The selection criteria for the $!e\mu$ mode are similar to those in Section 3.11, but with the added requirement that any event with both an electron and a muon in the final state (as identified by cut_muon and cut_electron) be removed.

A.4 Branching Ratios

The branching ratio of $\tau\tau \rightarrow mode$ are as follows:

- $\Gamma_{e\mu} = 6.2\%$
- $\Gamma_{!e\mu} = 54\%$

A.5 Selection Efficiency

Selection efficiency was determined by using the 1-prong mode signal MC and correcting for the loss of $e\mu$ events using PDG values. This resulted in 9,000 signal events per A^0 mass point from the original 10,000 event 1-prong signal MCs. The result and 4th order polynomial fit are shown in Fig. A.1. Note that the efficiencies in Fig. A.1 are in terms of percent, whereas the following equations are the ratio of final/initial with no scaling.

- $\epsilon_{e\mu} = -0.3658 + 0.39x - 0.1012x^2 + 0.01254x^3 - 0.0005807x^4$ where x = M_{A^0}[GeV].
- $\epsilon_{!e\mu} = -0.12913 + 0.23547x - 0.064551x^2 + 0.008258x^3 - 0.000404x^4$ where x = M_{A^0}[GeV].

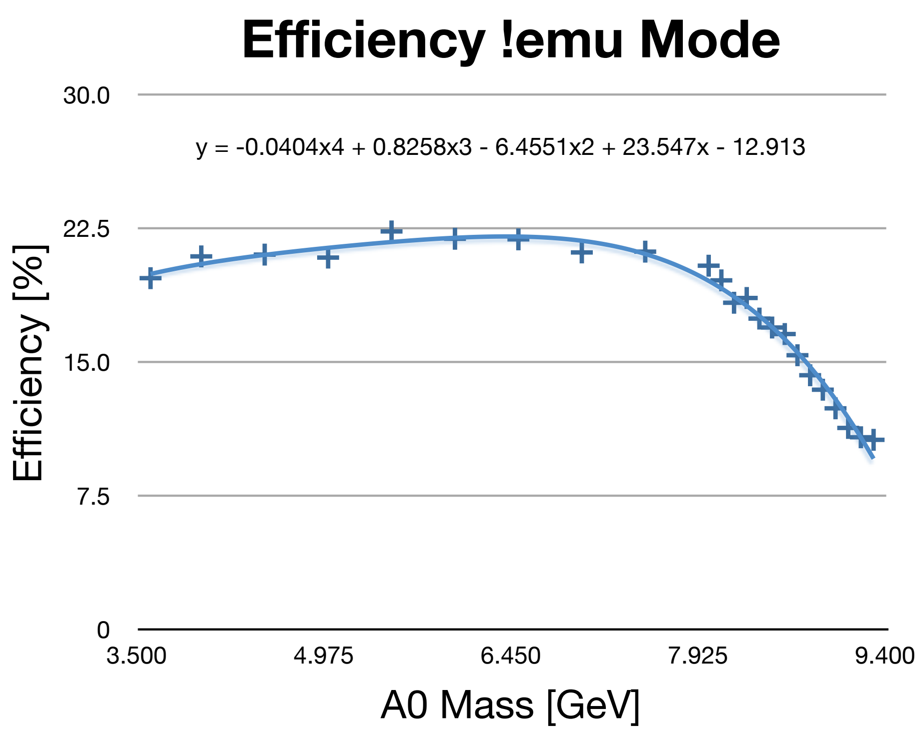

Figure A.1: Efficiency plot for the $!e\mu$ mode fit with a 4th order polynomial. Efficiencies are in percent.

A.6 Photon Background Fitting

The same background procedures used to fit the 1-prong mode were used to fit the backgrounds of $e\mu$ and $!e\mu$ modes. These procedures are discussed in detail in Sec. 3.12.

A.7 Simultaneous Fitting

The RooFit package allows for simultaneous fitting of separate decay channels via the RooSimultaneous class. A single root file was prepared for the both the $e\mu$ and $!e\mu$ MC samples; they were placed on trees h15 and h16 respectively. Models of background and signal for both $e\mu$ and $!e\mu$ samples were prepared separately as detailed in Sec. 3.12 with one exception: the signal yields (nsig) were declared to be functions of the same $\Upsilon(1S) \to \gamma A^0; A^0 \to \tau^+\tau^-$ branching ratio. Specifically:

$$nsig_{e\mu} = N_{\Upsilon(1S)} BR_{\Upsilon(1S)\to\gamma A^0} \times BR_{A^0\to\tau^+\tau^-} \times BR_{\tau^+\tau^-\to e\mu} \times \epsilon_{e\mu} \tag{A.7.1}$$

$$nsig_{!e\mu} = N_{\Upsilon(1S)} BR_{\Upsilon(1S)\to\gamma A^0} \times BR_{A^0\to\tau^+\tau^-} \times BR_{\tau^+\tau^-\to !e\mu} \times \epsilon_{!e\mu} \tag{A.7.2}$$

Scans of the $e\mu$ and $!e\mu$ photon spectrum were performed in parallel at each point and best fit values for $BR_{\Upsilon(1S)\to\gamma A^0} \times BR_{A^0\to\tau^+\tau^-}$ were returned. The fits at each point also produced a likelihood function for both the $e\mu$ and $!e\mu$ channels; the product of these forms a joint likelihood function for the combined result of the $e\mu$ and $!e\mu$ channels.

A.8 Upper Limit Calculation

Initial attempts at finding a 90% confidence level upper limit of the product branching ratio $BR_{\Upsilon(1S)\to\gamma A^0} \times BR_{A^0\to\tau^+\tau^-}$ using the BayesianCalculator in the manner described in Sec. 3.12.1 proved unsuccessful [49]. The joint likelihood function was too complicated to be integrated using the BayesianCalculator's adaptive integration technique. On the advice of RooStats experts on the RootTalk forum, we instead use the Markov Chain Monte Carlo (MCMC) technique to estimate the upper limit [50]. To test the stability of the MCMC result, we determine the upper limit for several different A^0 masses with the default 1,000 steps on the Markov chain. We then compare these to results found with 10,000 steps and 100 steps. The results for the 1,000 step and 10,000 step Markov Chains are found to be the same to within 1%. The 100 step Markov Chains varied more from the 10,000 step Markov

Chains and are not used. We set the MCMCCalculator function to take 10,000 steps at each test point with the first 50 steps discarded for "burn-in".

To compare with the 1-prong mode, we recalculated the upper limit of the 1-prong mode using the same MCMC technique. We then plot the upper limit vs A^0 mass for both the 1-prong mode with MCMC and the combined $e\mu$ and $!e\mu$ mode. The result of this is shown in Fig. A.2; we do not find that the combined upper limit offers any improvement over the 1-prong mode.

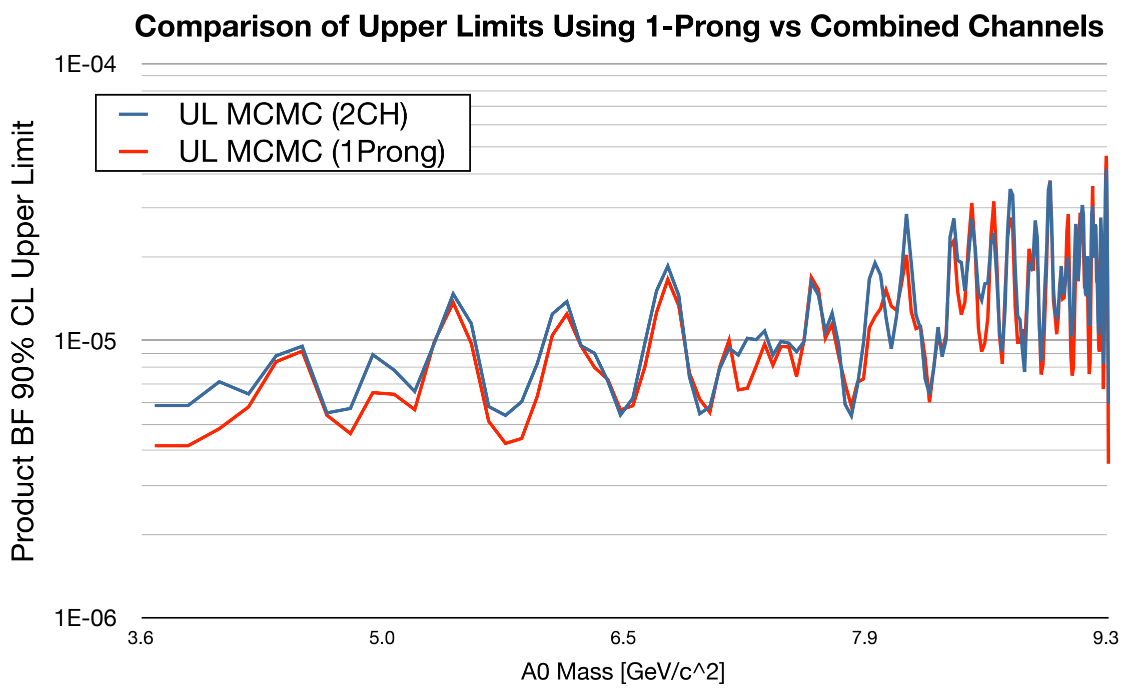

Figure A.2: Upper limit comparison between the 1-Prong mode (red) and the combined $!e\mu$ and $e\mu$ channels (blue).

Appendix B

Tables of Results

B.1 Introduction

This appendix presents the results of calculations that went into the significance plots for both the "e & μ" and 1-Prong modes.

B.2 Significance

The results for significances in the "1-prong" data scan are presented in Tables B.1, B.2, and B.3.

B.3 Upper Limit

The results for the 90% confidence level branching ratio (BR) upper limits in the "1-prong" scan are presented in Tables B.4 and B.5.

Table B.1: First table of significance results for the “1-prong ”data set.

A^0 Mass (GeV/c^2)	Significance	A^0 Mass (GeV/c^2)	Significance	A^0 Mass (GeV/c^2)	Significance
9.277	2.19	9.186	0.85	9.049	0.51
9.275	1.45	9.183	1.02	9.045	0.86
9.273	0.57	9.181	0.75	9.041	0.72
9.271	0.85	9.178	0.48	9.037	0.39
9.270	2.32	9.175	0.02	9.032	0.07
9.268	2.51	9.172	0.61	9.028	0.10
9.266	2.83	9.169	1.18	9.024	0.38
9.264	1.95	9.166	1.74	9.019	0.92
9.262	0.62	9.163	1.55	9.015	0.88
9.260	0.60	9.160	1.31	9.010	0.32
9.258	1.47	9.157	1.06	9.005	0.28
9.256	1.78	9.154	0.34	9.001	0.28
9.254	1.80	9.151	0.43	8.996	0.51
9.251	0.96	9.148	0.29	8.991	0.60
9.249	0.08	9.145	0.32	8.986	0.54
9.247	0.68	9.141	1.02	8.982	0.55
9.245	1.32	9.138	1.25	8.977	0.35
9.243	1.43	9.135	1.25	8.972	0.08
9.241	1.42	9.132	0.55	8.967	0.52
9.238	1.06	9.128	0.62	8.962	1.03
9.236	0.55	9.125	1.13	8.956	1.13
9.234	0.39	9.121	1.41	8.951	0.51
9.232	1.34	9.118	1.27	8.946	0.29
9.229	1.44	9.115	1.09	8.941	0.81
9.227	1.19	9.111	0.81	8.935	1.02
9.225	0.61	9.107	0.58	8.930	0.85
9.222	0.03	9.104	0.36	8.925	0.71
9.220	0.59	9.100	0.40	8.919	0.66
9.217	0.99	9.097	0.56	8.913	0.37
9.215	0.76	9.093	0.23	8.908	0.44
9.213	1.22	9.089	0.19	8.902	1.24
9.210	1.31	9.085	0.16	8.896	1.39
9.207	0.74	9.081	0.05	8.891	1.26
9.205	0.21	9.078	0.35	8.885	0.77
9.202	1.09	9.074	0.64	8.879	0.007
9.200	1.36	9.070	0.50	8.873	0.53
9.197	0.96	9.066	0.33	8.867	0.84
9.194	0.27	9.062	0.09	8.861	1.05
9.192	0.50	9.058	0.24	8.854	0.53
9.189	0.80	9.054	0.62	8.848	0.17

Table B.2: Second table of significance results for the “1-prong ”data set.

A^0 Mass (GeV/c^2)	Significance	A^0 Mass (GeV/c^2)	Significance	A^0 Mass (GeV/c^2)	Significance
8.842	0.04	8.523	0.42	8.025	0.90
8.835	0.18	8.513	0.62	8.010	0.37
8.829	0.31	8.503	0.80	7.994	0.26
8.822	0.42	8.493	0.95	7.978	1.19
8.816	0.56	8.483	0.64	7.962	1.42
8.809	1.15	8.473	0.23	7.945	1.62
8.802	1.35	8.462	0.10	7.929	1.40
8.795	1.45	8.452	0.16	7.912	1.19
8.789	1.02	8.441	0.15	7.895	1.13
8.782	0.30	8.430	0.58	7.878	1.12
8.775	0.32	8.419	0.27	7.860	0.72
8.767	0.95	8.408	0.13	7.843	0.41
8.760	0.74	8.397	0.49	7.825	0.55
8.753	0.60	8.386	0.68	7.807	0.10
8.746	0.39	8.374	0.75	7.788	0.18
8.738	0.17	8.363	0.75	7.770	0.24
8.731	0.39	8.351	0.48	7.751	0.21
8.723	0.72	8.339	0.06	7.732	0.24
8.715	1.25	8.327	0.30	7.713	0.22
8.708	1.19	8.315	0.54	7.693	0.37
8.700	1.60	8.303	0.38	7.674	0.27
8.692	1.07	8.290	0.16	7.654	0.12
8.684	0.59	8.278	0.08	7.633	0.07
8.676	0.03	8.265	0.02	7.613	0.10
8.667	0.25	8.252	0.17	7.592	0.18
8.659	0.37	8.239	0.02	7.571	0.60
8.651	0.09	8.226	0.16	7.550	0.81
8.642	0.08	8.213	0.31	7.528	0.69
8.634	0.21	8.199	0.10	7.507	0.63
8.625	0.69	8.186	0.59	7.484	0.15
8.616	0.70	8.172	1.19	7.462	0.31
8.607	0.88	8.158	1.14	7.439	0.42
8.598	1.04	8.144	0.61	7.416	0.25
8.589	0.46	8.130	0.36	7.393	1.07
8.580	0.27	8.116	0.10	7.370	1.40
8.571	0.78	8.101	0.62	7.346	1.97
8.562	0.80	8.086	0.91	7.321	1.80
8.552	0.81	8.071	1.04	7.297	1.19
8.543	0.62	8.056	0.98	7.272	0.35
8.533	0.24	8.041	0.88	7.247	0.26

Table B.3: Third table of significance results for the “1-prong ”data set.

A^0 Mass (GeV/c^2)	Significance	A^0 Mass (GeV/c^2)	Significance
7.221	0.76	5.821	0.06
7.195	1.10	5.773	0.01
7.169	1.93	5.725	0.66
7.142	2.13	5.675	1.11
7.115	2.39	5.624	1.02
7.088	2.05	5.572	0.13
7.060	1.48	5.520	0.87
7.032	0.55	5.466	1.47
7.004	0.22	5.411	1.98
6.975	1.12	5.355	1.56
6.945	1.42	5.298	0.74
6.916	1.67	5.240	0.45
6.885	1.91	5.180	0.37
6.855	1.72	5.120	0.61
6.824	1.09	5.057	0.35
6.792	0.23	4.994	0.36
6.760	0.50	4.929	0.18
6.728	1.17	4.862	0.09
6.695	1.56	4.794	0.49
6.661	1.71	4.724	0.73
6.627	1.22	4.652	1.03
6.593	0.66	4.579	0.94
6.558	0.003	4.503	0.94
6.522	0.40	4.426	0.94
6.486	0.62	4.346	1.28
6.450	0.27	4.264	0.67
6.412	0.19	4.180	0.35
6.375	0.53	4.093	0.14
6.336	0.56	4.003	0.45
6.297	0.60	3.910	0.79
6.257	0.17	3.814	1.00
6.217	0.05	3.714	1.00
6.176	0.05		
6.134	0.12		
6.092	0.06		
6.049	0.07		
6.005	0.48		
5.960	0.66		
5.915	0.49		
5.868	0.13		

Table B.4: First table of 90% confidence level BR upper limits in “1-prong” data.

A^0 Mass (GeV/c^2)	BR	A^0 Mass (GeV/c^2)	BR	A^0 Mass (GeV/c^2)	BR
9.275	1.1E-05	9.047	2.2E-05	8.522	1.7E-05
9.272	2.5E-05	9.039	2.0E-05	8.502	2.0E-05
9.268	4.5E-05	9.030	1.6E-05	8.482	1.7E-05
9.264	3.9E-05	9.021	2.0E-05	8.461	1.3E-05
9.260	1.5E-05	9.012	2.2E-05	8.440	1.4E-05
9.256	9.8E-06	9.003	1.5E-05	8.418	1.4E-05
9.252	1.2E-05	8.994	1.3E-05	8.396	1.1E-05
9.248	2.3E-05	8.984	1.4E-05	8.374	9.5E-06
9.243	3.2E-05	8.97	1.5E-05	8.350	1.1E-05
9.239	2.8E-05	8.965	2.3E-05	8.327	1.4E-05
9.234	1.6E-05	8.954	2.2E-05	8.302	1.4E-05
9.230	1.0E-05	8.944	1.3E-05	8.278	1.3E-05
9.225	1.3E-05	8.93	1.1E-05	8.252	1.3E-05
9.220	2.0E-05	8.922	1.2E-05	8.226	1.1E-05
9.216	2.4E-05	8.911	1.6E-05	8.200	1.2E-05
9.211	3.0E-05	8.900	2.7E-05	8.173	1.9E-05
9.206	1.7E-05	8.888	2.5E-05	8.145	1.6E-05
9.200	1.1E-05	8.877	1.4E-05	8.116	1.1E-05
9.195	1.4E-05	8.865	1.1E-05	8.087	8.4E-06
9.190	2.3E-05	8.852	1.3E-05	8.057	7.9E-06
9.184	2.7E-05	8.840	1.6E-05	8.027	8.0E-06
9.179	2.1E-05	8.827	1.8E-05	7.995	1.2E-05
9.173	1.5E-05	8.814	2.1E-05	7.963	2.0E-05
9.167	9.5E-06	8.800	2.7E-05	7.931	2.0E-05
9.161	1.0E-05	8.787	2.2E-05	7.897	1.8E-05
9.16	1.1E-05	8.773	1.2E-05	7.863	1.5E-05
9.15	1.5E-05	8.758	1.1E-05	7.827	1.3E-05
9.143	2.3E-05	8.744	1.3E-05	7.791	1.1E-05
9.136	2.8E-05	8.729	1.2E-05	7.754	1.0E-05
9.130	1.5E-05	8.714	9.2E-06	7.716	9.3E-06
9.123	1.0E-05	8.7	8.4E-06	7.677	9.4E-06
9.116	1.1E-05	8.682	1.2E-05	7.637	9.5E-06
9.11	1.3E-05	8.67	1.5E-05	7.596	8.8E-06
9.102	1.4E-05	8.649	1.5E-05	7.554	7.5E-06
9.094	1.4E-05	8.632	1.6E-05	7.511	7.2E-06
9.087	1.8E-05	8.615	1.9E-05	7.467	1.0E-05
9.079	1.5E-05	8.597	2.2E-05	7.422	9.1E-06
9.072	1.2E-05	8.579	1.2E-05	7.375	5.6E-06
9.064	1.5E-05	8.560	1.0E-05	7.328	4.9E-06
9.056	2.0E-05	8.541	1.1E-05	7.279	7.1E-06

Table B.5: Second table of 90% confidence level BR upper limits in the “1-prong” data.

A^0 Mass (GeV/c^2)	BR
7.23	1.21E-05
7.177	1.76E-05
7.124	2.24E-05
7.069	1.65E-05
7.013	8.88E-06
6.955	5.10E-06
6.896	4.43E-06
6.835	5.00E-06
6.772	9.20E-06
6.707	1.50E-05
6.640	1.37E-05
6.572	8.68E-06
6.501	6.43E-06
6.43	8.47E-06
6.35	1.03E-05
6.274	8.86E-06
6.194	7.53E-06
6.111	7.82E-06
6.025	9.20E-06
5.94	9.53E-06
5.844	7.10E-06
5.749	7.84E-06
5.649	1.19E-05
5.547	6.25E-06
5.440	4.18E-06
5.328	4.92E-06
5.213	6.01E-06
5.092	6.08E-06
4.965	6.48E-06
4.833	8.35E-06
4.694	1.03E-05
4.548	1.05E-05
4.394	1.08E-05
4.231	8.78E-06
4.059	5.72E-06
3.875	3.99E-06
3.68	4.06E-06

Appendix C

The STaR Board

C.1 Introduction

The Signal Timing and Readout (STaR) board was a prototype of an upgrade to the Belle Time of Flight (ToF) system. It was designed to handle the higher event rate expected from the 2006-2007 upgrade of the Belle detector. The STaR was to replace the time stretcher and readout described in Ref. [17] with a pipelined readout that connected to the Front-end Instrumentation Entity for Subdetector Specific Electronics (FINESSE) and Common Pipelined Platform for Electronics Readout (COPPER) [51]. The STaR itself consisted of two Large Analog Bandwidth Recorder and Digitizer with Ordered Readout version 3 (LABRADOR 3) [52] ASICs to sample analog signals from the ToF and two High Precision Time to Digital Converters HPTDCs [53]. Logic on the board was handled by an FPGA from Xilinx's Spartan-3 family. What follows is a summary of work on the STaR, concluded at the start of the $\Upsilon(1S)$ analysis.

C.1.1 Board Overview

The STaR follows the Time of Flight Front End Electronics (TOFFEE) [17] . The TOFFEE board sends to the STaR a copy of both the raw analog PMT signal and of a pulse correlated to the crossing of a low and high level threshold. The data is then recorded by the STaR and sent downstream via the COPPER.

Each STaR board can record the integrated charge and determine the threshold crossing time of 16 PMTs. The time-to-digital conversion (TDC), analog-to-digital conversion (ADC), and data formatting/transferring systems of the STaR can work independently, reducing the time the board is inactive after an event trigger from the GDL.

After initialization or reset of the board, the HPTDC and LABRADOR 3 continuously monitor the data from the TOFFEE. Upon receipt of a trigger from the GDL, the FPGA will ask the HPTDC to query its FIFO for events corresponding to that trigger. During this query the other components of the STaR work uninterrupted. If the query is negative, then the HPTDC will resume normal monitoring of the TOFFEE timing signal. If the HPTDC does find an event in its FIFO, it will return the timing data to the FPGA and then resume normal monitoring of the TOFFEE timing signal. The FPGA then orders LABRADOR 3 to perform an analog to digital conversion on the raw analog PMT signal from the TOFFEE. This is a three stage process: the LABRADOR 3 locks the voltage levels on the capacitors sampling the waveform, converts those locked values to digital values via an array of Wilkinson ADCs, and then transfers the digital values to the FPGA. During the second and third stages, the LABRADOR 3 can go back to sampling the raw PMT signal stream. When the data from the ADC arrives at the FPGA, the ADC and TDC information is then formatted via the COPPER standard and sent downstream.

C.2 Hardware

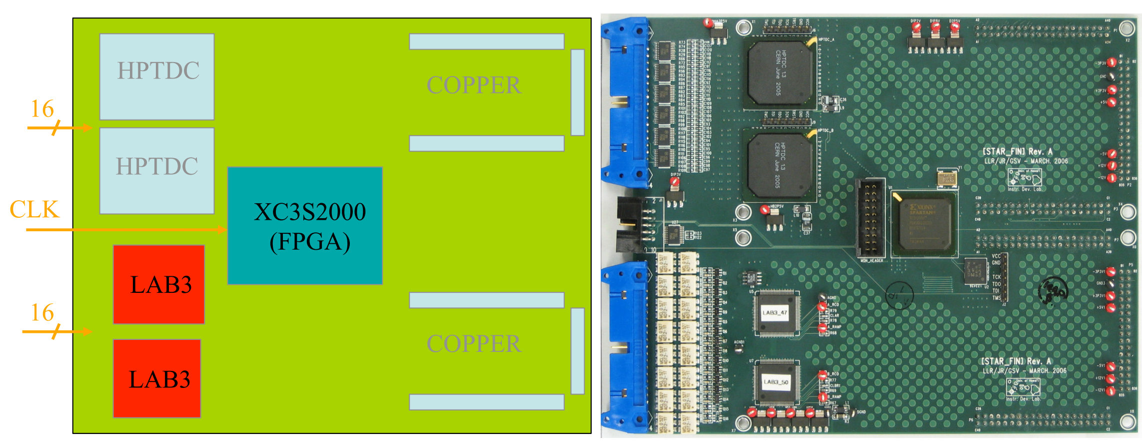

Figure C.1: Block diagram and photograph of the STaR board. Left: diagram showing the placement of the signal inputs, the LABRADOR 3 ADCs, the HPTDC TDCs, the FPGA used for control logic, and the output signal to the COPPER. Right: photograph of the STaR.

C.2.1 Data In

Each STaR has 16 ADC and TDC inputs. Both the ADC and TDC differential signals enter via 34-pin headers. The upper 34 pin connector leads to the TDC system; it accepts ECL signals and routes them to an LVDS converter before they arrive at an HPTDC. The lower 34 pin connector leads to the ADC block; it accepts a differential ADC signal from the TOFFEE and routes it to the LABRADOR3 chip.

C.2.2 Data Out

Data is sent via the 32 pins of the COPPER interface's A block. For more information on COPPER, see Ref. [54].

C.2.3 Clock

There are two clock sources on the STaR: an onboard 40MHz Schmitt oscillator for testing purposes and a dedicated clock input to receive a clock signal referenced to Belle. While the ADC and data formatting/transfer system can run off of the 40MHz clock during normal operation, one must pass in a clock signal derived from the Belle 512MHz clock for the HPTDC readings to be valid. The onboard clock can be monitored on the FPGA_CLK pin in the firmware or on the upper left pad of the Schmitt oscillator itself on the board.

C.2.4 COPPER Interface (I/O and Local Bus)

Each of the STaR I/O blocks conform to the COPPER standard where specified in for the COPPER interface. In normal firmware the upper block's data header is dedicated to the timing data, the lower block's data header is dedicated to the integrated charge information, and both blocks transfer data independently. In the counter test firmware both blocks are dedicated to the counter and both blocks act in parallel.

C.2.5 Diagnostics and FPGA Programming

The STaR board has JTAG programming pins for direct access to the FPGA and both HPTDCs. During normal operation the FPGA controls JTAG programming and readout of the HPTDCs, but this can be overridden if direct interface with the HPTDC JTAG is required. The FPGA has two sets of JTAG pins; one on the face of the board and another in the 10 pin breakout. The FPGA JTAG is been programmed in the Xilinx ISE

Suite using a platform cable model DLC9LP; the HPTDC JTAG is usually programmed via signals generated by the FPGA.

A 20 pin header is used to observe signals generated by or routed through the FPGA.

C.3 Firmware

C.3.1 HPTDC Operation

The HPTDC's operation are managed by two separate JTAG registers: the SETUP register and the CONTROL register. The code in the SETUP register determines the mode in which the HPTDC operates and must be programmed before the HPTDC starts taking data. This register cannot be altered during operation. The CONTROL register allows for enabling and disabling signals while the HPTDC is in operation. It also allows users to reset the PLL, the DLL, and the entire HPTDC via the JTAG. The JTAG can also be used as a status monitor during debugging with the STATUS register. All JTAG registers are programmed with a TTL signal operating at 20 Hz. Faster clock speeds are permitted by the HPTDC's JTAG, but fidelity issues with the signal from the FPGA prevented this.

Before the HPTDC can begin taking data, the SETUP register must be successfully programmed. It is recommended that the 40 MHz HPTDC clock input be held high during this time. To begin programming, reset the JTAG by holding the Test Data Input (TDI) pin high for five clock cycles and then proceed to access the JTAG Registers. When the SETUP string finishes a signal is sent to enable the HPTDC clock. Once the SETUP register has been programmed the HPTDC clock is applied and CONTROL registers are programmed. The HPTDC can be continually monitored via the STATUS register.

The parallel readout of the HPTDC has been enabled for event measurements. Trailers, headers, spacers, and non-catastrophic error flags have been turned off. Even though each HPTDC runs independently of the other, the 1 token per event system has still been implemented. The "get_data" signal is dependent on the "data ready" signal and the receipt of the GDL trigger.

C.3.2 LABRADOR 3 Operation

Firmware for the control of the LABRADOR 3 was provided by Larry Ruckman; information about the LABRADOR 3's operation and performance can be found in Ref. [52].

C.3.3 Testing

ADC capabilities of the STaR were tested in two ways: first by comparing the STaR ADC performance with that of a LeCroy 2249A ADC, and second by recording the waveform of a signal sent to the STaR ADC. The results of these tests are summarized in Sec C.4.

The TDC capabilities of the STaR were tested by sending timing signals directly to the STaR and trigger signals through various delay cables. The result from the TDC (the difference between each trigger and timing signal) was then recorded. Initial TDC testing did not include corrections for Integral Non-Linearity (INL); an example of the result from a set of tests with a single length of delay cable is given in Fig .C.2. Later tests attempting to create a look-up table to correct for INL were not successful.

Tests of the ADC and TDC systems operating simultaneously were performed. These tests revealed that a bug in the STaR firmware that caused the ADC system to sporadically ignore simulated triggers from the GDL. Work on the STaR was halted before the source of this bug could be found.

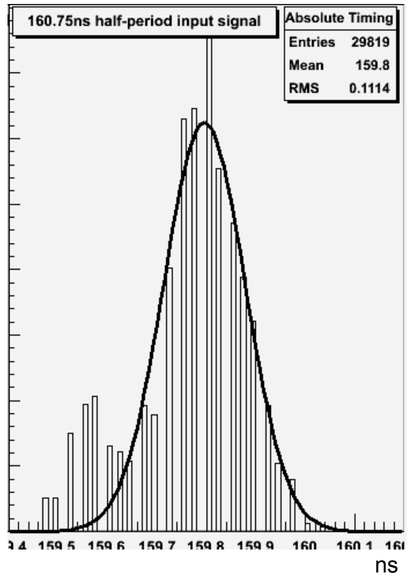

Figure C.2: HPTDC Testing. Measurement of the time delay between timing signal and a trigger signal routed through a 160 ns delay line. No INL correction has been applied.

C.4 IEEE Abstract

The STaR was presented at the IEEE Nuclear Science Symposium and Medical Imaging Conference in 2007; the submitted abstract follows.

Signal Timing and Readout (STaR) pipelined upgrade for the Belle TOF System

J. Rorie*, L. Ruckman and G. Varner

Department of Physics and Astronomy, University of Hawaii, 2505 Correa Road, Honolulu HI 96822, USA

Particle identification at KEKB facility's Belle Detector, – the world's highest luminosity collider – is performed by a composite system of sub-detectors. Of these, the TOF subsystem provides precision track timing information and uses pulse charge information to provide corrections to the event timing information. Continual accelerator upgrades have generated progressively higher detector hit rates and mandate readout system upgrades to manage larger event throughput. The STaR upgrade introduces a pipelined readout to the ToF system and will hopefully demonstrate reduced hit inefficiency and readout deadtime. Performance results for the ADC and TDC subsystems of the STaR are presented.

I. INTRODUCTION

Particle identification is crucial to the CP-violation and rare-decay physics program of a Giga B-meson pair "B Factory". Such an accelerator produces B mesons in sufficiently copious quantities to permit detailed scrutiny of standard model predictions in the flavor sector [1].

Belle's current ToF system utilizes scintillator bars and PMTs to precisely record the time of charged particle crossing. A bunch collision timing reference signal, based on the 508.9 MHz RF standard employed by the KEKB accelerator is used by a "time stretcher" circuit to expand the time interval from collision to this clock for recording by a multi-hit TDC with coarser time resolution. This same Fastbus TDC records the integrated charge using a charge-to-time (Q-to-T) circuit, where the resulting measured time is proportional to the charge [2].

By switching to a pipelined readout, we expect to effectively eliminate the dead time caused by the higher hit rate per channel at higher luminosities and background rates. The platform we have chosen to support this readout is the COmmon Pipelined Platform for Electronics Readout (COPPER) [3]. The Signal Timing and Readout (STaR) board is a daughtercard that plugs onto the COPPER mothercard, as depicted in Fig. 1.

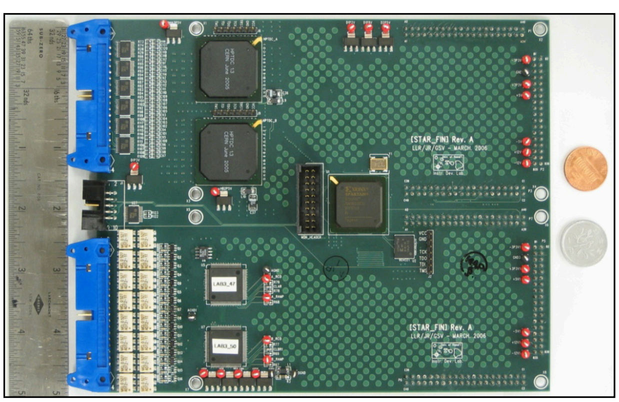

FIG. 1: Photograph of the STaR board

II. ARCHITECTURAL DETAILS

An overview of the ToF readout architecture is seen in figure 2.

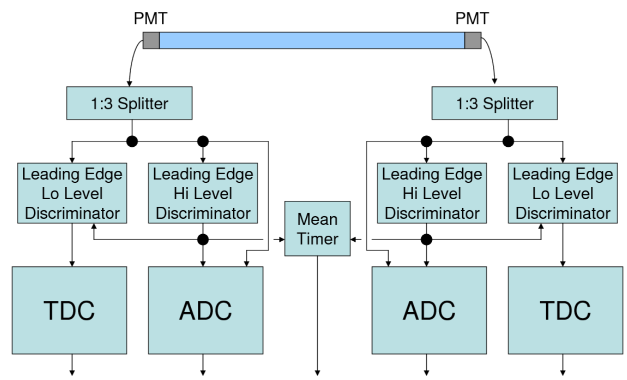

FIG. 2: A block diagram of the ToF readout scheme.

A. Time-to-Digital Conversion

The TDC block of the STaR board takes in 16 ECL pairs from Belle's TOFFEE board, converts them to a LVDS, and sends them to two High Precision Time to Digital Converter (HPTDC) ASICs[4]. There they are then measured with a precision of approximately 25 ps in high resolution mode. These measurements are stored in a 256 word deep FIFO which is read out upon request from the FPGA. The HPTDC can also send status and error updates via its parallel data pins and can be used for monitoring part of the TDC system.

B. Amplitude Recording

The ADC block of the STaR board takes in 16 analog signals from PMTs at the Belle detector. These signals are then routed to a pair of LABRADOR3 ADCs[5]. Each LABRADOR 3 can record up to 260 samples per channel per event. The window is set by adjusting the sample frequency. Data is sent from the COPPER to the FPGA where the data can then be pared down before being sent to the COPPER.

---

*Corresponding author: jrorie@hawaii.edu

C. Control Logic

Control of the STaR board is managed by a Spartan III FPGA. The STaR board has an on-board 40 MHz clock for bench testing but will accept an external clock for testing inside the Belle detector. The logic controls most of the functions of the LABRADOR3 and manages the readout of the HPTDC. It will also perform data manipulation and formatting before sending data packets to the COPPER's readout FIFO.

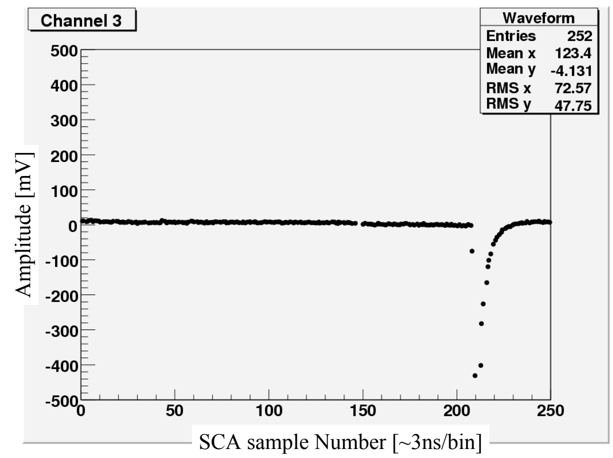

FIG. 3: Signal captured by the STaR block w/ pedestal subraction.

III. TEST RESULTS

Simulated PMT pulses approximately 15ns wide and ranging from 50mV to 2V amplitude were sent to the ADC block of the STaR. A sample waveform is shown in Fig. 3. Copies of these signals were also sent to a LeCroy 2249A ADC. QDC tests were performed using both integration and peak sampling techniques on the STaR and compared to results obtained by charge integration by the 2249A CAMAC module. A sample scan is plotted in Fig. 4. These results demonstrated that the STaR results agreed with the 2249A results to within a multiplicative factor and that the error on the STaR measurements were on the order of 1 percent.

IV. SUMMARY

By switching to a pipelined architecture, readout of the ToF subdetector should be able to handle the increased volume of data due to continual luminosity KEKB luminosity increases. This STaR prototype board evaluates this new readout scheme and provides valuable feedback for the production replacement system.

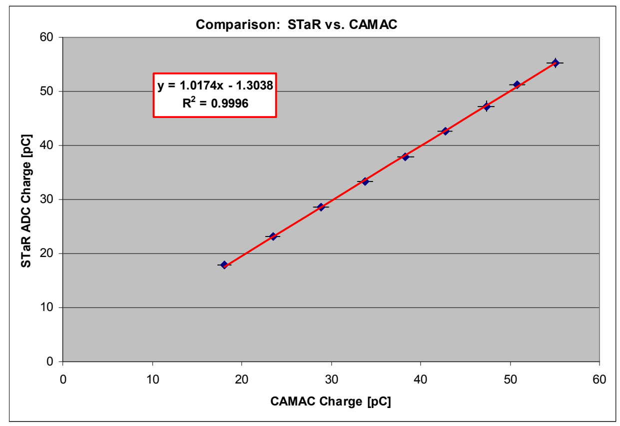

FIG. 4: Comparison of integrated charge calculated from STaR and LeCroy 2249A ADC data.

V. ACKNOWLEDGEMENTS

This work has been supported in part by the US-Japan Foundation, Department of Energy Award # DE-FG02-06ER41424, and the ARCS Foundation in cooperation with Doris and Bob Pulley.

[1] S. Hashimoto *(ed.) et al.*, KEK-Report-2004-4 (2004).
[2] H. Kichimi *et al.*,
[3] Y. Igarashi *et al.*, "The Data Acquisition System Based on PMC Bus", CHEP03 and available online as `physics/0304137`.
[4] J. Christiansen, HPTDC Manual ver 2.2 (2004). Available online at http://tdc.web.cern.ch/tdc/hptdc /docs/hptdc_manual_ver2.2.pdf
[5] G. S. Varner, J Cao, and M. Wilcox, LABRADOR User's Manual (2004). Available online at http://www.phys.hawaii.edu/~idlab/project_files /anita/docs/LABRADOR_Manual_v1.0.pdf

Appendix D

The Tau Skim

D.1 The Tau Skim

This appendix is a summary of the selection criteria for the most general tau skim, also known as Tau Skim B. This is located in Belle Note #0629 [26] and online at the URL given in Ref. [27].

- good charged track:(this depends on evtcls default)
- $Pt \geq 0.1$ GeV/c
- helix: $|dr| <$ 2 cm, $|dz|$ <5 cm
- good ECL cluster: $E_{ECLcluster} > 0.1$ GeV
- good Gamma: $E_{ECL} > 0.1$ GeV
- E_{rec} = Sum of P_{cm} (good charged tracks) in CM frame + Sum of Egamma in CM frame
- Pt_{max}: maximum Pt (good charged tracks)
- $E_{tot} = E_{rec} + |PmissCM|$
- N_{barrel}: No. of tracks with 30< θ <130° (barrel region)
- E_{ECLtrk}= Sum of E_{ECL} in CM - Sum of E_{gamma} in c.m.s.

1. 2≤ No. of good tracks ≤8

2. $|chargesum| \leq 2$

3. Sum of P_{cm}(good charged tracks)$<$ 10 GeV/c

4. Sum of $E_{ECL} < 10$ GeV

5. $Pt_{max} > 0.5$ GeV/c

6. Event vertex $|r| < 1$ cm,$|z| < 3$ cm

for 2 track events:

7. Sum of $E_{ECL} < 11$ GeV

8. $5^\circ < \theta$(missing momentum)$< 175^\circ$

9. $E_{rec} > 3$ GeV or $Pt_{max} > 1.0$ GeV/c

for 2-4 charged track case

10. $E_{tot} < 9$ GeV OR max opening angle $< 175^\circ$ OR 2 $<$Sum of $E_{ECL} < 10$ GeV

11. $N_{barrel} \geq 2$ or $E_{ECLtrk} < 5.3$ GeV

The value reported by evt_cls.flag(4) can further discriminate between the types of events in the sample.

1. 10-80 (Ntrk*10) : OLD condition cut-1 - cut-10 (see below)

2. 1010-1080 (Ntrk*10+1000) : except above

3. 1???? (Ntrk*10+1000+10000): only new criteria

Bibliography

[1] P. Langacker. *The Standard Model and Beyond*. Series in High Energy Physics, Cosmology and Gravitation Series. CRC Press, Inc, 2010. ISBN: 9781420079067.

[2] J. Beringer. "2012 Review of Particle Physics". In: *Phys. Rev. D* 86 (2012), p. 010001.

[3] D. Griffiths. *Introduction to Elementary Particles*. John Wiley & Sons, 1987. ISBN: 0-471-60368-4.

[4] F. Halzen and A. D. Martin. *Quarks and Leptons: And Introductiory Course in Modern Particle Physics*. John Wiley & Sons, 1984. ISBN: 0-471-88741-2.

[5] D. Perkins. *Introduction to High Energy Physics*. 4th Ed. New York, New York: Cambridge University Press, 2000. ISBN: 0 521 62196 8.

[6] C. Burgess and G. Moore. *The Standard Model: A Primer*. Cambridge University Press, 2006. ISBN: 978-0521860369.

[7] L. H. Ryder. *Quantum Field Theory*. 2nd Ed. Cambridge University Press, 2001. ISBN: 0521478146.

[8] P. Franzini and J. Lee-Franzini. "Upsilon Resonances". In: *Annual Review of Nuclear and Particle Science* 33.1 (Dec. 1983), pp. 1–28. ISSN: 0163-8998. DOI: `10.1146/annurev.ns.33.120183.000245`.

[9] C. Gay. "B Mixing". In: *Annual Review of Nuclear and Particle Science* 50.1 (2000), pp. 577–641. DOI: `10.1146/annurev.nucl.50.1.577`. arXiv:`0103016`.

[10] J. F. Gunion et al. *The Higgs Hunter's Guide*. Addison-Wesley Publishing Company, 1990. ISBN: 0-201-50935-0.

[11] S. Chatrchyan et al. "Observation of a new boson at a mass of 125 GeV with the CMS experiment at the LHC". In: *Physics Letters B* 716 (Aug. 2012), pp. 30–61. ISSN: 03702693. DOI: `10.1016/j.physletb.2012.08.021`.

[12] G. Aad et al. "Observation of a new particle in the search for the Standard Model Higgs boson with the ATLAS detector at the LHC". In: *Physics Letters B* 716.1 (Sept. 2012), pp. 1–29. ISSN: 03702693. DOI: 10.1016/j.physletb.2012.08.020.

[13] F. Wilczek. "Decays of Heavy Vector Mesons into Higgs Particles". In: *Physical Review Letters* 39.21 (Nov. 1977), pp. 1304–1306. ISSN: 0031-9007. DOI: 10.1103/PhysRevLett.39.1304.

[14] R. Dermíšek, J. F. Gunion, and B. McElrath. "Probing next-to-minimal-supersymmetric models with minimal fine tuning by searching for decays of the Υ to a light CP-odd Higgs boson". In: *Physical Review D* 76.5 (Sept. 2007). ISSN: 1550-7998. DOI: 10.1103/PhysRevD.76.051105.

[15] J. Ellis et al. "Is the mass of the Higgs boson about 10 GeV?" In: *Physics Letters B* 83.34 (1979), pp. 339–344. ISSN: 0370-2693. DOI: 10.1016/0370-2693(79)91122-5.

[16] D. Binosi and L. Theuß l. "JaxoDraw: A graphical user interface for drawing Feynman diagrams". In: *Computer Physics Communications* 161.12 (2004), pp. 76–86. ISSN: 0010-4655. DOI: 10.1016/j.cpc.2004.05.001.

[17] A. Abashian et al. "The Belle Detector". In: *Nuclear Instruments and Methods in Physics Research* 479 (2002), pp. 117–232.

[18] K. Nishimura. "First observation of the inclusive decay of B Xsη". In: *J. Phys. G* 37 (2010), p. 075021.

[19] C. W. Fabjan and F. Gianotti. "Calorimetry for particle physics". In: *Rev. Mod. Phys.* 75.4 (Oct. 2003), pp. 1243–1286. DOI: 10.1103/RevModPhys.75.1243.

[20] N. Takada. "Introduction to Belle Trigger". In: *Belle DAQ Workshop*. 2005.

[21] K. Hanagaki, M. Hazumi, and H. Kakuno. *BN0299: The Level 4 Software Trigger at Belle*. Tech. rep. 2000.

[22] K. Hanagaki et al. *BN0312: Status of Electron Identification*. 2000.

[23] L. Piilonen et al. *BN0338: Belle Muon Identification*. 2000.

[24] K. Miyabayashi. *BN0679: Shower Reconstruction and Photon Selection at Belle CsI (Tl) Calorimeter Shower Reconstruction Track Matching Photon Shower Selection*. 2003.

[25] X. L. Wang et al. *BN1138: Determination of the Number of Υ(1S) Events*. 2010.

[26] K. Inami. *BN0629: Note on the Tau Pair Skim*. 2003.

[27] K. Inami. *Tau Skim at Evtcls*.

[28] K. Hayasaka et al. "Search for Lepton-Flavor-Violating τ Decays Into Three Leptons with 719 Million Produced τ+τ- Pairs". In: *Physics Letters B* 687.2-3 (Apr. 2010), pp. 139–143. ISSN: 03702693. DOI: 10.1016/j.physletb.2010.03.037. arXiv:1001.3221.

[29] S. Banerjee et al. "Tau and Muon Pair Production Cross Sections in Electron-Positron Annihilations at sqrt[s]=10.58 GeV". In: *Physical Review D* 77.5 (Mar. 2008). ISSN: 1550-7998. DOI: 10.1103/PhysRevD.77.054012.

[30] V. Zhilich. *The Integrated Luminosity Collected with Belle*. 2010.

[31] S. Jadach, B. Ward, and Z. Was. "Coherent Exclusive Exponentiation for Precision Monte Carlo Calculations". In: *Physical Review D* 63.11 (May 2001). ISSN: 0556-2821. DOI: 10.1103/PhysRevD.63.113009.

[32] K. Inami. *Tau Analysis Page*. 2010.

[33] D. Lange. "The EvtGen Particle Decay Simulation Package". In: *Nuclear Instruments and Methods in Physics Research Section A: Accelerators,Spectrometers,Detectors and Associated Equipment* 462.1-2 (Apr. 2001), pp. 152–155. ISSN: 01689002. DOI: 10.1016/S0168-9002(01)00089-4.

[34] R. Brun, F. Carminati, and S. Giani. *CERN-W5013*. Tech. rep. 1994.

[35] S. Agostinelli et al. "Geant4: A Simulation Toolkit". In: *Nuclear Instruments and Methods in Physics Research Section A: Accelerators, Spectrometers, Detectors and Associated Equipment* 506.3 (2003), pp. 250–303. ISSN: 0168-9002. DOI: 10.1016/S0168-9002(03)01368-8.

[36] M. Lee. *Number of e+e- to tau+tau- to e nunu mu nunu [e,mu]*. 2010.

[37] M. Lee. *BN1088: Study of τ hh + h ν Decays with Unfolding Method*. 2010.

[38] W. Love et al. "Search for Very Light CP-Odd Higgs Boson in Radiative Decays of Υ(1S)". In: *Physical Review Letters* 101.15 (Oct. 2008), p. 12. ISSN: 0031-9007. DOI: 10.1103/PhysRevLett.101.151802. arXiv:0807.1427.

[39] R. Brun. “ROOT An object oriented data analysis framework”. In: *Nuclear Instruments and Methods in Physics Research Section A: Accelerators, Spectrometers, Detectors and Associated Equipment* 389.1-2 (Apr. 1997), pp. 81–86. ISSN: 01689002. DOI: 10.1016/S0168-9002(97)00048-X.

[40] W. Verkerke and D. Kirkby. “RooFit Users Manual v2 . 91”. 2008.

[41] K. Cranmer et al. “RooStats Users Guide”. 2010.

[42] S. S. Wilks. “The Large-Sample Distribution of the Likelihood Ratio for Testing Composite Hypotheses”. In: *The Annals of Mathematical Statistics* 9.1 (1938), pp. 60–62. DOI: 10.1214/aoms/1177732360.

[43] A. L. Read. “Modified Frequentist Analysis of Search Results (The CLs Method)”. In: *1st Workshop on Confidence Limits* (2000), pp. 81–101.

[44] G. Schott. “RooStats for Searches”. In: *ACAT2010 Conference Proceedings*. Mar. 2012. arXiv:1203.1547.

[45] L. Hinz. *BN0954: Lepton ID Efficiency Correction and Systematic Error*. 2006.

[46] B. Bhuyan. *BN1165: High PT Tracking Efficiency Using Partially Reconstructed D Decays*. 2010.

[47] H. W. Kim et al. *BN0499: Photon Detection Efficiency Using Radiative Bhabha Sample*. 2002.

[48] J. P. Lees et al. “Search for a Low-Mass Scalar Higgs Boson Decaying to a Tau Pair in Single-Photon Decays of Υ (1S)”. In: *PRD-RC (Submitted)* (2012). arXiv:1210.5669v1.

[49] J. Rorie and L. Moneta. *Combining Channels with Unbinned EML fits for Upper Limits*. 2012.

[50] J. Rorie and L. Moneta. *BayesianCalculator and Simultaneous Fit*. 2012.

[51] T. Higuchi et al. “Modular pipeline readout electronics for the SuperBelle drift chamber”. In: *Nuclear Science, IEEE Transactions on* 52.5 (2005), pp. 1912–1917. ISSN: 0018-9499. DOI: 10.1109/TNS.2005.856913.

[52] G. S. Varner et al. “The large analog bandwidth recorder and digitizer with ordered readout (LABRADOR) ASIC”. In: *Nuclear Instruments and Methods in Physics Research Section A: Accelerators, Spectrometers, Detectors and Associated Equipment* 583.23 (2007), pp. 447–460. ISSN: 0168-9002. DOI: `10.1016/j.nima.2007.09.013`.

[53] M. Mota and J. Christiansen. “A high-resolution time interpolator based on a delay locked loop and an RC delay line”. In: *Solid-State Circuits, IEEE Journal of* 34.10 (1999), pp. 1360–1366. ISSN: 0018-9200. DOI: `10.1109/4.792603`.

[54] T. Higuchi. *BN0791 - FINESSE Developer’s Guide*. Tech. rep. 2009.